# NOVEL SEMICONDUCTOR LASER-BASED ARCHITECTURES FOR DUAL-COMB SPECTROSCOPY IN THE NEAR-INFRARED, MID-INFRARED AND THz RANGES

by Borja Jerez González

in partial fulfilment of the requirements for the degree of Doctor in the Ph.D Program in Electrical Engineering, Electronics and Automation

**Universidad Carlos III de Madrid**

Advisor: Pablo Acedo Gallardo

Leganés, April 2019

*"Keep it nice, keep it sexy"*

# Acknowledgments / Agradecimientos

Diez años después de entrar en la Universidad Carlos III me hallo frente a una pantalla escribiendo la última página de esta Tesis Doctoral. Es una noche fría de Febrero, y creo que difícilmente pude imaginar allá por 2009, cuando iniciaba mi andadura en el mundo de la Ingeniería, que llegaría a este momento. Quiero aprovechar la ocasión para acordarme de todos aquellos que me habéis ayudado a ser lo que soy hoy. Este es mi pequeño homenaje para todos vosotros.

En primer lugar, quiero levantar la copa por aquellos que prendieron la mecha allá por 2013: Cristina de Dios y Rubén Criado, los que me acogieron en el grupo de investigación para empezar a empaparme de la vida en el laboratorio y, como no, por mi director de Tesis, Pablo Acedo, que me dio la oportunidad de seguir con el camino hasta el día de hoy a través de su eficiente y dedicada tutela. Gracias a todos por hacerme no solo mejor ingeniero, sino mejor persona.

No puedo olvidarme de toda la gente maravillosa que he conocido a lo largo de estos años de aprendizaje en el doctorado: Alba, Aldo, Dahiana, Dani, Dragos, Estefanía, Frederik, Guille, Helga, Jaime, Julio, Leonardo, Matteo, Miguel, Mónica y Wendy. Y como no podía ser de otra manera, mención especial para Óscar, por todos esos ratos de forzoso entendimiento intercultural, análisis futbolístico y cuñadismo en vena, y a Pedro, tanto por todo lo que me has enseñado dentro del laboratorio y tan esencial ha sido para esta Tesis como por los grandes momentos con una cerveza en la mano. Sin duda, la Tesis no habría sido ni de lejos lo mismo sin esas discusiones, referendos y planes para arreglar el país de los viernes.

Quiero también mandar un abrazo a esa gente irrepetible que conocí en los años en los que estuve estudiando el Máster. A Adri, Manu y Juanmi. Por las inigualables experiencias vividas juntos, y por todas las que nos quedan. Porque los años sigan pasando de esta manera. Por la *Whatever Crew*.

I would also like to thank my Liverpudlian friend, Andy, for his help in the production of this document and all the good moments. *When you walk through a storm, hold your head up high!*

A mis hermanos de la vieja escuela, Rafa y Gil. Por ser, utilizando el tópico, la familia que no se elige. Por tantos años de amistad y de fidelidad. Imagino que ya, habiendo pasado lo que hemos pasado, habrá que tirar para adelante. Porque, al fin y al cabo, siempre estáis ahí. O si no, en *La Sede*.

A mi familia. Sin lugar a dudas, sobre todo a mi padre, Juan, por su labor y comprensión a la hora de educarme y de facilitarme por todos los medios llegar hasta aquí. A mi madre, mis abuelos, y a todas esas personas que he perdido a lo largo de estos años y que desde algún lugar observan, espero que, con orgullo, la persona en la que me he convertido.

Y, por último, a Natalia. Por ser la luz en la oscuridad. Por tu complicidad. Por cómo me entiendes. Por ser tan única. Por nuestro humor incomprensible. Porque te quiero más que ayer, y menos que mañana. Sigamos bailando juntos y siendo parte de esto tan bonito que hemos creado.

# Abstract

The potential of Optical Frequency Combs as multimode sources featuring unprecedented high levels of accuracy, high resolution and broad bandwidth has rendered these instruments into one of the preferred tools across an ever-increasing range of disciplines. To fully capitalize on these astonishing virtues, one of the most successful approaches in recent years is the so-called dual-comb technique, or in a more general sense, dual-comb spectroscopy. The rationale of this method for comb detection lies in the employment of a second Optical Frequency Comb with different line spacing to simultaneously access to the whole spectral content of its counterpart, thus allowing for ultra-fast measurements (usually below one second) without sacrificing any of the outstanding capabilities of the Optical Frequency Combs. Nevertheless, in spite of the astounding development that dual-comb architectures have undergone in the past decade, advancements in terms of simplicity, robustness, associated cost, reduced footprint and adaptability to the target application are still underway.

In order to address this set of limitations, this Ph.D dissertation explores new possibilities for dual-comb spectroscopy and demonstrates their potential by means of several contributions across the most spectroscopically relevant regions of the electromagnetic spectrum (i.e., Near-Infrared, Mid-Infrared and the THz range). In particular, special emphasis has been laid on two aspects: the reduction in the design complexity regardless of the spectral region; and the external customization of the main set of parameters that dictate the performance of the sources so that they can easily fit the application of interest. For that purpose, different commercial off-the-shelf components, laser devices and well-established interdisciplinary techniques have been employed to establish synergies that have helped to increase the proficiency of these systems.

The present work has unveiled the first demonstrations of Near-Infrared (1.5 μm) dual-comb spectrometers whose operating principle stems from Gain-Switching in semiconductor lasers together with Optical Injection Locking and has further harnessed the use of the latter technique for the implementation of a novel multiheterodyne setup that relies on electro-optic modulation for remote comb detection. In a different original contribution, Near-Infrared dual-combs based on electro-optic modulation have been successfully shifted to the Mid-Infrared region via nonlinear mixing in a single periodically-poled lithium niobate crystal for ultra-fast absorption spectroscopy in the 3.5 μm region. Moreover, the use of large-

signal modulation has been applied to a single-mode Distributed Feedback Quantum Cascade Laser emitting at 7.5 μm to demonstrate the generation of coherent multiharmonic signals with adaptable line spacing for the first time in this kind of device. Finally, an innovative architecture based on electro-optic modulation and Optical Injection Locking has been devised for the photonic synthesis of THz dual-combs featuring a series of unprecedented characteristics in this spectral domain. This collection of schemes and methods have been successfully validated with a number of spectroscopic samples that exhibit different properties, from low-pressure gases (hydrogen cyanide or methane) and fibre Bragg grating sensors to electronic microwave filters, thus demonstrating the versatility of the proposed systems.

In summary, most of the efforts in this thesis have been devoted to the development of dual-comb architectures in the main spectral windows of interest for the scientific community, with special emphasis on flexible designs aimed to cater towards the requirements of a wide range of applications that may enable their eventual adoption beyond metrology laboratory environments.

# Resumen

El potencial de los peines de frecuencias ópticas como fuentes multimodo caracterizadas por su alta resolución, extenso ancho de banda o excepcional nivel de precisión ha permitido que estos instrumentos se hayan convertido en una de las herramientas preferidas para un número de disciplinas cada vez mayor. Con el fin de explotar estas virtudes, uno de los métodos que más éxito ha tenido en los últimos años consiste en la técnica de los peines duales (*dual-combs*), o, dicho de forma más común, espectroscopía con peines duales (*dual-comb spectroscopy*). Esta técnica para detección de peines de frecuencias ópticas se fundamenta en la utilización de un segundo peine con un espaciado en frecuencia distinto para acceder de forma simultánea a la totalidad del contenido espectral del primero, permitiendo así medidas ultrarrápidas (normalmente, por debajo de 1 segundo) sin la necesidad de sacrificar ninguna de las sobresalientes aptitudes que son características de los peines de frecuencias ópticas. No obstante, a pesar del gran desarrollo que las arquitecturas *dual-comb* han experimentado en la última década, existe todavía un gran número de avances en términos de simplicidad, robustez, coste asociado, tamaño y adaptabilidad a la aplicación de interés que se encuentran todavía en pleno desarrollo.

Con el objetivo de abordar estas limitaciones, esta Tesis Doctoral explora nuevas posibilidades para *dual-comb spectroscopy* y demuestra el potencial de las mismas a través de contribuciones a lo largo y ancho de las regiones del espectro electromagnético con más relevancia en términos espectroscópicos (es decir, Infrarrojo Cercano, Infrarrojo Medio y el rango de los THz). En particular, se ha hecho especial énfasis en dos aspectos: la reducción de la complejidad asociada al diseño con independencia de la región espectral, y la posibilidad de modificación externa del conjunto de parámetros que definen las propiedades de las fuentes ópticas, de tal manera que éstas puedan ajustarse fácilmente a la aplicación de interés. Con este fin, diversos componentes comerciales, dispositivos láseres y técnicas interdisciplinarias consolidadas han sido empleadas para crear sinergias que han permitido el desarrollo de las facultades de estos sistemas.

Expuesto lo anterior, el presente trabajo ha revelado las primeras demostraciones de espectrómetros *dual-comb* en Infrarrojo Cercano (1.5 μm) cuyo principio de operación reside en la técnica Gain-Switching en láseres de semiconductor junto con inyección óptica y, además, ha explotado la última de estas técnicas para la implementación un nuevo esquema multiheterodino basado

en modulación electro-óptica para la detección remota de peines de frecuencia óptica. Además, en otra contribución original, se ha llevado a cabo la transferencia de *dual-combs* basados en modulación electro-óptica desde el Infrarrojo Cercano hacia el Infrarrojo Medio a través de un proceso de mezclado no lineal en un único cristal periódicamente invertido de niobato de litio para realizar espectroscopía de absorción ultrarrápida en torno a 3.5 μm. Asimismo, el uso de modulación en gran señal se ha aplicado a un láser de cascada cuántica monomodo con emisión a 7.5 μm para demostrar la generación de señales multiarmónicas coherentes con un espaciado en frecuencia adaptable por primera vez en este tipo de dispositivos. Por último, se ha diseñado una arquitectura innovadora basada en modulación electro-óptica e inyección óptica para la síntesis fotónica de *dual-combs* en la región de los THz con una serie de características no vistas hasta la fecha en este dominio espectral. Esta colección de sistemas y métodos ha sido exitosamente validada por medio de una serie de muestras espectroscópicas que exhiben propiedades muy distintas, desde gases a baja presión (como ácido cianhídrico o metano) y sensores basados en redes de Bragg en fibra óptica hasta filtros electrónicos de microondas, demostrando, de esta manera, la versatilidad de los sistemas propuestos.

En definitiva, el trabajo principal de esta Tesis se ha dedicado al desarrollo de arquitecturas *dual-comb* en las principales regiones espectrales de interés para la comunidad científica, poniendo el acento sobre la realización de diseños flexibles orientados a satisfacer los requerimientos de un amplio número de aplicaciones que puedan permitir la eventual adopción de dichos sistemas más allá de los laboratorios de investigación.

# Published and Submitted Content

## Manuscripts Included in this Dissertation

**[M1]** **Borja Jerez**, Pedro Martín-Mateos, Estefanía Prior, Cristina de Dios and Pablo Acedo. "Dual optical frequency comb architecture with capabilities from visible to mid-infrared". Optics Express 24 (13), 14986-14994 (2016). DOI: 10.1364/OE.24.014986.

**[M2]** **Borja Jerez**, Pedro Martín-Mateos, Estefanía Prior, Cristina de Dios and Pablo Acedo. "Gain-Switching injection-locked dual optical frequency combs: Characterization and optimization". Optics Letters 41 (18), 4293-4296 (2016). DOI: 10.1364/OL.41.004293.

**[M3]** **Borja Jerez**, Frederik Walla, Cristina de Dios, Pedro Martín-Mateos and Pablo Acedo. "Fully frequency-locked multiheterodyne architecture for remote optical frequency comb rapid detection". Journal of Lightwave Technology 35 (19), 4195-4202 (2017). DOI: 10.1109/JLT.2017.2734895.

**[M4]** **Borja Jerez**, Pedro Martín-Mateos, Frederik Walla, Cristina de Dios and Pablo Acedo. "Flexible electro-optic, single-crystal difference frequency generation architecture for ultrafast mid-infrared dual-comb spectroscopy". ACS Photonics 5 (6), 2348-2353 (2018). DOI: 10.1021/acsphotonics.8b00143.

**[M5]** **Borja Jerez**, Rolf Szedlak, Pedro Martín-Mateos, Cristina de Dios, Pablo Acedo and Gottfried Strasser. "Large-signal modulation in distributed feedback quantum cascade lasers for coherent multiharmonic signal generation". Optical and Quantum Electronics, 50:351 (2018). DOI: 10.1007/s11082-018-1619-5.

**[M6]** **Borja Jerez**, Frederik Walla, Andrés Betancur, Pedro Martín-Mateos, Cristina de Dios and Pablo Acedo. "Electro-optic THz dual-comb architecture for high-resolution, absolute spectroscopy". Optics Letters 44 (2), 415-418 (2019). DOI: 10.1364/OL.44.000415.

*The content of these manuscripts represents the core of this Ph.D work and is fully covered in Chapters III, IV and V of this dissertation.*

# Published and Submitted Content

## Other Contributions during the Ph.D

**[X1]** Oscar Elías Bonilla-Manrique, Pedro Martín-Mateos, **Borja Jerez**, Marta Ruiz-Llata and Pablo Acedo. "High-resolution optical thickness measurement based on electro-optic dual-optical frequency comb sources". Journal of Selected Topics in Quantum Electronics 23 (2), 5300107 (2017). DOI: 10.1109/JSTQE.2016.2598607.

**[X2]** Julio Enrique Posada-Román, Hania Angelina, **Borja Jerez**, Marta Ruiz-Llata and Pablo Acedo. "Laser range finder approach based on a fieldable electro-optic dual optical frequency comb: A proof of concept". Applied Optics 56 (22), 6087-6093 (2017). DOI: 10.1364/AO.56.006087.

**[X3]** Pedro Martín-Mateos, **Borja Jerez**, Pedro Largo-Izquierdo and Pablo Acedo. "Frequency accurate coherent electro-optic dual-comb spectroscopy in real-time". Optics Express 26 (8), 9700-9713 (2018). DOI: 10.1364/OE.26.009700.

**[X4]** Pedro Martín-Mateos, **Borja Jerez**, Cristina de Dios and Pablo Acedo. "Mid-infrared heterodyne phase-sensitive dispersion spectroscopy using difference frequency generation". Applied Physics B, 124:66 (2018). DOI: 10.1007/s00340-018-6935-8.

**[X5]** Borislav Hinkov, Jakob Hayden, Rolf Szedlak, Pedro Martín-Mateos, **Borja Jerez**, Pablo Acedo, Gottfried Strasser and Bernhard Lendl. "High frequency modulation of mid-infrared ring quantum cascade lasers". Submitted to Optics Express (2019).

# Published and Submitted Content

## Conference Papers

**[C1]** Oscar Elías Bonilla-Manrique, José Antonio García-Souto, Pedro Martín-Mateos, **Borja Jerez** and Pablo Acedo. "Fast interrogation of fiber Bragg grating sensors using electro-optic dual optical frequency combs". The International Conference on Optical Fibre Sensors, paper 963422 (2015). DOI: 10.1117/12.2195288.

**[C2]** Pedro Martín-Mateos, **Borja Jerez**, Estefanía Prior, Cristina de Dios and Pablo Acedo. "Optical communication components characterization using electro-optic dual-combs". The European Conference on Lasers and Electro-Optics, paper AM2J.5 (2016). DOI: 10.1364/CLEO_AT.2016.AM2J.5.

**[C3]** **Borja Jerez**, Frederik Walla, Cristina de Dios, Pedro Martín-Mateos and Pablo Acedo. "Fully remote rapid multiheterodyne spectroscopy based on the remote detection of an optical frequency comb through optical injection locking and electro-optic comb generation". The European Conference on Lasers and Electro-Optics, paper ED_P_5 (2017). DOI: 10.1109/CLEOE-EQEC.2017.8087483.

**[C4]** Frederik Walla, **Borja Jerez**, Pedro Martín-Mateos, Cristina de Dios and Pablo Acedo. "Absolute-frequency high-resolution real-time terahertz dual-comb spectrometer". The International Conference on Infrared, Millimeter and Terahertz Waves, paper WA4.3 (2017). DOI: 10.1109/IRMMW-THz.2017.8067218.

**[C5]** **Borja Jerez**, Pedro Martín-Mateos, Frederik Walla, Cristina de Dios and Pablo Acedo. "Absolute-frequency, high-resolution terahertz dual-comb spectrometry based on electro-optic optical frequency combs". The EMN Meeting on Terahertz (Invited Talk) (2018).

**[C6]** **Borja Jerez**, Andrés Betancur, Pedro Martín-Mateos, Cristina de Dios and Pablo Acedo. "Multi-octave spanning, absolute frequency, high resolution THz dual-comb spectrometer based on electro-optic modulators: first spectroscopic measurements". Light, Energy and the Environment, paper JW4A.2 (2018). DOI: 10.1364/FTS.2018.JW4A.2.

# Table of Contents

# List of Acronyms and Chemical Compounds

| | |
|---|---|
| AOM | Acousto-Optic Modulator |
| $C_2H_2$ | Acetylene |
| CARS | Coherent Anti-Stokes Raman Spectroscopy |
| CCD | Charge-Coupled Device |
| $CH_4$ | Methane |
| CO | Carbon Monoxide |
| $CO_2$ | Carbon Dioxide |
| CW | Continuous-Wave |
| DFB | Distributed Feedback |
| DFG | Difference Frequency Generation |
| DKS | Dissipative Kerr Soliton |
| DM | Discrete Mode |
| EDFA | Erbium-Doped Fibre Amplifier |
| EO | Electro-Optic |
| EOM | Electro-Optic Modulator |
| FBG | Fibre Bragg Grating |
| FTIR | Fourier-Transform Infrared |
| FWHM | Full Width at Half Maximum |
| FWM | Four-Wave Mixing |
| GaAs | Gallium Arsenide |
| GaP | Gallium Phosphide |
| GaSe | Gallium Selenide |
| GS | Gain-Switching |
| $H_2O$ | Water / Water Vapour |
| HCN | Hydrogen Cyanide |
| ICL | Interband Cascade Laser |
| InGaAs | Indium Gallium Arsenide |

| | |
|---|---|
| LOD | Limit of Detection |
| MCT | Mercury Cadmium Telluride |
| MgO:PPLN | Magnesium-Doped Periodically-Poled Lithium Niobate |
| MLL | Mode-Locked Laser |
| $N_2O$ | Nitrous Oxide |
| NEA | Noise-Equivalent Absorption |
| $NH_3$ | Ammonia |
| NO | Nitric Oxide |
| OFC | Optical Frequency Comb |
| OIL | Optical Injection Locking |
| OP | Orientation-Patterned |
| OPO | Optical Parametric Oscillator / Oscillation |
| PCA | Photoconductive Antenna |
| PIC | Photonic Integrated Circuit |
| PPLN | Periodically-Poled Lithium Niobate |
| QCL | Quantum Cascade Laser |
| QPM | Quasi-Phase-Matching / Matched |
| RF | Radiofrequency |
| SHG | Second Harmonic Generation |
| SNR | Signal-to-Noise Ratio |
| VIPA | Virtually-Imaged Phased Array |
| WDM | Wavelength Division Multiplexer / Multiplexed |
| ZnS | Zinc Sulphide |
| ZnSe | Zinc Selenide |

# I

# Introduction

# 1.

# The Optical Frequency Comb. History and Applications

In theoretical terms, an Optical Frequency Comb (OFC) is an ensemble of evenly-spaced, tightly phase-locked optical frequencies, in a similar fashion to a collection of harmonized lasers operating simultaneously. A simplified version of an OFC is depicted in Figure 1. *A priori*, the non-expert reader may assume this is a simple concept, a basic tool in the field of Photonics; however, this apparently simple idea has had astonishingly far-reaching implications.

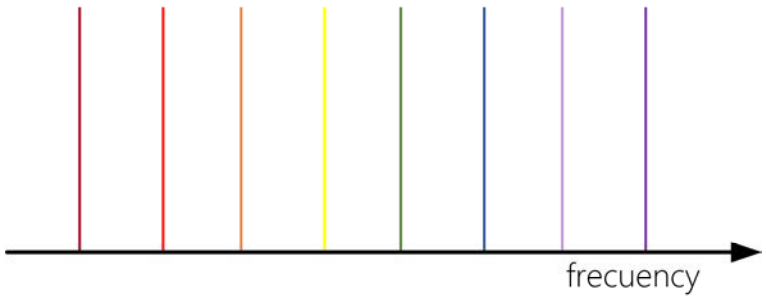


Figure 1. Basic illustration of an OFC. Each tooth or frequency of the comb corresponds to a different colour, arranged according to its frequency in the electromagnetic spectrum.

To understand the origin of OFCs, it is necessary to analyse how scientists used to measure light at the end of the 1980s. At that time, this process was carried out by bulky harmonic frequency chains starting with an atomic clock referenced to an atomic transition that, in conjunction with a collection of auxiliary oscillators and nonlinear elements, passed through several regions of the electromagnetic spectrum to measure one single optical frequency[1]. Work in this direction was performed by research groups across the world in order to perfect the measurements of light[2,3]. However, it all changed with the advent and evolution of

the OFCs, a milestone that led to a drastic reduction in the complexity associated with these experiments.

The basic method to create OFCs relies on the generation of a stable train of optical pulses in time. Of course, there are several mechanisms to create these pulses, as will be discussed in the following sections of this thesis, but the original method consisted of the use of Mode-Locked Lasers (MLLs) that emit a regular train of femtosecond pulses. In the frequency domain, an infinite number of copies of these pulses lead to the above-mentioned collection of sharp, equally-spaced lines. Figure 2 shows a realistic version of a frequency comb produced by an MLL. The frequency of any line of the comb ($f_N$) can be straightforwardly defined according to (1), where $f_{REP}$ is the repetition frequency or separation between adjacent teeth (which is the reciprocal of the repetition rate of the pulses in the time domain) and $f_{CEO}$ exemplifies the phase slips between pulses due to dispersion in the cavity, which translates into a nonzero frequency offset. Finally, the width of the pulses is inversely proportional to the bandwidth of the OFC. In this sense, the generation of ultra-short pulses is desired to produce broadband frequency combs, as the amplitudes of the lines will progressively decrease for any frequencies above the reciprocal temporal pulse width.

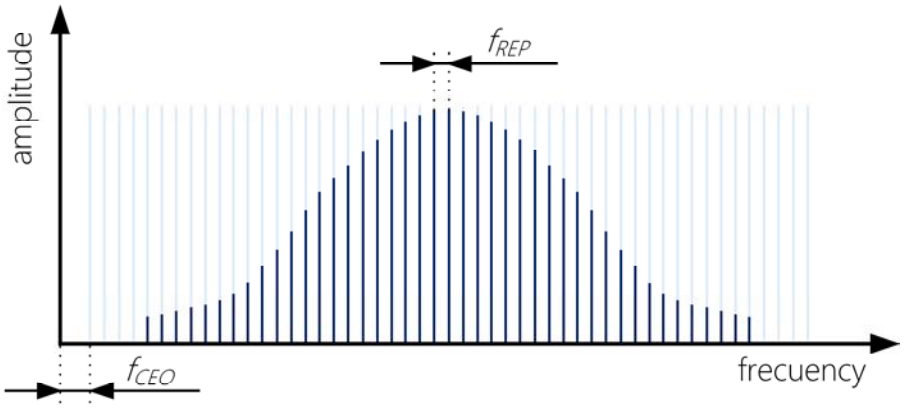


Figure 2. Sketch of a real OFC including its defining frequencies $f_{REP}$ and $f_{CEO}$. Note the unequal distribution of power across the lines.

$$f_N = f_{CEO} + nf_{REP} \tag{1}$$

It is clear, therefore, that if one can control both $f_{REP}$ and $f_{CEO}$, the frequency of any comb lines can be ascertained with an accuracy only limited by the stability of the frequency standard. The former can be monitored by detecting the beatnote of the comb teeth in a photodetector with enough bandwidth, whereas the latter can be detected providing that the comb bandwidth extends over one octave in frequency by means of a process which is usually denominated as *self-referencing*.

In this scheme, one of the frequency-doubled lines of the red end of the spectrum is heterodyned with the corresponding lines of the blue end, thus unveiling the offset in frequency of the comb. This being said, an OFC may be understood as a frequency ruler which can be used as a two-direction link between optical and microwave frequencies, providing an extremely accurate device for metrology purposes whose optical frequencies are exactly known if they are linked to a stable reference.

In the quest for the generation of pulse trains (and therefore, OFCs), one of the first demonstrations was reported in 1978 by the group of Theodor W. Hänsch, who revealed the generation of sub-picosecond pulses by means of a synchronously pumped dye laser[4]. However, at that time, they were unable to measure the absolute frequencies of each of the lines of their frequency comb due to its limited bandwidth. Remarkably, it took almost two decades to unveil the full potential of frequency combs in terms of accuracy. It was 1998 when the group of Theodor W. Hänsch finally demonstrated the astonishing performance of the Ti:Sapphire Laser-based OFC[5,6], an experiment which was rapidly followed by the first measurement of an absolute optical frequency by employing that instrument and an adaptation of the optical frequency internal dividers that they used in their harmonic chains[7].

This was only the beginning of the revolution of accuracy. Key factors of this maturity were both the availability of commercial femtosecond Ti:Sapphire Lasers and the development of nonlinear fibres with potential to expand the frequency span of the comb more than one octave. This approach greatly simplified the setup in comparison to the first demonstrations of absolute referencing, as new works of the group of John L. Hall shortly revealed[8–10]. The crowning point of this process took place in 2005, when Theodor W. Hänsch and John L. Hall were awarded half of the Nobel Prize in Physics for their outstanding contribution to laser-based precision spectroscopy[11,12]. Nevertheless, the work in this field has continued until our days with ever-increasing accuracies and fractional uncertainties which nowadays lie below $10^{-18}$ [13].

There is no doubt that OFCs have become standard tools for precision spectroscopy in metrology laboratories across the world[14], but perhaps, it is just as impressive the way this instrument has permeated an increasingly growing number of fields and applications. After the first successful demonstrations of their potential, it did not take long until frequency combs further evolved into a priceless instrument which has even become the workhorse of some disciplines. Some of the more relevant applications are listed below (Table 1) alongside a brief

description of the utility of the comb. For a more comprehensive description of the impact of the OFCs on the applications outlined here, the author refers to a number of papers covering the introduced notions in depth[13,15,16].

Table 1. Overview of applications involving frequency combs.

| Application | Utility of the Frequency Comb |
|---|---|
| Optical clocks[17] | Precise measurement of lasers locked to atomic transitions |
| Calibration of tunable lasers[18] | Use of the comb as a frequency ruler to know the frequency of the laser |
| Calibration of astronomical spectrographs[19] | Long-term stability to replace the optomechanical systems currently used in the calibration of spectrographs |
| Spectroscopy[20] | Direct interrogation of a sample. Retrieval of molecular line shapes or spectral information |
| Frequency/time transfer[21] | Synchronization across fibre networks taking advantage of the phase coherence of the OFC |
| Microwave generation[22] | Seed for the generation of high-quality RF waveforms after being phase-locked to a reference or cavity |
| Ranging[23] | Use of the comb as a spatial ruler to measure distances |
| Arbitrary waveform generation[24] | Feasibility for using the comb teeth to imprint specific amplitude and phase profiles and subsequent detection |
| Optical communications[25] | Coherent transmission and detection of the information associated with each of the teeth of the comb |

As the reader might probably infer, the employment of frequency combs and their specific features is truly application-dependent. For example, the calibration of astronomical spectrographs usually requires combs with mode spacings in the range of tens of GHz, whereas high-resolution spectroscopy of gas samples at low pressures demands repetition frequencies of only tens or hundreds

or MHz. Although an OFC can always be determined by the set of frequencies aforementioned, its elemental definition is purely functional; some authors claim that it is just any femtosecond lasers whose elemental parameters ($f_N$, $f_{REP}$ and $f_{CEO}$) can be measured and controlled[13], whereas others maintain that an OFC is any ensemble of correlated lines in the frequency spectrum which can be used for a specific purpose. In this sense, there is a set of main characteristics of an OFC to bear in mind for the application of interest:

- Phase correlation between lines. This is the essential feature of an OFC. If there exists no correlated phase noise behaviour between the modes of a comb, the multimode signal is not an OFC *per se*.
- Central wavelength. This parameter must be the first to assess to determine if the comb is useful for the intended application. OFCs centred in the telecom range (1550 nm) are the most widespread ones due to the maturity of the available technology at these wavelengths.
- Frequency spacing between lines ($f_{REP}$) and the possibility of tuning this parameter.
- Spectral bandwidth (also referred as optical span). This feature delimits the spectral coverage of the instrument due to the gradual decrease of the power of the comb lines.
- Frequency and amplitude noise of the comb lines, usually caused by diverse agents (noise of the pump laser, temperature, mechanical vibrations…) and linewidth of the teeth, which determines the ultimate resolution of the instrument.
- Flatness (or amplitude deviation) of the frequency comb lines around a specific wavelength.
- Size, weight and power. Although these factors may not seem relevant at first sight, the increasing demand of OFCs for field applications outside the lab is leveraging the implementation of new sources, with a clear trend towards compact, more efficient, more robust and inexpensive devices.

It comes as no surprise that one single source of pulses can provide the best performance in each and every one of the above-mentioned features at the same time. For this reason, there have been a number of evolving pulse generation methods and new approaches for the production of this collection of spectral lines in the frequency domain that have escorted the development of femtosecond

lasers, each of them with their own strengths and shortcomings. This will be discussed in the upcoming section in more detail.

# 2.

# Methods of Implementation of Optical Frequency Combs

## 2.1. Mode-Locking

The principle of mode-locking short pulse generation is the traditional approach which has been followed in the past century for frequency comb generation and absolute optical measurements using these instruments. Having been premiered in 1964[26], this technique stems from introducing coherence between the resonant modes of the cavity of a laser. Should a fixed relationship in terms of phase and amplitude is attained between modes of a multimode laser, the output field will consist of a train of regular pulses in time. A time-domain representation of this process is illustrated in Figure 3. Several methods to induce phase coherence between longitudinal modes can be found in the literature, but the most conventional ones are active mode-locking, passive mode-locking and hybrid mode-locking. For a detailed description of the physical processes underlying these methods, the author refers to Vasil'ev *et al.*[27].

One of the most salient features of MLLs is the width of the generated pulses. This technique can provide the shortest pulses, hence the widest optical spans reported to date, with up to $10^5$-$10^6$ comb lines. However, the tunability of the line spacing of the comb is highly limited, as it solely depends on the fabrication of the device. Since the repetition frequency is established by the separation in frequency between adjacent modes, only the length of the cavity will determine the line spacing and not any other external parameter which may allow for its uncomplicated modification. Still, by means of auxiliary methods, these

lasers can be arranged to emit pulse trains at integral multiples or sub-multiples of their fundamental repetition rate.

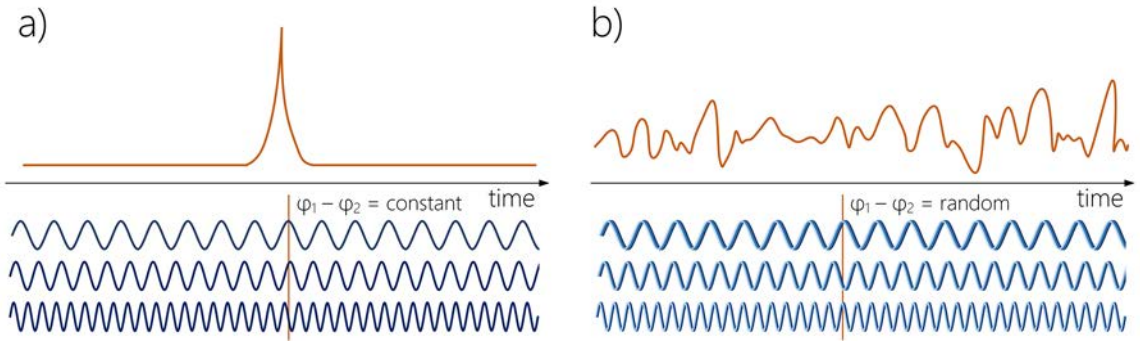


Figure 3. Temporal representation of the mode-locking process. A pulsed regime is only achieved when the modes are superimposed in phase (a), whereas a random output signal is obtained when random phase fluctuations take place between cavity modes (b). Adapted from Criado[28].

As stated in the previous section, Ti:Sapphire MLLs were the first ones to be used as the core part in a full demonstration of an OFC. These lasers are based in a Titanium-doped Sapphire crystal pumped by a laser with an emission wavelength usually located in the green region (around 500 nm). Superior levels of performances, with watt-level output powers, broad output spectra (typically from 700 – 900 nm directly from the oscillator) and a repetition rate which may cover from 0.1 to 10 GHz can be achieved depending on the device[29,30]. However, the necessity for bulky, free-space setups and the high cost of implementation and maintenance are factors that have hindered the wide adoption of these devices in field applications.

As an attractive solution to these drawbacks, Fibre Lasers using a variety of dopants and host materials have emerged as compact, inexpensive and robust alternatives to Ti:Sapphire Lasers. These synthesizers consist of optically-pumped doped fibres with rare earth ions arranged within a closed loop assembling a cavity. Depending on the dopant employed in the gain medium, different emission wavelengths can be tailored across the Near- and Mid-Infrared windows of the electromagnetic spectrum. Nowadays, the most widespread dopants for Fibre Lasers are erbium, ytterbium and thulium. Particularly, erbium-doped Fibre Laser-based frequency combs (emitting in the vicinity of 1.5 μm) can be implemented by means of the extremely reliable all-fibre standard technology of the telecom range and 980 nm-pump laser diodes[31,32]. With repetition frequencies in the range of the hundreds of MHz and average power levels of hundreds of mW, these OFCs feature long-term stability, lower cost and turnkey operation[33], with even recent demonstrations of outside-the-lab operation[34,35]. In the route towards miniaturization, it is also noteworthy the development of MLLs

integrated in photonic integrated circuits (PICs). However, this technology still lacks the maturity required in terms of efficiency and robustness[36].

## 2.2. Electro-Optic Modulation

The inherent features of traditional MLL-based OFCs in terms of complexity, environmental control and cost are sometimes obstacles which are hard to overcome. Furthermore, despite their unequalled spectral coverage, these sources feature an intrinsic restriction in the tunability of their mode spacing and emission wavelength which may further hamper their applicability. It is indeed the lack the versatility of these tools that leaves plenty of room for other alternatives to sprout, particularly when the applications do not require such impressive levels of performance.

In this way, electro-optic (EO) OFCs based on the EO modulation of a single continuous-wave (CW) laser have gained wide acceptance between the scientific community[37]. As can be seen in Figure 4, the operating principle is straightforward: the radiofrequency (RF) modulation applied to an electro-optic modulator (EOM) that contains a material featuring second-order nonlinearities imposes a number of sidebands to a seed laser in the frequency domain. As a result, a frequency comb arises whose central wavelength is defined by the emission wavelength of the seed laser and the mode spacing by the RF signal of the external oscillator driving the modulator. Additionally, the modulation power of the driving signal also has an impact on the number of generated sidebands within a specific bandwidth. This is clearly evident in the case of EO phase modulation, a process which can be modelled by a series of Bessel functions with different orders that determine the intensity of each line[38].

With the current EO modulation technology, EO-OFCs can be mostly generated in the wavelength range covering 0.4-2 μm, limited by the transparency of the nonlinear crystal material inside the modulator, with repetition frequencies up to several tens of GHz. Current research is seeking to surpass these limits towards their implementation deeper in the Mid-Infrared[39]. In any case, the possibility of using commercial off-the-shelf EOMs as well as the mature technology developed in the 1.5 μm range allows for the easy implementation of these setups in a fully-fiberized fashion, thus facilitating its deployment for applications outside the lab. Clearly, all the above-mentioned characteristics not only endow these systems with high frequency tunability and customization

capabilities, but also with simplicity of operation, robustness and additional benefits in terms of size, cost and power per spectral line.

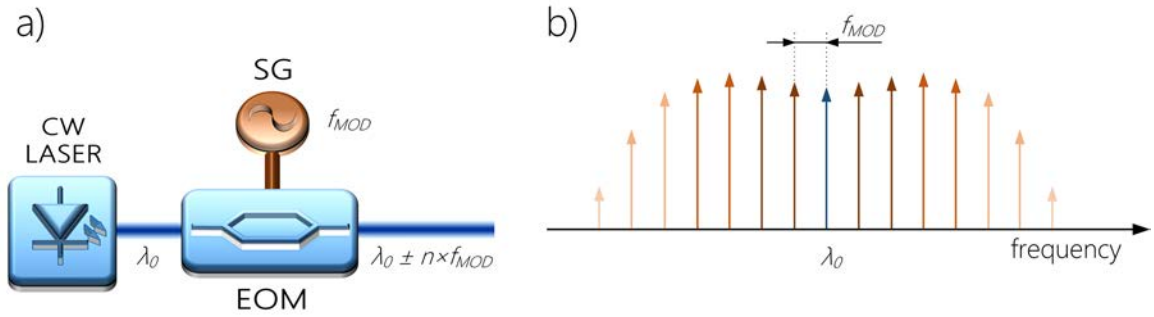


Figure 4. EO modulation. a) Basic schematic of an EO-OFC generator. b) Example of a typical spectrum. SG: Signal generator.

The main limitations of these OFCs are their finite spectral coverage, which is to a large extent limited by the modulator bandwidth, and the non-uniform spectral power distribution across the lines when the driving RF signal is composed by one single frequency component. However, since their inception in the early 1970s[40], significant efforts to develop modulators with lower driving voltages and higher power handling capabilities as well as the advent of new platforms with enhanced EO response have supported the optimization of these devices and have led to wider spans[41]. Furthermore, different methods and techniques can also be harnessed to expand the span of these combs and to improve their flatness. To name a few: arrangements of EOMs in cascade[42] or recirculating ring configurations[43], the incorporation of highly nonlinear fibres[44] and silicon nanowaveguides[45], the application of pulse shaping methods to compress the chirped pulses[46] or the employment of tailored sequences of modulating signals[47]. Very recently, new demonstrations of EO-OFCs with seed lasers locked to molecular absorption resonances for absolute calibration[48] and, more importantly, the first demonstrations of self-referencing with these combs[49,50] have offered new and exciting prospects to unleash the potential of these sources for metrology applications.

## 2.3. Gain-Switching

In the search for compactness and integration, one of the classic methods for pulse generation is Gain-Switching (GS). Introduced in the early 1980s[51], this technique allows for the formation of optical pulses (and therefore, OFCs) within

the laser device in a one-stage scheme, thus without resorting to any external component.

The principle of operation of GS relies on the periodic and sudden switch of the gain in the active medium of the resonator. In the case of a semiconductor laser, this can be attained by means of current modulation. When a large electrical signal is applied to one of these devices when is biased below threshold (thus prompting its switch-on), the photon density (output power) will feature a transient second order response characterized by relaxation oscillations. Notably, the first pulse of these oscillations will have a higher frequency than the rise time of the current. Therefore, if the laser is quickly switched off again before the outset of the next optical oscillation, the output power will show a pulsed response, with the peculiarity that the optical pulses are much shorter than the electrical pulses. Obviously, if the current modulation is periodic, the laser will emit an optical pulse train and, therefore, a frequency comb. This phenomenon is qualitatively illustrated in Figure 5. For a more in-depth analysis, there are several articles in the literature covering the mathematical description of the dynamic behaviour governing the GS mechanism[27] and comprehensive experimental studies based on the driving conditions[52,53].

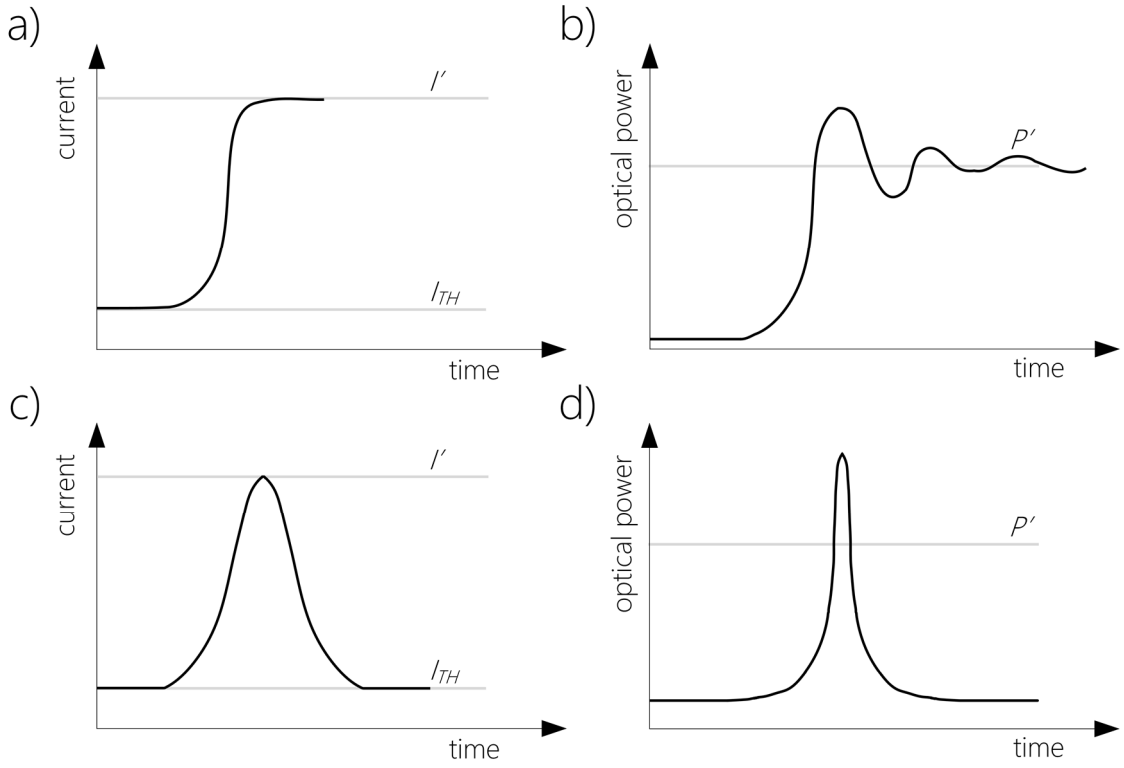


Figure 5. Time-domain representation of the principle of GS in semiconductor lasers. a) Fast switch-on of a laser that produces (b) an underdamped second order response in the output power. If the laser is suddenly switched-off again (c), the output power will exhibit a pulsed response (d) that emanates from the relaxation frequencies. Adapted from de Dios[54].

One of the most distinguished characteristics of this method for OFC generation is the complete frequency tunability, as with EO modulation. The central wavelength of the comb and its line spacing can be freely adjusted in semiconductor lasers, as this technique allows for the precise control of the pulse repetition rate only limited by the bandwidth of the device (which can reach several tens of GHz) and independently from physical properties of the device.

In order to force the device to operate in GS regime, the input pulsed current is often replaced by a large sinusoidal current modulation or even by optical pumping. However, the pulses GS can provide are wider in comparison to MLLs (usually tens of picoseconds) with limited peak power and worse performance in terms of jitter[54], although recent works have proven the generation of femtosecond pulses through extreme optical pumping[55]. To overcome this issue, pulse compression (comb expansion) stages are usually included in GS-based OFC setups based on EOMs[56] and highly nonlinear fibres[57].

GS-based OFCs have been successfully demonstrated in a number of laser devices, such as Distributed Feedback (DFB)[57], Fabry-Pérot[56], Discrete Mode (DM)[58], Vertical-Cavity Surface-Emitting[59] and Mid-Infrared and THz Quantum Cascade Lasers (QCLs)[60,61]. Furthermore, recent works have also reported monolithically integrated GS-based OFCs using some of the previous laser sources[62,63], and GS can even be used to induce a pulsed response in Fibre Lasers by means of an adequate design of the pump source[64]. Although each device possesses their own limitations to this mechanism for pulse generation −particularly in the case of QCLs-, the number of demonstrations across the electromagnetic spectrum makes GS one of the most versatile techniques for comb generation.

## 2.4. Microresonator-based Frequency Combs

Until the early 21st century, frequency comb generation relied on producing periodic pulse trains in the time domain, with efforts focused on improving their main attributes for increased performance. Nevertheless, in 2007, the group of Tobias J. Kippenberg revealed one of the first approaches for monolithic comb generation in whispering gallery mode microresonators. This milestone marked the beginning of the era of microresonator-based OFCs, or *microcombs*[65].

This method for comb generation is based on the parametric interaction between of a pump CW laser and the optical modes of a monolithic microresonator

with an ultra-high-quality factor, a process which is governed by a cascaded third-order nonlinear process called four-wave mixing (FWM). As they proved, when a resonator exhibiting inversion symmetry (and therefore, prone to FWM) is pumped with a laser emitting at a certain wavelength, a new pair of photons is created whose frequencies are rigidly equally-spaced and shifted up and down from the frequency of the pump laser. The striking factor of this energy-conserving mechanism is that if the cavity is carefully engineered so that its modes match the frequencies of the new generated sidebands, the process is boosted and higher-order sidebands emerge at exactly the very same initial frequency difference. As the arising sidebands interact with each other, this phase-sensitive amplification process leads to a cascaded collection of stable markers with constant but arbitrary phases in the frequency domain (i.e., an OFC) which can span hundreds of nanometres in the spectrum without external broadening. Figure 6 shows a typical setup for OFC generation with microresonators and also a representation of the aforementioned process.

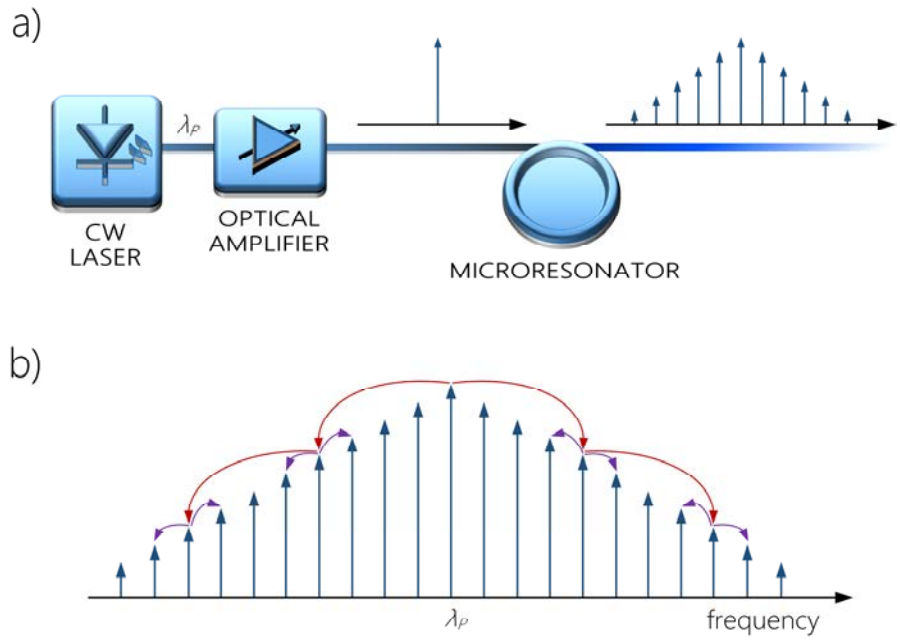


Figure 6. Microresonator-based comb generation process. a) Experimental setup. A CW laser beam with emission wavelength $\lambda_P$ is amplified to pump an ultra-high-quality factor cavity to produce a parametric frequency conversion by means of FWM (b) in which, first, pairs of evenly-spaced sidebands around $\lambda_P$ are generated (red lines) and then, other frequency markers arise from the interaction of the new lines between themselves (purple lines).

Microresonator-based OFCs can be designed in a number of platforms, with different materials and geometries, leading to unique features and optimal performance in varying wavelength ranges[66]. In general, they feature wide spans (in some cases, octave-spanning[67]) due to the broadband gain of the resonator and

line spacings ranging from tens of GHz up to THz which are intrinsically determined by the free spectral range of the cavity. Additionally, one of the most remarkable advancements in this research area was the discovery of the formation of dissipative Kerr solitons (DKS) into the cavity and the corresponding generation of femtosecond-level optical pulse trains by means of adequate dispersion engineering and careful control of the pump power[68]. The DKS regime leads to OFCs in the frequency domain that exhibit improved performance in terms of noise, smoother spectral envelopes and, particularly, enhanced long-term stability (frequency and amplitude noise)[69], one of the main issues that have hindered the development of these systems in outside-the-lab environments[70].

Clearly, the development of *microcombs* have evolved into a field research on its own, offering new promising routes towards chip-level integration. As notable examples of their potential, an absolute optical frequency synthesizer and a battery-operated comb generator using integrated photonics have been recently reported[71,72]. Still, work towards low pump-power requirements, lower thresholds for nonlinear interaction, improved conversion efficiency and robustness are in progress until this technology achieves the level of penetration of benchtop MLL-based OFCs. For a broader coverage of this technology and the introduced notions, including successful demonstration of *microcombs* in different operation regimes and new intriguing perspectives, the author refers to some exhaustive reviews in the literature[73,74].

## 2.5. Optical Frequency Combs in Quantum Cascade Lasers

Quantum Cascade Lasers[75] are unipolar devices with potential to be engineered with emission wavelengths across the whole Mid-Infrared and THz ranges by means of an adequate design[76]. One of the most actively pursued features in these devices is the possibility to generate frequency combs within the active region, offering much promise for the implementation of chip-sized multimode sources. Still, the inherent features of Mid-Infrared QCLs in terms of gain recovery time make the stable creation of pulses particularly unfavourable[77] and restricted to complex, specially engineered devices based on the mode-locking technique[78] or GS under very specific operating conditions[60]. It should be noted, however, that QCLs in the THz range are more amenable to pulsed operation regimes[79].

In this sense, Mid-Infrared QCL-based OFCs have recently gained much attraction since the group of Jérôme Faist first proved in 2012 the generation of

OFCs in electrically-pumped, free-running Fabry-Pérot QCLs through a natural FWM process in broadband gain, low dispersion waveguides[80]. This approach offered a phase-locked, well-defined comb structure in the frequency domain, despite not creating pulses in the active region of the laser, in a direct and compact scheme. In fact, the lasers operate in a natural regime of self-frequency modulation periodic with the cavity round trip time, with the temporal profile of the output signal resembling that of a pseudo-random frequency modulated signal with quasi-constant power. Additionally, with some modifications in the design, a similar approach was also followed in Fabry-Pérot THz QCLs to demonstrate comb operation in these devices[81]. Figure 7 shows a typical spectrum of a Mid-Infrared comb based on this technology.

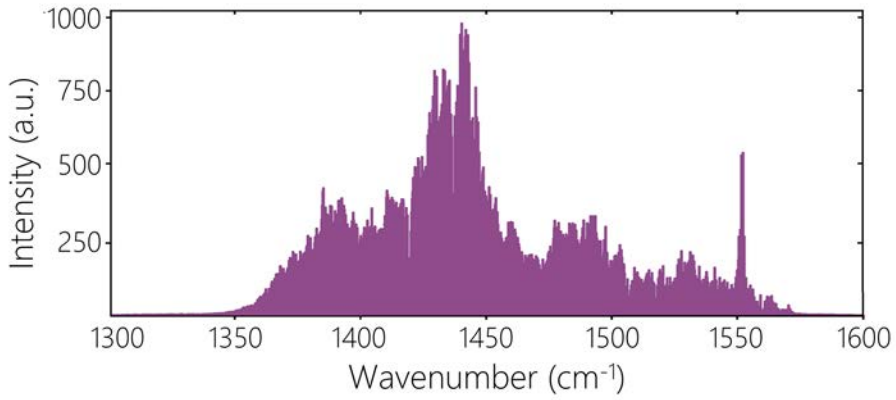


Figure 7. Spectrum recorded with a FTIR spectrometer of a frequency comb based on a Fabry-Pérot QCL centred at 1450 $cm^{-1}$ (6.9 μm). Adapted from Hugi *et al.*[80].

From that day on, the research focus shifted towards the confirmation and analysis of the mechanisms governing this behavior through detailed theoretical studies[82,83]. On the other hand, some groups devoted their efforts towards the optimization of the intrinsic comb operation within the device (which is usually restricted to a reduced part of the dynamic range of the laser operation) through dispersion engineering[84,85], while others realized studies of the noise properties and coherence of these sources[86,87]. All this evolutive process has been compiled in some reviews where the phenomenon of comb formation within QCLs is carefully detailed[88].

In a similar fashion to *microcombs*, QCL-based OFCs feature repetition frequencies in the range of the GHz (fixed by the free spectral range of the laser cavity) with limited tuning capabilities, as well as independent control over the emission wavelength and the line spacing. In terms of spectral coverage, spans above 700 nm have been reported in Mid-Infrared QCL-based OFCs[85], whereas some demonstrations with THz QCL-based OFCs have reached octave-spanning

spectra[89]. Moreover, it is also noteworthy the recent discovery of a new comb state, denominated as *harmonic state*, with repetition rates in the range of THz due to the suppression of adjacent cavity modes[90].

With significant advancements in terms of room-temperature operation, watt-level (in the Mid-Infrared) and milliwatt-level (in the THz region) output power, tuning capabilities and increasing wall-plug efficiencies, QCLs have undoubtedly become one of the preferred devices for comb generation in the Mid-Infrared and THz ranges[91]. Arguably, one could even say that QCL-based OFCs hold promise for becoming the workhorse of future ultra-compact broadband spectrometers in the Mid-Infrared, as it is possible to find commercial benchtop instruments based on this technology[92].

## 2.6. Other Methods for Frequency Comb Generation

So far, the most widespread methods for comb generation have been discussed. Nevertheless, there are other comb generation methods with limited scope whose application is mostly restricted to specific purposes or, alternatively, require specialized equipment and operating conditions. In this section, some of these techniques are briefly reviewed.

*Q-Switching* is a classic short pulse generation mechanism based on the modulation of the quality factor of the optical cavity of the laser[27]. As the quality factor is suddenly changed from low to high condition, it is possible to release the energy stored by means of an optical pulse which usually features high power (even orders of magnitude higher than the power in CW operation). The repetition rate of the pulses can be established by external parameters depending on the method (active or passive) for Q-Switching, allowing for a wide tuning range of the comb line spacing in the MHz and GHz range[93]. The width of the pulses is usually in the order of the tens of picoseconds or even nanoseconds. Still, the need for specially manufactured devices to proceed with this pulse generation method restricts its widespread use[27].

*Synchrotron radiation* in its coherent mode (low-$\alpha$) is known to generate a continuum of equally-spaced frequencies in the sub-THz and THz range[94]. The origin of these combs derives from the radiation emitted from successive short electron bunches which are accurately separated in time within synchrotron facilities[95]. This way, a train of ultra-short pulses is generated with two repetition rates: one defined by the bunch-to-bunch spacing and other by the length of the

ring resonator. As a result, high-power, offset-free combs with line spacing in the order of kHz to MHz are generated. Nowadays, there are several electron storage rings around the world which can provide coherent synchrotron radiation[96].

*High-order sideband generation* is a phenomenon that has been observed in semiconductors which are simultaneously illuminated by a Near-Infrared CW laser and a strong THz electric field[97]. Under these conditions, when the emission wavelength of the former is tuned near the exciton resonance of the sample (i.e., a layer containing GaAs quantum wells), a number of sidebands *n*-times spaced the frequency of the THz field (with *n* being an even number) are produced around the emission wavelength of the CW laser due to electron-hole re-collisions[98]. Depending on the properties of the samples and the conditions of the experiment, it is possible to create OFCs centred at different frequencies with a varying number of sidebands that can even exceed a hundred[99].

*Supercontinuum generation* encompasses all mechanisms of nonlinear frequency conversion of light focused on a dielectric medium as the former propagates through the latter[100]. These processes, which are usually triggered by ultra-short pulsed sources featuring high peak power, rely on the interaction between nonlinear effects (such as self-phase modulation or FWM) and the linear dispersion taking place in nonlinear fibres or integrated waveguides to produce broadband spectra[101]. One of the most important features of this process is that the supercontinuum can preserve the coherence properties of the incoming light, in such a way that, for example, if a frequency comb is used as incident light, all the new frequency components will be perfectly phase-locked to the original comb. This was the basis of the first octave-spanning demonstrations of OFCs in the search for absolute measurements of the frequency of light[8]. Nowadays, dispersion tailoring into optical fibres and new waveguide platforms have paved the way for the implementation of supercontinua from a broad range of pump pulsed lasers, allowing for the generation of coherent radiation covering from the Ultraviolet region to the Mid-Infrared[102].

# 3.

# Methods of Detection of Optical Frequency Combs

In the previous section, OFCs have been presented as versatile tools which can be generated through a number of mechanisms to serve a range of specific applications. Some of the above-mentioned applications resort to OFCs as passive tools against which other devices are referenced or measured, as in the case of optical clocks or the calibration of astronomical spectrographs. Nevertheless, an OFC can also be conceived as an instrument to directly probe and measure atomic and molecular samples or, in other words, to perform *direct comb spectroscopy*. In this way, the structure of the frequency comb can be frequency-selectively attenuated and phase-shifted by a sample or device under test while taking full advantage of the excellent frequency accuracy of the OFC, its broad bandwidth and the high spectral quality of the array of lines of which it is constituted.

Of course, using the OFC as the active element to measure conveys an additional challenge: it is necessary to develop a detection system which can secure the spectral information imprinted into the modes of the OFC. For this reason, an adequate detection method must provide broadband capabilities while being able to resolve the spectral components of the OFC in the frequency domain within a reasonable lapse of time. As an example, a commonplace spectrometer can be used to measure an OFC, but since its minimum resolution usually exceeds the line spacing of the comb, most of the information in terms of resolution and accuracy is lost.

Detecting combs can be performed in a number of different ways. As an illustration, it could be realized in such a simple way as beating the comb with a CW laser in a photodetector with suitable bandwidth[103], or by means of elaborate methods (still in their infancy) encompassing temperature-stabilized, specially-tailored multimode fibres and cameras to reconstruct the speckle pattern stored in

a transmission matrix[104]. Each detection system provides a different combination of accessible spectral coverage, attainable resolution, measurement speed, sensitivity, noise performance, complexity and long-term stability, and clearly, one single technique cannot be the best one in all possible scenarios. This section will discuss some of the most conventional comb detection methods.

## 3.1. Comb Vernier Spectrometers

A comb Vernier spectrometer is based on a grating spectrograph which permits evaluating an input signal in different periods of time, allowing for the virtual increase of the grating spectral resolution. The operating principle of this approach consists of an input OFC with a repetition frequency that is purposefully mismatched to the free spectral range of a Fabry-Pérot cavity so that only one of every $x^{th}$ comb line is resonant to some specific mode of the cavity[105] (see Figure 8).

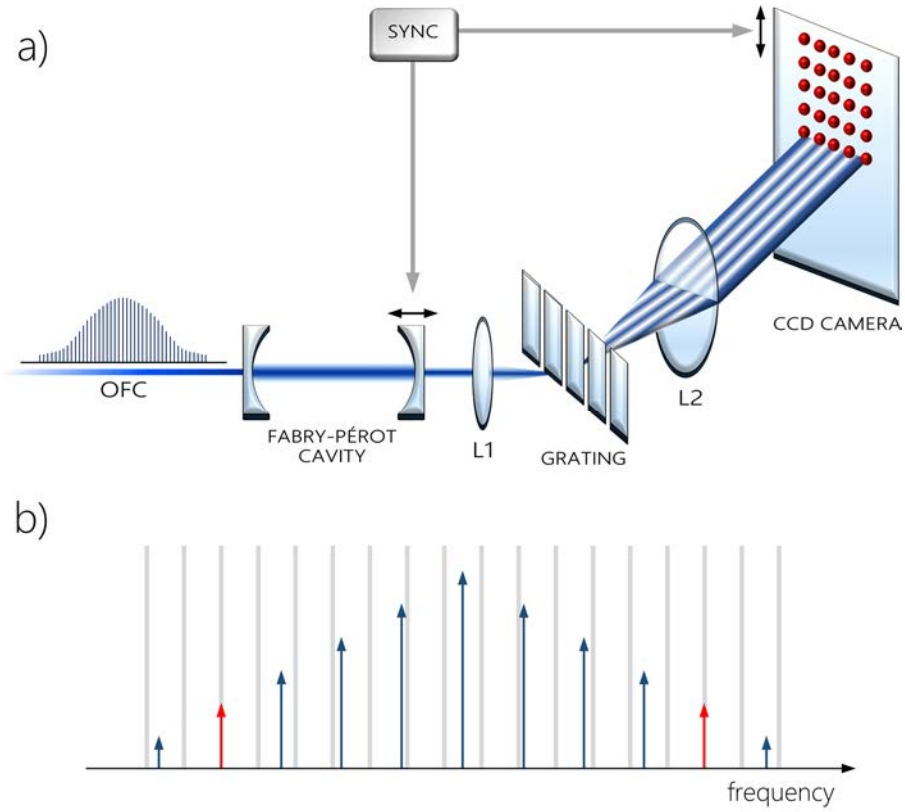


Figure 8. Comb Vernier spectrometer-based detection approach (see text for details). a) Experimental setup. The two-dimensional detector is synchronously scanned together with the Fabry-Pérot cavity to map the temporal sweep of the cavity onto the CCD camera. L1 and L2: Focusing lenses. b) Principle of operation. The comb lines in red denote those modes which are matched to resonances of the cavity (grey lines).

As a result, the detected signal derives from a single comb line, thus increasing the functional resolution of the grating. In order to analyse all the comb teeth, the locking points between comb lines and cavity modes must be either changed or the comb repetition frequency swept. The acquisition of several spectra after a complete sweep allows for the reconstruction of the whole spectrum with a resolution given by the line spacing of the comb (and ultimately limited by the linewidth of every mode). It must the highlighted that the cavity also extends the interaction length, thus greatly improving the sensitivity.

This method, however, puts stringent requirements on the locking electronics, the design of the optical cavity and the acquisition process (which is inherently sequential), hence complicating data acquisition. As a method to simplify the readout, a charge-coupled device (CCD) camera can be employed as a two-dimensional detector array to map the time dimension onto the spatial dimension of the camera. Therefore, the information of the sample is included in the brightness, shape and position of the two-dimensional array of spots recorded by the CCD camera[105]. Still, this may impede the adequate detection of combs in other spectral regions (such as Mid-Infrared), as infrared cameras usually feature lower sensitivity beyond the Near-Infrared region.

## 3.2. Virtually Imaged Phased Array Spectrometers

As an alternative to using time as the second dimension, Virtually Imaged Phased Array (VIPA) spectrometers make use of spectral dispersion to project the comb lines in two pure spatial dimensions[106].

Originally devised for wavelength multiplexing, a VIPA is a special type of etalon which allows the light to enter only through a narrow stripe located in a highly reflective surface. The output surface, on the other hand, is only partially reflective, as in a Fabry-Pérot etalon. The distinctive feature of a VIPA is the slight tilt, which allows for the transmission of every single incoming wavelength with different output angles, thus providing an extremely high angular dispersion in the vertical axis. The intrinsic effect of the etalon manifests through a repetitive pattern with the free-spectral range of the cavity. In order to separate the VIPA orders, a cross-dispersion grating is employed in the orthogonal axis (usually, the horizontal axis). The dispersed comb is then directed to a camera on which every pixel of the two-dimensional array provides singular spectral information (e.g. absorption) within the repetitive pattern formed in the images. After calibration in

the frequency axis, the one-dimensional information associated with each pixel can be retrieved[106]. Figure 9 depicts a typical setup of a VIPA spectrometer.

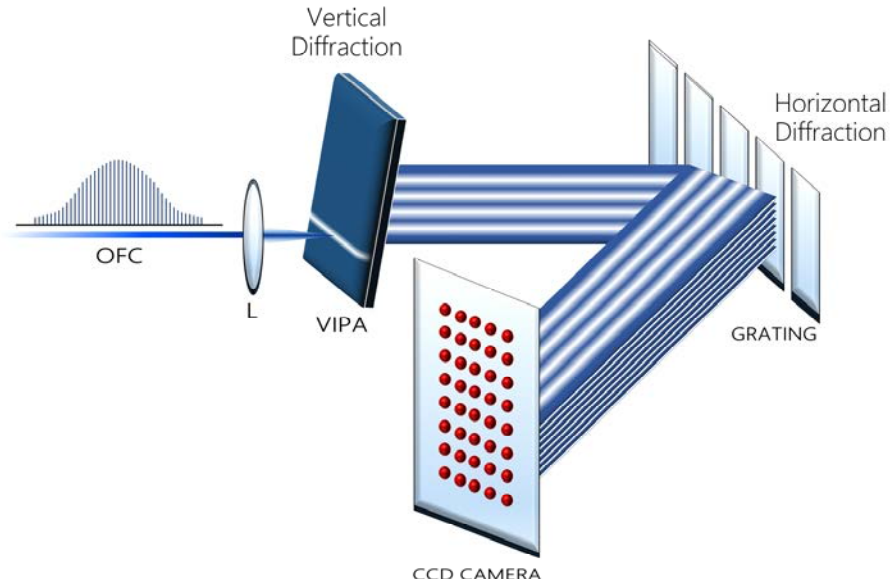


Figure 9. VIPA spectrometer setup (see text for further details). L: Focusing lens. The dispersion of the light in the vertical and horizontal axis is realized by the VIPA spectral disperser and a conventional diffraction grating, respectively, to produce a two-dimensional image.

With this technique, broad spectral regions can be acquired simultaneously in a very short period of time (in the order of milliseconds) with high resolution (~500 MHz at 1550 nm)[20]. However, its disadvantages stem mainly from its lack of robustness to environmental instabilities, as the fringe pattern is particularly sensitive to optical alignment. Furthermore, as in comb Vernier spectrometers, the necessity of a camera to acquire the spectral information may limit the application of this type of spectrometer to longer wavelengths, although there are recent examples that have demonstrated the feasibility of this technique in the Mid-Infrared[107].

## 3.3. Michelson-based Fourier-Transform Spectrometers

Of all the technologies for the implementation of spectrometers, Fourier-transform infrared (FTIR) interferometry is undoubtedly the most recognized approach to perform wavelength-dependent characterizations of optical spectra[108]. The original designs commonly included a thermal light source, but modern arrangements have replaced the incoherent source with a frequency comb, thus incorporating all its associated benefits[109].

FTIR spectrometry is often accomplished with the help of a Michelson interferometer in order to measure the optical spectrum by way of time-domain interference. The basic architecture is shown in Figure 10. The light from the comb is first split into two paths (interferometer arms) so that it reaches a couple of mirrors, one of them being mechanically adjustable. After that, the reflected light is recombined and directed to a single photodetector. The key concept of this technique relies on the motion of the scanning mirror, which permits adjusting the path difference between both interferometer arms, thus leading to constructive or destructive interference depending on the path delay. Therefore, a uniform sweep of the moving mirror generates a signal containing the sinusoidal modulation of the intensity of each spectral component of the comb, which is usually known as interferogram. The digitization and Fourier-transformation of this time-domain signal allows for the retrieval of the intensity as a function of the frequency, as in the classic representations of frequency combs[108].

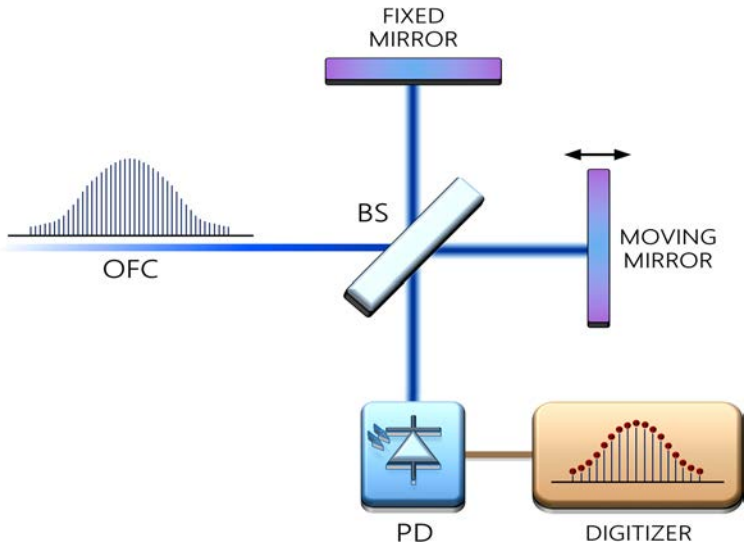


Figure 10. Setup of the classic architecture of an FTIR spectrometer (see text for additional details). BS: Beam splitter; PD: Photodetector.

This architecture allows for the detection of any type of frequency comb as long as the photodetector has suitable bandwidth. However, the mechanical stage plays a major role in the performance of the system, in such a way that the resolution of the spectrometer is restricted by the maximum scanning range of the mirror and the speed of acquisition by its velocity, usually in the order of Hz. In fact, resolution and speed are inherently interwoven. There are examples of rapid-scan FTIR spectrometer that can operate at high acquisition rates, but at the unavoidable expense of lower spectral resolution. Furthermore, the difference between path lengths must be sampled at exact time intervals, so a precise control

of the movement of the mirror is of utmost importance for high frequency accuracy. Recently, new ingredients, such as lock-in detection schemes[110] or techniques of dynamic phase-control[111] have been incorporated to upgrade the performance of the classic scheme in terms of noise cancellation, measurement speed and, in general, overall efficiency.

## 3.4. Dual-Comb Spectrometers

The development of OFCs in such a variety of platforms and the preponderance of FTIR spectrometers (with their mechanical limitations) have converged into, perhaps, the most spellbinding and popular method for frequency comb detection nowadays: dual-comb spectroscopy (also known in the literature as dual-comb or multiheterodyne interferometry, linear or asynchronous optical sampling or even coherent Fourier-transform spectroscopy)[112].

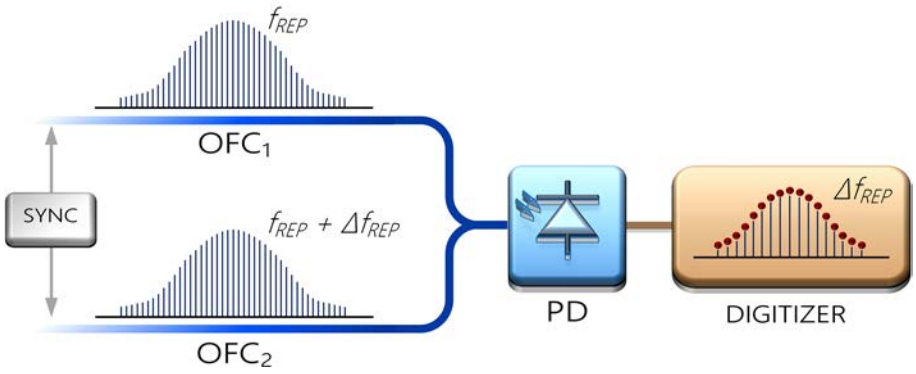


Figure 11. Basic setup of a dual-comb architecture (see text for details). The example illustrates the scenario when both OFCs are synchronized to properly exploit the potential of the technique. PD: Photodetector.

The principle of dual-comb spectrometers (see Figure 11) very much resembles that of FTIR spectrometers, but, in this case, a second OFC with slightly different repetition frequency ($\Delta f_{REP}$) is used instead of a scanning mirror to induce a rapidly-changing time delay between both OFCs[113]. The combination and photodetection of these frequency combs give rise to an interferometric pattern in a similar fashion to FTIR spectrometers which repeats at a rate of $1/\Delta f_{REP}$. The Fourier-transformation of the interferograms originates a new comb in the RF domain compressed by a factor of $f_{REP}/\Delta f_{REP}$, with an offset frequency fixed by the mismatch between the $f_{CEO}$ of the OFCs and a repetition frequency of $\Delta f_{REP}$. Since the RF comb mirrors the impact of external agents on the optical characteristics of the OFCs, any variation in the comb structure due to, for example, the absorption of light, will be reflected in the RF comb, whose digitization and processing can be

readily carried out by means of the vast number of accessible tools and techniques in the RF domain[114].

With only a single-point detector, this multiheterodyne approach allows for the simultaneous acquisition of broad optical spans within an extremely short time lapse. Remarkably, this is also compatible with very high resolutions, since this parameter is platform-independent and is only limited by the linewidth of the comb lines. Despite not resorting to restricting mechanical elements, this method still possesses a Nyquist-limited trade-off between speed, spectral resolution and the optical bandwidth that can be simultaneously acquired[115]. Furthermore, it demands either two tightly-synchronized combs or post-correction schemes to fully capitalize on its potential (i.e., comb-tooth resolved spectra), a requirement which can be difficult to fulfil depending on the employed comb sources and in spectral regions beyond Near-Infrared[116]. In any case, it seems clear that dual-comb spectroscopy will not cease to mature, as this technology will always parallel the development and sophistication of the comb generators[112].

# 4.

# Thesis Overview and Objectives

The work presented in this Ph.D dissertation has been developed in the framework of the project TEC-2014-52147-R funded by the Spanish Ministry of Economy and Competitiveness and a Formación del Profesorado Universitario program #FPU014/06338 granted by the Spanish Ministry of Education, Culture and Sports. The overall structure of this work encompasses three main general objectives:

1. The development of Optical Frequency Combs in different portions of the electromagnetic spectrum, namely, the Near-Infrared (0.8 – 2.0 μm), the Mid-Infrared (2.0 – 20.0 μm) and the sub-THz and THz ranges (30 – 3000 μm, or similarly, 0.1 – 10 THz). These photonic sources will be employed as active tools following specific requirements for target applications.
2. The implementation of a method for frequency comb detection in every instance. Along this thesis, dual-comb spectroscopy will be the selected method for the retrieval and analysis of the spectral information.
3. The validation of the full system, including generation and detection schemes (i.e., the dual-comb architecture altogether) by means of the measurement of volatile organic compounds, fibre optic sensors (such as fibre Bragg gratings) or other components.

In this way, this thesis work will be divided into several chapters on a spectral region-to-spectral region basis in consonance with the aforementioned objectives.

Chapter II will present a comprehensive review of the state-of-the-art of dual-comb schemes across the different electromagnetic spectral ranges of study.

This analysis will be the cornerstone to understand the potential of this technique, the current level of development and the common limitations which are intended to be overcome in this work.

In Chapter III, the demonstration of novel dual-comb modalities in the Near-Infrared will be provided. Some of the classic comb generation methods, such as electro-optic modulation or Gain-Switching will be used, characterized and validated for the first time in a dual-comb architecture with the detection of a gas sample in the C-band. Additionally, an original architecture for remote comb detection will also be presented following some of the ideas that emerged from the previous work. In the latter case, a fibre Bragg grating sensor will be used as device under test to measure the level of strain applied to the sensor.

Chapter IV will introduce a twofold contribution to dual-comb architectures in the Mid-Infrared range. In the first experiment, the generation and detection of the combs will rely on a Difference Frequency Generation process held in a nonlinear crystal for the transference of the previously validated Near-Infrared setups to the Mid-Infrared. Again, a sample in gaseous phase will be targeted to examine the performance of the system. The second contribution, on the other hand, will unveil a study for the feasibility of comb generation using Quantum Cascade Lasers by way of large-signal modulation. Here, no detection system (i.e., dual-comb scheme) will be realized, but the practical implications for an eventual detection process in this manner will also be considered.

The research work focusing on the sub-THz and THz range will be dealt with in Chapter V. Starting from some of the previously introduced methods for comb generation (i.e., electro-optic modulation), this approach will aim to extend the wavelength of operation by taking advantage of optical downconversion to synthesize THz radiation. Hence, a new architecture for THz comb generation will be proposed, developed and validated via dual-comb detection with a commercial microwave filter as device under test.

Finally, Chapter VI will gather the main conclusions from this dissertation and outline some of the main prospects for future work.

# II

# Dual-Comb Spectroscopy

# 1.
# Description of the Principle

The supremacy of dual-comb architectures as comb detection mechanisms can be summarized in one sentence: ultra-fast measurements at no expense of any other parameters such as spectral bandwidth, resolution, accuracy or sensitivity. This new generation of spectrometers without moving parts was first proposed by Schiller in 2002[113]. However, credit should also be given to two earlier demonstrations. First, a patent filed in 1998 by Van der Weide and Keilmann in which they defined the basis of this technique[117]; and second, an optical coherence tomography system proposed by Lee *et al.* in 2001 encompassing a pair of EOMs with slightly different repetition frequencies[118]. From that day forward, the work of research groups across the globe has led to many dual-comb demonstrations (which nowadays exceeds a hundred) using various laser platforms across different wavelength regions and for a variety of intended applications or purposes.

Although the operating principle of these spectrometers was briefly reviewed in the previous chapter, this and the following sections mean to go into further detail and fully grasp the rationale behind this method. To that end, the first step relies on assuming the electric field of an OFC as a superposition of plane monochromatic waves given the periodicity of the pulse envelope[119]

$$E(t) = \sum_N A_N \cdot e^{-i(2\pi f_N t)} \tag{2}$$

where $A_N$ is the amplitude of the $N^{th}$ line of the comb and $f_N$ its corresponding optical frequency according to (1). The initial phase is assumed to be zero in all cases. Of course, in a dual-comb configuration, two combs following the former expression with repetition frequencies $f_{REP.1}$ and $f_{REP.2} = f_{REP.1} + \Delta f_{REP}$ take

part in the scheme. Let us now assume that the system presents a dispersive arrangement, in which one of the OFCs interacts with an element (e.g. a gas sample) causing a frequency-dependent attenuation and phase shift in each of the comb modes. The electric field of the signal encompassing both overlapped OFCs is now defined as

$$E_1(t) + E_2(t) = \sum_N A_{N,1} \cdot e^{-i(2\pi f_{N,1} t)} \cdot e^{-\alpha_{N,1} - i\varphi_{N,1}} + A_{N,2} \cdot e^{-i(2\pi f_{N,2} t)} \tag{3}$$

where $\alpha_N$ represent the attenuation and $\varphi_N$ the phase shift of every frequency marker of the probe comb. When both OFCs impinge on a photodetector with adequate bandwidth, the generated photocurrent is expressed as follows:

$$I(t) \propto [E_1(t) + E_2(t)] \times [E_1(t) + E_2(t)]^* \tag{4}$$

According to this expression, the photocurrent contains all possible combinations of beatnotes between the modes from both OFCs. For the sake of clarity, only one beatnote between two neighbouring comb teeth *N,1* and *N,2* of the OFCs will be considered. Therefore, the photocurrent is now

$$\begin{aligned} I_N(t) \propto & \left[A_{N,1} \cdot e^{-i(2\pi f_{N,1} t)} \cdot e^{-\alpha_{N,1} - i\varphi_{N,1}} + A_{N,2} \cdot e^{-i(2\pi f_{N,2} t)}\right] \\ & \times \left[A_{N,1} \cdot e^{i(2\pi f_{N,1} t)} \cdot e^{-\alpha_{N,1} + i\varphi_{N,1}} + A_{N,2} \cdot e^{i(2\pi f_{N,2} t)}\right] \end{aligned} \tag{5}$$

which, further simplified, is also denoted as

$$\begin{aligned} I_N(t) \propto & \; A_{N,1}^2 \cdot e^{-2\alpha_{N,1}} + A_{N,2}^2 + A_{N,1} A_{N,2} \\ & \cdot e^{-\alpha_{N,1}} \left[e^{i(\varphi_{N,1} + 2\pi(f_{N,1} - f_{N,2})t)} + e^{-i(\varphi_{N,1} + 2\pi(f_{N,1} - f_{N,2})t)}\right] \end{aligned} \tag{6}$$

and, finally, being replaced by Euler's formula, can be expressed as follows

$$\begin{aligned} I_N(t) \propto & \; A_{N,1}^2 \cdot e^{-2\alpha_{N,1}} + A_{N,2}^2 + 2A_{N,1} A_{N,2} \cdot e^{-\alpha_{N,1}} \\ & \cdot \cos\left(2\pi\left(f_{N,1} - f_{N,2}\right)t + \varphi_{N,1}\right) \end{aligned} \tag{7}$$

Alternatively, in collinear arrangements, both OFCs traverse the sample of study. Following the same procedure as with the dispersive arrangement, the final expression of a beatnote between two neighbouring comb teeth is now

$$\begin{aligned} I_N(t) \propto & \; A_{N,1}^2 \cdot e^{-2\alpha_{N,1}} + A_{N,2}^2 \cdot e^{-2\alpha_{N,2}} + 2A_{N,1} A_{N,2} \cdot e^{-\alpha_{N,1}} \cdot e^{-\alpha_{N,2}} \\ & \cdot \cos\left(2\pi\left(f_{N,1} - f_{N,2}\right)t + \left(\varphi_{N,1} - \varphi_{N,2}\right)\right) \end{aligned} \tag{8}$$

In summary, as the last summand in (7) and (8) reveals, a pair of comb lines gives rise to a downconverted beatnote by a factor of $f_{REP}/\Delta f_{REP}$ in the more accessible RF domain which carries the spectral information encoded into the optical domain. This conclusion can also be applied to every pair of neighbouring lines at different optical frequencies, thus creating an array of uniformly-spaced frequency components in the RF domain with a separation of $\Delta f_{REP}$ whose central frequency is defined by the difference between the offset frequencies of the OFCs. An illustration of this process from a frequency-domain point of view is shown in Figure 12. Note that (7) also presents other zero-frequency terms whose spectral content cannot be unambiguously resolved and, therefore, are irrelevant in this analysis.

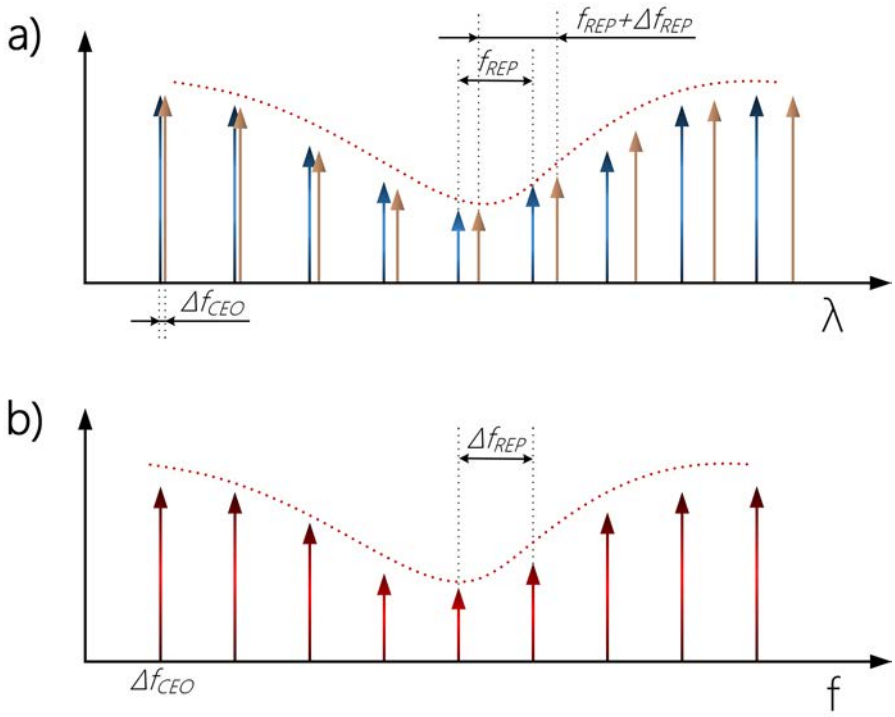


Figure 12. Principle of operation of dual-comb spectroscopy. Two combined OFCs with different repetition frequencies $f_{REP}$ and $f_{REP} + \Delta f_{REP}$ create a downconverted RF comb with line spacing $\Delta f_{REP}$ after photodetection. The optical information engraved by, for example, an absorption feature is directly transferred to the RF domain. The RF spectrum is scaled to faithfully reproduce the optical spectrum.

It has to be stressed that the arrangement of the dual-comb architecture plays a major role for the extraction of spectral information. Dispersive arrangements allow for the retrieval of both amplitude and phase information associated with each comb line, whereas collinear arrangements only permit procuring the former information (the last difference term in (8) shows that only if the phase difference between neighbouring comb lines is abrupt, would its impact on the RF beatnote be perceptible, which in practical terms is undetectable).

Furthermore, in (8), one can also see that the parameter related to the attenuation that can be retrieved is not amplitude but intensity, as the former is multiplied by a factor of $e^{\alpha}$. In any case, a normalization process must be carried out using an unperturbed signal as reference to obtain the response of the sample.

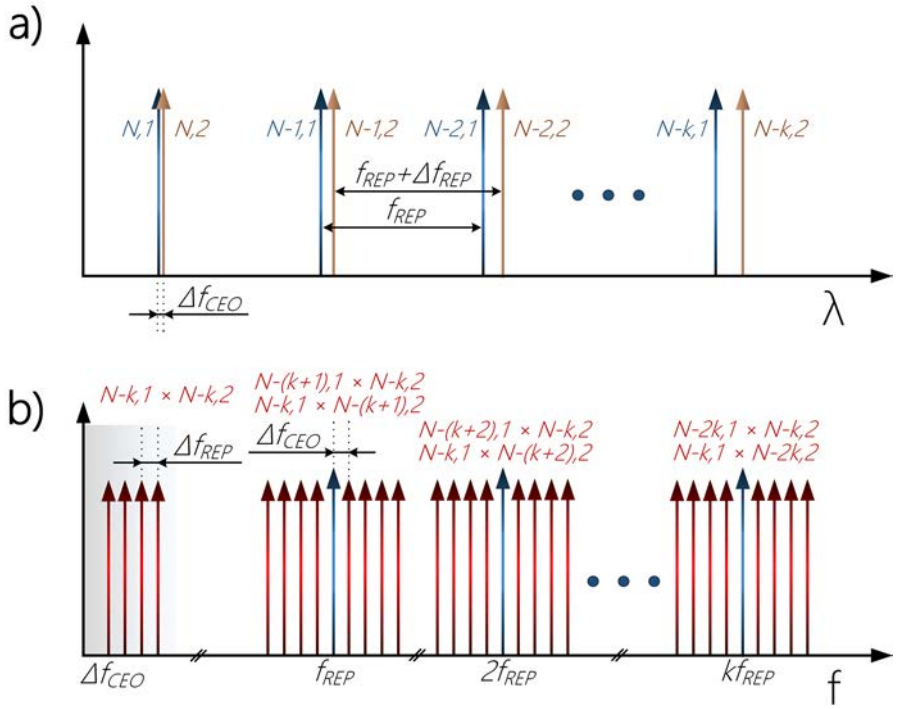


Figure 13. Full downconversion process from the optical (a) to the RF domain (b) between two OFCs (see text for details). The families of comb teeth with different orders that produce the RF combs in each Nyquist region around $kf_{REP} \pm f_{CEO}$ are specified above each one of them (for simplicity, only four pairs of comb teeth in a single-sided optical spectrum are considered). The grey shaded area shows the first Nyquist region, which is usually low-pass filtered and employed for spectroscopy purposes.

So far, only the beating between two neighbouring modes from the two frequency combs has been considered. However, as mentioned earlier, all the possible beatnotes between comb lines are present in the photodetected signal. As a representative case of this process, let us now consider the beating signal between two non-neighbouring lines *N-1,1* and *N,2* from the first and the second comb, respectively. Assuming a dispersive arrangement, and following the same reasoning as before, the final expression for a single beatnote would be

$$I_{N,}(t) \propto A_{N-1,1}^2 \cdot e^{-2\alpha_{N-1,1}} + A_{N,2}^2 + 2A_{N-1,1}A_{N,2} \cdot e^{-\alpha_{N-1,1}} \cdot \cos\left(2\pi\left(f_{N,1} - f_{N,2} + f_{REP1}\right)t + \varphi_{N-1,1}\right) \quad (9)$$

This expression is basically similar to (7), but with the addition of a new frequency term in the last summand. This analysis can also be applied to other pairs of non-neighbouring lines, yielding a $k$ times $f_{REP}$ term depending on the order

*k* of the separation between comb lines from the first and second comb (being *k* an integer). This concept is graphically explained in Figure 13. Plainly speaking, the structure of the downconverted RF comb is replicated around every multiple of the repetition frequency of the comb, regularly displaying the same spectral information sampled by the comb in a dispersive arrangement (note that in the case of a collinear arrangement, this information would become mixed up). In any case, it is sufficient to analyse only the first Nyquist region where the beatnotes from the neighbouring lines of the combs lie, while the higher-order regions are usually filtered out.

Analogously, the time-domain picture is also important to understand this process. Here, each comb can be considered a pulse train with a different and linearly increasing time delay, with the faster pulse train (corresponding to the comb with the wider line spacing) smoothly gliding over the slower pulse train (see Figure 14). When both pulse trains reach a photodetector, an interference pattern (interferogram) arises. This signal originates from the cross-correlation between the electric fields and exhibits a centerburst caused by the temporal coincidence of the two optical pulses in the detector. The elapsed time until one interferogram fully crystallizes is defined by the reciprocal of the difference between the repetition rates, i.e., $1/\Delta f_{REP}$. In other words, the mismatch between the repetition frequencies of the combs not only determines the compression factor to downconvert the combs from the optical to the RF domain but also the measurement speed. Finally, the interferogram can be Fourier-transformed to generate the above-mentioned RF comb and process the spectral information.

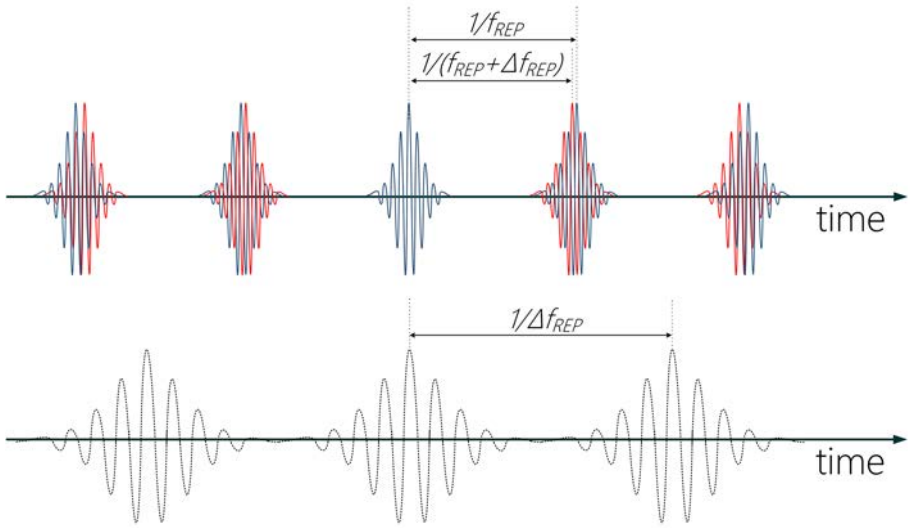


Figure 14. Time-domain representation of dual-comb spectroscopy showing the walk-off between optical pulses (top) and the generated interferogram in the RF domain after photodetection (bottom).

# 2.

# Practical Implications

In the previous section, dual-comb spectroscopy was introduced as a technique which granted for ultra-fast acquisition of high-resolution broadband spectra. There is no doubt that this could be accepted as true; however, there exists an interplay between several of these parameters which in fact does introduce a penalty when leveraging one or more of these outstanding features. What is more, the level of performance of the system is often evaluated by the signal-to-noise ratio (SNR), which is in fact closely linked to the measurement time and the ability to preserve the coherence between two independent frequency combs. Finally, it is also important to consider how this tool could serve purposes in field, outside-the-lab applications and not only in restricted laboratory environments. All these practical implications will be discussed in this section.

## 2.1. Speed, Resolution and Acquisition Bandwidth

The possibility to simultaneously record and observe the full bandwidth of an OFC in real-time is perhaps the most striking feature of the dual-comb technique. Nevertheless, there is a soft limitation in terms of the accessible spectral bandwidth that can be mapped to a narrow band in the RF domain in a single-shot manner. In the previous section, the effect of higher-order arrays of beatnotes was visible through the replication of the comb structure around multiples of the repetition frequency. This effect underlies the aforementioned constraint: if the compressed optical bandwidth exceeds a certain RF bandwidth, a phenomenon of aliasing may take place due to the overlapping of beatnotes from different orders. This process is illustrated in Figure 15.

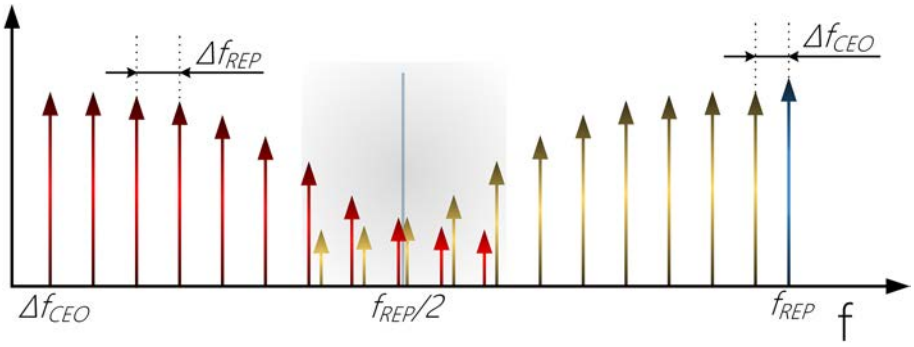


Figure 15. Aliasing process in a dual-comb system. When the difference between the repetition frequencies or the span of the comb is too large, the RF beatnotes from adjacent Nyquist regions may merge and, therefore, aliasing occurs (grey shaded area). This phenomenon happens when the downconverted RF comb exceeds a bandwidth of $f_{REP}/2$. For simplicity, only a single-sided optical spectrum is considered.

Of course, strict control of both $f_{CEO}$ and $f_{REP}$ may circumvent the aliasing effect, but this is usually restricted in comb sources with limited frequency tunability. In general terms, it is safe to say that the one-to-one mapping from the optical to the RF domain is preserved providing that

$$\frac{\Delta\nu}{\frac{f_{REP}}{\Delta f_{REP}}} < \frac{f_{REP}}{2} \tag{10}$$

or, similarly, that the downconverted optical bandwidth does not surpass half of the repetition frequency of the comb (see Figure 15). Considering that the optical span of the comb ($\Delta\nu$) contains $M$ lines spaced $f_{REP}$, the previous expression can be reformulated as follows

$$\Delta f_{REP} < \frac{f_{REP}}{2M} \tag{11}$$

which, as a function of the minimum integration time $T$ (i.e., the elapsed time until a single interferogram is created so that it contains all the information from the OFCs) can be also represented as

$$T > \frac{2M}{f_{REP}} \tag{12}$$

Both equations (11) and (12) show the direct interplay between acquisition speed, single-shot attainable optical bandwidth and spectral resolution (the latter is fundamentally limited by the linewidth of every comb tooth, but *de facto* fixed by the line spacing of the comb –$f_{REP}$-). Clearly, depending on the comb technology,

some systems will favour one or two of these ingredients over the other(s). For example, MLL-based OFCs with $10^5$-$10^6$ spectral elements and resolutions in the order of hundreds of MHz can be acquired in tens of milliseconds, whereas microresonator-based OFCs can benefit from faster measurement speed (in the range of microseconds or nanoseconds) due to their broader tooth spacing for a similar optical span. Still, this Nyquist constraint only applies when taking advantage of these three specifications at once (i.e., single-shot acquisitions). In order not to penalise one of these parameters, alternative procedures such as coherent stitching of narrower optical spans[115] or spectral interleaving for improved resolution[119] can also be adopted.

## 2.2. Coherence and Signal-to-Noise Ratio

The trade-off between high resolution, acquisition bandwidth and speed represents a soft constraint which can easily be overcome. However, the most stringent requirement to perform dual-comb spectroscopy stems from the ability to synchronize a pair of free-running comb sources.

If both comb sources are not phase-locked to each other (i.e., they do not feature high coherence between them), their characteristic frequencies $f_{CEO}$ and $f_{REP}$ will not remain fixed due to phase drifts and will fluctuate randomly. When both OFCs are overlapped on a photodetector, the power will be spread across the entire RF bandwidth instead of over the discrete comb structure of the multiheterodyne beatnotes. As a consequence, the beatnotes will exhibit linewidths in the order of the MHz and, in some cases, they will randomly blend together. In practical terms, this means that the beatnotes will no longer remain at their established differential frequencies. This contamination between adjacent comb lines is translated into the loss of orders of magnitude in terms of resolution and accuracy, hence depriving the dual-comb technique of two of their most outstanding features.

In fact, this is not the only implication associated with the coherence of the system. An unstable dual-comb source presents an inherent limitation in the attainable SNR, and hence, in the level of performance of the system. The SNR will depend on the prevailing noise source; however, if the dual-comb system is actively stabilized, it will consistently scale with the square root of the integration time up to a point set by the reciprocal of the linewidth of the RF comb teeth. For that purpose, the consecutive acquisition of interferograms must be properly aligned in phase during the acquisition time for averaging purposes. It is clear, therefore, that preserving the coherence of the system is an essential requisite not

only to capitalize on the virtues of the approach but also to reach a specified level of performance, as the minimum acquisition time is often set by the required SNR. For a deeper insight into the subject of SNR in dual-comb arrangements, the reader is referred to an exhaustive analysis of the achievable limits of the SNR due to different factors reported by Newbury *et al.*[115].

Ensuring mutual coherence between independent combs is not usually straightforward, with different degrees of sophistication for increasing levels of coherence. Furthermore, not all the dual-comb architectures are amenable to locking mechanisms, particularly in spectral regions beyond Near-Infrared. Others, on the other hand, feature an intrinsic mutual coherence that drastically relaxes their synchronization complexity and hence, their effective operation resolving each spectral element (this is the case of EO dual-comb architectures). In the most elaborate scenario, a pair of mutually coherent OFCs can even be traced back to a reference standard to upgrade the accuracy of the resolved spectra down to the kHz level. In any case, the goal is to spectrally resolve each comb tooth pair avoiding crosstalk between adjacent lines. Naturally, the intricacy of the mechanism will depend on the target specifications. To that end, there are a number of methods which have been proposed to induce mutual coherence between combs. Some of them have been used in conjunction for extended averaging periods and, therefore, enhanced SNR:

- Active phase-locked feedback between OFCs. This was the first technique which was followed to ensure one-to-one spectral correspondence while maintaining absolute frequency accuracy[120,121]. The error signals between the combs and one or two cavity-stabilized CW lasers are used as the input of phase-locked loops to actively stabilize the comb sources with the help of high-bandwidth actuators. To lessen the complexity of this approach, new schemes encompassing free-running CW lasers[122,123] and quartz oscillators[124] as well as feed-forward adjustments in which one of the combs tracks the instabilities of its counterpart[125] have also been successfully demonstrated.

- Designs sharing a common laser source, cavity or platform. This is the case of EO dual-comb arrangements, in which a single CW laser feeds a pair of EOMs sharing the same RF time base[126]; or MLLs emitting two interlaced pulse trains with different repetition frequency while sharing a single cavity[127]. The common-mode noise cancellation secures comb-tooth resolved spectra without the necessity for active stabilization. Dual-comb systems comprising two cavities integrated in a single platform also benefit from short-term mutual coherence[128].

- Adaptive interferogram digitization. First proposed by Ideguchi *et al.*[129], this approach harnesses the heterodyning of a pair of lasers with the two MLL-based OFCs to generate two adaptive clock signals that compensate the timing jitter and the fluctuations of the relative carrier-envelope phase, respectively. A re-engineered approach has also been devised for EO dual-comb architectures to reinforce mutual coherence[130].
- Digital interferogram correction. Introduced by Giaccari, Deschênes *et al.*[131,132], this method relies on the simultaneous acquisition of the time-domain fluctuations of two loosely stabilized combs in order to resample the interferometric signal. The refinement of this technique has allowed for long averaging periods in real-time (covering hours and days) through the calculation of correction factors that restore the mutual coherence[133].
- Pure computational correction. Driven by the advancements in dual-comb architectures based on QCLs, Burghoff *et al.* demonstrated that the phase and timing signals could be computationally extracted from the downconverted RF comb without any additional measurement or optical element[134]. Recently, efforts have been made towards the mitigation of the computational complexity of these correction mechanisms[135].

## 2.3. Fieldable Capabilities

So far, two of the fundamental technical implications underlying the dual-comb technique have been assessed. Nevertheless, as the comb technology and the dual-comb detection process mature, new capabilities are increasingly demanded. Perhaps, one of the most actively pursued attributes is the possibility of operating dual-comb setups in field applications. To that end, there are some implications which must be carefully considered. This section aims to review the current status and future prospects of dual-comb sources for this purpose.

As expected, the first requirement for a fieldable dual-comb system is to be lightweight and compact. However, even more importantly, the main challenges are usually related to 1) adopting a system to preserve the mutual coherence and 2) defining which is the required level of performance (particularly in terms of accuracy), as the complexity of the setup usually parallels the last condition.

In line with the maturation of OFCs, the advent of robust Mode-Locked Fibre Lasers has driven the development of dual-comb spectroscopy beyond laboratory environments (see Figure 16)[124]. This interest was first evinced with the

measurement of gas-phase atmospheric constituents over kilometre air paths[136,137] and has recently culminated with fully-fieldable demonstrations for the quantification of regional trace-gas emission sources[138] and exhaust gases in an industrial power plant[139] Still, these systems resorted to quite sophisticate active phase-locked feedback between OFCs and digital correction algorithms for long-term averaging which increased both the complexity and the footprint of the setup.

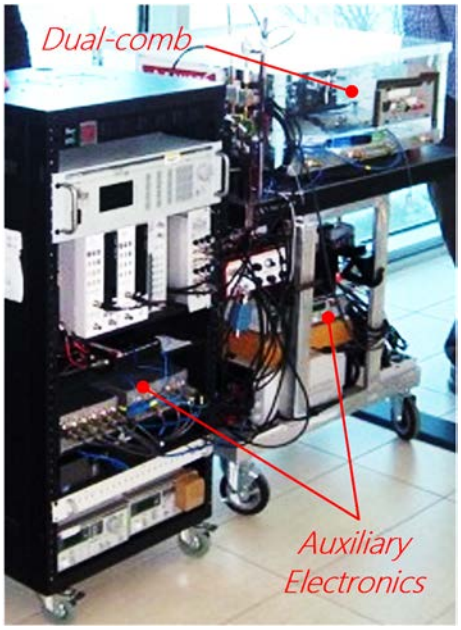


Figure 16. Full setup of a fieldable dual-comb spectrometer based on erbium-doped Fibre Lasers. Adapted from Truong *et al.*[124].

In fact, the chief motivation for developing dual-comb architectures with fieldable capabilities is mostly aligned with the conception that non-metrology-grade applications do not usually require 1) more accuracy than that provided by a commercial microwave reference; 2) more time stability than a hundred of milliseconds due to the ultra-fast nature of these systems; and 3) ultra-wide spans to successfully retrieve consistent spectral information. Bearing this in mind, one of the most appealing approaches harnesses the inherent passive mutual coherence of some systems instead of forcing an active tight lock, thus ensuring a level of short-term stability that is enough for a broad range of applications. Although this approach provides no *a priori* knowledge of the absolute frequency scale, the frequency detuning between pairs of comb teeth is more stable than their absolute frequencies, which is the essential requisite for line-resolved spectroscopy.

This is the case of novel MLL-based demonstrations which have proved to be well-suited for dual-comb generation based on either one source emitting two interwoven pulse trains multiplexed in wavelength[140], polarization[141], propagation

direction[142] or by pulse-shaping mechanisms[143] at different repetition rates; or single platforms that integrate a pair of free-running waveguide lasers[144]. Similarly, EO dual-comb architectures have also recently found their niche as portable spectrometers following the same principle[126]. In exchange for a narrower optical span, this approach has recently enjoyed success owing to its virtually limitless adaptability to the target application due to the absolute control over the repetition frequencies of the combs. A clear example of this can be found in the literature with a recent demonstration of an easy-to-operate laser range finder based on a field-deployed EO dual-comb[145]. An illustration of the implemented system is shown in Figure 17.

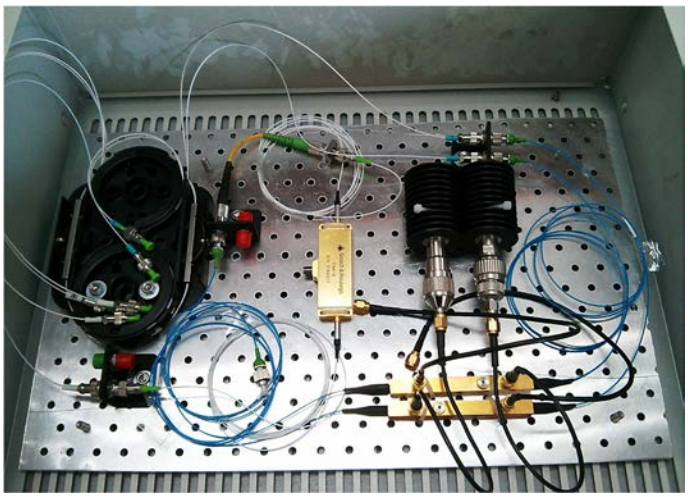

Figure 17. Optical setup of a field-deployed EO dual-comb architecture mounted into a 19'' rack module. The auxiliary electronics were placed in a package of similar size.

Finally, this discussion must also address the potential of miniaturized sources such as *microcombs* and QCLs. Despite relying on tailored designs with fixed line spacings, their potential for chip-level integration and aptitudes across varying spectral ranges makes them firm candidates to be the core element of future lightweight spectrometers[92]. In some cases, they benefit from mechanisms to induce short-term mutual coherence, as in the case of a pair of QCLs mounted on the same platform which can partially compensate thermal fluctuations and environmental instabilities[128,146]. As for microresonator-based dual-combs, this can be attained in architectures which share the same pump source[147] or by means of novel mechanisms that can simultaneously generate multiple solitons within the same resonator[148]. Nonetheless, active stabilization techniques are commonplace in these devices for robust comb operation and there is work ahead until they are routinely employed in less controlled environments. To that end, and not to neutralize their inherent advantage in terms of size, special emphasis must be

placed on pure computational phase correction algorithms in which these laser sources are particularly amenable[134,135], a promising alternative which can pave the way for the operation of these devices beyond laboratory constraints.

# 3.

# Demonstrations across Different Spectral Regions

This section will review the most relevant demonstrations of dual-comb architectures across different spectral regions. As the maturation of dual-comb sources will generally go hand-in-hand with the development of OFCs, those spectral regions where a frequency comb can be engendered may be susceptible to enjoy the range of advantages of this multiheterodyne detection method.

This way, the Near-Infrared portion of the electromagnetic spectrum (0.8 – 2.0 μm) is the region where the OFC technology has become more robust, and therefore, where the largest part of demonstrations has materialized. Deeper in wavelength towards the Mid-Infrared (2.0 – 20.0 μm) and THz (30 – 3000 μm, or equivalently, 0.1 – 10 THz), the technology is still rather scarce despite the healthy increase in interest due to its potential for some applications such as ultra-sensitive spectroscopy, as these regions contain the fundamental absorption bands of many organic and inorganic substances.

These three spectral regions will comprise the core of this analysis. First, in the Near-Infrared, examples based on MLLs, EO modulation and microresonator-based OFCs will be reviewed in detail. Afterwards, the analysis of Mid-Infrared will encompass two different types of sources: on the one hand, those that need to resort to intermediate stages (such as Difference Frequency Generation –DFG- or Optical Parametric Oscillators –OPOs-) to reach this wavelength range; and on the other hand, those emitting their radiation in this region of the spectrum directly (i.e., QCLs and specially-designed MLLs and microresonators). Finally, the THz region will be also assessed in a similar fashion (indirect and direct sources). This section will conclude with an additional brief discussion about the impact of this technique on other parts of electromagnetic spectrum.

## 3.1. Dual-Comb Spectroscopy in the Near-Infrared

### 3.1.1. Mode-Locked Laser-based Dual-Combs

In the previous section, MLL-based dual-combs were introduced as the driving force of dual-comb spectroscopy beyond laboratory environments. In fact, Fibre Lasers not only have led the progress in this area but also the evolution of the dual-comb technology in its broadest sense. Arguably, the Near-Infrared spectral range, with the advanced nature of its associated optical componentry (Fibre Lasers, fibre-coupled components and high-speed photodetectors) has been the theatre of operations of dual-combs in the past years. This framework has sparked off two different research lines: a first one aimed at the depuration of the technique and a second one which addresses the utilization of these architectures for specific applications beyond instrument demonstrations.

With regard to the first research line, one of the most actively pursued features in these systems has been the search for mutual coherence between independent OFCs, as explained in the previous section. Coddington *et al.* showed in 2008 the first comb-tooth resolved spectra with erbium-doped Fibre Lasers to recover the full complex spectrum of hydrogen cyanide[120] and later its time-domain free-induction decay[149] by means of an active phase-locked feedback between OFCs. Other research groups followed the same approach but attempted to reduce the complexity of the locking mechanism by means of different configurations to compensate the drifts of the lasers[122–125]. Alternatively, adaptive interferogram digitization[129] and digital interferogram correction[131–133] methods were also conceived for MLL-based dual-combs (a more detailed description of the operating principle of the aforementioned coherence-reinforcing mechanisms has been reviewed in Section 2.2 of Chapter II). It is, however, important to highlight that the combination of some of these techniques to coherently sum interferograms in platforms such as field-programmable gate arrays[121,133] has also paved the way for real-time acquisition over virtually unlimited long acquisition times (coherent averaging of interferograms for 24 hours has yielded an unmatched SNR of 316000)[133].

Another intriguing feature that has been validated with Fibre Lasers is the compatibility of dual-comb spectroscopy with cavities. Long interaction paths are feasible due to the excellent spatial beam quality of the OFCs, leading to impressive figures in terms of sensitivity, as the work of Benhardt *et al.* first revealed in 2009[150] and Hoghooghi *et al.* further refined a few years later to cover broader bandwidths

with longer averaging times and enhanced sensitivity[151]. Furthermore, nonlinear spectral broadening has also proven to be successful for the interrogation of gas phase molecules (such as $CH_4$, $CO_2$, $C_2H_2$, and $H_2O$) over bandwidths of tens of THz. Truly remarkable are the contributions of Zolot *et al.*[152] and Okubo *et al.*[153] performing single-shot fully-resolved dual-comb spectroscopy with frequency combs spanning from 1360 to 1690 and 1000 to 1900 nm (see Figure 18) in 2012 and 2015, respectively.

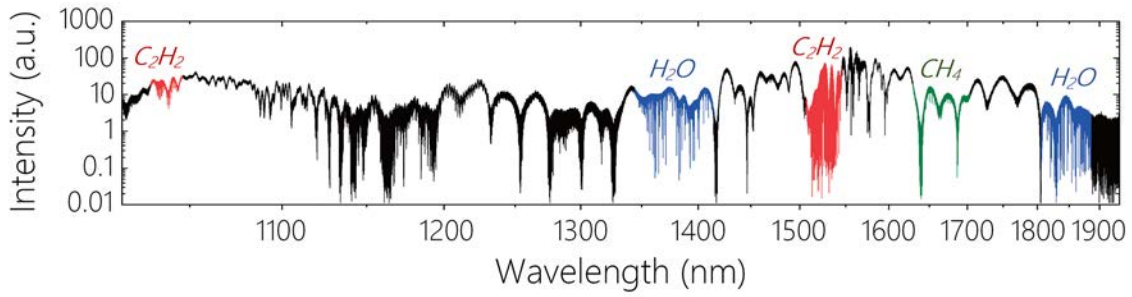


Figure 18. Ultra-broadband spectrum from 1.0 to 1.9 μm based on an erbium-doped Fibre Laser-based dual-comb architecture. The absorption bands (coloured traces) of some gas-phase constituents are visible across the spectrum (black trace). Adapted from Okubo *et al.*[153].

In recent years, it is also notable the development of innovative MLL-based dual-comb architectures where a single cavity or platform houses two mutually-coherent pulse trains with slightly different mismatch in their repetition rates. Some of these arrangements are depicted in Figure 19. For instance, Link *et al.* introduced in 2015 a Mode-Locked Integrated External-Cavity Surface-Emitting Laser whose output consisted of two collinearly overlapped cross-polarized pulse trains[141]. The design of this source was recently perfected by Nürnberg *et al.* to provide broader bandwidths[154]. Moreover, polarization-multiplexing in Fibre Lasers has also been reported in the literature[155,156]. In 2016, Ideguchi *et al.* proposed a ring Kerr-lens Ti:Sapphire Laser emitting two bidirectional frequency combs[127], while Mehravar *et al.* and Olson *et al.* followed the same principle with erbium- and thulium-doped Fibre Lasers, respectively[142,157]. An all-optical multiplexed dual-wavelength scheme for dual-comb generation has been also unveiled by Zhao *et al.* and Liao *et al.* in the vicinity of 1.5 and 2.0 μm, respectively[140,158]. Moreover, Liu *et al.* proposed pulse-shaping mechanisms to generate two interwoven pulse trains within the same cavity[143]. A related approach was followed by Bourbeau-Hébert *et al.* in 2017 with a chip-based multi-laser platform integrating two Mode-Locked Waveguide Lasers that exhibited a high degree of mutual stability[144].

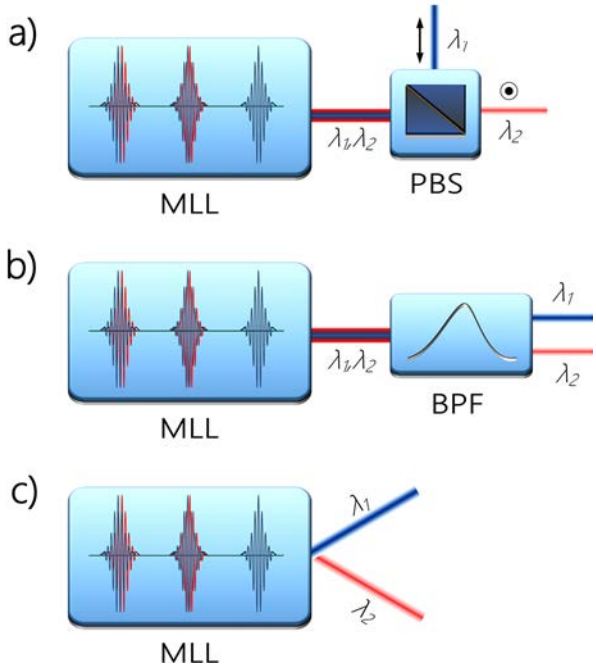


Figure 19. Representative schemes of single-cavity MLL-based setups for dual-comb spectroscopy. a) Polarization multiplexing. Two interlaced pulse trains are generated inside the laser cavity. A polarization beam splitter (PBS) is used to split the OFCs for dual-comb interferometry. b) Dual-wavelength multiplexing. Two combs with different central emission wavelengths are separated by means of a band-pass filter (BPF). c) Bi-directional multiplexing. The pulse trains propagating in clockwise and counter-clockwise directions exit the cavity either in different angles or in opposite directions.

The primary motivation of Near-Infrared dual-comb architectures based on MLL-based OFCs was high-precision spectroscopy of trace gas samples[112], since the repetition frequency of these combs (and hence, the spectral resolution) is well-matched to the Doppler widths of the molecular transitions (usually in the range of hundreds of MHz). However, as these systems can be used to determine the attenuation and the phase shift of the transmitted optical field (with absolute frequency accuracy in some cases), dual-comb spectrometers have been appealing to an ever-increasing number of applications in the last years. Table 2 gathers the applications demonstrated with Near-Infrared MLLs to date with examples and a summary of the main results. Note that linear spectroscopy of gas samples in single or multipass cells in laboratory environments under semi-static conditions has not been included in the list due to its ubiquity as validation tool in these systems. Nonlinear dual-comb spectroscopy has also been omitted from this classification, as it will be discussed later in the document.

Table 2. List of applications based on Near-Infrared MLL-based dual-comb architectures.

| Application | Contributions and Main Results |
|---|---|
| Absolute distance metrology | Demonstration of an absolute ranging system with a precision of 5 nm at 60 ms and an ambiguity range of 30 km (Coddington *et al.*)[23] |
| Absorption spectroscopy in industrial combustion environments | Measurement of the concentration of $H_2O$, $CO_2$ and temperature in a gas turbine exhaust (Schroeder *et al.*)[139]<br><br>Measurement of a gas mixture of $CH_4$ and $N_2$ and its temperature in a rapid compression machine at shorter timescales (Draper *et al.*)[159] |
| Accurate measurement of molecular line centres | Atomic standard-referenced Doppler-limited spectra of methane and acetylene (Zolot *et al.*)[160]<br><br>Measurement of speed-dependent Voigt lineshape parameters of pure (Schroeder *et al.*)[161] and Argon-broadened water vapor (Yang *et al.*)[162] |
| Analysis of the impact of external factors on gas molecules | Observation of pressure-broadening and pressure-shift effects in acetylene (Iwakuni *et al.*)[163]<br><br>Development of a method based on a model function for temperature determination of acetylene (Shimizu *et al.*)[164] |
| Atmospheric gas monitoring over air paths | Time-resolved measurement of atmospheric gas constituents across a 2 km horizontal air path with sub-ppm precision (Rieker *et al.*[136] and Giorgetta *et al.*[165]) and intercomparison between instruments over measurement campaigns (Waxman *et al.*)[166]<br><br>Extension to vertical paths for spatial mapping using an unmanned aircraft system (Cossel *et al.*)[137]<br><br>Extension to continuous and regional coverage over multiple-square kilometre areas (Coburn *et al.*)[138] |
| Characterization of complex optical properties of solids | Measurement of the refractive index of erbium-doped yttrium aluminium garnet and a silicon semiconductor wafer (Asahara *et al.*)[167] |
| Characterization of fibre Bragg grating (FBG) sensors | Measurement of the optical response of an FBG under strain with a resolution of 34 nε (Kuse *et al.*)[168] |

| | |
|---|---|
| Characterization of laser-induced plasmas | Detection of trace amounts of rubidium and potassium in solid samples using a single laser ablation shot (Bergevin *et al.*)[169] |
| Characterization of microresonators | Measurement of the impulse response of the microcavity and the material surrounding the resonator (Michaud-Belleau *et al.*)[170] |
| Characterization of samples in condensed phases | Measurement of IR140 (dye molecule) dissolved in ethanol (Cho *et al.*)[171] |
| Characterization of telecommunication components | Measurement of the optical response of a spool of optical fibre with 91 dB of dynamic range (Coddington *et al.*)[172] |
| Ellipsometry | Retrieval of parameters related to the polarization state of light for the measurement of thin-film samples with an accuracy of 38.4 nm (Minamikawa *et al.*)[173] |
| Hyperspectral lidar | Measurement of HCN absorption lines at 20 metres (Boudreau *et al.*)[174] |
| Imaging | Optical coherence tomography for biological imaging and technical applications (Kray *et al.*)[175]<br><br>Line-scan spectrum-encoded imaging to measure three-dimensional profiles with absolute distance measurements (Wang *et al.*)[176]<br><br>Scan-less confocal amplitude and phase microscopy with milliradian phase resolution under micrometre depth selectivity (Hase *et al.*)[177] |
| Metrology of laser sources | Time-resolved, absolute-frequency measurements of dynamic, arbitrary CW waveforms at time resolutions below 1 ms (Giorgetta *et al.*)[178]<br><br>Coherent sampling of THz QCLs for the unambiguous measurement of their emission frequencies with hertz-level precision (Kliebisch *et al.*)[179] |
| Time-frequency transfer | Demonstration of optical time-frequency transfer via two-way exchange between OFCs with 1 fs timing deviation (Giorgetta *et al.*)[180] |

Finally, it is also noteworthy the work of some research groups that have explored the potential of dual-comb spectroscopy for various purposes or under specific conditions. This is the case of the generalized methods proposed by Bourbeau-Hébert *et al.* to reduce the spectral line spacing independently of the fixed repetition rate of MLL-based OFCs involving, first, two combs with quasi-integer repetition rates by multiplexing the interferograms in time[181], and second, binary pseudo-random phase modulation of the pulse train[182]. Okubo *et al.* also contributed to these techniques for higher resolution with a method based on discrete Fourier-transforms and spectral interleaving[183]. Likewise, other groups have conducted studies revealing the optimal dual-comb parameters with the objective of either improve some characteristics, such as sensitivity[184], or enhance the performance of particular applications, namely ranging[185] or determination of spectral line properties[186].

### 3.1.2. Electro-Optic Dual-Combs

EO dual-combs embody one of the most promising alternatives to MLL-based dual-combs. With only a few commercial off-the-shelf components, an EO dual-comb spectrometer may be readily assembled. A schematic of the basic setup is depicted in Figure 20. The light of a CW laser is split into two paths to create a pair of OFCs with two EOMs driven at slightly different repetition frequencies. As these combs share the same central frequency (the emission wavelength of the CW laser), one of them is usually frequency-shifted by means of an acousto-optic modulator (AOM) to resolve the symmetric appearance of the dual-comb and thereby ensuring the unique mapping of the downconverted combs. Finally, both OFCs are merged and overlapped on a single photodetector, as in ordinary dual-comb schemes.

The great success that these architectures have enjoyed in the past years stems from three main reasons:

- The intrinsic mutual coherence. As both EOMs are fed by the same single CW laser and the EOMs are driven with RF signals referenced to the same time base, the system features very high mutual coherence (and hence, comb-line resolved spectra) without resorting to complex methods for the stabilization of the two combs.
- The virtually unlimited and agile control over the spectral resolution, acquisition speed, central wavelength and offset frequency (ultimately

limited by the transparency range and bandwidth of the EOMs and the tuning range of the CW laser) to easily match the experimental needs.

- The modular and compact nature of the system. Using telecom-grade components in fully-fiberized setups allows for easy external customization and endows the systems with improved robustness.

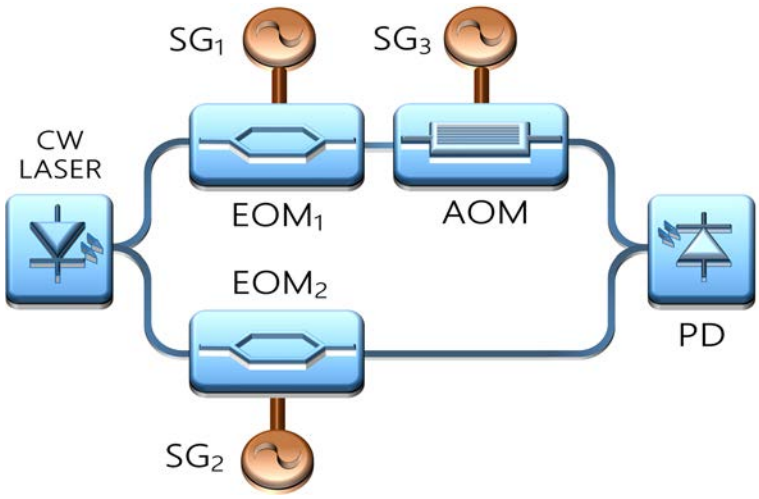


Figure 20. Basic schematic of an EO dual-comb spectrometer. PD: Photodetector; SG: Signal generator.

The main drawbacks related to EO dual-combs are their restricted optical bandwidth (usually comprising < 100 spectral points) and their limitations in terms of accuracy, as there exists no *a priori* absolute calibration of the frequency axis. Some of the methods that have been employed to overcome these handicaps have already been discussed in Section 2.2 of Chapter I. Nevertheless, as collateral advantages in exchange for the narrow linewidth, it is worth mentioning that the requirement for high-dynamic range linear photodetectors and digitizers is drastically alleviated and the power per spectral component is higher than that of MLL-based OFCs[115].

Surprisingly, the first EO dual-comb demonstration was also one of the first dual-comb architectures reported in the literature. Lee *et al.* proposed in 2001 a novel optical coherence tomography system with an equivalent scanning speed of 12.5 km/s[118]. Favoured by the higher attainable repetition frequencies (up to tens of GHz) linked to stable RF references, one of the earliest motivations for EO dual-comb interferometry was the measurement of distances by recovering the interferometric phase information of multiple comb lines. In 2003, Lay *et al.* reported an absolute metrology system with sub-nanometre accuracy up to 1 m[187]. Yang *et al.* expanded the capabilities of these schemes up to 10 m with a multi-phase digital lock-in detection method in 2014[188]. The refinement of this method

has led to more recent demonstrations up to 1.2 km[189], new schemes to achieve simultaneous resolution and non-ambiguity range[190] and even the photonic integration on silicon of an optical distance sensor[191]. In this context, it is also remarkable the work of Weimann *et al.* based on dual-colour EO dual-combs for improved robustness which were deployed under industrial conditions for precise surface profilometry of technical samples[192].

The large frequency spacing of EO dual-combs has also proven useful for the generation and characterization of optical arbitrary waveforms. In 2009, Ferdous *et al.* presented an electric-field cross-correlation method for the latter purpose, which essentially involved a classic EO dual-comb scheme[193]. A few years later, Durán *et al.* re-conceptualized the method to exploit the trade-off between speed, spectral resolution and acquisition bandwidth to operate at ultra-high refresh rates (40 ns) with a $\Delta f_{REP} > f_{AOM}$ to record the phase profiles imparted onto the spectrum by a pulse shaper[194]. More recently, the same authors further applied these principles over the entire telecommunication C-band to measure the dispersion introduced by low dispersive spectroscopic samples[195].

The application of EO dual-comb architectures to spectroscopy of gas samples is even newer. The first proofs of principle were realized by Long *et al.*[126] and Martín-Mateos *et al.*[196,197] in 2014 and 2015, respectively, with measurements of the full complex spectrum of $CO_2$ and HCN. Soon after, the techniques for spectral broadening were introduced for the analysis of multiple interfering absorbing species. Fleisher *et al.* used step-recovery diodes to drive the EOMs to generate OFCs with >250 teeth along with an enhancement cavity for increased sensitivity[198] (a recent work by the same authors has even disclosed a quantitative model for cavity-enhanced EO dual-comb spectroscopy)[199]. More than 1200 lines were later reported by Millot *et al.* by counter-propagating both combs in a highly-nonlinear fibre of normal dispersion to interrogate gases in a gas-filled fibre[200]. Alternatively, Wang *et al.* proposed a comb densification method based on two-stage modulation with an arbitrary waveform generator for small line spacing in a broader span resulting in 1500 lines to measure several transitions of HCN[201]. Very recently, Carlson *et al.* set an unprecedented record of 12000 lines covering from 1150 to 2150 nm by means of cascaded spectral broadening in highly nonlinear fibres and silicon-nitride photonic waveguides to probe $CO_2$ and $H_2O$ at high pressure[202] (see Figure 21).

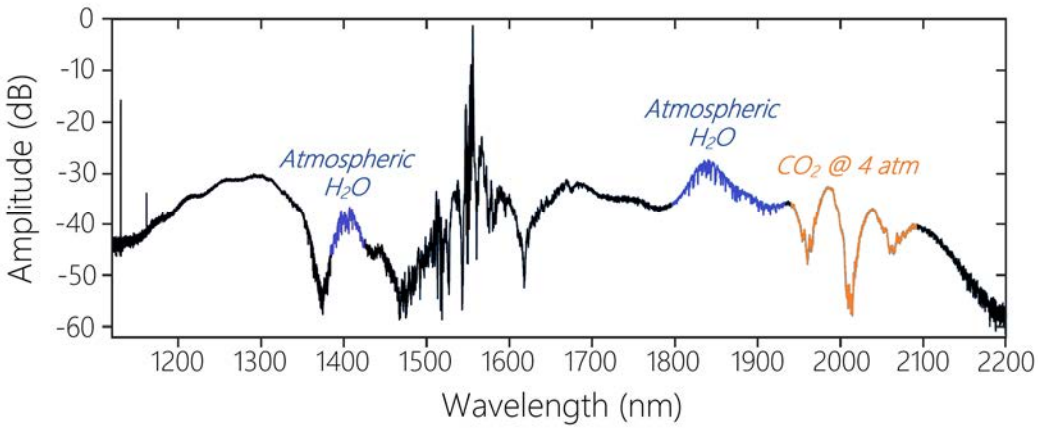


Figure 21. Ultra-broadband spectrum from 1.2 to 2.2 μm based on an EO dual-comb architecture. Some absorption features due to high-pressure water vapour and carbon dioxide are discernible. Adapted from Carlson *et al.*[202].

The rapid advance of EO dual-combs has also inspired other applications to take advantage of the range of virtues associated with these systems. To name a few, interrogation of FBG sensors for measuring fast phenomena (e.g., ultrasounds)[203], measurement of the thickness of transparent samples[204], vibrometry of dynamic samples with sub-nanometre precision[205], characterization of wavelength division multiplexed (WDM) signals[206], analysis of high-Q-factor resonators with MHz-level resolution in a quasi-integer ratio mode[207] or even a new version of video-rate optical coherence tomography with centimetre-level imaging depth[208]. All of them have contributed to expand the landscape of EO dual-comb applications, with special emphasis placed on the first demonstration of an in-field EO dual-comb implemented in a 19'' rack module to operate as a range finder[145]. Additionally, it is also noticeable the recent interest of some groups in coherence-reinforcing techniques for extended averaging times despite the intrinsic mutual coherence of EO dual-comb systems. Some examples of these methods are the design of a phase-locked loop acting on the frequency of the AOM reported by Fleisher *et al.* that enabled >2 hours of coherent averaging[198]; a novel adaptive interferogram acquisition approach re-engineered for EO dual-combs by Martín-Mateos *et al.*[130]; or the *a posteriori* phase-correction algorithms applied by Guay *et al.* for precision spectroscopy of HCN[209].

Finally, it is worthwhile to draw attention on some other emerging contributions which have reshaped the layout of classic EO dual-comb schemes. For example, Bourbeau-Hébert *et al.* reported a self-heterodyne detection scheme removing one of the two EOMs taking part in the dual-comb architecture[103]. This way, the optical bandwidth is compressed by a factor of $f_{REP}/2$ (instead of $f_{REP}/\Delta f_{REP}$), an interesting alternative when the optical span is not excessively large (in exchange of faster electronics for detection) with striking aptitudes for the

observation of high-speed dynamical processes[210]. A full experiment harnessing this type of architecture to probe low-pressure acetylene in gas phase can be found in Appendix I. Durán *et al.* also proposed an original CW laser-seeded dual-comb source in which the comb generation process is based on frequency-shifting loops involving AOMs. More than 1500 coherent lines were generated and used to measure HCN[211]. Carlson *et al.* unveiled a peculiar technique for dual-comb interferometry which relied on using one single EOM (this time placed before splitting the power into the two interferometer paths) whose repetition frequency was rapidly switched. Thus, this method provides an alternating pulse train that creates an interference pattern after being delayed and heterodyned with itself. The authors further proved the efficacy of the method for applications such as spectroscopy, vibrometry or absolute distance metrology[212]. Very similarly in concept to the previous work, Kayes *et al.* also reported the operation of an imbalanced dual-comb interferometer fed by only one EO-OFC, but, on this occasion, the repetition frequency was swept in order to create an interferometric signal[213]. As a last exotic example, Wang *et al.* also demonstrated the feasibility of a hybrid dual-comb comprising a free-running MLL and an EO frequency comb[214].

### 3.1.3. Microresonator-based Dual-Combs

Despite the short life of microresonator-based OFCs, researchers have remained open to the possibility of duplicating the arrangement to exploit one of the most compelling methods of detection. Propelled by the realization and control of DKS within their cavities, the full miniaturization of dual-comb platforms is one step closer since the combination of these two fields of research has materialized.

The first demonstration of dual-combs with microresonators took place in 2016 for spectroscopy of HCN in gaseous phase[215]. Suh *et al.* employed a pair of free-running microresonators with extremely limited mutual coherence to probe the gas and a synthetic absorber, but the spectral resolution was insufficient to precisely retrieve the molecular spectrum of the former. Dutt *et al.* reported the generation of two *microcombs* in the same chip using microheaters and a single seed laser to ensure higher mutual coherence between combs and also reducing the complexity of the setup. In a single-soliton mode-locked state, the dual-comb instrument was used to observe the formation dynamics of the combs and perform liquid-phase absorption spectroscopy of dichloromethane[147]. Dual-combs with high relative coherence based on counter-propagating solitons within the same spatial mode of a single device were proposed by Yang *et al.*[216], while, more

recently, Lucas *et al.* demonstrated the simultaneous generation of multiple solitons –and hence, combs- also within a single cavity in different spatial modes pumped by only one CW laser and a single-sideband modulator. With this mutually coherent scheme, the authors retrieved the full complex spectra of pre-programmed synthetic absorption features and sampled a breathing soliton[217]. On the other hand, other research groups focused on proof-of-concept demonstrations of microresonator-based dual-combs in different platforms using diverse fabrication techniques[218], novel methods to create two orthogonally interlaced combs in a single microresonator[219] or theoretical studies for dual-comb generation in a single microresonator with orthogonally polarized dual-pumping[220].

Beyond spectroscopy, microresonator-based dual-combs have proven useful for range measurement due to their characteristic high repetition frequencies. In this sense, Suh *et al.* revealed a dual-comb system within a single microresonator with counter-propagating solitons that features time of flight measurements with 200 nm precision in ranges up to 25 metres[148]. Trocha *et al.* deployed a free-running dual-comb for the same purpose, but the ultra-short coherence time did not prevent the authors from measuring distances with Allan deviations down to 12 nm within ~10 μs. Under these conditions, gun projectiles moving at 150 m/s were successfully sampled[221]. Figure 22 shows the profile measured with the instrument together with an image of the projectile.

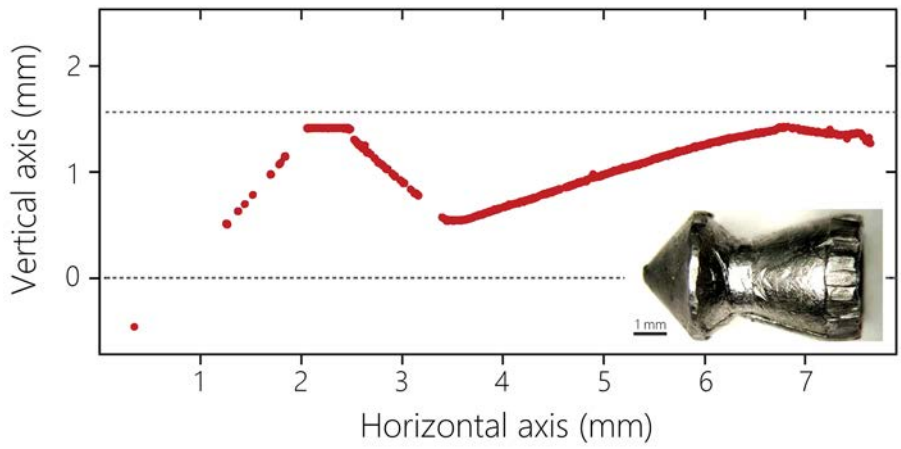


Figure 22. Microresonator-based dual-comb ranging interferometry. In-flight measured profile of a rapidly-moving gun projectile at 150 m/s. Inset: Actual image of the projectile. Adapted from Trocha *et al.*[221].

Undoubtedly, microresonator-based dual-combs will be finding an increasing number of applications as they evolve over the years. Some recent examples of peculiar demonstrations that illustrate this potential are the utilization of these devices for communication, imaging purposes and measurement of frequencies. In the first case, Marin-Palomo *et al.* reported a dual-comb DKS

architecture to transmit and coherently detect WDM data streams at a rate of tens of Tb/s[222]. Bao *et al.*, for their part, employed a pair of microresonator-based OFCs to monitor the flow of microparticles in a fluid cell with frame rates as high as 200 kHz[223], while Yang *et al.* implemented a Vernier spectrometer with two counter-propagating soliton *microcombs* to track the frequencies of rapidly tuned lasers and multimode spectra[224].

## 3.2. Dual-Comb Architectures in the Mid-Infrared

### 3.2.1. Indirect Mid-Infrared Dual-Comb Architectures

The development, exploitation and increasing capabilities of dual-comb spectroscopy in the Near-Infrared shows no signs of abating. However, beyond this spectral region, the possibilities of this technique have opened up new intriguing prospects. More specifically, the Mid-Infrared domain is of particular interest, as the electromagnetic radiation emitted in this range of wavelengths can resonate with the strongest vibrational transitions of many species (see Table 3 for a comparison of absorption line strengths between Near-Infrared and Mid-Infrared), thus favouring the unambiguous and ultra-sensitive identification of composites not only in gas but also in the liquid or even solid phase. For this reason, the role of Mid-Infrared dual-comb schemes is almost exclusively confined to molecular spectroscopy.

Despite this promising scenario, the technical challenges have hampered the adequate progress of instrumentation in this part of the electromagnetic spectrum and, in general terms, the technology has remained scarce. As a consequence, the most widespread method to implement dual-comb architectures in this spectral region relies on transferring the fully-grown Near-Infrared dual-comb sources (together with all their outstanding features) to the Mid-Infrared by means of nonlinear conversion mechanisms, such as DFG or OPO. A schematic illustrating the generation process of Mid-Infrared radiation with these approaches is shown in Figure 23. At this point, it is important to remark on the fact that the Mid-Infrared can also be reached via nonlinear processes such as Raman scattering. This and other nonlinear mechanisms that may provide access to different portions of the electromagnetic spectrum will be discussed in Section 3.4 of this chapter.

Table 3. Absorption line strengths in $10^{-21}$ cm²/(molecule×cm) for common molecules in the Near-Infrared and Mid-Infrared at room temperature. Extracted from Adler *et al.*[20].

| Molecule | Near-Infrared (0.8 – 2.0 µm) | Mid-Infrared (2.0 – 20.0 µm) |
|---|---|---|
| $CO_2$ | 0.3 | 3000 |
| CO | 0.02 | 300 |
| $CH_4$ | 1 | 100 |
| $C_2H_2$ | 10 | 200 |
| $H_2O$ | 20 | 200 |
| $NH_3$ | 5 | 200 |
| NO | 0.04 | 20 |

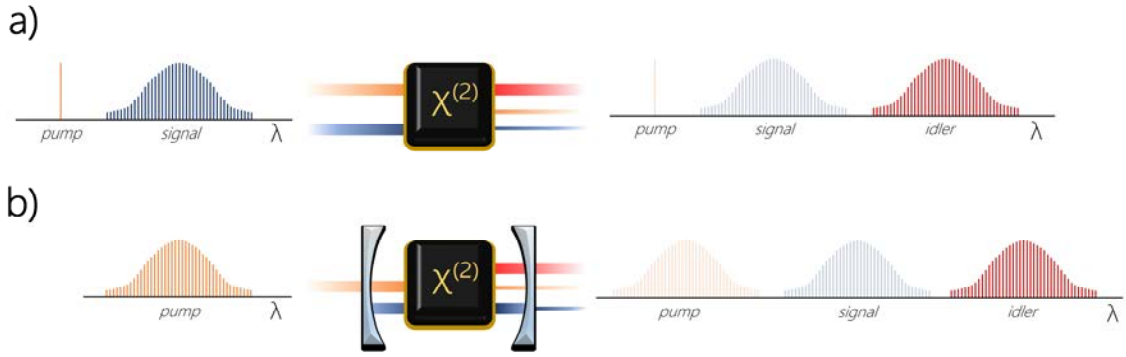


Figure 23. Principle of operation of the indirect methods to access the Mid-Infrared with OFCs. a) DFG. Mixing the teeth of a Near-Infrared *signal* comb with a CW *pump* laser (or alternatively, other teeth of the same *signal* comb) in a second-order nonlinear medium produces a Mid-Infrared *idler* comb under specific conditions. b) OPO. When a nonlinear media placed within an optical resonator is strongly pumped by an OFC, *signal* modes can be excited into the cavity and, concurrently, *idler* radiation is generated if the gain exceeds the threshold for parametric oscillation. In both cases, the energy conservation dictates the frequency of the *idler* radiation, which is the difference of frequencies between *pump* and *signal*.

DFG represents the most straightforward method to reach the Mid-Infrared. The underlying principle of this technique consists of mixing a Near-Infrared *signal* OFC with a CW *pump* laser (with frequency $f_{CW}$) in a second-order susceptibility medium ($\chi^{(2)}$), which is usually a nonlinear crystal[225]. Therefore, the appropriate selection of the CW laser and the crystal will effectively transfer the structure of the Near-Infrared OFC to the Mid-Infrared according to the expression $f_{N,DFG} = f_{CW} - f_N$, where $f_{N,DFG}$ is the frequency of the *idler* Mid-Infrared frequency comb. The

suitability of this process is highly dependent on two factors: the strength of the optical nonlinearity and the attainable phase-matched bandwidth (i.e., the bandwidth which allows for the generation of Mid-Infrared radiation as the input light propagates through the medium). For that purpose, one of the most common approaches takes advantage of the use of engineered quasi-phase-matched (QPM) materials[226] to ensure that the number of DFG photons grows along the crystal coherently (i.e., constructive interference) and therefore, the nonlinear conversion takes place efficiently. Furthermore, as the temperature changes the phase-matching conditions of the crystal, QPM-based DFG processes allows for the external tuning of the wavelength of the generated Mid-Infrared frequency combs. There are several nonlinear crystals with varying nonlinear figures of merit and transparency ranges across Mid-Infrared. Figure 24 gathers some of them for comparison purposes. Note that not all of them are quasi-phase-matchable and it is necessary to appropriately adjust some other parameters of the crystal (e.g., the birefringence) in order to carry out the nonlinear conversion efficiently.

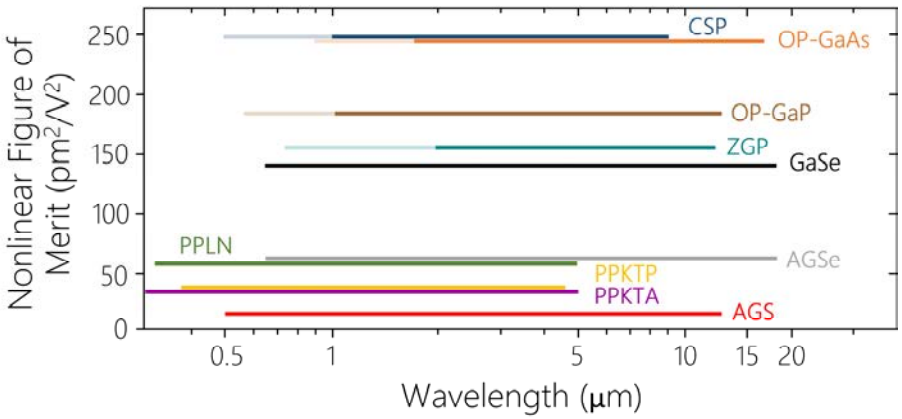


Figure 24. Transmission range of phase-matched nonlinear crystals for Mid-Infrared DFG and OPO together with their nonlinear figures of merit. The shaded areas represent the parts of the transmission ranges at which the crystals cannot be efficiently pumped. Those materials orientation-patterned (OP) or periodically-poled (PP) are quasi-phase-matchable. AGS: Silver gallium sulphide; AGSe: Silver gallium selenide; CSP: Cadmium silicon phosphide; KTA: Potassium titanyl arsenate; KTP: Potassium titanyl phosphate; ZGP: Zinc germanium phosphide. Adapted from Maidment *et al.*[227].

The first demonstrations of Mid-Infrared dual-comb spectroscopy date back to 2004 and relied on a pair of free-running Ti:Sapphire Lasers shifted to this region by means of DFG in GaSe. The nonlinear process was carried out with *pump* and *signal* frequencies from teeth of the same OFC, thus creating a pair of harmonic, offset-free combs in the Mid-Infrared. With this setup, Keilmann *et al.* performed low-resolution measurement of trichloroethylene[228] and real-time recording of ammonia over a path of 44 metres in the 9-12 μm region[229]. A few years later, the

authors also extended the applicability of this system to scanning near field optical microscopy[230] and characterization of the optical properties of metamaterials[231].

Highly coherent DFG-based Mid-Infrared dual-comb spectroscopy was premiered in 2011 by Baumann *et al.* for the accurate line centre determination of methane around 3.4 μm overlapping a CW *pump* laser and an erbium-doped *signal* Fibre Laser in periodically-poled lithium niobate (PPLN)[232]. The commercial availability of this crystal was also harnessed by other groups to perform high-sensitivity measurements of methane in ambient air in a multipass cell using a single Fibre Laser-based comb as *pump* and *signal* to generate *idler* OFCs without $f_{CEO}$[233] or to demonstrate high-power, nonlinear fibre-broadened Mid-Infrared dual-combs for low-resolution detection of $C_2H_2$[234]. It is particularly remarkable the work of Ycas *et al.*, including a chirped PPLN waveguide to simultaneously acquire the instantaneous broad bandwidth across the full transparency range of PPLN. Using digital signal processing, the authors developed an instrument that successfully identified and quantified propane, carbonyl sulphide and every constituent of a mixture of methane, acetylene and ethane at high resolution[235], and recent experiments have also tested the feasibility of the system for open-path detection of acetone, isopropanol and ethane[236]. Chirped PPLN crystals were also utilized for intra-pulse DFG using few-cycle erbium-doped Fibre Lasers by Lind *et al.* together with an in-line method for $f_{CEO}$ stabilization to realize dual-comb spectroscopy of acetone and carbonyl sulphide in the 3-5 μm range[237]. Furthermore, Yan *et al.* reported the first demonstration of dual-comb spectroscopy with EOMs in the Mid-Infrared with a configuration involving two PPLN crystals to retrieve molecular line parameters of methane and measure ethylene in natural abundance[238].

Recent works have also explored new possibilities based on DFG for dual-comb architectures. For example, Herman *et al.* reported liquid-phase absorption spectroscopy using attenuated total reflection to monitor chemical reactions and extract kinetics parameters[239]. Nader *et al.* presented an original instrument that encompasses a Mid-Infrared frequency comb generated by means of DFG in PPLN and a supercontinuum produced in a tailored silicon-on-sapphire waveguide to perform dual-comb spectroscopy of carbonyl sulphide at 4.8 μm[240]. A full demonstration with two $Si_3N_4$ waveguides pumped by erbium-doped Fibre Lasers was only recently reported by Baumann *et al.* to acquire dual-comb spectra of CO and $CO_2$ from 2 to 2.5 μm[241]. Beyond the use of PPLN as nonlinear medium, other groups have extended the capabilities of dual-combs deeper in the Mid-Infrared with the use of other crystals, such as orientation-patterned (OP) GaP. Timmers *et al.* reported a super-octave bandwidth dual-comb from 4 to 12 μm based on intra-

pulse DFG to measure methanol and ethanol and analyse the temporal evolution of the evaporation of the former (see Figure 25)[242]. The same architecture was further enhanced by Kowligy *et al.* to cover the range between 3 and 27 μm using a collection of three different crystals (PPLN, OP-GaP and GaSe) and an EO sampling scheme to detect the Mid-Infrared dual-combs, thus circumventing the bandwidth limitation of commercial off-the-shelf Mid-Infrared photodetectors. Ammonia, carbon dioxide and even the vibrations of amides were resolved with this apparatus[243].

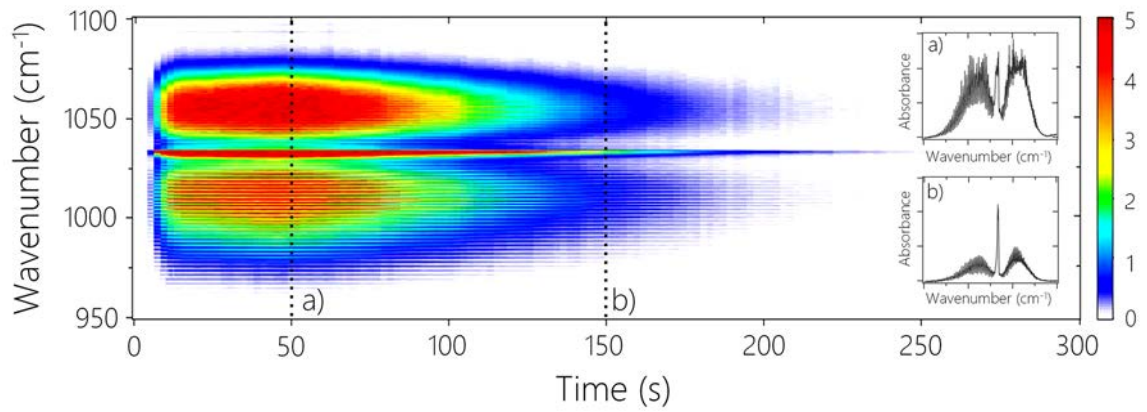


Figure 25. Evaporation of methanol examined by a DFG-based Mid-Infrared dual-comb system in the range 950-1100 $cm^{-1}$ (9.0 – 10.5 μm). The insets show two instantaneous spectra taken at a time of a) 50 and b) 150 seconds. The vertical bar on the right side indicates the absorbance. Adapted from Timmers *et al.*[242].

Alternatively, OPOs symbolize a different route for indirect Mid-Infrared dual-comb generation. In these schemes, the nonlinear medium is placed within an optical resonator, in such a way that when the crystal is strongly pumped by a Near-Infrared OFC, two output frequency combs at lower frequencies (*signal* and *idler*) with identical repetition frequencies can be generated. If the *pump* power exceeds a specific threshold level, the phase-matching conditions are fulfilled, and the dispersion of the resonator is carefully controlled so that the evenly-spaced *signal* comb teeth match the longitudinal modes of the cavity, the interaction between waves may lead to the parametric amplification of *signal* and *idler* combs along with the attenuation of the incoming *pump* OFC. The frequency of the *idler* comb is defined by the difference between the generated *signal* and the absorbed *pump*, as in DFG. With this arrangement, the photonic conversion efficiency is much higher than in DFG and output powers in the order of watts have been reported in the literature. As with DFG, broader wavelength tuning ranges can be easily attained by adequately influencing the phase-matching conditions. However, unlike DFG, it requires additional complex stabilization mechanisms to control not only the length of the cavity and the intra-cavity dispersion but also the offset frequency of either the *signal* or the *idler* comb. This task can be alleviated in

the case of degenerate OPOs (in which the frequencies of the *signal* and *idler* are exactly the same and half of the *pump* frequency).

The first OPO-based dual-comb systems were reported by Zhang *et al.* in 2012 and 2013[244,245]. These architectures encompassed a single-cavity OPO operating at 3.3 μm which contained a PPLN crystal. The OPOs were simultaneously pumped by two free-running ytterbium-doped Fibre Lasers and included schemes for the stabilization of, first, the repetition rate difference[244], and later, the carrier-envelope offset frequency[245]. However, a non-stabilized version of this setup was used in the first demonstration of dual-comb spectroscopy with OPOs using methane as target gas[246]. On the other hand, Jin *et al.* re-engineered the OPO cavity and introduced two PPLN crystals in a singly resonant ring cavity in which the *pump* combs counter-propagated[247]. This way, the full complex spectrum (absorption and dispersion) of both acetylene and methane could be retrieved with additional advantages in terms of stability and SNR[248]. With this system, time-resolved spectroscopy of methane in an electrical discharge has also been recently reported[249].

A system with two independent OPOs was employed by Kara *et al.* together with a digital cross-correlation protocol that utilized the recorded instantaneous frequencies of $f_{REP}$ and $f_{CEO}$ of both free-running Mid-Infrared OFCs as well as the arisen interferogram to perform absolute wavelength calibration and coherent co-alignment of interferograms. As a result, recognizable absorption spectra of methane in the region of 3.3 μm was successfully retrieved[250]. With a similar setup and following the same correction procedures, the authors also extended the performance of the OPO-based dual-comb architecture to perform combined spectroscopy of methane and water vapour between 6 and 8 μm by replacing the PPLN with an OP-GaP crystal[251]. Lastly, it is also noteworthy how the dual-comb technique has been applied to a pair of subharmonic OPOs (i.e., OPOs operating at degeneracy) pumped by fully-stabilized thulium-doped Fibre Lasers. Using OP-GaAs as nonlinear medium, Muraviev *et al.* reported the generation of two Mid-Infrared combs spanning well above one octave. With this scheme, the impressive detection and quantification of up to 22 molecular species in a gas mixture (including isotopologues) was uninterruptedly performed between 3.1 and 5.5 μm (see Figure 26)[252]. In a newer contribution, the same authors also demonstrated the potential of the system for background-free absorption spectroscopy for enhanced detection sensitivity[253].

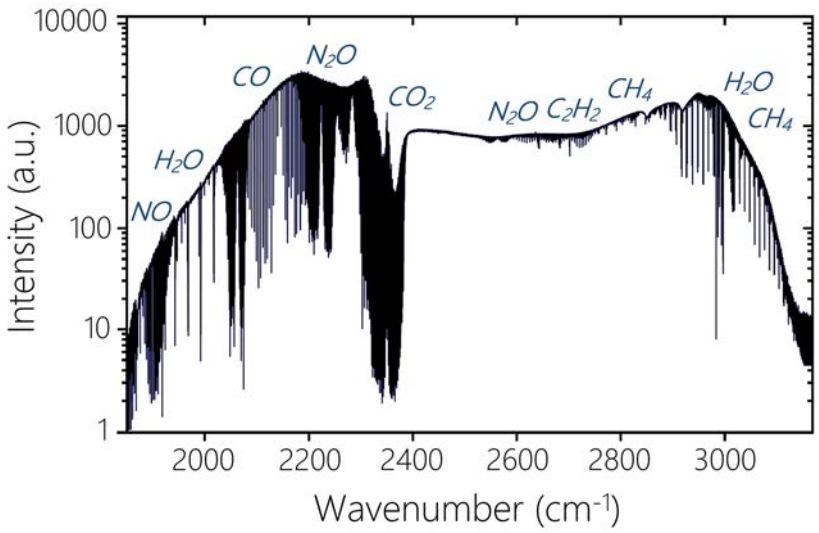


Figure 26. Mid-Infrared dual-comb spectroscopy using subharmonic OPOs for the detection of a number of trace molecular species in a mixture of gases between 1800 and 3200 $cm^{-1}$ (3.1 – 5.5 μm). Adapted from Muraviev *et al.*[252].

Finally, the epilogue of this discussion should also address a new method of nonlinear conversion which, so far, has been validated at the edge of the Mid-Infrared region. This method is based on the fourth-order modulation instability that manifests in the normal dispersion regime of highly nonlinear fibres when both *pump* and *signal* propagate through this medium. Under a very specific frequency detuning between *pump* and *signal* and within a particular bandwidth, new *idler* spectral components may symmetrically arise with respect to the *signal* in terms of frequency. Parriaux *et al.* used this approach to perform dual-comb absorption spectroscopy of $CH_4$ at 2 μm and measure the collisional broadening coefficient of some of the transitions[254]. Nevertheless, this method features a very low conversion efficiency and the optimal range of Mid-Infrared frequencies where the Near-Infrared *signal* frequency comb can be transferred is entirely dependent on geometric parameters of the fibre, thus lacking any possibility of external tuning.

### 3.2.2. Direct Mid-Infrared Dual-Comb Architectures

In consonance with the advancement of the technology in this spectral domain, the number of demonstrations of dual-comb sources that directly emit in the Mid-Infrared is much lower than those involving DFG or OPO schemes. Still, the progressive standardization of QCLs as laser sources beyond Near-Infrared and the momentum gained by QCL-based OFCs in engineered Fabry-Pérot devices has sparked off the use of these instruments for dual-comb purposes beyond 5 μm.

However, there are other laser sources apart from QCLs whose performance in the dual-comb modality has been validated from 2 to 10 μm. Figure 27 collects some of the most relevant demonstrations of Mid-Infrared dual-comb spectroscopy based on these sources that can be found in the literature.

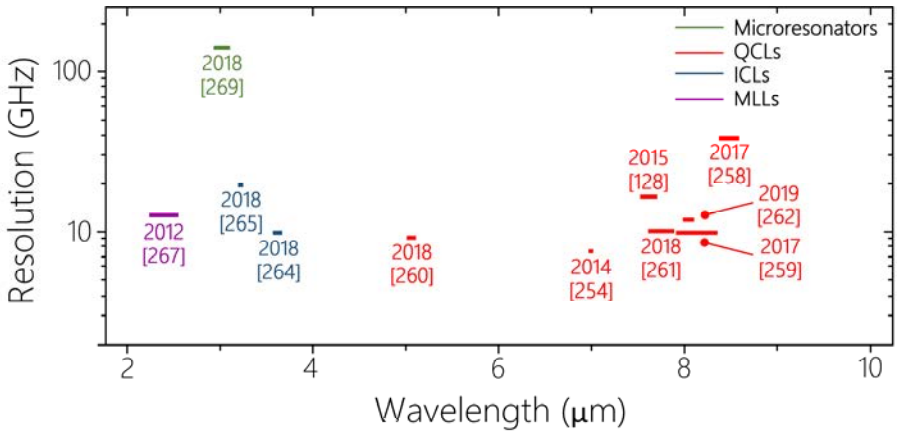


Figure 27. Dual-comb spectroscopy in the Mid-Infrared with direct laser sources. Performance in terms of emission wavelength and optical bandwidth versus effective resolution. The width of each bar represents the usable spectral span for multiheterodyne spectroscopy. Citations are shown in square brackets together with the year of publication of each contribution.

With respect to QCLs, the first proof-of-principle validation of dual-comb spectroscopy took place in 2014. Villares *et al.* used a pair of free-running QCLs to measure a GaAs etalon and water vapour at 7 μm[255]. Due to the low resolution of QCLs (line spacing in the order of tens of GHz), the authors implemented an arduous mechanism to interleave spectra as well as post-correction procedures for co-aligning interferograms to reduce the detrimental effect of slow frequency drifts. An on-chip version of this architecture was reported by the same authors one year later, exhibiting improved robustness against temperature drifts and full control over the comb parameters ($f_{CEO}$ and $f_{REP}$) of the lasers[128]. With two QCLs on the same substrate (but with some crosstalk) and interleaving a few beatnotes, Wang *et al.* also realized dual-comb spectroscopy of $NH_3$ and $N_2O$ at 8.4 μm[256]. In the same setup, Hangauer *et al.* implemented a feedback control on the injection current to reinforce the mutual coherence between independent lasers, which was the first all-electrical stabilization technique in a QCL-based dual-comb scheme reported in the literature[257]. This mechanism enabled the demonstration of wavelength modulation spectroscopy together with multiheterodyne detection for enhanced sensitivity[257] as well as rapidly swept dispersion spectroscopy of nitrous oxide using a single-channel phase detection setup[258]. This inter-locking procedure was later upgraded to a two-stage stabilization system involving an optical phase-locked loop for further suppression of the frequency drifts between the lasers and

was also successfully employed to retrieve the absorption and the dispersion spectra of ammonia and isobutane at atmospheric pressure[259].

The work of research groups in this direction has recently contributed to expand the possibilities of dual-comb systems based on QCL-based frequency combs. This is the case of proof-of-concept experiments that have demonstrated the feasibility of watt-level QCLs at 8.2 μm[260] or even at the short wavelength of 5.0 μm[261] in dual-comb arrangements. Furthermore, Westberg *et al.* applied for the first time purely computational correction algorithms to a dual-comb system based on a pair of dispersion-compensated QCLs. Using this method, coherently-averaged spectra of bromomethane and freon 134a was recorded at 7.8 μm with good fidelity[262]. Hillbrand *et al.* also locked the repetition frequency of a pair of QCLs on the same chip to an external RF source to realize self-detected dual-comb interferometry with extraordinary potential against optical feedback[263]. Nevertheless, one of the most stunning demonstrations of the potential of QCL-based dual-combs was recently reported by Klocke *et al.*[264]. Such an experiment aimed to observe the kinetics of irreversible protein reactions. This ambitious goal was achieved: the authors succeeded in recording the spectra and the transients of a photoactivated bacteriorhodopsin. Even more, owing to the high measurement speed of the instrument, several intermediates in the biological photoreaction could also be successfully characterized. An illustration of the spectrally recorded photocycle of the protein is shown in Figure 28.

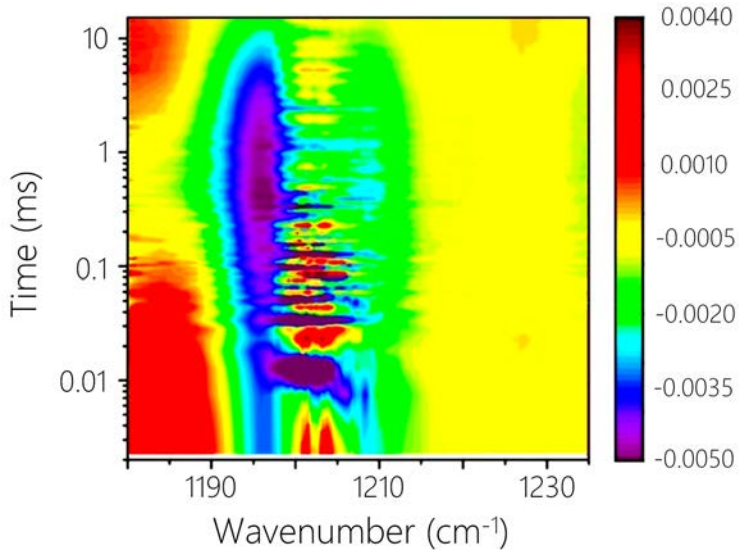


Figure 28. Time-resolved spectral analysis of the photocycle of a target protein between 1180 and 1240 $cm^{-1}$ (8.1 – 8.5 μm) using a QCL-based dual-comb source. The vertical bar on the right side indicates the difference in absorbance in comparison to the reference. Adapted from Klocke *et al.*[264].

Other than QCLs, dual-comb spectroscopy in the Mid-Infrared has also been realized with other laser sources directly emitting in this range of wavelengths. This is the case of Interband Cascade Lasers (ICLs), a hybrid between a laser diode and a QCL which not only exhibit a similar phase-locking mechanism to QCLs to operate as an OFC but also are amenable to pulsed operation regimes. Moreover, they can work between 3 and 5 μm, a less favourable range of operation for QCLs. This way, Bagheri *et al.* reported the first passively Mode-Locked ICL emitting at 3.6 μm and further performed a multiheterodyne beatnote experiment (which also involved a computational phase correction method) to show the potential of this source as dual-comb instrument[265]. Additionally, Sterczewski *et al.* utilized a pair of multimode Fabry-Pérot ICLs in comb regime as dual-comb spectrometer. With this arrangement, both the rapidly-swept absorption and dispersion narrowband spectra of low-pressure ethylene and the broadband spectra of methane around 3.2 μm were satisfactorily recorded[266].

Direct Mid-Infrared OFC generation can also be performed with MLLs based on chalcogenide hosts (such as ZnSe or ZnS) doped with certain transition metals with broad gain bandwidth in the Mid-Infrared (for example, chromium or iron)[267]. Following this principle, Bernhardt *et al.* implemented a delicate dual-comb architecture encompassing two free-running $Cr^{2+}$:ZnSe femtosecond oscillators pumped by the same erbium-doped Fibre Laser to probe acetylene at 2.4 μm[268]. To date, this is the only demonstration of Mid-Infrared dual-comb spectroscopy using MLLs directly emitting in this spectral region, but the employment of other dopant ions may pave the way for further laser sources deeper in wavelength[269]. Finally, this analysis should also mention a proof-of-concept demonstration of dual-comb spectroscopy using a pair of silicon microresonators spanning from 2.6 to 4.1 μm pumped by a single CW OPO[270]. With some technical limitations, Yu *et al.* acquired spectra of acetone with a resolution of 127 GHz at 3 μm, which represents the first successful validation of this type of chip-sized spectrometer in the Mid-Infrared.

## 3.3. Dual-Comb Architectures in the sub-THz and THz Region

### 3.3.1. Indirect THz Dual-Comb Architectures

The unique features of non-ionizing THz waves for some applications such as contactless labelling (as they can travel through materials that are opaque at shorter wavelengths) or the vast number of resonances allocated in this region for

molecular spectroscopy are only two examples that evince the strong appeal of the THz domain for a wide range of disciplines[271]. Still, the THz region is arguably the most uncharted portion of the electromagnetic spectrum. For this reason, if one intends to review the most relevant contributions of dual-comb interferometry in the THz domain, it would not be, in principle, unexpected if the literature did not include more than a few isolated demonstrations. Counter-intuitively, this is not the case, and there are early examples of THz dual-comb interferometry already in the first years of the 21st century. The explanation to this inconsistency lies in the use of indirect mechanisms to produce THz frequency combs, in a similar fashion to the Mid-Infrared. This way, Near-Infrared sophisticated tools for comb generation (particularly, MLLs) have been routinely used for THz dual-comb spectroscopy in conjunction with a pair of photoconductive antennas (PCAs) (or in some cases, just one) that act both as transmitter and receiver of THz radiation. Moreover, THz radiation is less sensitive to relative time fluctuations between consecutive pulses, which further simplifies the implementation of dual-combs.

THz dual-comb spectroscopy is considered to have been premiered by Janke *et al.* and Yasui *et al.* in 2005[272,273]. These early demonstrations involved two loosely-stabilized Ti:Sapphire MLLs with marginally different line spacings in the Near-Infrared. One of them was used to drive an emitter PCA for the generation of a probe THz comb consisting of an array of offset-free frequency markers (traceable to a microwave standard) whose regular frequency separation is inherited from the Near-Infrared laser source. Then, this comb propagated in free-space before reaching another PCA (used as detector) which was pumped by the second Near-Infrared comb. As a result of the interference in the detector PCA, the incoming THz pulse train is sampled in such a way that its time scale is stretched and, consequently, the comb structure is downconverted to the RF domain[274]. A cross-correlator is usually employed to provide a time origin signal for the acquisition of the temporal waveform. Alternatively, the detection process can also be realized through EO sampling instead of using the receiver PCA.

A schematic of a classic THz dual-comb architecture based on MLLs is illustrated in Figure 29. Although this process is equivalent to dual-comb interferometry in practical terms, it is noticeable that it has become well-known in the THz region under the alias *Asynchronous Optical Sampling*, owing to a much earlier pump-probe experiment that involved two lasers with slightly detuned repetition rates[275]. In fact, most of the contributions to this field can be found in the literature under this moniker, while the concept *THz dual-comb* has only been applied to recent works.

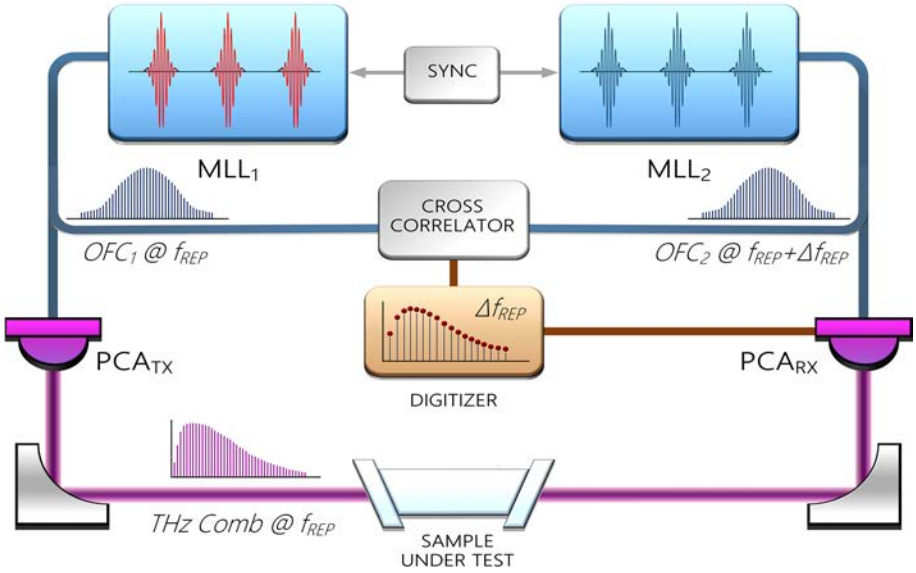


Figure 29. Traditional experimental setup for THz *Asynchronous Optical Sampling* (dual-comb spectroscopy) based on phase-locked MLLs and a pair of PCAs (transmitter –Tx- and receiver –Rx-). Note the offset-free nature of the generated THz comb (see text for further details).

Shortly after the first demonstrations, some research groups focused on upgrading the performance of this architecture. In this sense, it is outstanding the work of Bartels *et al.*, with progressive advancements in terms of time resolution (with re-engineered stabilization schemes), scan rates (i.e., $\Delta f_{REP}$), spectral coverage and SNR[276–279]. Some years later, Finneran *et al.* further perfected the system and the locking mechanism, thus reporting enhanced precision, accuracy and comb-tooth linewidth over multi decade-spanning spans[280]. On the other hand, Kliebisch *et al.* reported an ultra-fast version of a THz dual-comb spectrometer with repetition rates of 10 GHz and scan rates of hundreds of kHz[281].

With such refined features, diverse experiments have been satisfactorily conducted with varying purposes. Dual-comb absorption spectroscopy of gas-phase constituents such as acetonitrile, methanol and water vapour in ambient air has been frequently performed over bandwidths of several THz with different resolutions in the MHz and GHz range[279–281]. Figure 30 shows the recorded spectrum containing the omnipresent absorption features of atmospheric water vapour across a spectral bandwidth of 6.5 THz. As with Mid-Infrared dual-combs, two initial applications that took full advantage of the potential of this multiheterodyne architecture based on Ti:Sapphire Laser sources were THz near-field microscopy[282] and characterization of metamaterials[231]. The application scope of this method has also been expanded with the detection of transient reflectivity changes in multi-layer structures by means of pump-probe spectroscopy[278,281], the readout of transmission resonances of frequency-selective surface sensors[283] or the

determination of absolute distance measurements with sub-micrometre precision[284]. The aptitudes of THz dual-comb interferometry for ranging purposes were further explored with moving targets, with the detection of stepped objects having rough surfaces and with the estimation of the thickness of paint films[285]. For a deeper analysis, the reader is referred to some thorough reviews that compile the above-mentioned refinement work as well as its application to molecular spectroscopy[286,287].

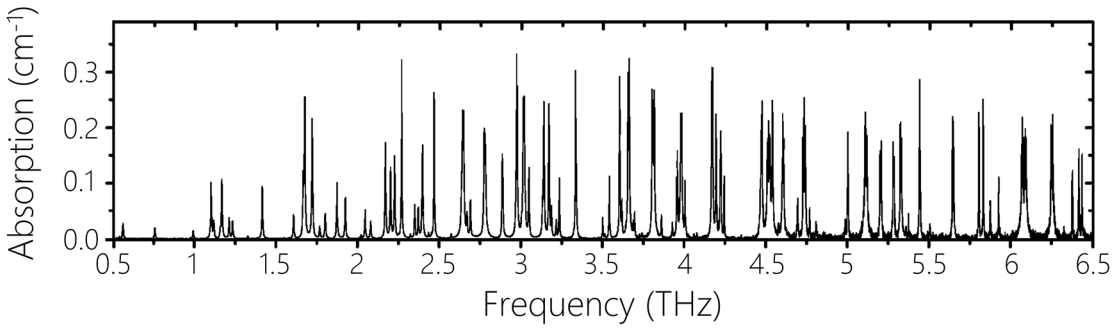


Figure 30. THz dual-comb spectroscopy based on Ti:Sapphire MLLs and a pair of PCAs (as in the setup outlined in Figure 29). Normalized absorption spectrum of water vapour in ambient air from 0.5 to 6.5 THz. Adapted from Klatt *et al.*[286].

After some years of incessant maturation, the interest of some research groups shifted towards the search for robust and cost-efficient THz dual-comb instruments for outside-the-lab applications. A clear example of this trend was the combination of a Ti:Sapphire Laser and a semiconductor Disk Laser reported by Gebs *et al.*[288]. However, one of the most crucial factors for the development of these architectures was the incorporation of erbium-doped Fibre Lasers as comb sources. Yasui *et al.* presented the first THz dual-comb spectrometer based on this approach in 2010[289]. This technology exhibited superior capabilities in terms of accuracy and resolution, and it did not take long until it was satisfactorily tested for spectroscopy of gas-phase acetonitrile at low pressure and pharmaceutical tablets such as lactose and D-maltose in the 0-2 THz range[290,291]. A recent extension of this work also revealed the potential of THz dual-comb spectroscopy in the presence of unwanted aerosols owing to the less susceptibility of THz waves to light scattering[292]. Furthermore, the same authors also harnessed the ultrafast nature of this detection process for real-time monitorization and absolute-frequency measurement of CW THz radiation[293].

Remarkably, this THz Fibre Laser-based dual-comb system has also proved to be amenable to well-known techniques usually applied to Near-Infrared dual-combs, such as interleaving[294] and discrete Fourier-transforms[295] to enhance the resolution down to the linewidth of the comb tooth (the former has also been

applied to Ti:Sapphire Laser-based THz dual-comb spectroscopy of acetonitrile at sub-Torr pressures[287]) or pulse-picking procedures to flexibly modify the repetition rates of the THz frequency combs[296]. In addition to this, adaptive interferogram digitization methods to reconstruct the coherence between free-running THz frequency combs have also proved to outperform classic stabilization schemes in these architectures[297].

Finally, the last aspect to mention in this analysis is the current trend in THz multiheterodyne interferometry towards compact and lightweight spectrometers based on the integration of single-cavity comb sources. This is the case of the works of Hu *et al.*, who incorporated a dual-wavelength MLL in a THz dual-comb arrangement for the first time and demonstrated its feasibility for both real-time measurement of CW THz radiation[298] and absorption spectroscopy of acetonitrile at atmospheric pressure[299], in both cases without any degradation of the performance. On the other hand, Baker *et al.* also reported a THz dual-comb scheme encompassing a bi-directional Mode-Locked Fibre Laser. Without phase-control electronics, the water absorption features in ambient air up to 1 THz were accurately recorded in this proof-of-concept experiment[300]. These examples clearly illustrate the potential of multiplexed OFC platforms for the implementation of passively stable dual-comb sources across different portions of the electromagnetic spectrum and offer intriguing prospects for the eventual deployment of THz dual-comb architectures in outside-the-lab environments.

### 3.3.2. Direct THz Dual-Comb Architectures

In a similar fashion to the Mid-Infrared, the implementation of dual-comb setups based on direct emission of THz radiation has resorted to QCLs. However, the degree of development of the instrumentation in this window of the electromagnetic spectrum is even lower than in the Mid-Infrared. Nowadays, direct THz dual-comb spectroscopy requires cryogenically cooled QCLs and square-law detectors if a high level of performance is expected. Furthermore, as with THz dual-comb architectures based on PCAs, the presence of water vapour across the THz region may prevent the correct transmission of the THz radiation and purging often becomes imperative. On top of all, a QCL-based THz dual-comb system requires a complex setup which is particularly prone to the generation of mechanical vibrations that may have a detrimental effect on the SNR.

Even with such discouraging prospects, it is possible to find examples of THz dual-comb architectures with QCL-based frequency combs in the literature.

The first demonstration took place in 2016, when Rösch *et al.* disclosed a self-detected THz dual-comb source at 2.5 THz encompassing two free-running QCLs assembled on the same platform and using one of them as a detector itself. In this proof-of-principle implementation, the multiheterodyne spectrum was revealed without active stabilization of the OFCs owing to the mutual coherence of the on-chip source[146]. The same authors recently reported an upgraded version of the system emitting at 3 THz with substantial improvements in terms of spectral bandwidth, dynamic range and output power[301]. The first spectroscopic validation of these dual-comb architectures was performed by Yang *et al.* In this work, two free-running QCLs mounted on the same cryocooler and emitting at 2.8 THz were used in a balanced detection scheme in conjunction with a hot-electron bolometer and a Schottky diode. With the application of additional phase-timing computational correction algorithms, the authors succeeded in measuring the transmission spectrum of an etalon made from an undoped GaAs wafer[302]. More recent examples of THz QCL-based dual-comb spectroscopy can be found in the works of Westberg, Sterczewski *et al.*, who used a similar arrangement involving two THz QCLs placed on a copper submount to realize the first measurement of a molecular sample in gas phase with this type of architecture (in this case, ammonia at 2.8 THz)[303] and hyperspectral imaging of a prepared tablet including pharmaceutical excipients mixed with an amino-acid at 3.4 THz[304]. The recorded spectra of the samples under tests by means of this QCL-based THz dual-comb system are shown in Figure 31.

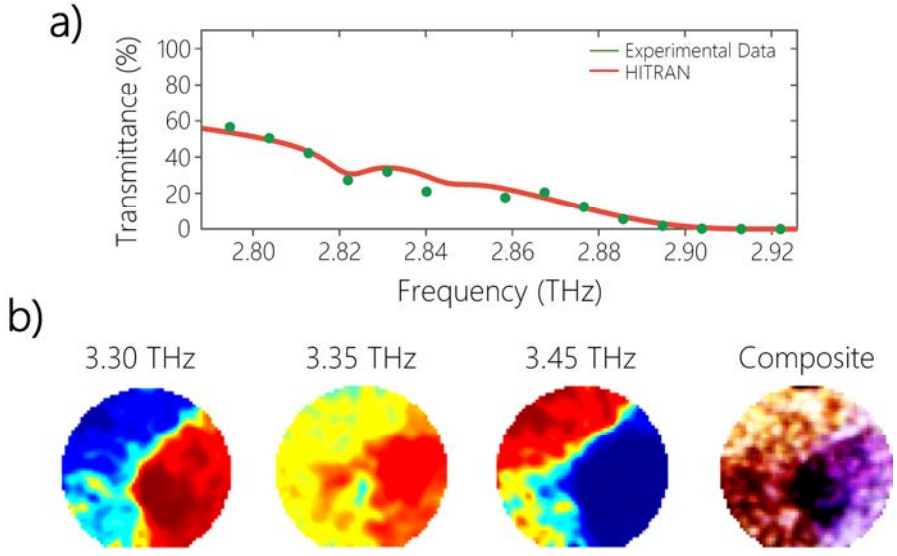


Figure 31. Examples of direct THz dual-comb spectroscopy based on QCL-based frequency combs. a) Absorption spectrum of ammonia between 2.8 and 2.92 THz together with the fitting curve retrieved from the HITRAN database. b) Hyperspectral imaging on a prepared multi-component sample at three different THz frequencies and composite image obtained from the three slices. The false colours of each slice are related to the absorbance of the sample at each frequency. Adapted from Westberg, Sterczewski *et al.*[303,304].

## 3.4. Dual-Comb Architectures in Other Spectral Regions

Apart from Near-Infrared, Mid-Infrared and the THz range (this is, all the electromagnetic spectrum above the infrared frontier at 0.8 μm), dual-comb spectroscopy has been successfully validated below this wavelength to a lesser extent. This section will therefore discuss the most relevant contributions of this technique to the Visible and Ultraviolet range regardless of the method of comb generation. Moreover, and with the objective of completing the analysis of the state-of-the-art of dual-comb demonstrations, this section will also review the application of these architectures to nonlinear spectroscopy based on processes such as stimulated Raman scattering or two-photon absorption spectroscopy, among others.

In the green region, dual-comb spectroscopy was proposed by Ideguchi *et al.* using frequency-doubled ytterbium-doped Fibre Laser-based combs by way of Second-Harmonic Generation (SHG) in a barium borate crystal. By implementing an adaptive interferogram digitization method, the authors could retrieve the molecular spectrum of iodine at 520 nm[305]. With the same SHG mechanism, Potvin *et al.* reached the 775 nm range using a pair of erbium-doped Fibre Laser-based OFCs. This time, a digital interferogram correction method was used to measure the spectra of oxygen and acetylene calibrated against hyperfine rubidium absorption lines[306]. Furthermore, in this near-to-red range of wavelengths, Long *et al.* took full advantage of an EO self-heterodyne scheme to perform sub-doppler pump-probe spectroscopy on atomic potassium and resolve their hyperfine transitions[307]. This work was further extended to observe the electromagnetically induced transparency in the same element at high temperature[308] and, more recently, also in Rubidium[309]. Finally, it should also be highlighted that Carlson *et al.* have proposed dual-comb spectroscopy in the Ultraviolet based on intracavity high harmonic generation[310].

The discussion concerning nonlinear dual-comb spectroscopy would not be feasible if OFCs did not consist of a train of ultrashort pulses with high peak intensity, since this is the basis to produce nonlinear effects. In relation to this topic, there are several works in the literature that aim to provide a theoretical framework to different nonlinear processes and configurations using dual-combs[311–313], but the first experimental demonstration was reported by Ideguchi *et al.* in 2012 with the application of stimulated Raman scattering to imprint the excited molecular vibrations into an erbium-doped Fibre Laser. This way, Raman transitions at 3.3 μm of benzonitrile and p-xylene were successfully resolved[314]. Shortly after, the same authors premiered dual-comb coherent anti-Stokes Raman

spectroscopy (CARS), a compelling technique which not only proved to be valid to measure the Raman excitation spectra (from 7 to 25 μm) of a mixture of liquid chemicals but also to perform spectro-imaging of the mixture placed on a capillary plate[315]. Some of the produced images are shown in Figure 32. Recent works have also extended the capabilities of CARS with Ti:Sapphire MLLs with higher repetition rates to analyse Raman spectra of different liquid samples and polystyrene microparticles flowing in an acousto-fluidic device between 7 and 50 μm[316,317], and also with ytterbium-doped Fibre Lasers for hyperspectral imaging of a mixture of chemical substances between 5.5 and 9 μm with improvements in refresh rates and measurement times[318]. Besides, new schemes have been reported in the literature for CARS purposes, such as a fully-fiberized Raman spectrometer developed to observe the shifted spectra of acetonitrile and ethyl acetate with coverage from 8 to 100 μm[319]; or even an ultra-broadband EO dual-comb spectrometer exploited to analyse a wide variety of solid samples such as silicon, gallium arsenide, diamond and calcium fluoride in the range between 5 and 50 μm[320].

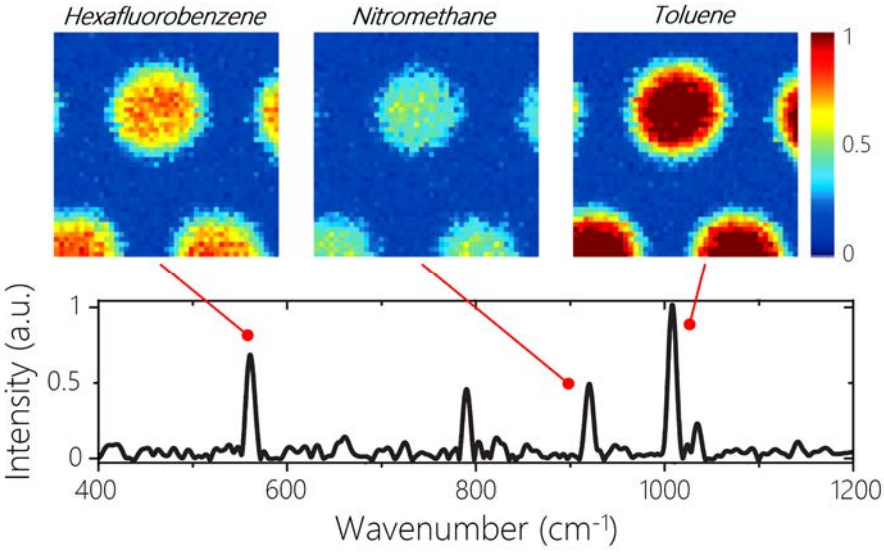


Figure 32. Dual-comb coherent anti-Stokes Raman spectro-imaging of a capillary plate filled with hexafluorobenzene, nitromethane and toluene between 400 and 1200 $cm^{-1}$ (8.3-25 μm). The vertical bar on the right side indicates the intensity of the pixels. Adapted from Ideguchi *et al.*[315].

Another nonlinear process which has been accurately identified with dual-comb architectures is two-photon spectroscopy. The first demonstration was realized by Hipke *et al.* in 2014 using two SHG-based frequency-doubled erbium-doped Fibre Laser-based OFCs on atomic rubidium vapour. In this proof-of-principle experiment, the Doppler-broadened fluorescence signal corresponding to the two-photon comb excitation of the sample at 390 nm was successfully measured[321]. Recent progress in this direction has also revealed Doppler-free two-

photon dual-comb spectra, thus displaying the hyperfine transitions of rubidium at the same wavelength[322], and also the application of well-known techniques such as pulse shaping or coherent averaging to provide the system with enhanced precision and sensitivity[323].

Time-resolved dual-comb spectroscopy has also been demonstrated, thus enabling observation of the transient response of optical spectra by means of the pump-probe method. The first proof-of-principle experiment was realized by Asahara *et al.* in 2017 to investigate the relaxation dynamics (amplitude and phase spectra) of a photo-excited InGaAs saturable absorber in the 1.5 μm region[324]. In a more recent set of experiments, Kim *et al.* refined the technique to measure the electronic population relaxation and the frequency-resolved transient absorption and refraction spectra of dye molecules in ethanol with a dynamic range up to nanoseconds in the region from 650 to 950 nm[325,326].

Finally, the last nonlinear method that has harnessed the potential of dual-comb schemes is FWM signal generation by pulse-excited samples. Lomsadze and Cundiff performed FWM spectroscopy on a GaAs quantum well with a pair of Ti:Sapphire MLLs emitting at 800 nm to successfully retrieve the FWM contribution of the sample in the RF domain[327]. However, the most appealing aspect of this nonlinear method is the applicability to multi-dimensional spectroscopy. The FWM signals emitted by samples excited with two mechanically time-delayed combs and downconverted to RF by means of a third one allowed the same authors to discern the Doppler-broadened features of two natural isotopologues of rubidium and also to record a multi-quantum well GaAs sample, in both cases in agreement with the sequence of energy states in a bi-dimensional spectrum[328,329]. In a recent extension of this method, the mechanical delay stage that controlled the excitation of the pulses has been replaced with a frequency comb with different line spacing, thus providing the two-dimensional spectrum with comb-level resolution in both axis in a sub-second timescale[330].

# III

# Contributions to Dual-Comb Spectroscopy in the Near-Infrared

# 1.
# Introduction and Motivation

The third chapter of this dissertation presents the author's contributions to the development of dual-comb schemes in the Near-Infrared. More specifically, two new arrangements relying on some of the methods introduced in the previous chapters for comb generation will be employed, characterized and validated.

First, and seduced by the possibility of extending the capabilities of EO dual-comb architectures beyond the transparency range of EOMs, a new dual-comb system based on gain-switched semiconductor lasers along with a new mechanism (Optical Injection Locking –OIL-) to provide a pair of free-running OFCs with mutual coherence will be presented. The fundamentals of these methods that can be implemented in any semiconductor laser will be further reviewed to gain a better insight into the obtained results and the expected behaviour with focus on the optimization of the system. This proof-of-principle experiment will be validated using HCN as gas sample to retrieve the full-complex spectral profile of one of its absorption features in the vicinity of 1538 nm. These results can be found in the manuscripts [M1] and [M2] of the author's list of scientific contributions.

Furthermore, a novel architecture based on OIL and dual-comb detection to retrieve the spectral information encoded into remote OFCs will be introduced. The approach relies on the generation of a second OFC via a filtered line from a remote comb (a method which has already been proven to track two independent combs for superchannel coherent detection), but on this occasion, the spectral information of the remote comb will be recovered as a whole. This can be fulfilled by realizing multiheterodyne detection to coherently and simultaneously extract the spectral content of the OIL-synchronized external comb on a real-time basis. The system is satisfactorily validated using EO frequency combs in the C-band and

an FBG sensor as device under test to measure the applied level of strain and spectrally imprinted into the remote OFC. A thorough discussion of this work is included in the manuscripts [M3] and [C3] of the above-mentioned contribution list at the beginning of the document.

# 2.
# Gain-Switching-based Dual-Comb Architectures

## 2.1. Description of the System

The basic sketch of the GS-based dual-comb experimental setup may resemble that of EO dual-comb architectures, but there are some substantial differences that must be discussed (see Figure 33). First, a pair of semiconductor lasers are gain-switched to create two pulse trains with slightly detuned repetition rates and, subsequently, a pair of combs with different line spacing. As in other common dual-comb arrangements, one of the OFCs can be frequency-shifted by means of an AOM before both OFCs are combined and heterodyned on a photodetector in order to eventually digitize and process the arisen RF comb. The sample or device under test may be located either in one branch of the interferometer (dispersive arrangement) or after recombination (collinear arrangement). The RF signals employed to drive the lasers and the AOM are locked to the same common RF oscillator.

Apart from the method for comb generation, there is one additional element to consider in the presented system: a third semiconductor laser whose output light is split and injected into the cavity of the aforementioned gain-switched lasers. This mechanism (OIL) and its effect is the key to endow the system with mutual coherence. To put the reader into context, the fundamentals of this mechanism are to be briefly reviewed.

Injection locking was first observed by Huygens in the 17$^{th}$ century when he perceived that the pendulums mounted on the same wall would eventually oscillate at the same frequency. Almost 300 years later, the first experiments in the optical domain were reported with the advent of the first laser oscillator[331], and it

was not until 1980 when semiconductor lasers were subject to this mechanism[332]. Since then, the potential of this interdisciplinary technique has been extensively studied with the ultimate goal of improving the performance of a vast number of applications in virtually every corner in the field of Photonics.

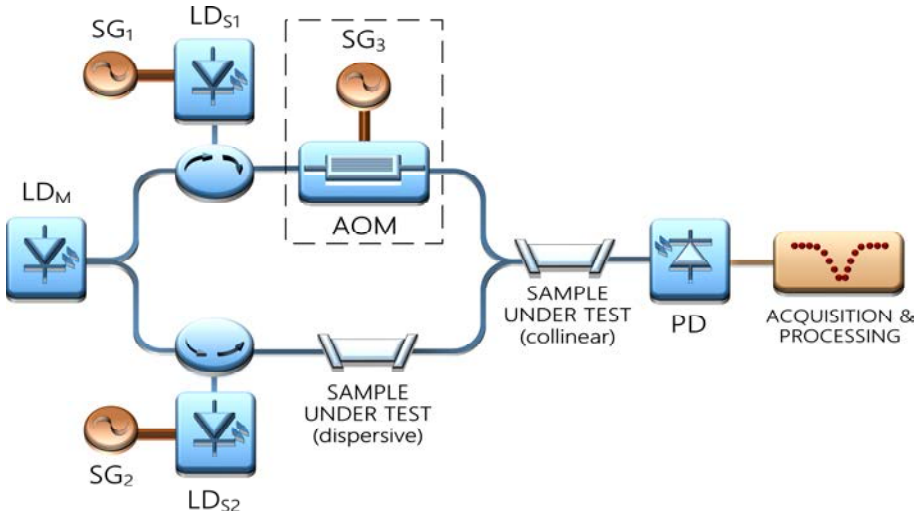


Figure 33. Basic Near-Infrared GS-OIL-based dual-comb architecture. Note the two possible locations of the sample under test depending on the type of measurement (dispersive or collinear). The frequency-shift stage involving the AOM (dashed box) can be omitted under specific experimental conditions (see text for further details). LD M/S: Laser diode (*master/slave)*; PD: Photodetector; SG: Signal generator.

The underlying principle of OIL stems from injecting the output light of one main laser (*master*) into a secondary device (*slave*). When the frequencies (or emission wavelengths) of the *master* and *slave* lasers are close enough, the *master* changes the optical field of the *slave* laser and pulls its emission wavelength until it equals that of the *master*: this is, the *slave* laser is obliged to perform on the injected wavelength and no longer on that of its former free-running state. This process is illustrated in Figure 34. This way, the frequency of the *slave* will be locked to the frequency of the *master* as long as the *master* laser remains within a certain capture range called *locking range* in the vicinity of the frequency of the *slave* laser. The locking range increases as the ratio of optical powers between *master* and *slave* becomes larger, so careful control is essential to achieve stable locking conditions. Remarkably, diverse experiments and theoretical studies have also revealed a number of additional benefits of injection-locked sources which can manifest in the devices simultaneously. To name a few, inheritance of the properties of the *master* laser (such as narrow linewidth or absolute frequency accuracy), increase of the resonance frequency for broader modulation bandwidth, suppression of relative intensity noise and phase noise, minimization of nonlinear distortions, chirp reduction or improvement of the side-mode suppression ratio are some examples that have been reported in the literature[333]. Furthermore, by

perturbing semiconductor lasers with optical injection, a wide range of induced dynamical regimes (self-pulsations, chaotic behaviour or FWM, among others) have also been demonstrated[334].

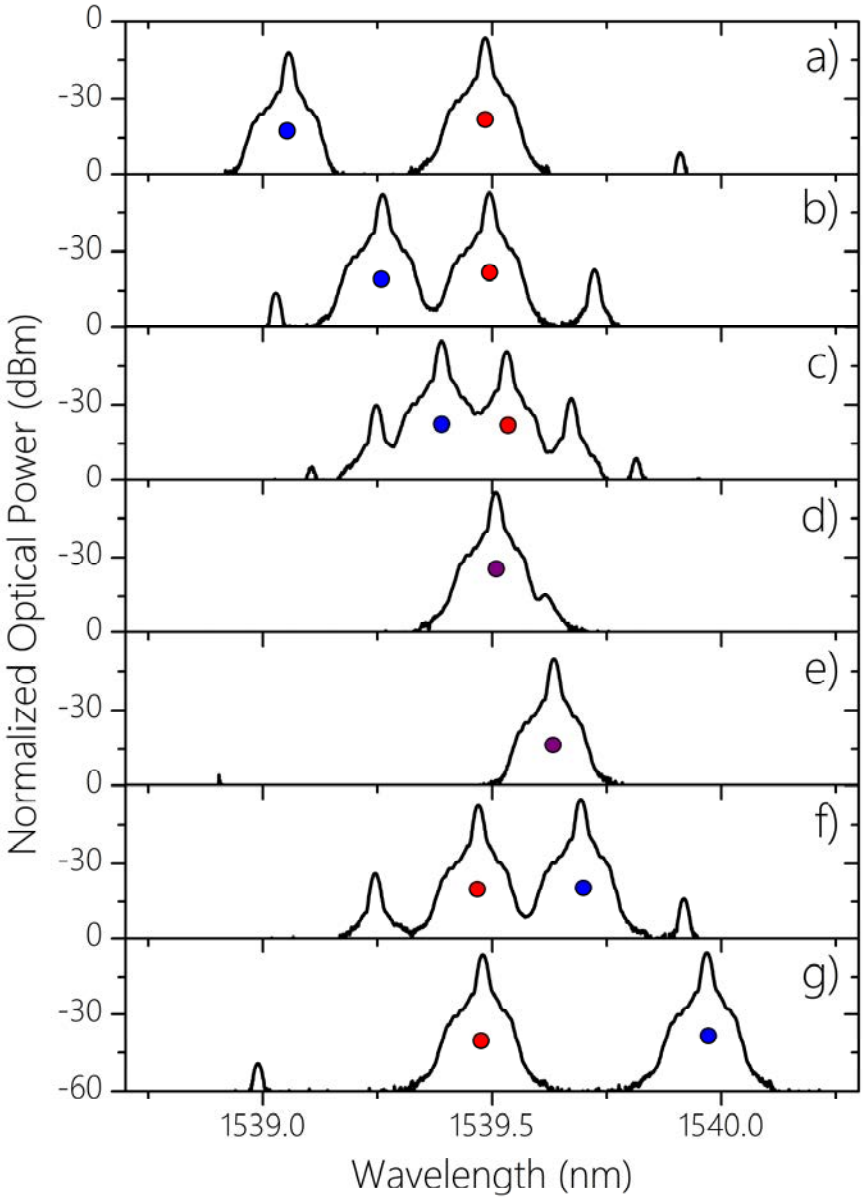


Figure 34. OIL process in the optical domain. The emission wavelength of the *master* laser (blue dot) is swept across the emission wavelength of the *slave* laser (red dot) (a-g). Only when the *master* laser is close enough to the *slave* laser is the latter forced to follow the former (d-e). Other nonlinear dynamics can be observed under unstable locking regimes (c).

Beyond the impressive batch of advantages of OIL, the primary motivation for its application to dual-comb architectures is that the locking mechanism can induce a stable (but non-zero) phase relationship between independent sources. In other words, a *master* laser injecting two free-running *slave* OFCs can reconstruct the mutual coherence between them, thus allowing for high-resolution, accurate

dual-comb spectroscopy. If there is coincidence within a certain locking range between the CW *master* laser and two lines of the *slave* OFCs, the former will simultaneously lock both combs so that any phase fluctuations between them are automatically compensated. The frequency-domain description of OIL-based multiheterodyne spectroscopy is depicted in Figure 35. Note that the pair of lines injected by the *master* laser will have the same emission wavelength, hence the frequency origin of the downconverted RF comb will be dictated by the position of the injected lines in the spectrum. As a consequence, any comb lines on the left side (lower wavelength) will be averaged with their counterparts with similar repetition frequency mismatch on the right side (higher wavelength). To cancel mode averaging, an AOM may be inserted into one of the branches of the interferometer in a similar fashion to EO dual-comb arrangements.

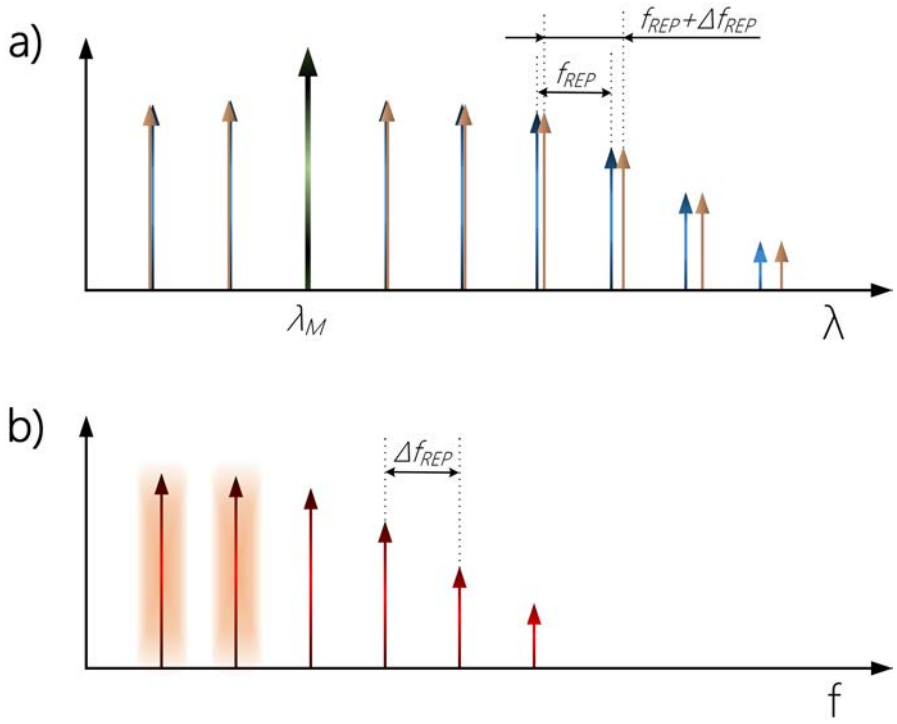


Figure 35. Principle of operation of injection-locked dual-comb interferometry. The *master* laser with emission wavelength $\lambda_M$ injects two comb lines at the same time if they fall within the locking range (a). The induced mutual coherence between OFCs allows for comb-tooth resolved spectra in the RF domain (b). Each of the two leftmost lines of the offset-free RF comb (highlighted in red) result from averaging two pairs of comb lines in the optical domain; thus, its spectral information cannot be unequivocally resolved.

## 2.2. Characterization

In the first chapter of this dissertation, the operating principle of GS was discussed along with some of the main features of the technique (e.g., broad

frequency tunability capabilities in a wide range of laser platforms across different spectral domains). Still, there are a number of important considerations to bear in mind if one intends to generate GS-based OFCs for dual-comb spectroscopy. To that end, this section will present the characterization of free-running GS sources according to certain operating conditions as well as some examples of their application to multiheterodyne interferometry once the OIL mechanism takes part in the system. In any case, special emphasis will be placed on the optimization of the processes.

The GS-based OFCs generated in this work encompass a seed laser driven by two superimposed currents: a direct bias current ($I_{BIAS}$) and an amplified sinusoidal modulation current $I_{RF}$ at a frequency $f_{REP}$ that will operate the device above and below threshold. The seed is a DM laser, which is a semiconductor ridge-waveguide Fabry-Pérot laser that has been engineered to obtain single-mode operation[335]. The DM laser (Eblana Photonics, Ltd. ) exhibits a threshold current of $I_{TH}$ = 12.5 mA and an emission wavelength of 1538.5 nm at room temperature. A sample of a GS-based OFC when the DM laser is biased at 60 mA and modulated with an amplified RF sinusoidal signal at 28.5 dBm with repetition frequency of 10 GHz is shown in Figure 36.

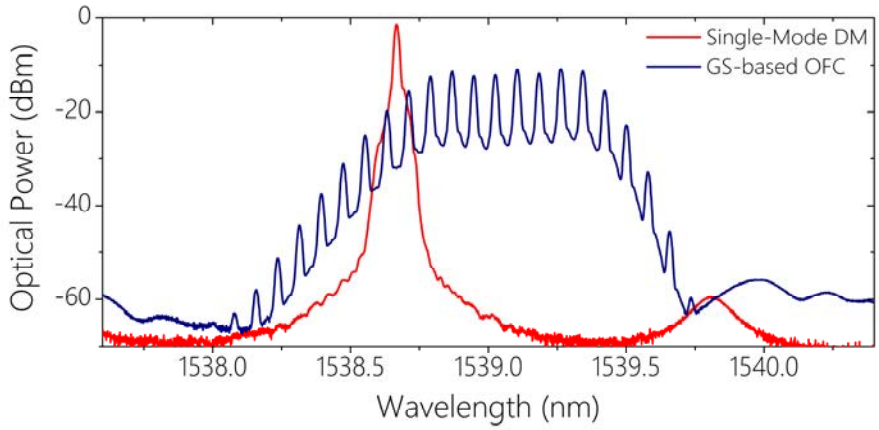


Figure 36. Example of GS-based OFC. In this case, the driving conditions are $f_{REP}$ = 10 GHz, $I_{BIAS}/I_{TH}$ = 5 and $I_{RF}/I_{BIAS}$ = 1.8. The single-mode emission of the seed laser is also shown for comparison purposes.

This set of parameters ($I_{BIAS}$, $I_{RF}$ and $f_{REP}$) plays a fundamental role in the formation of the GS-based comb. The relation between the driving conditions not only has a profound impact on either the span or the flatness of the OFC but also can turn high-quality coherent combs into incoherent spectra in case they are not appropriately selected. This effect can be observed using the previous GS-based OFC and analysing the evolution of the optical span with the modulation current $I_{RF}$ for a fixed $I_{BIAS}$ and $f_{REP}$. As can be seen in Figure 37, larger modulation currents lead to wider spans up to a certain point in which the shape of the comb becomes

distorted due to the presence of new interleaved harmonic sidebands in the spectrum (i.e., double period). This phenomenon is attributed to the loss of coherence between pulses caused by an increased temporal jitter when the modulation amplitude is excessively large, as the optical pulses are built up from spontaneously emitted radiation with random initial phases[52,53].

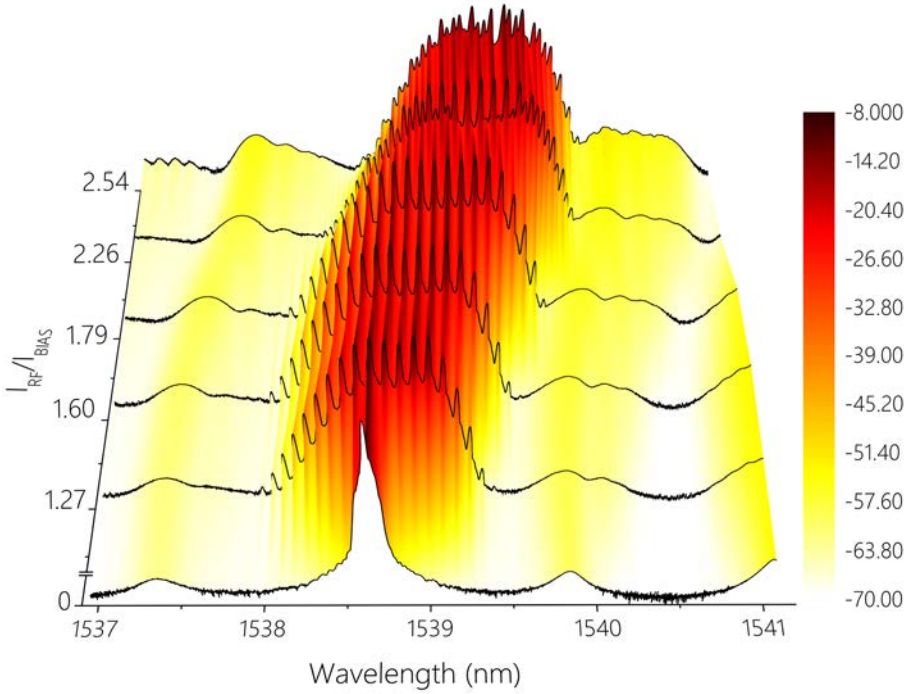


Figure 37. Evolution of GS-based OFCs with the parameter $I_{RF}/I_{BIAS}$ for an $I_{BIAS}$ = 60 mA and $f_{REP}$ = 10 GHz. The vertical bar on the right side indicates the optical power in dBm.

A different analysis, perhaps more attractive for dual-comb spectroscopy, can be performed from a frequency-domain point of view. It is well-known that GS-based OFCs exhibit improved performance when the devices are modulated with frequencies close to the relaxation oscillation frequency of the laser[52]. However, this parameter is dependent on the device properties and may not fit the requirements of the target application in terms of spectral resolution. To assess the impact of the modulation frequency on the resultant spectrum, different OFCs have been generated under similar driving conditions ($I_{RF}$ and $I_{BIAS}$) for a batch of varying repetition frequencies (note that the actual value of the modulation current $I_{RF}$ is only approximate, as it is challenging to ascertain the exact value due to the frequency response of the RF components −amplifiers, cables, input impedance of the laser- taking part in the setup). The results are displayed in Figure 38. Clearly, as the modulation frequency decreases, the OFCs gradually exhibit a more structured shape with poorer flatness. Still, equally-spaced comb lines are visible down to 3 GHz, only limited by the resolution of the optical spectrum analyser

(0.02 nm), while there is no sign of harmonic interleaved sidebands neither in the optical domain nor in the RF region after photodetection. In this situation, it is possible to harness the potential of the dual-comb technique to downconvert the OFC of interest to the RF domain and hence exploring the structure of the combs that cannot be fully resolved owing to the resolution of the instrument.

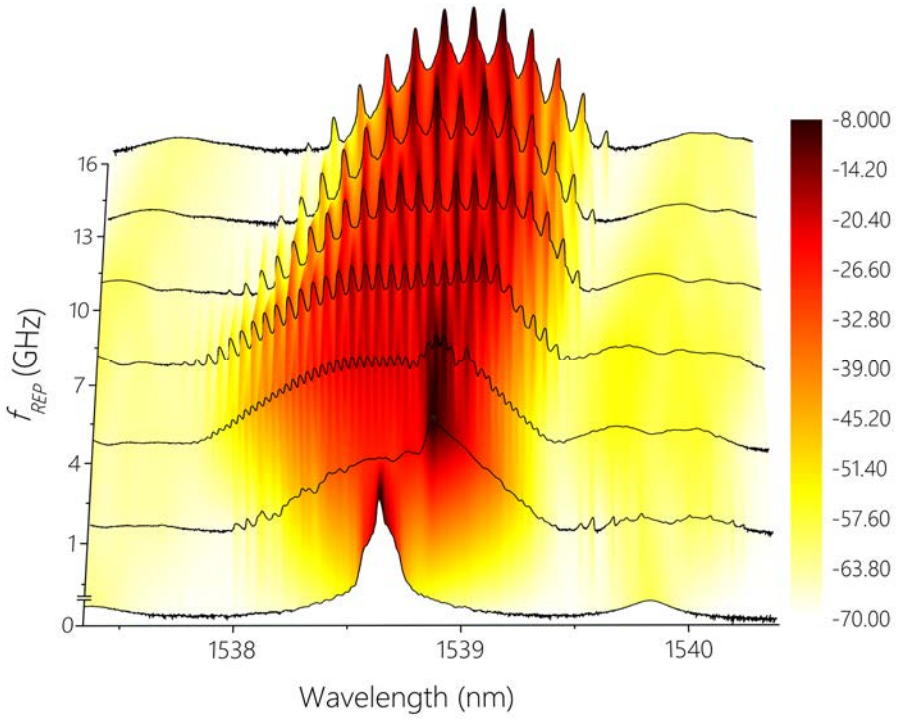


Figure 38. Spectral analysis of GS-based OFCs as a function of the modulation frequency ($f_{REP}$) with $I_{BIAS}/I_{TH}$ = 5 and $I_{RF}/I_{BIAS}$ = 1.8. Note the optimal performance of the OFC in the region near the relaxation oscillation frequency of the laser (around 8 GHz). The vertical bar on the right side indicates the optical power in dBm.

Once the GS-based OFC has been generated after careful selection of the driving parameters, dual-comb interferometry can be realized with a second GS-based OFC with slightly different frequency mismatch and a *master* CW laser that injects both twin combs following the operating principle of Figure 35. Accordingly, three DM lasers with similar emission wavelengths take part in a setup which is fully-fiberized with standard single-mode optical fibre and commercially available components. By acting on their temperature, the *slave* OFCs can be tuned to cover a comparable span over the same wavelength range. Synchronization between overlapping combs occurs by tuning the *master* laser and the *slave* OFCs so that the former can simultaneously inject one line of each comb. An isolator (not shown in Figure 33) is also placed after the *master* laser to suppress unwanted feedback reflections. Two identical circulators allow the input and output light of *slave* lasers to follow different paths. Depending on the experiment, one of the OFCs is launched into an AOM (Gooch & Housego, Inc.) driven at 40

MHz with an RF power around 24 dBm to guarantee that each spectral feature in the optical domain is unequivocally mapped onto the RF domain. Fibre polarization controllers (not shown in Figure 33) are introduced to ensure both proper coupling of the injected light into the *slave* lasers and suitable matching of the OFCs polarization state for interference. Finally, after recombination, a single-point InGaAs transimpedance photodetector (Thorlabs, Inc.) with bandwidth up to 300 MHz is employed to detect both combs.

Figure 39 shows some examples of combined OFCs and the resultant RF comb after photodetection displayed on an optical and an electrical spectrum analyser, respectively. The driving conditions of the OFCs as well as their main attributes are gathered in Table 4. From inspection of the results, it is clear that the RF comb faithfully reproduces the comb structure of the optical domain (which also reveals the structure of the above-mentioned GS-based OFCs whose comb lines could not be resolved because of the insufficient resolution of the optical spectrum analyser). It is therefore evident that, although the driving conditions of the GS-based OFCs may not be optimal, the formation of regular pulse trains for the generation of convenient OFCs in a wide range of frequencies is feasible. This process is strongly favoured by the injection locking mechanism[336]. Furthermore, the 3-dB linewidth of the RF comb teeth lies below the resolution bandwidth of the electrical spectrum analyser (1 Hz), which is a clear indicator of the mutual coherence between injection-locked frequency combs. Note that no control over the injection ratio (and therefore over the locking range) has been considered for the current experiment. The impact of the locking range on these systems will be discussed in the next section.

Table 4. Summary of driving conditions and main attributes of the GS-OIL-based dual-comb sources presented in Figure 39.

| Attribute | Dual-Comb Source I [Figure 39 (a)] | Dual-Comb Source II [Figure 39 (b)] | Dual-Comb Source III [Figure 39 (c)] |
|---|---|---|---|
| $f_{REP}$ | 8 GHz | 1 GHz | 500 MHz |
| $\Delta f_{REP}$ | 100 kHz | 100 kHz | 100 kHz |
| Ratio $I_{BIAS}/I_{TH}$ | ~4 | ~4 | ~4 |
| Ratio $I_{RF}/I_{BIAS}$ | ~2.2 | ~1.8 | ~ 2.2 |

| | | | |
|---|---|---|---|
| Number of RF comb lines (20-dB bandwidth) | 13 | ~70 | ~100 |
| Frequency-shift stage | Yes (40 MHz) | Yes (40 MHz) | No |

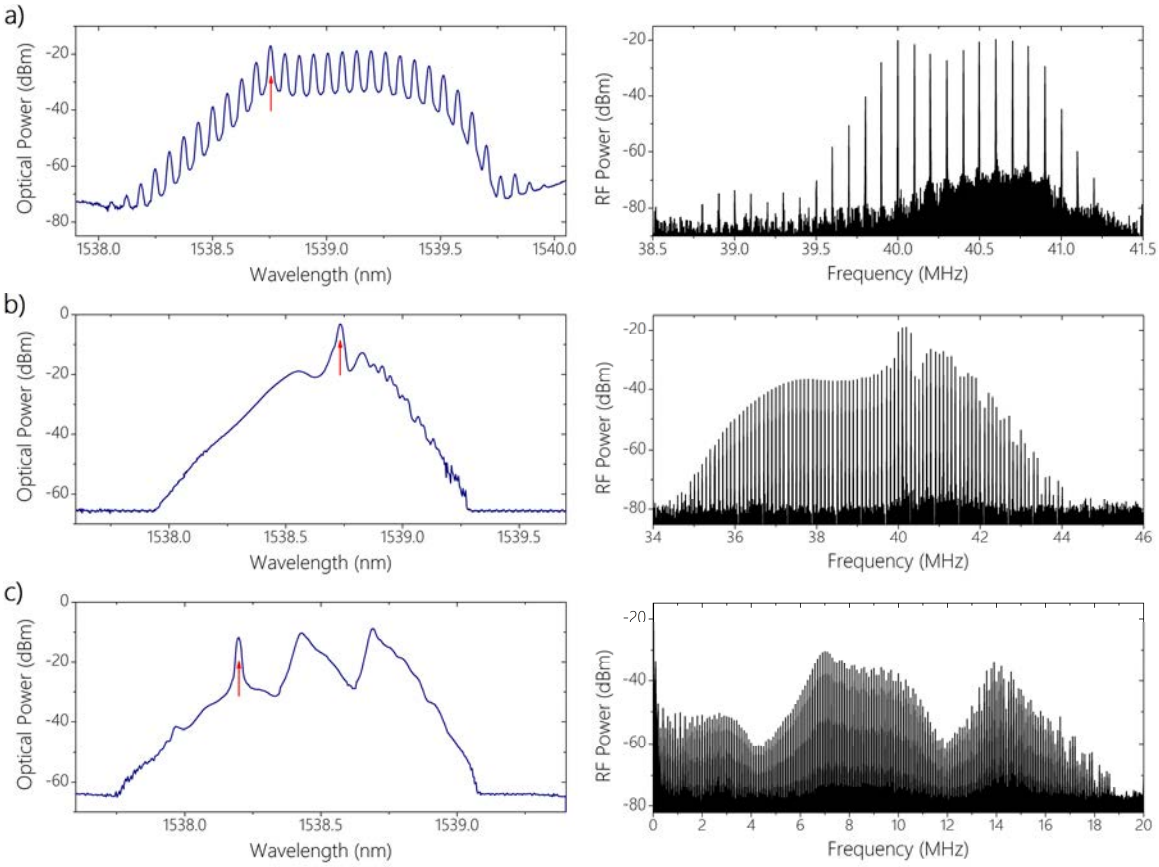


Figure 39. Optical and downconverted RF spectra of GS-OIL-based dual-combs under different driving conditions (see Table 4). The red arrow marks the wavelength of the *master* laser that injects the *slave* OFCs.

At this point, it is important to remark on the RF spectrum displayed in Figure 39 (c). Unlike the other examples represented in the same figure, this RF comb is not centred at a specific frequency, what indicates that none of the OFCs have been frequency-shifted by means of an AOM. However, GS-based OFCs feature an inherent asymmetric distribution of their teeth with respect to the single-mode emission spectrum of the seed laser (see Figure 36). Therefore, one can take full advantage of this feature in conjunction with the possibility of selecting the pair of comb lines that are injected by the *master* laser to map the largest part of the optical spectrum to the RF domain. This way, mode averaging can be reduced to the minimum only by precisely tuning the wavelength of the *master* laser and without resorting to any frequency-shift stage (i.e., an AOM).

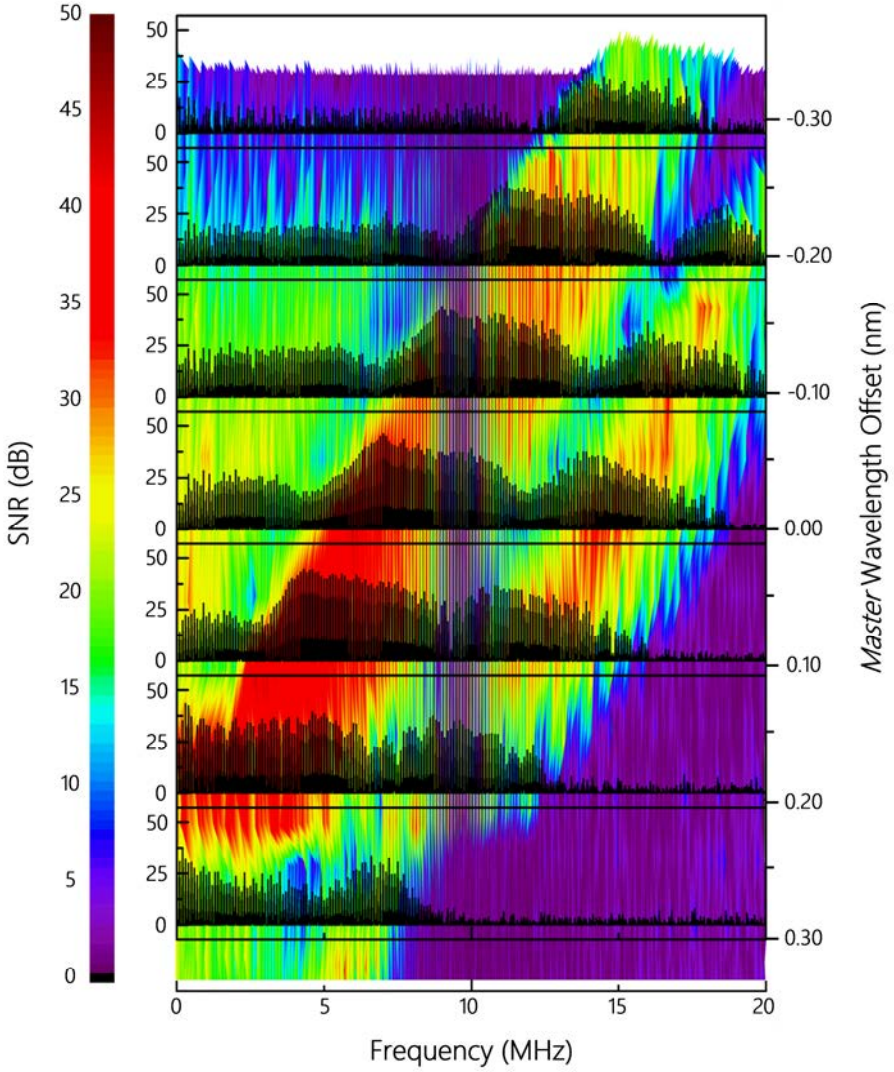


Figure 40. Impact of the emission wavelength of the *master* laser on the recovered RF comb. The background colour map shows the evolution of the SNR of the RF comb lines over a 20 MHz bandwidth when the wavelength of the *master* varies with respect to an initial point (chosen arbitrarily as zero-point). In the foreground, the 2D-plots of seven RF combs for several wavelength offsets are shown. Either a negative offset (*master* farther from the *slaves* OFCs) or positive offset (*master* closer to the *slave* OFCs) leads to a lower SNR in comparison to the zero-point case.

Nonetheless, this process of mode averaging reduction by selecting the *master* laser injection wavelength conveys some limitations. So far, the emission wavelength of the *master* CW laser has been arbitrarily selected with the sole condition of injecting a pair of comb lines. However, the position in the spectrum of this laser source may have detrimental effects which must be borne in mind for dual-comb interferometry. To analyse this issue, the influence of the *master* laser emission wavelength has been evaluated in terms of number of lines of the RF comb and associated SNR (defined here as the ratio of the amplitude of the comb lines to the noise floor) while maintaining the emission wavelength of the *slaves* at a fixed value. Using the spectra of Figure 39 (c) as reference, an offset to the selected

emission wavelength of the *master* laser (around 1538.20 nm) has been introduced by slightly adjusting its temperature. The results of this experiment are illustrated in Figure 40, where the SNR of the RF comb teeth is depicted versus the continuous offset introduced with respect to the reference (i.e., *master* wavelength offset = 0.00 nm) over an RF bandwidth of 20 MHz. Additionally, in the interest of clarity, seven RF combs are also 2D-plotted for a set of discrete offsets. This being said, one can see that there exists an optimal injection point in which the number of lines (and SNR) of the RF comb is maximum. On the other hand, several non-optimal cases can be identified. By detaching (blue-shifting) the *master* from the *slave* OFCs (negative offset in Figure 40) the SNR of the teeth deteriorates, whereas by moving it closer (red-shifting) to the OFCs (positive offset) the effect of the edge-line injection vanishes, thus leading to a narrower RF comb with lower SNR. It is also noteworthy to mention that the injection ratio did not have any effect on the depicted results as long as the *master* laser had enough power to lock both *slave* OFCs. Additional effects of the OIL mechanism on GS-based OFCs (beyond the scope of this experiment) are also discussed in Appendix II.

## 2.3. Experimental Validation

The proficiency of the architectures is validated with the measurement of the ro-vibrational transition of HCN at 1538.52 nm. For this purpose, the sample under test in Figure 33 comprises a 55 mm length gas cell filled with HCN at 100 Torr at room temperature (Wavelength References, Inc.) with full width at half maximum (FWHM) of ~8 GHz at that pressure[337]. Together with the gas cell, an optical switch is inserted to allow the OFCs to bypass the cell and therefore obtain a reference RF comb without the need for an additional photodetector.

First, the gas sample is probed in a collinear arrangement. To adequately discriminate the target gas, the spectral resolution of the dual-comb source (i.e., the line spacing) must be carefully chosen. To fulfil these requirements, the dual-comb source whose spectra and attributes has been depicted in Figure 39 (b) and Table 4 ($f_{REP}$ = 1 GHz) is employed. The emission wavelength of the dual-comb source is then roughly adjusted into the vicinity of the molecular transition. Once the dual-comb source illuminates the photodetector, the time-domain signal is band-pass-filtered with standard RF filters (Mini-Circuits, Inc.) and digitized with a 14-bit waveform digitized board (Signatec, Inc.). The acquired (reference and measurement) time-domain signals are synchronously subsampled at 36 MS/s, thus displacing the RF combs to an equivalent normalized frequency of 4 MHz

while preserving the repetition rate and the spectral information. Figure 41 shows a representative interferogram under these conditions. The generation of all RF signals (*slave* lasers modulation, AOM modulation and acquisition clock) is carried out by the same phase coherent synthesizer (Holzworth Instrumentation Inc.). Neither active temperature stabilization nor vibration isolation procedures are implemented.

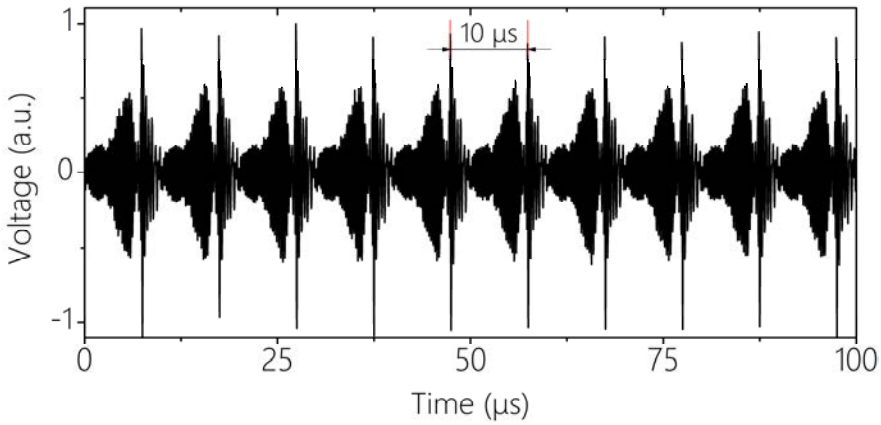


Figure 41. Time-domain interferogram. The time elapsed between two consecutive pulses (10 µs) corresponds to the reciprocal of the difference between the repetition frequencies of the OFCs (in this example, 100 kHz).

The processing method is based on a multichannel digital lock-in detection system (further detailed elsewhere[196]) implemented in Matlab that allows for flexible configuration in terms of reference frequencies, number of channels and integration time. The reference frequency of each channel can be set to coincide with the frequencies of the lines of the RF comb, thus allowing each channel to be concurrently analysed to extract the amplitude or phase of each comb line. After processing, the resultant traces representing the ratio between the amplitudes of the measurement and reference combs are shown in Figure 42 together with Voigt profiles for four different integration times: 10, 50, 100 and 500 µs. Additionally, a plot including an average of 20 spectra over an integration time of 20 ms is presented. In this case, the residuals between the experimental spectra and the fitted Voigt profile show a standard deviation of 0.57%. The peak absorption of ~1.07 dB (~22%) at the central wavelength and FWHM of ~8 GHz denotes excellent agreement with the expected result reported in the literature[337], while the measurement time is also in consonance with the expected ultra-high-speed measurement capabilities of the spectrometer. The noise-equivalent absorption (NEA) of the system normalized to 1 cm of absorption length, 1 second of averaging and one spectral element is defined according to the following expression[338]

$$NEA = \frac{1}{L \cdot SNR}\sqrt{\frac{t}{M}} \tag{13}$$

where $L$ is the effective absorption length (55 mm) and $M$ is the number of spectral elements (comb lines, 70). The SNR is the spectral signal-to-noise ratio, which is here defined as the ratio of the amplitude of every RF beatnote to its standard deviation when no sample is placed. In this case, the SNR averaged over all the RF comb lines for an integration time $t$ of 1 millisecond is approximately 100. These figures yield a resultant NEA of $6.87 \times 10^{-6}$ cm$^{-1}$ Hz$^{-1/2}$.

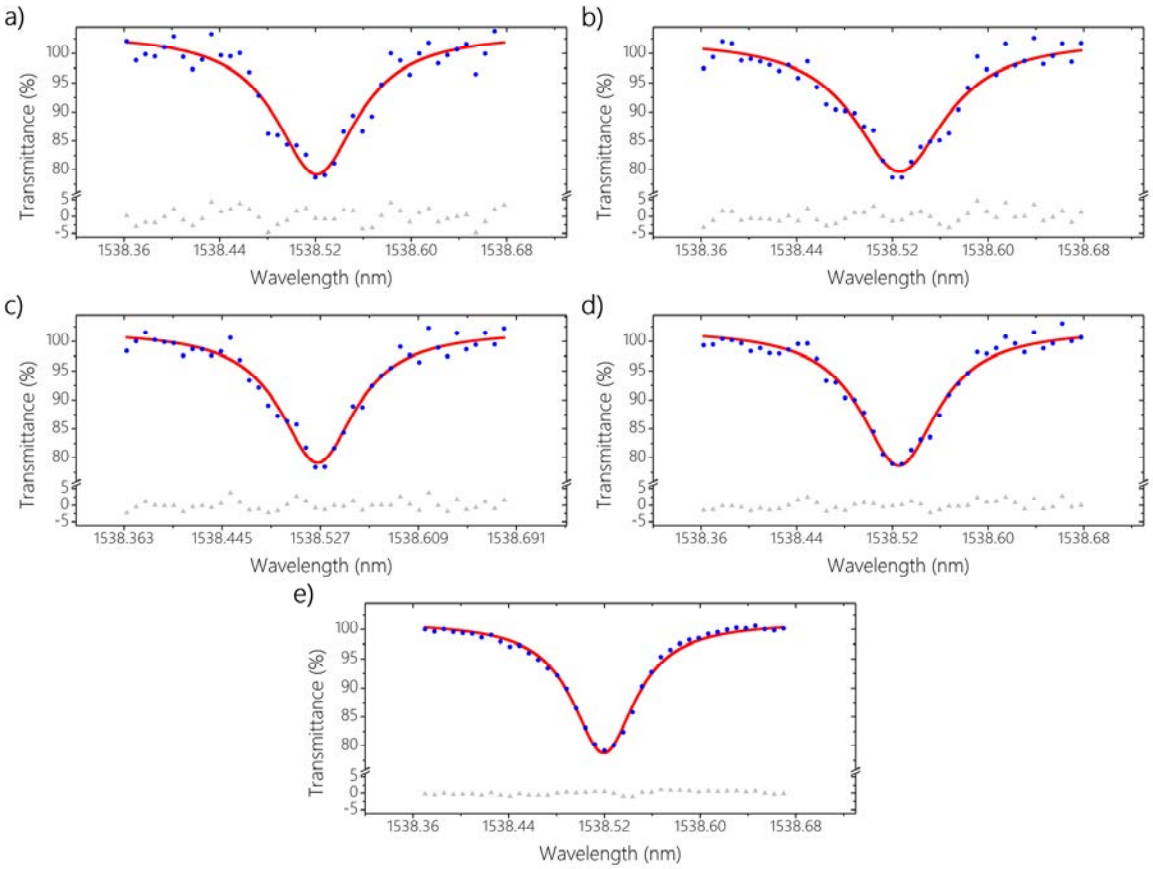


Figure 42. Experimental validation of the GS-OIL-based dual-comb system in the 1.5 μm region. The dots represent the trace of the R(5) line of the HCN 2ν3 band for different measurement times together with the residuals: a) 10 μs; b) 50 μs; c) 100 μs; d) 500 μs; e) Average of 20 spectra integrated over 20 ms. The solid line shows the Voigt fitting of the results, leading to standard deviations between the experimental data and the fitted curves of a) 2.34%; b) 1.89%; c) 1.49%; d) 1.27%; and e) 0.57%.

In a second experiment, the same gas sample is probed in a dispersive arrangement to retrieve the full complex spectrum of the target gas. The sample is accordingly placed within one of the arms of the interferometer. In this case, the dual-comb source employed to interrogate the sample encompasses two OFCs with $f_{REP}$ of 500 MHz (see Figure 39 (c) and Table 4 for additional information). No

AOM is inserted into the dual-comb architecture and mode averaging is mostly cancelled with precise tuning of the *master* laser and the *slave* OFCs. Following the same digitization and processing method, both absorption and dispersion profiles are retrieved. Figure 43 shows the latter after averaging ten spectra over an integration time of 10 ms and applying a box-smoothing prior to fitting to filter out multiplicative phase noise[121] (the absorption spectrum has been overlooked in this section). Again, there is good agreement with the expected FWHM of the molecular transition. For this scheme, the NEA is $5.75 \times 10^{-6}$ $cm^{-1}$ $Hz^{-1/2}$, calculated using the above-mentioned expression (13) under the same conditions with the exception of the number of spectral points (on this occasion, $M = 100$).

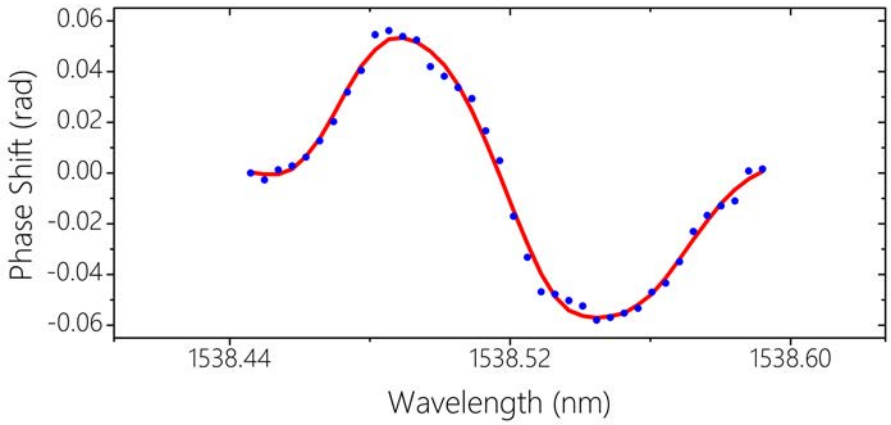


Figure 43. Dispersion profile of the measured ro-vibrational transition of the HCN 2ν3 band at 1538.52 nm (R(5) line). The experimental profile (dots) shows the average of 10 box-smoothed spectra over an integration time of 10 ms. The solid line represents the fitting of the results.

# 3.

# Dual-Comb Architecture for Remote Detection of Optical Frequency Combs

## 3.1. Description of the System

The underlying principle of the method for coherent detection of remote OFCs based on a dual-comb architecture is twofold: firstly, the selection of one optical line of a remote comb through OIL to be subsequently used as carrier to generate a second OFC (denominated as *local oscillator*) with different mode spacing; and secondly, the generation of an RF signal which allows for the effective lock between both combs to ensure the relative stability of their repetition frequencies without any electrical connection. The basic diagram of the setup is shown in Figure 44.

Starting with a remote OFC (with the information of interest encoded into the amplitude and phase of each tooth) that enters the detection scheme, a set of optic couplers (with different coupling ratios) directs the optical power to fulfil various purposes. First, a small part of the input power (upper branch in Figure 44) is employed to extract the beatnotes (at $f_{REP}$) and eventually originate a reference clock signal. The rest of the power is split by means of a 50/50 coupler (lower branches in Figure 44). While one output remains unaltered (preserving the original remote comb and the information it carries), the other one is used to generate a new comb with a small difference in the frequency spacing. For that purpose, one of the lines of the remote comb is filtered through the injection locking mechanism to be the seed of a new OFC. When these two combs are combined and shined onto a photodetector, the RF comb generated after Fourier-transformation of the time-domain interference pattern can then be acquired and

processed to extract the information engraved in each of the spectral components covered by the remote comb.

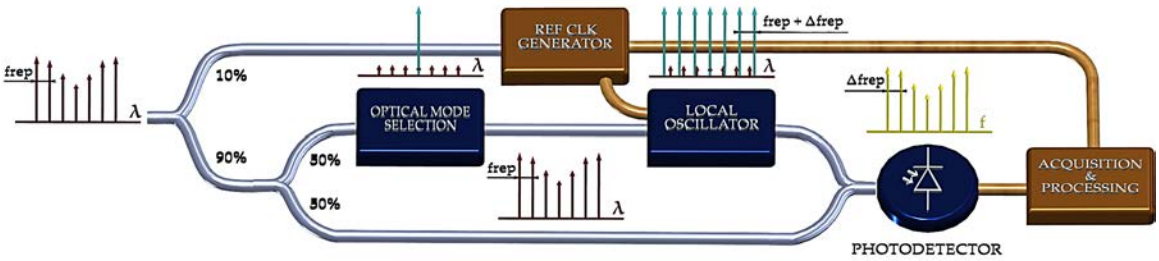


Figure 44. Basic schematic of the setup for remote comb multiheterodyne detection (see text for details).

A detailed schematic of the optical mode selection and *local oscillator* sub-stages is depicted in Figure 45 while the principle of operation is outlined in Figure 46. The selection of an optical line from the remote comb is based on the OIL mechanism to effectively filter one of the lines while establishing a phase-lock to the incoming comb. To that end, a CW laser is tuned into the vicinity of one of the comb lines, as shown in Figure 46 (a). In this way, after adjusting the injection ratio and polarization state of the injected light, the mode selected by the *slave* laser becomes the embryo of the new *local oscillator* comb (Figure 46 (b)). The light is then electro-optically modulated to create a comb with repetition frequency $f_{REP}$ + $\Delta f_{REP}$ and also further frequency-shifted $f_{AOM}$ after going through an AOM (see Figure 46 (c)). Therefore, the wavelength of the local *slave* laser filtering one of the teeth of the incoming comb will be associated with the central frequency ($f_{AOM}$) of the RF comb. At this point, it is also important to remark on the fact that this frequency-shift might be dispensable by properly selecting the injecting line, as explained in the previous section of this chapter. However, on this occasion, the AOM is included to avoid any sort of limitation in this sense.

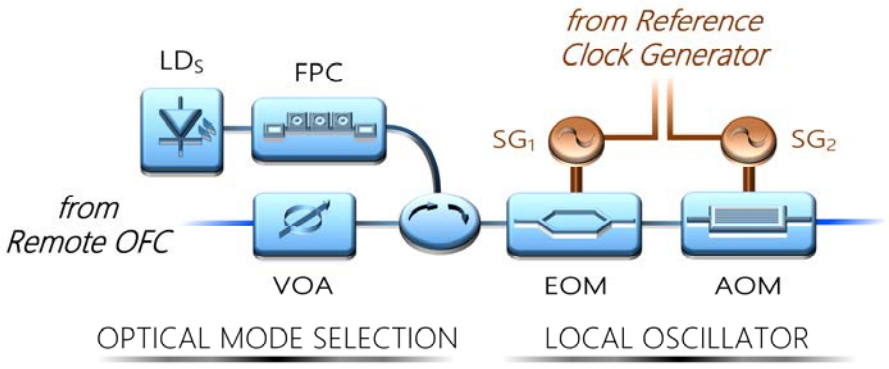


Figure 45. Detail of the optical mode selection and *local oscillator* generation sub-stages of Figure 44. FPC: Fibre polarization controller; LD S: Laser diode *slave*; SG: Signal generator; VOA: Variable optical attenuator.

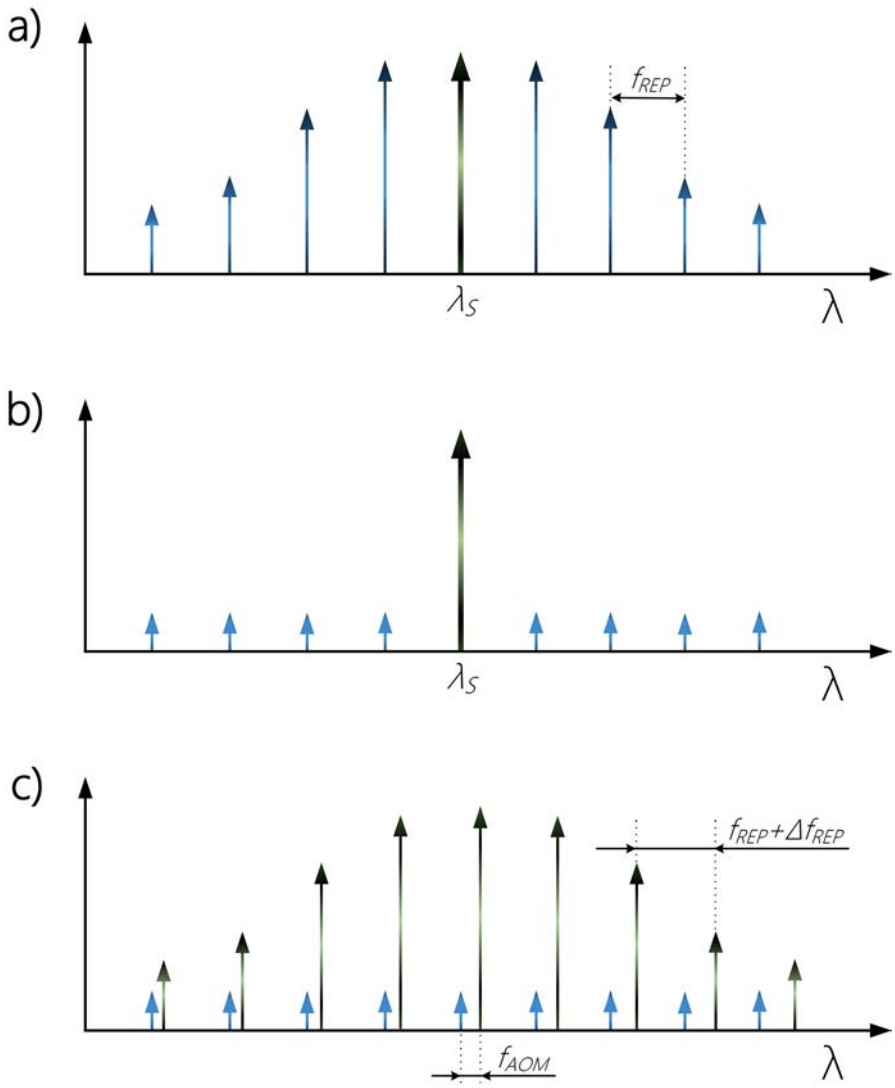


Figure 46. *Local oscillator* comb generation process. (a) A slave laser ($\lambda_S$) is tuned into the proximity of one of the lines of the remote comb with repetition frequency $f_{REP}$. (b) To properly carry out the injection process, strict control over the injection ratio (and polarization state) is kept to select one of the lines of the remote comb as a source to generate a (c) new OFC with slightly different line spacing ($f_{REP} + \Delta f_{REP}$). An additional frequency-shift $f_{AOM}$ is introduced to this comb to allow for the unambiguous mapping onto the RF domain.

Finally, as a complement to optically phase-locking two independent combs to stabilize their offset frequencies, an RF link must also be guaranteed to compensate the drifts between their repetition frequencies for stable dual-comb generation. Since there is no direct RF synchronization between the incoming comb and the *local oscillator* comb generated in the detection scheme, the RF locking between them is based on the extraction of one of the harmonics from the remote comb at $f_{REP}$ and its further division and signal conditioning to eventually generate a 10 MHz reference signal which will serve as the common time base of the detection arrangement.

## 3.2. Characterization

The characterization of the system is carried out with the creation of a stage that emulates the performance of a remote comb. This stage is based on an EO-OFC encompassing a CW DM semiconductor laser (Eblana Photonics, Ltd.) emitting at 1538.5 nm at room temperature and an EO phase modulator (EOSpace, Inc.) driven with an amplified RF signal up to a power level of 32 dBm at two repetition frequencies in successive experiments (7 GHz and 4 GHz). The system is fully-fiberized. An optic coupler is first used to direct 10% of the signal to eventually generate a 10 MHz RF reference. The rest of the power is 50/50 split in the two arms of the interferometer. A similar DM laser is used to filter one of the lines of the remote comb. To that end, its emission wavelength is roughly tuned around one of the lines of the comb by acting on its temperature and current. A circulator is used to route the input and output light of the *slave* laser along different paths. Finer adjustment of the injection mechanism is accomplished with a fibre polarization controller placed at the input of the *slave* laser and also by regulating the power with a variable optical attenuator to gain control over the locking range. A stable regime was achieved with an injection ratio (input power to output power) around -35 dB. All the lasers were stabilized in current and temperature with standard laser diode controllers.

The filtered seed line is then used to create the *local oscillator* comb with an EO phase modulator driven under similar conditions that the one taking part in the remote stage but with a slight difference in the mode spacing of $\Delta f_{REP} = 100$ kHz. This comb is further frequency-shifted 40 MHz with an AOM (Gooch & Housego, Inc.) excited with an RF power of 24 dBm before combination with the primary remote comb travelling along the other arm of the interferometer. An extra fibre polarization controller is inserted to control the polarization state of this comb so that it matches with that of the remote comb. The final (optical) result after merging both remote and *local oscillator* combs is depicted in Figure 47 (red trace) for the same two aforementioned repetition frequencies (7 GHz and 4 GHz). For comparison purposes, the spectra of the filtered lines from the remote combs is also shown (blue trace). One might infer from this figure that an expansion of the OFC takes place by properly selecting the injected line, but, although this is clearly visible in the optical domain (red trace), the number of spectral points will always be limited by the narrower comb (and ultimately by the Nyquist criterion) as long as both combs overlap well with each other. The mixture of optical pulses with different time delays corresponding to the combined remote and *local oscillator* combs is then heterodyned on an InGaAs photodetector (Thorlabs, Inc.). In the

frequency domain, the generated RF combs are observed on an electrical spectrum analyser (see Figure 47, black traces), where the presence of resolved comb lines is a clear indicator of the mutual coherence between both combs induced by the OIL mechanism. The 3-dB linewidth of the lines yields a value which lies below the minimum resolution bandwidth of the instrument (1 Hz).

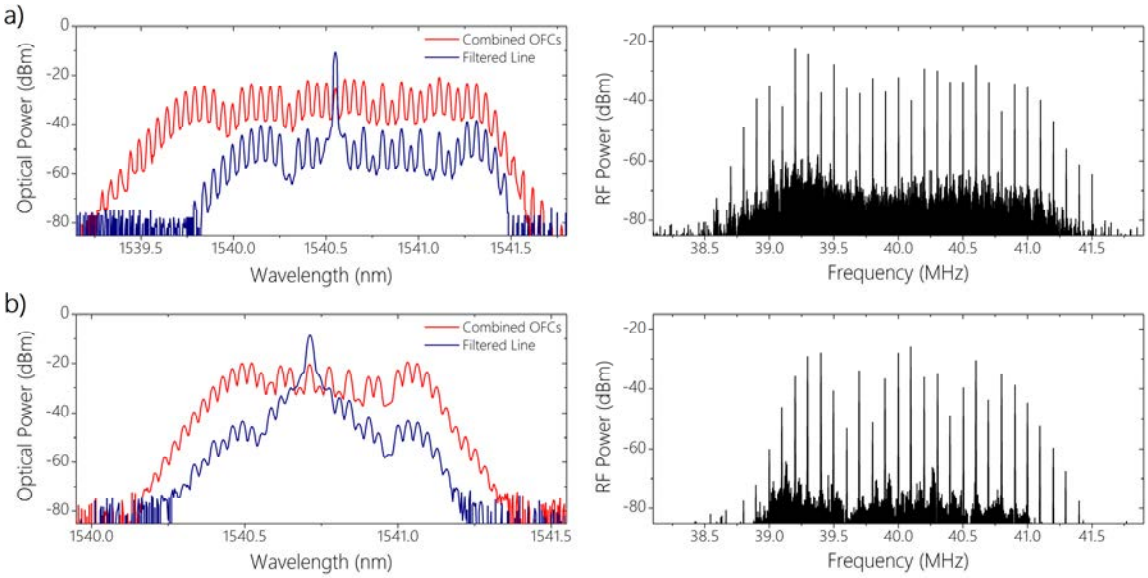


Figure 47. Illustration of the generated OFCs and RF combs after photodetection. Two different scenarios involving OFCs with repetition frequencies of (a) 7 GHz and (b) 4 GHz. The blue lines denote the filtered line from the remote comb with an injection ratio around –35 dB, whereas the red lines represent the final mixed signal after combination of the remote and *local oscillator* combs (with a mismatch in their line spacings of 100 kHz). The RF combs are centred at 40 MHz ($f_{AOM}$) and exhibit a line spacing of 100 kHz ($\Delta f_{REP}$). The discrepancies in bandwidth and number of lines are mainly due to the electronic response of the two different amplifiers used to drive the EOMs at each of these frequencies.

To generate a common RF reference, a fast photodetector (u2t Photonics, Inc) with 50 GHz bandwidth is employed to extract one of the beatnotes of the remote comb at $f_{REP}$ together with fixed ratio ($N$) frequency dividers (being $N = f_{REP}/10$ MHz) and standard band-pass filters (Mini-Circuits, Inc.). Since the amplitude of the RF beatnotes may significantly vary due to a number of factors (such as the remote comb technology, the responsivity of the photodetector or the effect of the target device under test on the remote comb), an erbium-doped fibre amplifier (EDFA) and a variable optical attenuator are harnessed to keep control over the power of the beatnotes and adjust it to the input power specifications of the frequency divider and RF generators. The 10 MHz signal is then used as the common time base of all the RF synthesizers taking part in the detection scheme

The impact of the RF reference locking on the generated RF comb is then evaluated to analyse the degree of synchronization between independent OFCs. The first consequence of keeping the combs unlocked is shown in Figure 48 (a).

Together with an increase of the noise floor, a growing frequency disparity between comb lines shows up as they are farther from the centre of the RF comb. This relative drift between the repetition frequencies of the OFCs is further assessed by observing the long-term frequency stability of one of the RF comb teeth. To this end, the temporal evolution of the 5$^{th}$ line to the right of the central line (i.e., the line at 40.5 MHz in the locked case, and at 40.528 MHz –due to the frequency disparity- in the unlocked case) is observed during a 20-minute experiment. The results reveal a time-varying offset of the line with respect to its central frequency (determined by the relative stability between the RF generators driving the EOMs) when no locking between synthesizers takes effect (see Figure 48 (b)). In contrast, when the locking between the oscillators is forced, no sign of frequency mismatch is noticed throughout the duration of the experiment and the evaluated line rigidly remains at its initial and expected value with barely noticeable excursions, as can be seen in Figure 48 (c). In the last case, the Overlapped Allan deviation is calculated. The results are shown in Figure 48 (d), showing a type of noise between white FM and Flicker FM[339].

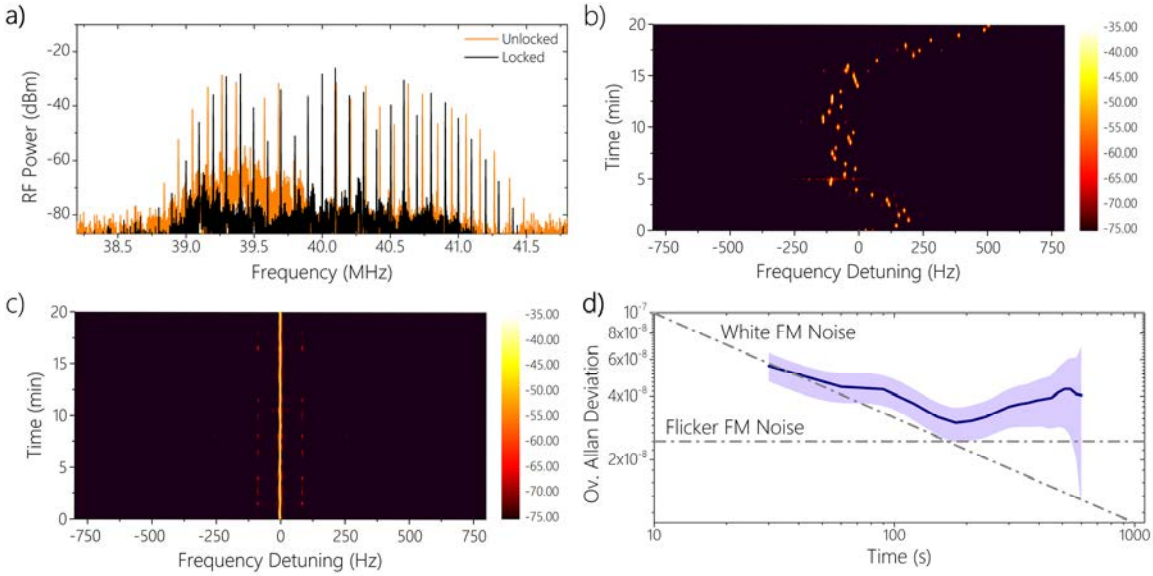


Figure 48. Analysis of the RF locking. a) Comparison between two RF combs generated from the OFCs from Figure 47 (b) without (orange line) and with (black line) RF locking between independent OFCs. b) and c) Long-term stability analysis of the RF comb tooth at 40.5 MHz over 20 minutes in steps of 30 seconds without and with RF locking, respectively. The vertical bar on the right side indicates the electrical power in dBm. d) Overlapped Allan deviation (blue trace) of the fractional frequency of the signal at 40.5 MHz under RF locking conditions and error region (purple trace).

## 3.3. Experimental Validation

The proposed architecture is experimentally validated with the utilization of the remote comb stage to interrogate a device under test whose spectral content is to be retrieved using the local dual-comb coherent detection system. In this case, the device under test is a fibre-coupled FBG sensor (FiberSensing, Ltd.) with a central wavelength of 1539.98 nm, FWHM of 0.2 nm (~25 GHz) and a measured sensitivity of 1.11 pm/με. The FBG sensor is attached to a dovetail single-axis linear translation stage that allows manually adjusting the strain applied to the FBG sensor (and therefore, tuning its transmission spectrum). Figure 49 shows the experimental assembly of the FBG sensor and its characteristic transmission spectra for a set of discrete levels of strain measured with an optical spectrum analyser. In principle, the sensor is arranged in such a way that when no strain is applied, there is no effect on the remote comb lines.

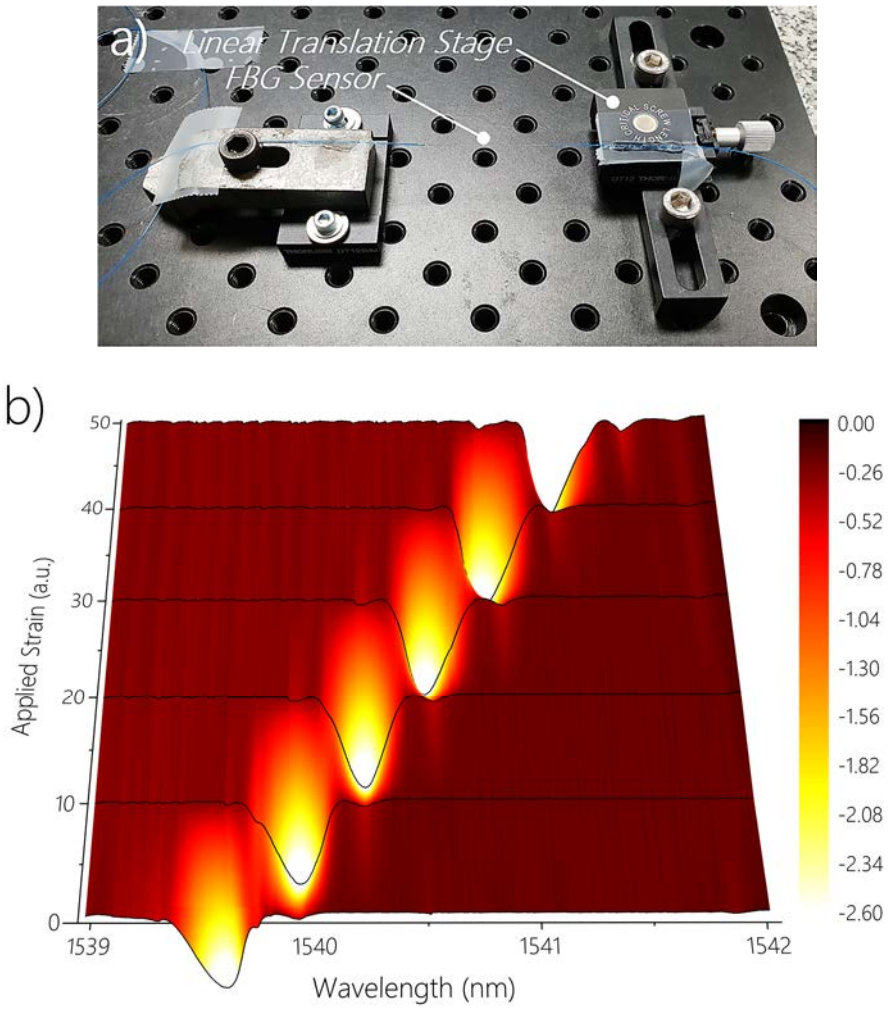


Figure 49. Experimental setup of the FBG sensor used as device under test (a) and transmission spectra under different levels of strain (b). The vertical bar on the right side indicates the normalized optical power in dBm.

The generated OFC with amplitude-encoded information by the FBG is transmitted along 100 metres of optical fibre and then is used as input of the local, detection stage. Fibre-coupled isolators are also inserted to suppress any reflection between the remote stage and the detection scheme. Under the same conditions of injection locking and comb generation established in the previous section (OFCs with $f_{REP}$ = 7 GHz and 4 GHz and $\Delta f_{REP}$ = 100 kHz), a dual-comb interference signal is created once both combs overlap on the photodetector (see Figure 50). The time-domain signal is then band-pass filtered with standard RF filters (Mini-Circuits, Inc.) before being finally digitized with a 14-bit waveform acquisition board (Signatec, Inc.). The signal is then synchronously subsampled at 36 MS/s, thus modifying the central frequency to a normalized frequency of 4 MHz at the same time that the repetition rate is kept unmodified at 100 kHz. The Fourier-transformation of this signal unveils the RF comb generated, which is similar to the ones previously displayed on the spectrum analyser (Figure 47).

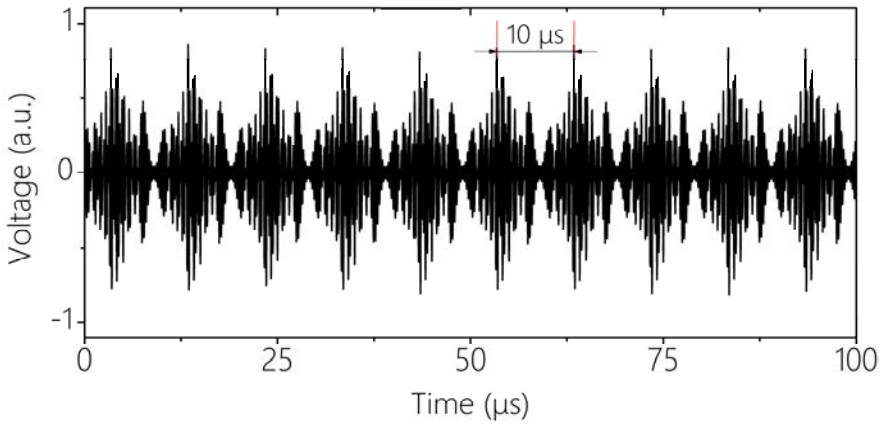


Figure 50. Time-domain interferogram generated when the optical pulse trains from the remote and *local oscillator* combs are photodetected. The separation between adjacent pulses is 10 µs, which is the reciprocal of the line spacing mismatch between OFCs.

Processing the beatnotes of the RF comb to retrieve their corresponding amplitude discloses the spectral information of the FBG sensor. The results are illustrated in Figure 51, where the ratio between a reference (no strain) and an actual measurement (after applying strain –around 490 µε-) is shown for the two different comb repetition frequencies (7 GHz and 4 GHz). It is important to note that, in any case, both signals (reference for normalization purposes and effective measurement of the sensor) originate from the remote comb. The dots show the spectral profile after averaging 10 measurements over an integration time of 100 µs for a repetition frequency of 7 GHz (Figure 51 (a)). With the same integration time, the same profile is also retrieved after averaging 15 measurements for a line spacing of 4 GHz (Figure 51 (b)). In both cases, a Gaussian profile is fitted, showing

good agreement with the expected value of the FWHM. The residuals between the experimental data and the fitting reveal a standard deviation of 2.10% and 3.59% for 7 GHz and 4 GHz, respectively. The average spectral SNR of the lines of the comb (at 7 GHz and 1 ms integration time) is 30. The normalization of this figure to the number of spectral points and for a standard integration time of 1 second yields a figure of merit of $SNR \times M = 2.85 \times 10^4$ (in this case, for $M = 30$ spectral points)[112].

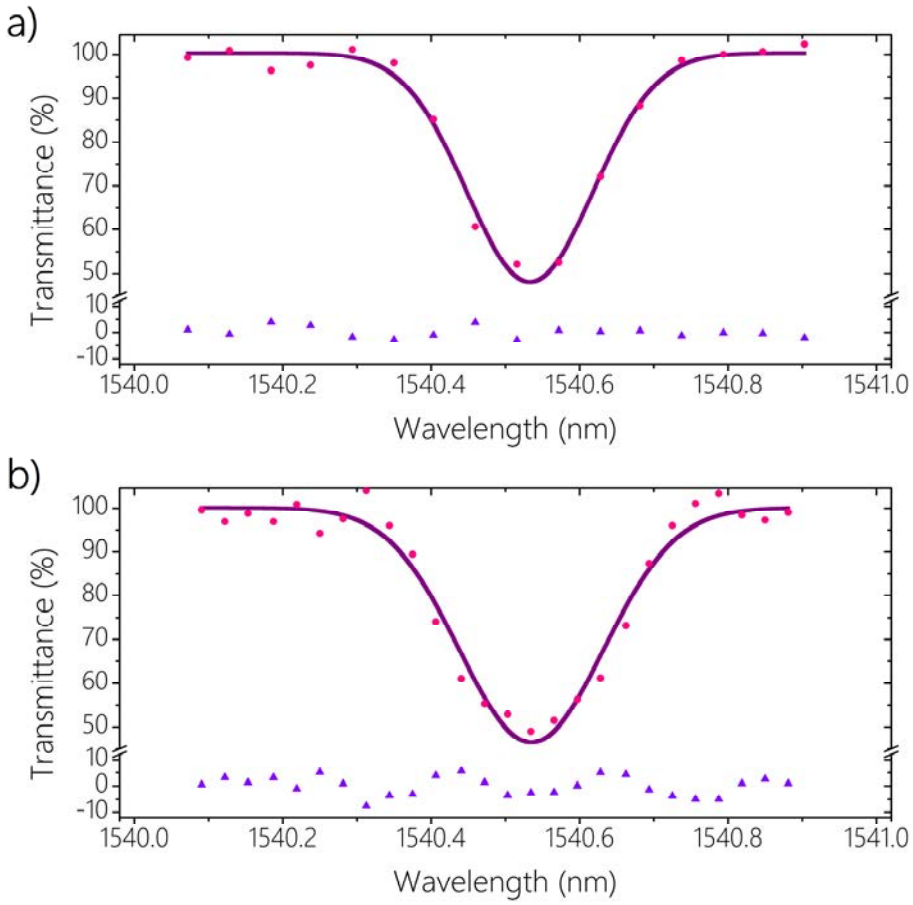


Figure 51. Transmission spectrum (magenta dots) of the FBG sensor when interrogated with combs with repetition frequencies of (a) 7 GHz and (b) 4 GHz. The applied strain is roughly 490 με, which leads to a wavelength shift in the transmission spectrum of 0.54 nm. The reference spectrum when no strain is applied (used for normalization purposes) is centred at 1539.98 nm. The solid purple lines show a Gaussian fitting in both cases with a FWHM of (a) 0.20 nm and (b) 0.23 nm.

# 4.

# Discussion of the Results

This chapter has introduced two original architectures in the Near-Infrared that harness the potential of the dual-comb technique for different purposes. To that end, some of the well-established methods for comb generation have been exploited in two separate arrangements that are based on OIL as mechanism to reconstruct the mutual coherence between free-running, independent combs.

First, a dual-comb modality whose performance relies on GS to induce a pulsed operation regime in two semiconductor lasers (and consequently, to generate a pair of slightly detuned OFCs) has been demonstrated. In conjunction with OIL and the use of a common RF reference, the system maintains the range of advantages of classic EO dual-comb arrangements and also allows for a reduction in the number of components involved only by efficiently applying the techniques on which this system is based. The GS-OIL-based dual-comb architecture is first validated in the Near-Infrared region with the measurement of the full complex response of HCN at 1538 nm. However, the potential of the architecture for deployment beyond this region must be highlighted, owing to the ubiquitous nature of the employed techniques across a wide variety of laser platforms and regions of the electromagnetic spectrum as well as the absence of wavelength-restrictive optical components. Besides that, the possibility to incorporate this arrangement into PICs using generic platforms[63] also offers new and exciting prospects for the cost-efficient implementation of this setup in field applications.

From the point of view of the technique, OIL can be found in the literature as a usual complement of GS in order to improve the performance of the generated combs[56,57,63], with particular emphasis placed on communication applications[340]. Beyond this research field, the combined use of GS and OIL has also proven valid

for the generation of microwave combs based on the exploitation of the nonlinear dynamics of semiconductor lasers[341]. However, no demonstration of the utilization of these well-known techniques for spectroscopy purposes has been reported to date. Only recently, Chandran *et al.* performed a proof-of-concept experiment of cavity-enhanced absorption spectroscopy for the detection of hydrogen sulphide using a few lines of a GS-based OFC[342].

Second, a novel system for OFC detection which allows for the retrieval of the information imprinted into a remote comb by means of a local multiheterodyne detection scheme has been proposed. The system exploits the benefits of the OIL mechanism to generate a phase-locked local OFC with stable offset frequency and different frequency spacing from a filtered line of a sensing, remote comb, thus yielding mutual coherence between both OFCs and, hence, fully-resolved, sub-Hz-linewidth RF spectra. A straightforward method to lock and synchronize all RF synthesizers (and hence, both combs and their repetition frequencies) also endows the system with time stability, allowing for the recording of free-distortion fully-frequency-locked spectra and coherent averaging.

The architecture is validated with the detection of an EO-OFC and the spectral measurement of the deformation of an FBG encoded into it. For that purpose, a second EO-OFC has taken part in the detection scheme. In this sense, it seems crucial that this comb had, at least, the same number of lines that the remote comb to correctly extract the information carried by the latter at once, but considering a general framework, this limitation may be overcome with coherent stitching of a number of spectra to recover the full spectral content of the remote comb. In this experiment, the very high mutual coherence of the system endowed by the OIL mechanism and the RF locking has enabled the recovery of the FBG transmission spectrum by averaging with an integration time of 100 μs. With the current selection of OFC generators, the system preserves all the virtues associated with traditional EO dual-comb spectroscopy, but this detection approach can also be readily extended to other comb sources. Diverse applications that may require a remote comb, such as monitoring of industrial risks or sensing of toxic gases and biological agents may benefit from this comb detection approach.

Finally, the author would like to conclude this section with a brief remark on the effect of the injection locking mechanism on dual-comb architectures. Unlike other methods that aim to synchronize a pair of free-running OFCs, the OIL technique might alter the characteristics of the generated combs. This is caused by the intrinsic dynamics of the OIL mechanism: when a *master* laser injects a *slave* comb line, the adjacent teeth will also be to some degree influenced if there is not

proper control over the locking range[343]. In order to attain a fine and effective locking to only one tooth of the comb, the locking range must be reduced to less than half of the repetition rate of the OFC, which, in the case of OFCs with line spacings below 1 GHz, would require injection ratios in the order of -40 dB. However, the main challenge is related to the frequency drifts of non-stabilized *master* lasers, which may lead to unstable locking. To circumvent this problem, the injection locking mechanism can be upgraded with the inclusion of phase-locked loops for enhanced robustness and improved long-term stability against frequency drifts and with the use of ultra-low noise controllers to drive the laser sources[344].

In the first experiment, no active control over the locking mechanism was implemented, as the main objective was to demonstrate that the OIL technique could be useful to induce mutual coherence between unrelated combs. To that end, the injection ratio was set to 10 dB, thus ensuring a broad locking range. In return for a simpler locking scheme, not only one but several comb lines were simultaneously affected by the presence of the *master* laser. This was translated into disturbances due to locking crosstalk that led to lower SNR or even the eventual loss of usable spectral elements. Still, as the combs remained effectively locked to each other, the unaffected lines were perfectly valid to probe the gas sample and to retrieve the spectral profiles of the absorption features in this proof-of-principle experiment.

On the other hand, the second experiment has intended to explore this limitation in more depth. It was found that, with the current instruments and without any active control over the injection mechanism, the minimum spectral point spacing of the injected comb that did not lead to crosstalk between adjacent lines was in the region of 4 GHz. Further measurements below 4 GHz were also realized, but no acceptable spectral information could be properly retrieved from most of the distorted lines of the RF comb. All these evidences lead to the final conclusion in relation to OIL-based dual-comb systems: provided that the whole comb structure is to be retrieved in a one-shot fashion without undesired perturbations, the minimum resolution of the dual-comb spectrometer (i.e., the minimum tolerable repetition frequency of the comb that conveys the spectral information) will ultimately be limited by the injection locking mechanism.

# IV

# Contributions to Dual-Comb Spectroscopy in the Mid-Infrared

# 1.
# Introduction and Motivation

The research contributions of the author to the Mid-Infrared spectral range are addressed in the fourth chapter of this document. Of all the techniques and devices introduced in Chapter II for the development of Mid-Infrared dual-comb sources, the presented work will be primarily focused on two of them: the nonlinear conversion of Near-Infrared dual-combs through DFG, and the application of QCLs as direct sources of radiation in this spectral domain.

The possibility of extending the potential of EO dual-comb architectures beyond Near-Infrared was already referred to as one of the leading motivations behind the demonstration of GS-OIL-based dual comb schemes. Here, this objective is effectively fulfilled with the implementation of a modular instrument devised to perform Mid-Infrared dual-comb spectroscopy based on DFG using a QPM magnesium-doped periodically-poled lithium niobate (MgO:PPLN) crystal as nonlinear media. The selection of this crystal is fundamental to access the appealing 3-5 μm range, which is a spectral region rich in strong fundamental molecular transitions of a number of well-known greenhouse gases and pollutants that also features a relative transparency to atmospheric attenuation. In this scenario, methane will be used as target gas to retrieve the absorption profile of one of their features located in the P-branch at 3.45 μm. The rationale that lies behind DFG processes in QPM crystals as well as the main features and limitations of the instrument will also be discussed. Further details of this work can be found in the manuscripts [M4] and [X4] of the catalogue of scientific contributions.

Moreover, this chapter will also unveil the results of an experimental study which was realized in collaboration with the group of Gottfried Strasser (Technische Universität Wien) for the generation of OFCs in QCLs based on large-signal modulation. In the previous chapters, QCL-based OFCs were introduced as

compact sources whose line spacing (in the range of GHz) were strictly determined by the physical properties of Fabry-Pérot devices with highly limited tuning capabilities. In this work, large-signal modulation techniques are applied to a single-mode DFB QCL to demonstrate their feasibility as methods for tunable coherent multiharmonic signal generation. Despite not creating pulses due to the ultra-fast dynamics of these lasers, the results reveal that a comb structure with uniform mode spacing and varying properties depending on the driving parameters can be generated when the device is adequately driven above and below threshold. This section will not include the further application of this method to dual-comb spectroscopy, but the main implications for this purpose will also be discussed. These results are included in the manuscript labelled as [M5] in the author's research work list at the beginning of the document.

# 2.

# Mid-Infrared Electro-Optic Dual-Comb Spectroscopy based on Difference Frequency Generation

## 2.1. Description of the System

The devised instrument to perform Mid-Infrared dual-comb spectroscopy presents a modular design, encompassing two autonomous units entirely built by commercial off-the-shelf components. The schematic of the experimental setup is sketched in Figure 52. First, a classic EO dual-comb system is implemented via EO modulation of a CW semiconductor laser with an emission wavelength in the range of 1538 nm. Two mutually-coherent *signal* OFCs with different line spacing (one of them additionally frequency-shifted with an AOM) are then generated and combined in the same fibre. All RF signals driving the modulators are referenced to the same time base.

The *signal* combs are then amplified with an EDFA before combination with a free-running CW pump laser emitting in the vicinity of 1064 nm in a fibre-coupled WDM. The process to reach the Mid-Infrared is held in a single-crystal DFG module whose core is a bulk MgO:PPLN crystal. To that end, the Near-Infrared *signal* and *pump* beams are jointly collimated and focused with an achromatic lens on the centre of one of the gratings of the crystal. Fibre polarization controllers are inserted to match the polarization state of the combs and to maximize the conversion efficiency into the crystal, which is attained when the polarization axis of the light is aligned to the thickness of the crystal.

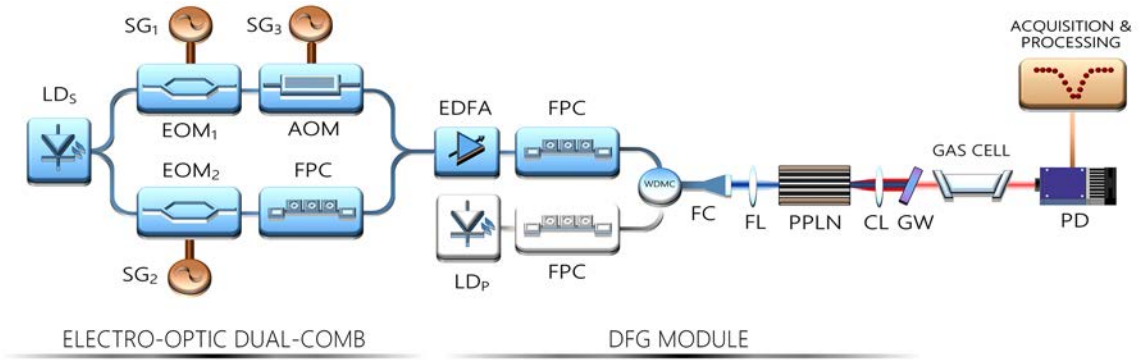


Figure 52. Schematic of the experimental setup for Mid-Infrared EO dual-comb spectroscopy (see text for details). CL: Collimating lens; FC: Fibre collimator; FL: Focusing lens; FPC: Fibre polarization controller; GW: Germanium window; LD S/P: Laser diode (*signal*/*pump*); PD: Photodetector; SG: Signal generator; WDMC: Wavelength division multiplexer coupler.

*Idler* combs can thus be solely generated with proper selection of *pump* and *signal* wavelength across the transparency range of the crystal, as PPLN crystals are engineered to be quasi-phase-matchable by spatially choosing the poling period of the crystal at a given temperature. From the frequency-domain point of view, the *pump* source at frequency $f_P$ drives the process, downconverting the Near-Infrared *signal* EO combs of frequencies $f_{S1} = f_{S0} \pm n \times f_{REP}$ and $f_{S2} = f_{S0} + f_{AOM} \pm n \times (f_{REP} + \Delta f_{REP})$ into Mid-Infrared *idler* combs at $f_{DFG1} = f_P - f_{S1}$ and $f_{DFG2} = f_P - f_{S1}$ (with $f_{S0}$ being the emission frequency of the Near-Infrared CW *signal* laser). Since both Mid-Infrared OFCs are generated from the same Near-Infrared laser sources (*pump* and *signal*), the system exhibits excellent passive mutual coherence.

The Mid-Infrared *idler* beam is then collimated by a calcium fluoride lens and filtered out from the residual Near-Infrared radiation with a germanium window before probing a gas sample in a collinear arrangement. Finally, the Mid-Infrared dual-comb is overlapped on a photodetector. As in other standard dual-comb systems, acquisition and processing of the multiheterodyne beatnotes can then be realized using commonplace electronics to extract their spectral content.

## 2.2. Characterization

The fundamentals of DFG processes were previously outlined in the third chapter of this dissertation. Arguably, DFG has been the preferred mechanism to access the Mid-Infrared owing to its inherent simplicity: in a single-pass fashion, without resonant cavities, Mid-Infrared radiation can be produced with the same properties and characteristics of the input Near-Infrared *signals*. Nevertheless, the adequate implementation of these sources demands detailed consideration of the

underlying principles that govern this nonlinear process. This section will briefly review the influence of the main parameters of design on the final results, which will serve to gain insight into the capabilities of the instrument for its application to dual-comb spectroscopy.

First, it is necessary to analyse the expected output power in this type of system. In the classic scheme, two Near-Infrared sources *pump* and *signal* with powers $P_P$ and $P_S$ for *pump* and *signal*, respectively, feed a second-order susceptibility nonlinear crystal with length $L$. Assuming collinear Gaussian beams with identical confocal parameters $b$, the output (*idler*) power $P_I$ can be expressed as follows[345]

$$P_I = \frac{4}{\pi \cdot \varepsilon_0 \cdot c^3} \cdot f_I^2 \cdot \frac{d_{eff}^2}{n_P \cdot n_S \cdot n_I} \cdot \frac{h(\mu, \xi)}{k_P^{-1} + k_S^{-1}} \cdot L \cdot P_P \cdot P_S \cdot e^{-\alpha L} \tag{14}$$

where $c$ is the speed of light; $\varepsilon_0$ denotes the permittivity of the medium; $f_I$ is the frequency of the *idler*; $n_P$, $n_S$, and $n_I$ represent the refractive index of the crystal at the *pump*, *signal* and *idler* frequencies, respectively; $d_{eff}$ indicates the nonlinear coefficient; $k_P$ and $k_S$ are the wavevectors of *pump* and *signal*, respectively; the term $e^{-\alpha L}$ denotes the frequency-dependent absorption of the crystal and $h(\mu,\varepsilon)$ is the focusing function which accounts for the influence of walk-off and focused beams effects on the crystal with $\mu = k_P/k_S$ and $\xi$ defined according to this expression

$$\xi = \frac{L}{b} = \frac{L \cdot \lambda}{2 \cdot \pi \cdot \omega_0^2 \cdot n} \tag{15}$$

where $\lambda$ is the wavelength of the beam $\omega_0$ its waist radius.

From inspection of equation (14) it is possible to draw some conclusions, which are listed below:

- The output power is proportional to the square of the *idler* frequency, so DFG processes that intend to produce radiation deeper in the Mid-Infrared will be less efficient.
- The *idler* power is proportional to the nonlinear figure of merit $d_{eff}^2/(n_P n_S n_I)$ (see Figure 24 for more details of this figure for a number of nonlinear crystals).
- The DFG power is linearly dependent on the square of the input powers (*pump* and *signal*). However, maximum incident powers are often limited by the damage threshold of the crystal.

- The output power varies linearly with the length of the crystal, but it is also restricted by diffraction effects and scattering noise that arises when the used crystal is excessively long, as the *idler* beam diverges much faster than the *pump* and *signal*.
- The focusing function $h(\mu,\varepsilon)$ maximizes the *idler* power for $\xi = 1.3$ in the case of Gaussian beam coupling. Still, optimal focusing conditions may vary in each scenario due to a number of factors[346]. If a loose focusing parameter is used ($\xi \ll 1$), the h-function approximates the value of $\xi$ and the DFG power is proportional to $L^2$ [347].

All these properties firmly hold as long as the most critical requirement in relation to frequency conversion is fulfilled: the interacting waves must remain in phase along the nonlinear optical medium (phase-matching). These waves travel at difference velocities because of frequency dispersion in the refractive index of the nonlinear crystal, resulting in a phase drift that grows along the length of the medium and prevents the production of a monotonic power flow in the generated *idler* direction. Maximum conversion efficiency is attained when the phases of the waves are matched and, hence, $\Delta k = 0$. Traditionally, the birefringence of the crystals has been harnessed to adjust the phase-matching conditions by means of the tuning of the angular orientation of the incident beams, the crystal temperature or the pumping wavelength. However, the approach that more success has enjoyed in the past years is the use of QPM materials that are explicitly manufactured to compensate the phase mismatch and access the highest nonlinear coefficient[226]. In materials such as lithium niobate, this is attained by the periodic reversal of the sign of the nonlinear coefficient via electric poling along the propagation direction. Furthermore, QPM materials can be engineered so that the phase mismatch is compensated within the full transparency range of the crystal with adequate selection of the poling period (in the range of tens of μm). To that end, easy-to-operate commercial nonlinear crystals usually incorporate multi-grating designs that allow for extensive frequency tuning for a given combination of input wavelengths and temperature using a single optical architecture.

Among the large commercial selection, the nonlinear conversion in this architecture will rely on the well-established QPM PPLN technology, which also features high thermal conductivity and large optical damage threshold when operated at high temperatures. The 40 mm-long, 0.5 mm-thick MgO:PPLN crystal taking part in the system (Covesion, Ltd) (see Figure 53) includes nine periodically poled gratings with periods ranging from 27.91 to 31.59 μm (the shorter periods provide access to longer wavelengths) for *idler* tuning in the range of 2.1 to 4.6 μm

for a set of externally adjustable temperatures that stretch from 30 °C to 200 °C. Still, QPM technology can only offer discrete tuning capabilities, since the chosen poling period is only optimized for a range of wavelengths and one must sequentially select the available periods if full spectral coverage is intended. The phase-matching bandwidth scales inversely with the length of the crystal, but other factors such as the temperature or the period of the grating also affect it. In this sense, the engineerable nature of QPM materials has propelled the advent of tailored aperiodic grating structures that allow for broader phase-matched bandwidths[226].

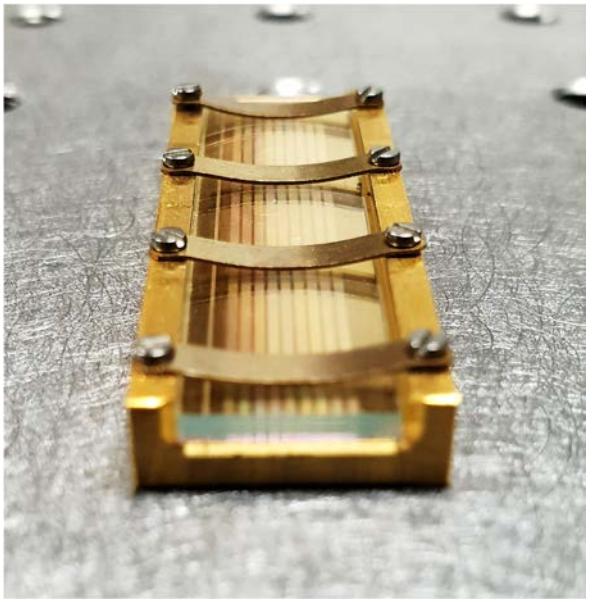

Figure 53. Illustration of the MgO:PPLN crystal for DFG used in the experiment. The nine different poled gratings for wavelength tuning are clearly visible.

To analyse the performance of the system in terms of conversion efficiency and acceptance bandwidth, the DFG module is fed by both *pump* and *signal* operating in CW. This way, the pump laser (QPhotonics, Inc.) is biased to emit ~250 mW of optical power at 1064.25 nm while the *signal* output power of a DM laser (Eblana Photonics, Ltd.) emitting at 1538.63 nm is adjusted with the EDFA from 30 mW up to 770 mW (in both cases, including all optical losses). The beams are then incident into the grating with period of 29.98 μm of the bulk MgO:PPLN crystal mounted in a temperature-stabilized oven at 140.7 °C with the help of a collimator with a diameter of 1.6 mm and an achromatic focusing lens with 150 mm focal length. The Mid-Infrared *idler* beam at 3452 nm is then collimated by a 50 mm focal length calcium fluoride lens and filtered from the input Near-Infrared radiation with a germanium window with cut-off wavelength at 1900 nm prior to being focused on a thermoelectrically cooled mercury cadmium telluride (MCT)

photodetector (Vigo Systems, S.A) with an active area of 1 $mm^2$, sensitivity of 82 nW at 3.5 μm, and 3-dB cut-off frequency of ~180 MHz. The generated DFG power is then monitored with either a high-sensitivity thermopile or a chopper head and a lock-in amplifier. Figure 54 illustrates the linear dependence between the squared input power and the Mid-Infrared *idler* power with an average experimental conversion efficiency of 73 $\mu W/W^2cm$. This figure is rather lower than the manufacturer's specifications (200 $\mu W/W^2cm$ for an *idler* at 3.5 μm[348]), as the efficiency is mainly limited by the above-mentioned strong sensitivity of the conversion process to the relative overlap between both input beams.

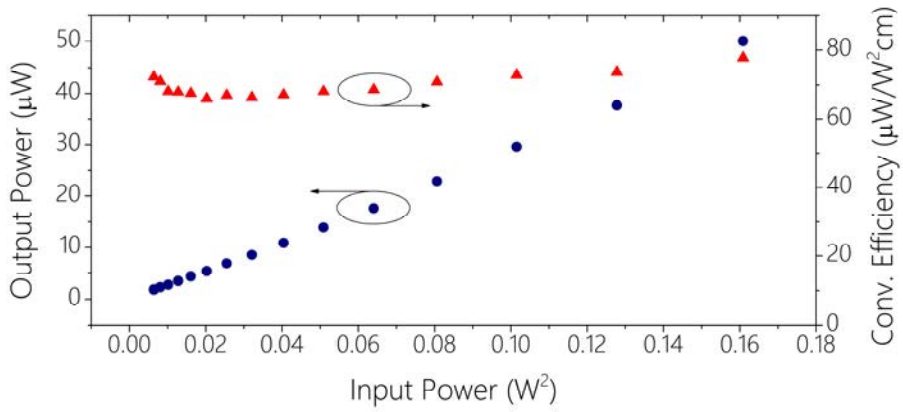


Figure 54. *Idler* output power as a function of the squared input power and estimated conversion efficiency of the bulk MgO:PPLN crystal employed in the experiment.

Particularly, for the presented instrument using optical fibre components and a single free-space arrangement, the calculated waist radii at the focusing point (assuming Gaussian beams) are 63.7 and 92.4 μm for *pump* and *signal*, respectively, which translates into focusing parameters $\xi$ of 1.68 and 1.16 (measured in air). Nonetheless, at the expense of lower conversion efficiency, the employment of a single-crystal arrangement dramatically lessens the complexity of the system, ensuring alignment-free coupling of the beams and reducing the free-space section to a single-pass Mid-Infrared generation process. In such a way, this layout features improved performance against environmental instabilities, for example, temperature-related misalignments or mechanical vibrations.

To assess the phase-matching bandwidth, the emission wavelength of the DM *signal* laser is tuned by acting on its temperature. All the parameters previously utilized to determine the conversion efficiency (*pump* input power and wavelength, temperature of the crystal, and selected poling period) remain unchanged with the exception of the *signal* input power, which is fixed at 500 mW. As depicted in Figure 55, the experimental bandwidth for the input *signal* has a FWHM in excess of 270 GHz. Clearly, the acceptance bandwidth imposes an

additional constraint on the accessible spectral coverage of the frequency combs for single-shot dual-comb spectroscopy. If bulk crystals are to be utilized with broad bandwidth OFCs (e.g., those based on Fibre Lasers), spectral stitching procedures become imperative to retrieve the full bandwidth of the comb.

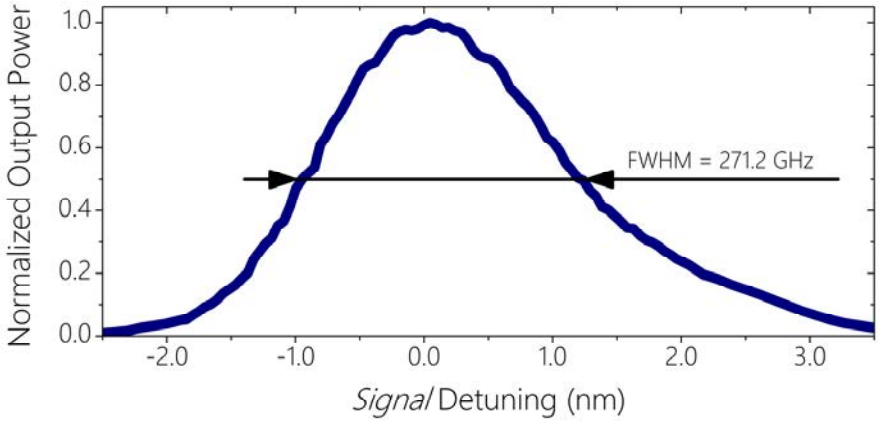


Figure 55. Phase-matching acceptance bandwidth for the grating with period of 29.98 μm at 140.7 °C. The length of the crystal is 40 mm.

Once the instrument has been statically characterized, its performance as dual-comb spectrometer is studied. Accordingly, two Near-Infrared *signal* OFCs are generated with a pair of EO phase modulators (EOSpace, Inc) in a classic fully-fiberized EO dual-comb arrangement whose central wavelength is that of the DM laser (1538.63 nm). In this case, the modulation frequency is $f_{REP}$ = 151 MHz and the frequency detuning $\Delta f_{REP}$ = 100 kHz. Both twin EOMs are fed by RF signals previously amplified with commercial off-the-shelf RF amplifiers up to a power level of 30 dBm. One of the combs is further frequency-shifted $f_{AOM}$ by means of an AOM (Gooch & Housego, Inc.) driven at 82.5 MHz with an RF input power of 24 dBm. The recombined Near-Infrared *signal* combs are then amplified in the EDFA up to 1.5 W and coupled into the WDM together with 300 mW of *pump* power. Both Near-Infrared sources are focused on the same poling period of the crystal (29.98 μm) at the same temperature (140.7 °C) under the same focusing conditions as before. These conditions allow for the production of up to 84 μW of DFG power.

The structure of the Near-Infrared OFCs is then transferred to the Mid-Infrared. The photodetection of these combs reveals the multiheterodyne beatnotes (RF comb) owing to the slight mismatch between their repetition rates, which are then displayed on an electrical spectrum analyser. In this case, the number of generated teeth of the RF comb and their power distribution has been dynamically controlled through the algorithm for two-modulator EO dual-comb modalities presented elsewhere[349]. A minimum number of 50 adjacent lines within a 20-dB bandwidth is addressed for the aforementioned $f_{REP}$ = 151 MHz. The

resultant RF comb generated is shown in Figure 56. More than 60 clearly resolved beatnotes are generated (with 50 of them within the 20-dB bandwidth) in the downconversion process with a 3-dB linewidth below the resolution of the instrument (1 Hz). The one-to-one correspondence represents an optical bandwidth of 9.2 GHz. Broader bandwidths could also be achieved at the expense of comb lines with reduced dynamic range. The average *idler* power per comb line is ~0.7 μW in each of the two combs, which is sufficient for high-sensitive absorption spectroscopy. Note that the delimited bandwidth of the EO frequency combs easily circumvent any constraint in relation to the phase-matching bandwidth without any significant loss of power.

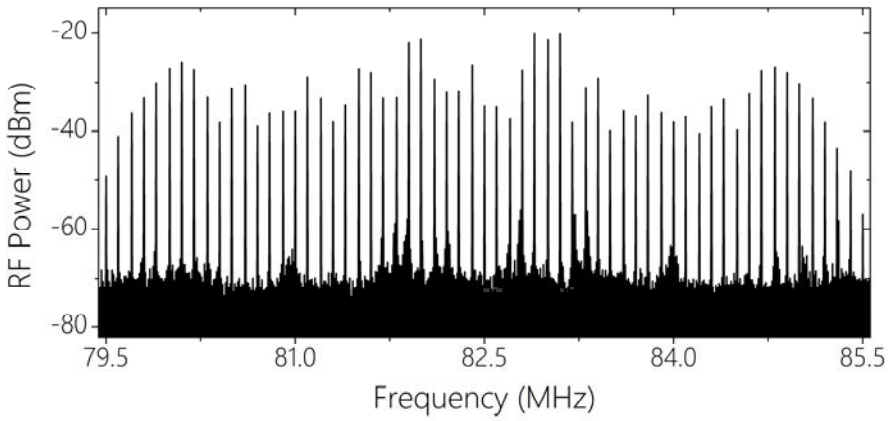


Figure 56. Illustration of the RF comb generated from the Mid-Infrared dual-comb signal impinged on the photodetector. The central line corresponds to the frequency-shift induced by the AOM (82.5 MHz) and the line spacing to the mismatch between the repetition frequencies of the combs (100 kHz).

## 2.3. Experimental Validation

The suitability of the instrument is tested by targeting the absorption feature of methane in the P(12) manifold of the ν3 band at 3451.87 nm (2896.98 $cm^{-1}$). To that end, a 5 cm single-pass cell filled with 1% $CH_4$ balanced with $N_2$ at 400 Torr at room temperature was placed in the *idler* beam path during the experimental tests without any additional modification in the EO dual-comb scheme and DFG module. The gas cell is installed in a custom-made flip mount, which allows for the easy and swift change between measurement ($CH_4$) and reference conditions (in the present experiment, ambient air is used as reference gas) in the *idler* combs' path.

To fully exploit the speed capabilities of the system, the frequency detuning between combs ($\Delta f_{REP}$) is increased to 2.5 MHz by rapid tuning of the RF electronic

settings of the EOMs without altering any of the features of the Mid-Infrared combs described in the previous sections. Therefore, the temporal trace refresh rate is squeezed down to $1/\Delta f_{REP}$ = 400 ns. Under these conditions, the time-domain signal is synchronously sampled at 5 GS/s with a fast oscilloscope (Rohde & Schwarz, Inc.) yielding up to 400 μs of integration time (or 2 × $10^6$ samples). The Fourier-transformation of the set of interferograms unveils an RF comb whose beatnotes are then processed to extract the information associated with every spectral point, in this case, the intensity. This method is employed in order to retrieve the spectral profile of the target absorption feature, as shown in Figure 57, where the ratio between a reference and a measurement of the gas is depicted. The dots represent the profile containing the amplitude-encoded information after an average of 100 interferograms over a total integration time of 40 μs. In comparison to the line parameters retrieved from the HITRAN database (solid line)[350], the experimental profile shows good agreement with the residuals, revealing a standard deviation of 1.23%.

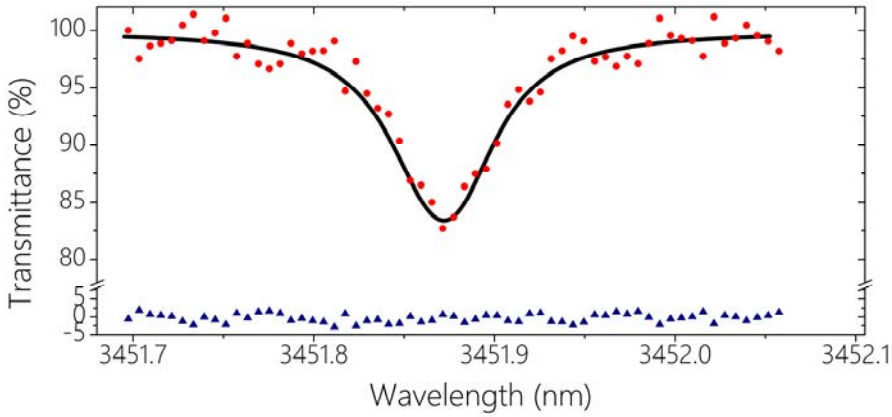


Figure 57. Experimental validation in the 3.5 μm region. The optical axis is recovered by upconversion from the RF axis. The red dots represent the trace of the measured transition of methane at 3451.87 nm in the P(12) manifold of the ν3 band for a measurement time of 40 μs. The solid line shows the spectrum calculated from the HITRAN database at the same pressure and temperature conditions. The residuals (blue dots) present a standard deviation of 1.23%, showing no systematic deviation.

The spectral SNR for each comb line is defined as the amplitude of every RF beatnote divided by its standard deviation when no gas sample is placed in the beam path. From this definition, we establish the SNR of the instrument as the average SNR over the whole set of lines of the RF comb. As can be seen in Figure 58, this value scales with the square root of the number of samples (or, similarly, with the integration time). The equivalent average SNR at 1 second integration time is 8.6 × $10^3$. From this value, the 3-sigma limit of detection (LOD) achievable is estimated as the concentration of methane that yields a signal equal to three times the standard deviation of the baseline. The trend of the minimum detectable

signal as a function of the integration time is also illustrated in Figure 58. From these values, the equivalent LOD of the instrument at 1 second and 1 metre absorption path is 1.05 ppm×m×$Hz^{-1/2}$ for $CH_4$ at 2896.98 $cm^{-1}$. It is also noteworthy that a quick extrapolation of this result to stronger absorption features of methane (for instance, in the Q branch) leads to a LOD in the region of ~100 ppb×m×$Hz^{-1/2}$. For a more instrument-specific comparison without reference to the target gas, the NEA is provided following the expression in (13). For the aforementioned SNR at 1 second integration time, an effective absorption length of 5 cm and 60 spectral elements, the resultant NEA is $3.0 \times 10^{-6}$ $cm^{-1}Hz^{-1/2}$.

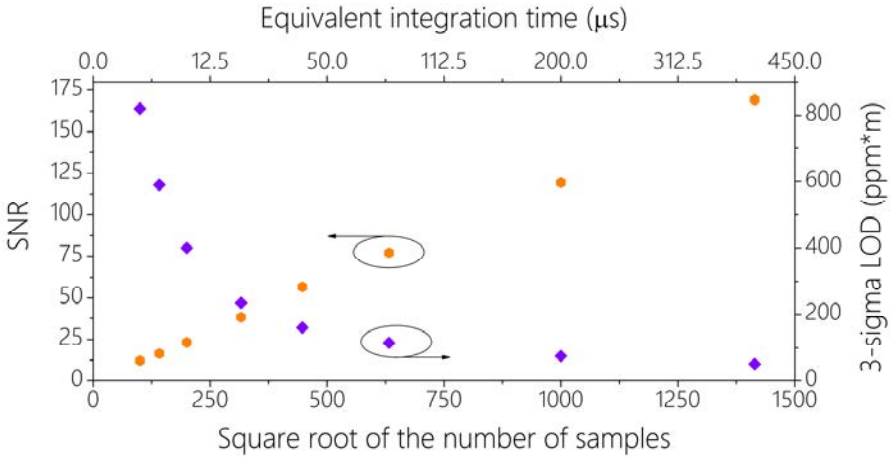


Figure 58. Evolution of the SNR and 3-sigma LOD (for the target absorption feature) as a function of the integration time. The SNR scales linearly with the number of samples, thus exhibiting the very high passive mutual coherence of EO dual-comb architectures.

# 3.

# New Prospects towards Mid-Infrared Dual-Comb Spectroscopy: Coherent Multiharmonic Signal Generation in Quantum Cascade Lasers

## 3.1. Description of the System and Principle of Operation

The approach for coherent multiharmonic signal generation is based on the direct modulation of the laser by means of a large RF signal that takes the device above and below threshold to create phase-locked sidebands, and therefore, a comb-like spectrum. The experimental setup is shown in Figure 59. A free-running DFB QCL is biased by means of a direct current and an RF modulating signal which are combined through a bias-tee. The RF component of the input signal is amplified to ensure that the laser is turned off and on within the same period of the signal. The output beam is split so the signal is simultaneously monitored with a FTIR spectrometer and an electrical spectrum analyser after heterodyning on a thermoelectrically cooled MCT photodetector (Vigo Systems, S.A).

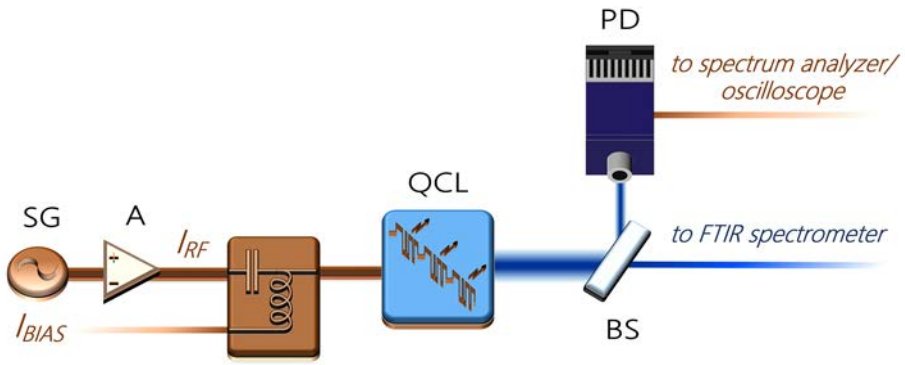


Figure 59. Coherent multiharmonic signal generation based on large-signal modulation in DFB QCLs. Experimental setup. A: Amplifier; BS: Beam splitter; PD: Photodetector; SG: Signal generator.

The QCL is a 3.2 mm long, 10 μm wide standard ridge-type, face-emitting DFB laser that exhibits a single-mode regime across the whole range of operation with emission wavelength in the vicinity of 7.58 μm (1320 $cm^{-1}$)[351]. In this case, prior to driving the laser with external modulation, the QCL is cooled down to 80 K to guarantee its operation in CW regime. Figure 60 (a) shows the copper mount with the electrical connections to which a batch of DFB QCLs (all of them with similar characteristics) are wired. This mount is attached to a metal tip that is then inserted into the cryostat. The emission spectra of one specific device from the collection of QCLs with threshold current ≈ 230 mA can be seen in Figure 60 (b).

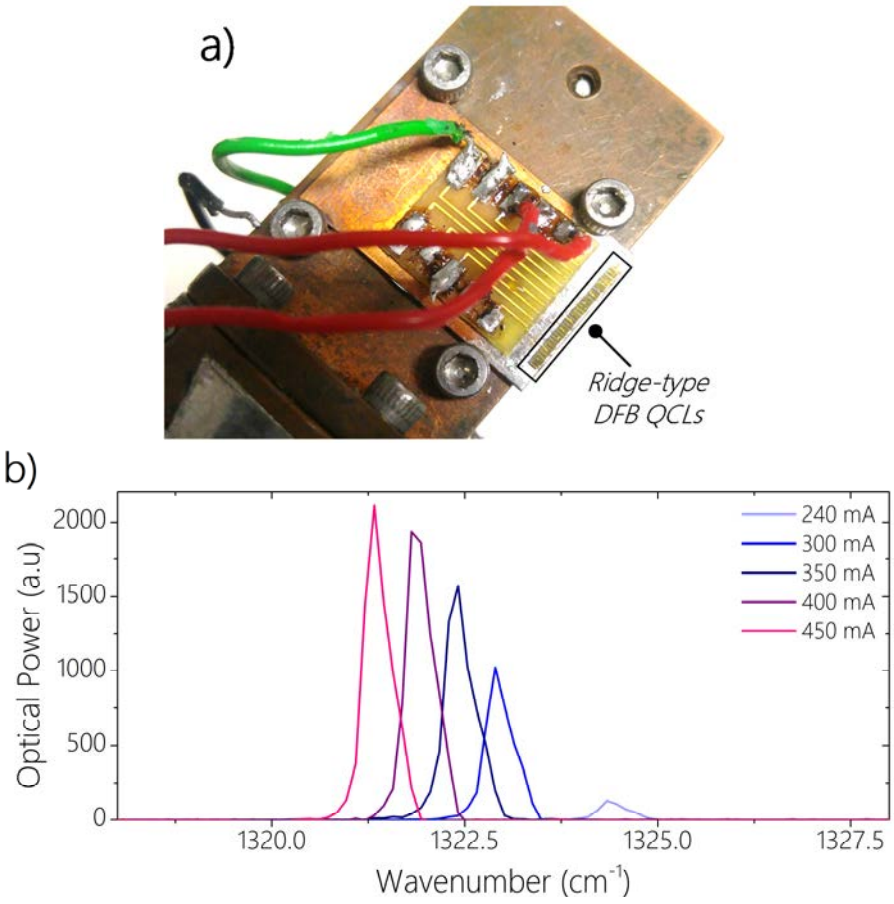


Figure 60. DFB QCLs used in the experiment. a) Illustration of the sample containing some of the ridge-type devices. b) Emission spectra under different bias current conditions of one of the DFB QCLs.

Unlike interband lasers, large-signal modulation in QCLs does not usually give rise to GS operation regimes which take advantage of the excitation of the first spike of the relaxation oscillations typical of second order laser-type systems. In the case of QCLs, these oscillations are overdamped due to carrier dynamics[60], making traditional pulse generation schemes challenging. Nevertheless, this on/off modulation may induce the laser device to respond in a nonlinear fashion leading to the broadening of the spectrum caused by the unveiling of sidebands whose line

spacing is precisely defined by the modulation frequency of the QCL. Figure 61 illustrates this effect on the single-mode DFB laser. Figure 61 (a) shows the time trace recorded after photodetection by means of a fast oscilloscope revealing the distortion of the temporal signal −which in this case resembles that of a regime of strong amplitude modulation[86]- while Figure 61 (b) depicts the envelope of the optical spectrum exhibiting a redistribution of the optical power across all the arisen lines in the spectrum. The sidebands are not visible due to the resolution of the spectrometer (0.2 $cm^{-1}$) but can be resolved after photodetection.

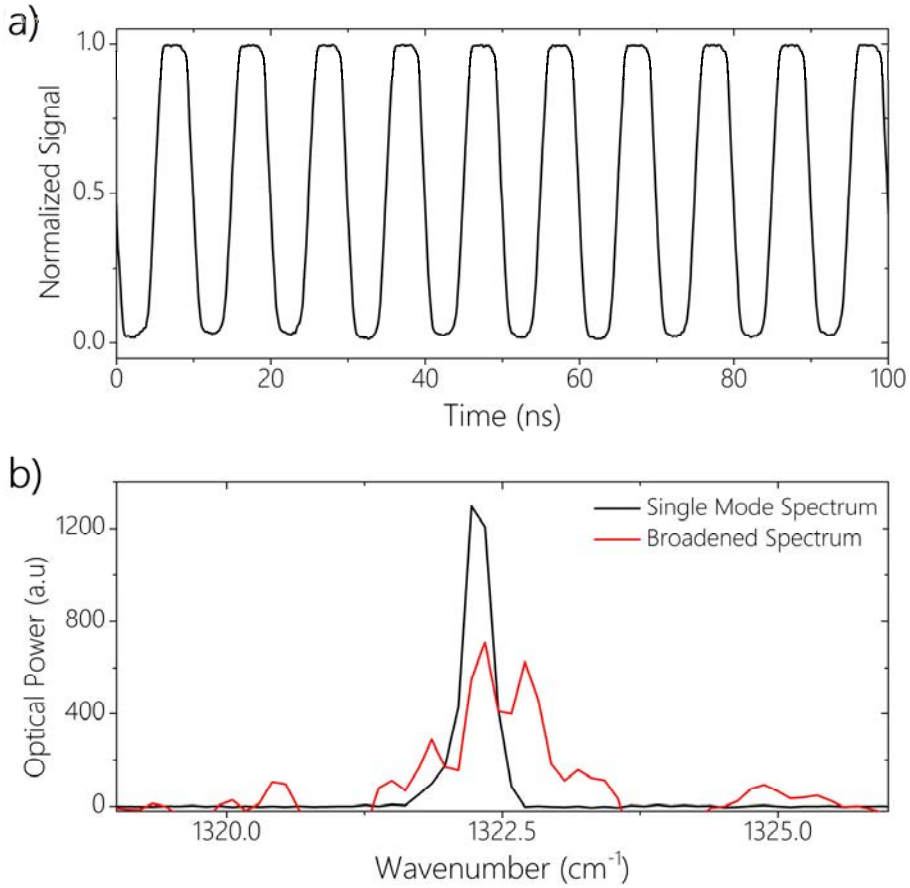


Figure 61. Illustration of the effect of large-signal modulation at 100 MHz on the DFB QCL. In this example, the parameters $I_{BIAS}/I_{TH}$ (bias current over threshold current) and $I_{RF}/I_{BIAS}$ (modulation current over bias current) were set at 1.2 and 0.2, respectively. a) Time-domain photodetector signal. b) Broadened optical spectrum recorded with a FTIR spectrometer with 0.2 $cm^{-1}$ resolution.

## 3.2. Experimental Results

The expansion of the optical spectrum is proven to be controllable through the set of parameters which determine the applied modulation conditions, namely the bias current of the laser, the modulation power and the modulation frequency

(or repetition frequency, since it determines the frequency spacing between the lines). Therefore, an experimental analysis of the parameters which influence the comb structure is performed in the QCL device and their impact on the resultant optical spectrum is assessed.

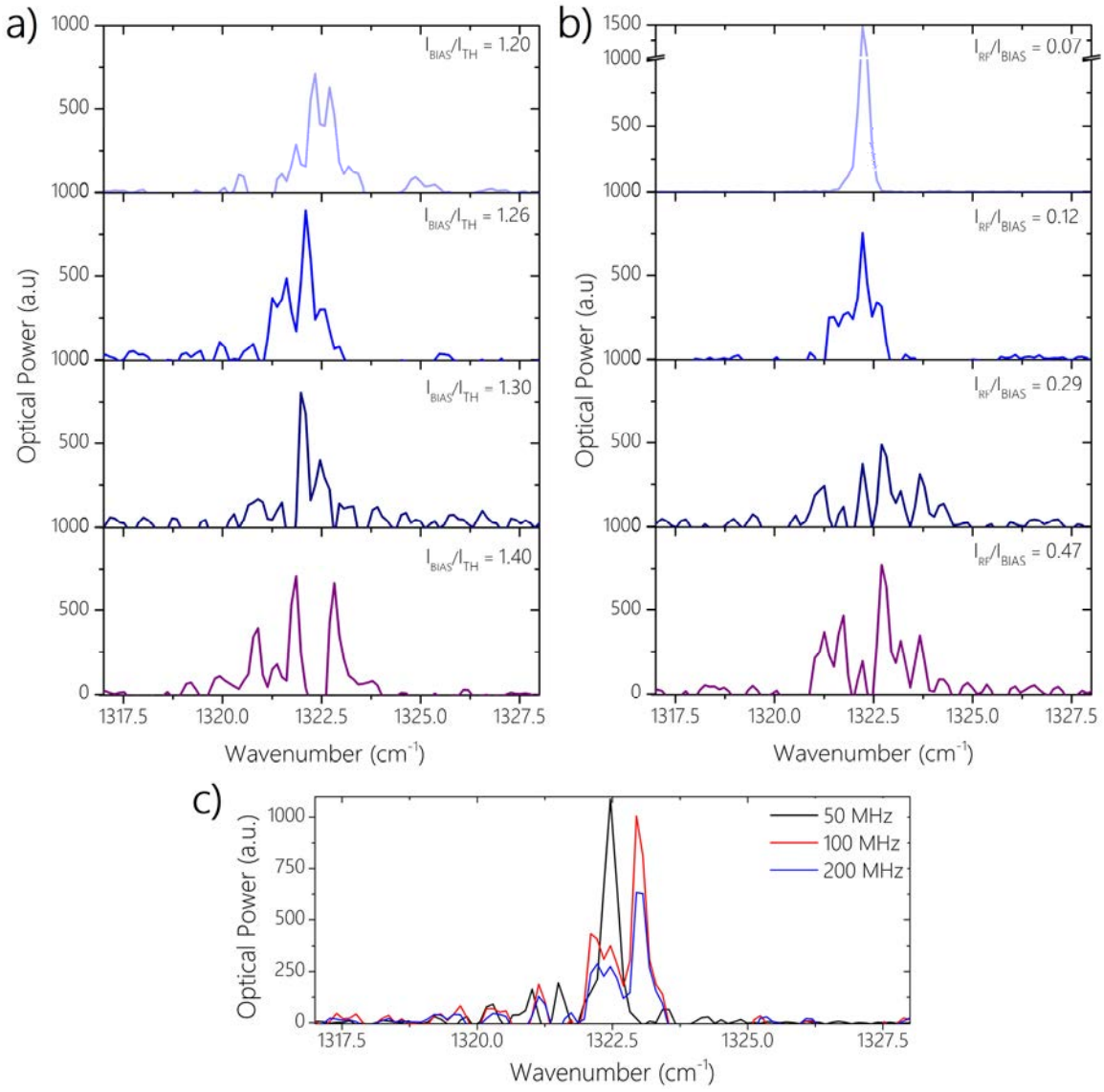


Figure 62. Evaluation of the expansion of the DFB QCL spectrum as a function of different driving conditions. a) Bias current analysis at 100 MHz repetition frequency and $I_{RF}/I_{BIAS}$ = 0.2. b) Modulation power analysis at 100 MHz and $I_{BIAS}/I_{TH}$ = 1.2. c) Modulation frequency analysis at $I_{RF}/I_{BIAS}$ = 0.4 and $I_{BIAS}/I_{TH}$ = 1.1.

Figure 62 depicts this effect in different scenarios, where it is visible the way the power spreads across the lines and therefore, the significant change of the envelope of the resultant spectrum. In general, there is reasonable agreement with the typical behaviour of laser diodes under regimes of large-signal modulation[27]. Particularly, Figure 62 (a) illustrates the effect of modifying the bias current of the laser for a fixed external modulating signal. The results are normalized to the

threshold current of the laser. On the other hand, Figure 62 (b) details the evolution from a single-mode-like spectrum when the modulation power with respect to the bias current is too low to an enlarged, widened spectrum as the power gradually increases. Again, this behaviour is consistent with the large-signal modulation regime, where a larger modulation depth translates into a wider comb-like optical spectrum. In Figure 62 (c), a comparison between three different modulation frequencies is also shown, revealing the influence of this parameter on the optical spectrum. In agreement with the trend in this type of modulation regime, a higher modulation frequency results in optical spectra with wider spans and more complex structures when the modulation frequency increases within the modulation bandwidth of the laser device. A further comparison with upper frequencies was not performed due to the limited bandwidth of the detector (~180 MHz). It is important to note that no analysis of the frequency response or optimization of the comb operation of the device was realized, as the purpose of this analysis is to illustrate the impact of this set of parameters on the final multiharmonic signal, which can be conveniently selected in order to generate a suitable signal for the application of interest.

In order to better understand the structure of the resultant optical spectra, especially when the resolution of the spectrometer is insufficient, an analysis of the electrical signal after downconversion from the optical to the RF domain needs to be carried out. For that purpose, the aforementioned MCT photodetector and an electrical spectrum analyser are employed. The outcome of this analysis can be seen in Figure 63. Numerous beatnotes, equally-spaced at the multiples of the modulation frequency of the laser are clearly visible even beyond the roll-off frequency of the photodetector. They originate from the recombination of all the optical lines which were not previously resolved because of the resolution of the spectrometer. Figure 63 (a) and (b) shows the resultant spectrum in the case of two different repetition frequencies of study (100 MHz and 50 MHz) for a specific pair of parameters $I_{RF}/I_{BIAS}$ and $I_{BIAS}/I_{TH}$. Further experiments with different values of these ratios and modulation frequencies were also realized leading to slight changes in either the amplitude of the beatnotes or the noise floor. However, no fluctuations of the lines were observed in the frequency domain and the beatnotes rigidly remained at multiples of the repetition frequency. Despite the limited bandwidth of the detector, this technique clearly shows that the generation of equally-spaced sidebands neighbouring the excited mode of the cavity is feasible.

Finally, the linewidth of the beatnotes is also assessed and compared with that of the original signal from the employed RF generator (see Figure 63 (c)). For a repetition frequency of 100 MHz, a 3-dB linewidth in the sub-hertz region is

obtained (this value is limited by the resolution of the instrument −1 Hz-). This very narrow beatnote is also observed for different operating conditions and multiples of the modulation frequency (higher order beatnotes), an indicator of high phase correlation between the teeth of the multiharmonic optical signal.

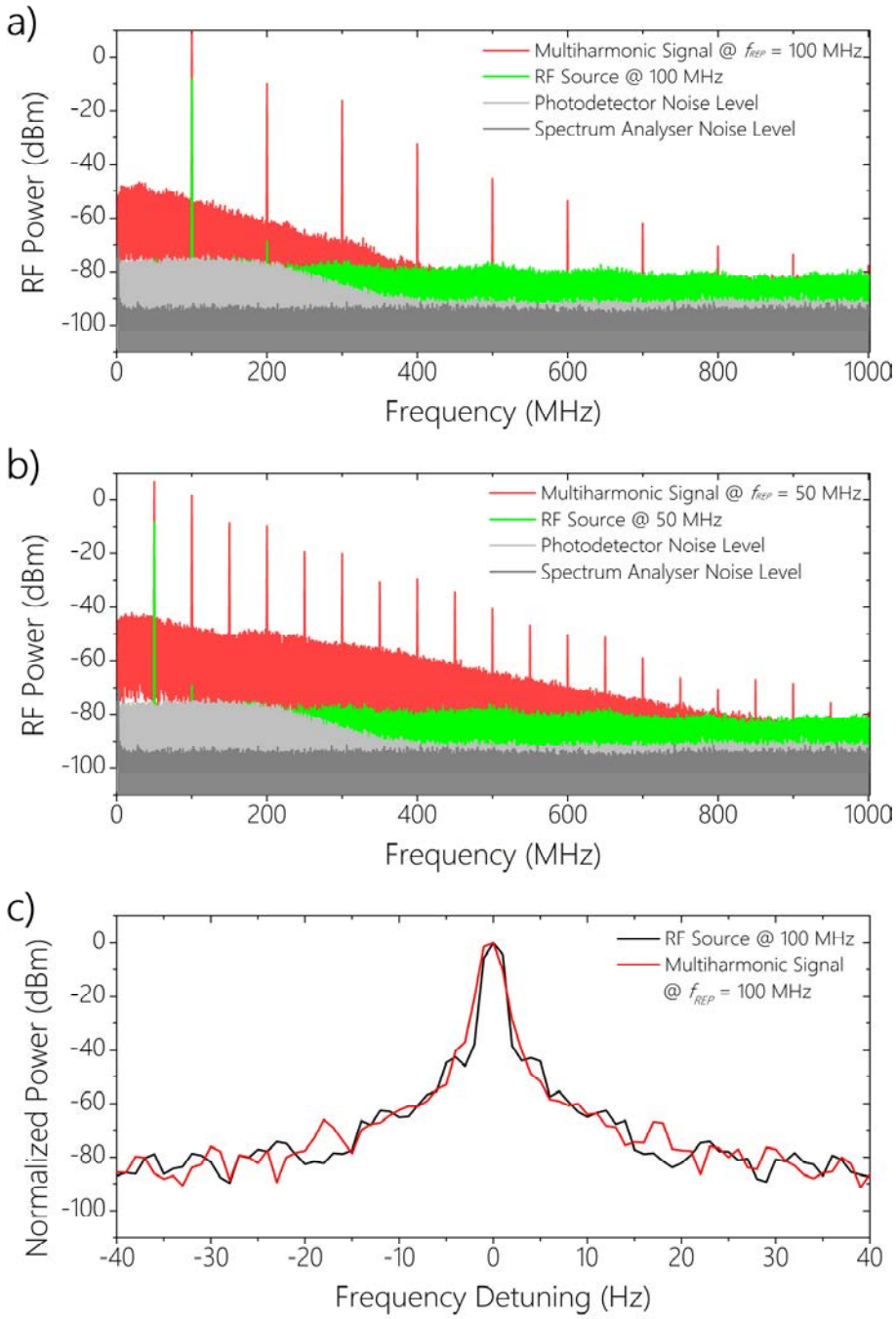


Figure 63. Evaluation of RF spectra after photodetection of the modulated optical signal. In this case, the QCL at $I_{RF}/I_{BIAS}$ = 0.2 and $I_{BIAS}/I_{TH}$ = 1.2 is modulated at (a) 100 MHz and (b) 50 MHz. For comparison purposes, the noise level of the instrument and photodetector are included in the plots together with the spectrum of the modulating signal provided by the RF generator used in the experiment. c) Comparison between the RF signal and the multiharmonic signal beatnote at the same modulation frequency (100 MHz).

# 4.
# Discussion of the Results

In this chapter, two methods for the effective extension of the dual-comb principle towards Mid-Infrared have been introduced. To serve this purpose, some of the most conventional techniques and sources of the state-of-the art have been conveniently utilized to create synergies that have helped to expand the current range of available mechanisms to implement dual-comb spectrometers. Particular stress has been laid on the implementation of easy-to-operate systems that allow for the external customization of the main optical parameters.

First, an instrument that incorporates a simplified single-crystal DFG module allowing for the rapid frequency-shifting of EO dual-combs into the Mid-Infrared region has been introduced. The system features adequate power per comb line and intrinsically uncomplicated wavelength-tuning capabilities without sacrificing any of the virtues of EO dual-comb architectures. Moreover, the use of QPM nonlinear crystals offers additional control over many design parameters and capabilities of the Mid-Infrared source. Altogether, the presented tool exhibits straightforward access to the fingerprint region with complete adaptability to the target spectral feature. Furthermore, since the gas sample under test does not take part in the setup, the system features distinctive robustness to environmental conditions. The performance of the system has been validated by recovering the absorption profile of the molecular transition of methane at 3451.87 nm (2896.98 $cm^{-1}$) with high fidelity within tens of microseconds, resulting in an equivalent sensitivity of ~1 ppm×m in 1 second.

Beyond the basic architecture, the modular nature of the instrument paves the way for incorporating the range of advancements associated with EO architectures and DFG systems. In the latter respect, it is important to remark on the new and exciting possibilities offered by waveguide nonlinear crystals with

improved efficiency (~20% $W^{-1}$ in the case of PPLN)[352] or new semiconductor nonlinear crystals with higher nonlinear coefficients and increased transparency deeper in the Mid-Infrared that can also be fed by EO dual-combs at 1.5 μm, such as OP-GaP[353]. In any respect, the robustness of telecom-grade fibre-coupled components and the versatility of EO dual-combs and QPM nonlinear crystals endows the instrument with improved reliability and user-friendly operation. Besides, the small footprint on which it can be implemented (in this case, all fibre-coupled components easily fit in a 19'' rack module, while the free-space module covered an area of 250 $cm^2$) certainly offers new prospects for the gradual standardization of table-top, lightweight Mid-Infrared dual-comb platforms beyond laboratory environments.

Accessing the Mid-Infrared portion of the electromagnetic spectrum to probe the properties of matter with instruments that exhibit outstanding features in terms of resolution, sensitivity and speed of operation is crucial for an increasing number of applications. Atmospheric monitoring, characterization of complex biochemical molecules, non-invasive medical diagnostics or real-time control of industrial processes are some examples of applications that may take advantage of an EO dual-comb spectrometer. With a finite number of commercial components, it is possible to implement a compact EO dual-comb spectrometer with tailor-made capabilities and sufficient optical power in the 3 μm spectral region, which contains fundamental structural information of hydrocarbons. In return for a moderate number of spectral elements, these arrangements enable single-shot acquisitions at ultra-fast measurement rates. In this sense, one can envision that the monitoring of transient chemical reactions (such as the ones found in processes of combustion) or real-time control of gas leaks, for security purposes or environmental studies, may profit from the flexibility and ultra-fast capabilities of the presented architecture.

Second, an experimental study has unveiled a new approach for comb generation in QCLs. The large-signal modulation of QCLs above and below threshold is demonstrated as a viable method to create a well-defined series of evenly-spaced lines. The effect of the external modulation on the spectrum of a DFB laser has been studied, showing that an expansion of the initial spectrum occurs while preserving a stable phase relationship between the comb teeth, as the multiharmonic beatnotes reveal. The line spacing can be readily tuned by changing the modulation frequency and the high-speed capabilities of QCLs might extend the potential modulation bandwidth up to tens of GHz[354]. It should be stressed that QCL-based OFCs have until now relied on tailored, dispersion-compensated designs with severely restricted tuning capabilities and mode spacings of GHz,

which are usually mismatched to perform spectroscopy of small molecules. In this context, the suggested method provides QCL-OFCs with a level of versatility that may render them well-suited to fill the existing gap for high-resolution (Figure 27), species-specific spectroscopy with these sources.

This experiment is the only original contribution of the author to this Ph.D work that does not comprise a dual-comb detection method. In order to do so, there are a number of considerations that must be borne in mind which are mainly related to the reconstruction of mutual coherence between a pair of free-running QCLs. The first step would involve the stabilization of the repetition frequencies of the OFCs, a task which may be straightforwardly realized by referencing both RF modulation signals to a common time base. The more stringent requirement is set by the cancellation of the random fluctuations of the QCLs central frequencies. Short-term mutual coherence can be accomplished with the assembly of both devices on the same chip[128], but if this is not the case, other rather simple methods such as all-electrical feedback control of the injection current[257] or optical phase-locked loops[259] have also proven to be effective to perform dual-comb spectroscopy with QCLs. Pure computational phase correction algorithms may also constitute an elegant alternative to physical locking mechanisms. However, their application has hitherto been confined to QCL-based dual-combs with line spacings in the order of tens of GHz[262]. Hence, the outcome of this procedure may be rather unexpected when applied to combs with repetition frequencies of MHz. Finally, OIL also represents an innovative approach to establish mutual coherence between combs, as introduced in the works detailed in Chapter III of this thesis. In a similar fashion to GS-OIL-based dual-comb interferometers, a third QCL that simultaneously injects both QCL-based OFCs may be incorporated to the setup. Still, the need for a supplementary stabilization setup to ensure proper injection locking in only one of the closely-spaced lines of the OFCs and the additional complexity derived from the implementation of a free-space injection locking mechanism renders this alternative highly impractical in comparison to the previous methods.

# V

# Contributions to Dual-Comb Spectroscopy in the sub-THz and THz Region

# 1.
# Introduction and Motivation

The fifth chapter of this dissertation will be devoted to the extension of the author's work in dual-comb spectroscopy towards the sub-THz and THz regions. This purpose will be successfully accomplished by means of a novel system that seamlessly integrates several of the principles and techniques for comb generation and synchronization that have been already discussed in the previous chapters of this document.

Following the overall trend of this research work, the main motivation for the development of dual-comb architectures in this range of frequencies is the possibility of spreading the potential of EO-OFCs in a region that has hitherto been monopolized by bulky and elaborate setups based on MLLs with only a few recent demonstrations with THz QCL-based combs that still need to overcome a number of technical challenges for their widespread adoption. The selected approach for the synthesis of THz combs will be the optical downconversion of coherent multimode signals based on OIL and EO modulation in a photomixer. Succinctly, an optical line of a *master* frequency comb will serve as the seed to electro-optically generate a pair of new OFCs which will be photomixed with another coherent line from the same original *master* comb in order to generate a narrow-linewidth terahertz dual-comb with teeth frequencies that can be readily referenced to an RF standard. The main implications and limitations of this approach will also be exhaustively discussed. The system is validated with the measurement of the transmission response of a microwave filter in the W-band. Additional details of this work are reported in the manuscripts [M6], [C4], [C5] and [C6] tabulated in the list of scientific contributions of the author.

# 2.

# Absolute THz Dual-Comb Spectroscopy based on Electro-Optic Modulation

## 2.1. Description of the System

The operating principle of the electro-optically synthesized THz dual-comb spectrometer is based on the generation of THz waves from multimode optical signals (in this case, OFCs). For this purpose, the key requirement is that the optical span of a specific comb must be broad enough to cover the THz range, as the THz signals will be produced from two of its teeth. The scheme of the system and the downconversion process across frequency domains are illustrated in Figure 64. In the present approach, the starting point is a Near-Infrared *master* EO-OFC, in which two modes that are separated $f_{THz}$ (which is an exact multiple of the repetition frequency of the *master* comb) are filtered through OIL. One of the selected modes acts as reference tone for the THz generation, whereas the other mode is used as seed for dual-comb generation. To this end, the latter is split into two paths to be electro-optically modulated at marginally different frequencies ($f_{REP}$ and $f_{REP} + \Delta f_{REP}$). Additionally, one of these combs is frequency-shifted $f_{AOM}$ by an AOM to later resolve the symmetric appearance of the dual-comb and ensure the unique frequency-mapping of the downconverted combs. Each of the two OFCs is then mixed with the reference tone in a photodetector to create the THz dual-comb. The central frequency of the THz dual-comb is thus exactly given by the difference frequency of the two modes previously selected from the *master* OFC and the frequency-shift of the AOM (i.e., $f_{THz}$ and $f_{THz} + f_{AOM}$), while the line spacing is transferred from the optical domain (i.e., $f_{REP}$ and $f_{REP} + \Delta f_{REP}$).

It is important to remark on the fact that the main parameters of the THz combs (i.e., their characteristic frequencies defined according to $f_{THz}$, $f_{REP}$, $\Delta f_{REP}$ and $f_{AOM}$) are purely electronically governed by a number of oscillators locked to the same common RF reference, which ultimately fixes the accuracy of the synthesized THz dual-comb. Furthermore, the use of a common *master* source and a technique such as OIL, which allows the *slave* lasers to inherit the phase coherence of the injecting source (in this case, the *master* OFC), provides the system with an ultra-high degree of mutual coherence.

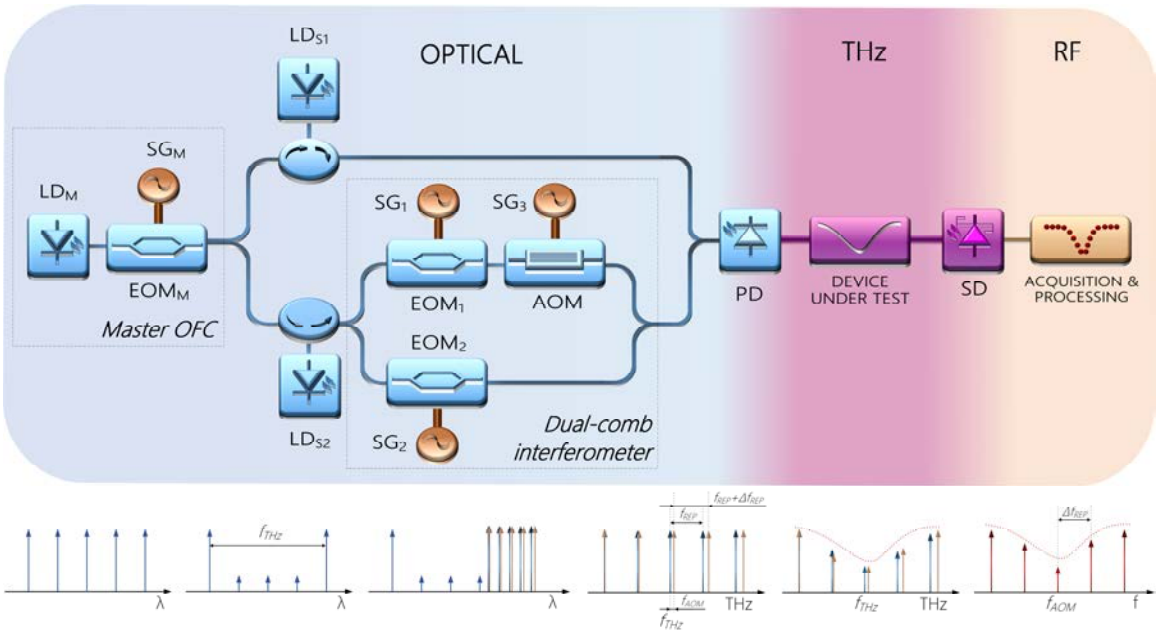


Figure 64. Experimental setup (top) and sketch of the generation process (bottom) of the electronically synthesized THz dual-comb (see text for details). LD M/S: Laser diode (*master/slave*); PD: Photodetector; SD: Schottky diode; SG: Signal generator.

The THz dual-comb is then transmitted through a device under test (in this case, a microwave filter) that inscribes its spectral response into the combs. Finally, both THz combs are overlapped on a Schottky diode, triggering a multiheterodyne process that gives rise to the final RF comb, which exhibits a central frequency defined by the offset frequency between the THz combs (i.e., $f_{AOM}$) and a line spacing equal to the mismatch between their repetition rates (i.e., $\Delta f_{REP}$). The time trace of this downconverted comb can then be readily acquired and processed via Fourier-transformation or multi-channel lock-in detection to simultaneously reveal the spectral information encoded into each of the teeth of the THz dual-comb.

## 2.2. Characterization

The THz EO dual-comb approach involves signals which are processed in three different spectral regions. The optical domain section is fully-fiberized. First, a CW DM seed laser emitting at 1542.5 nm laser (Eblana Photonics, Ltd.) is used in conjunction with two cascaded EO phase-modulators (EOSpace, Inc.) in order to produce a *master* OFC. The same amplified RF signal (with a power of 32 dBm) is used to drive both EOMs with freely selectable frequencies. A phase shifter is also included to match the phase of the input RF signals for optimal comb generation. With the *master* OFC as frequency reference, two of its optical teeth are selected. To that end, the *master* OFC is split and injected into a pair of CW DFB *slave* lasers (QPhotonics, Inc.) whose emission wavelength (centred at 1543 nm) can be tuned into the proximity of the *master* comb lines of interest by acting on their current and temperature to adjust the central dual-comb frequency $f_{THz}$. Two identical circulators are used to route the output light of the injected *slave* lasers. The OIL mechanism is further optimized by adjusting the injection ratio (and hence, the locking range) with variable optical attenuators (not shown in Figure 64), resulting in an output power of ~10 mW for each *slave* laser. A representative sample of a *master* comb with a 20-dB span of ~0.95 THz with two of its lines filtered by the *slave* lasers can be seen in Figure 65.

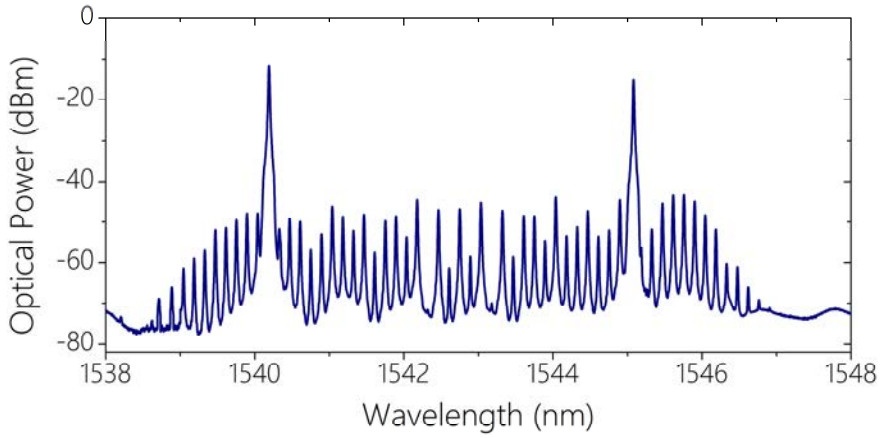


Figure 65. Optical domain spectrum. *Master* OFC including the filtered modes by way of OIL with the *slave* lasers. In this example, $f_{THz}$ = 0.612 THz.

The light coming from one of the OIL stages is afterwards employed as the embryo of an EO dual-comb by dividing its optical power into two paths (as in classic EO dual-combs arrangements). Two EOMs (similar to the one taking part in the *master* OFC) generate a pair of combs with repetition frequencies of $f_{REP}$ = 100 MHz and $f_{REP} + \Delta f_{REP}$ = 100.1 MHz, with the latter being further shifted in frequency

$f_{AOM}$ = 40 MHz by means of an AOM (Gooch & Housego, Inc.). The RF signals that feed the EOMs and the AOM are previously amplified up to 30 and 24 dBm, respectively. The result of the combination of the first reference line and the two combs generated out of its counterpart (not resolved because of the resolution of the spectrum analyser −0.02 nm-) is depicted in Figure 66 (a) for a $f_{THz}$ = 96 GHz.

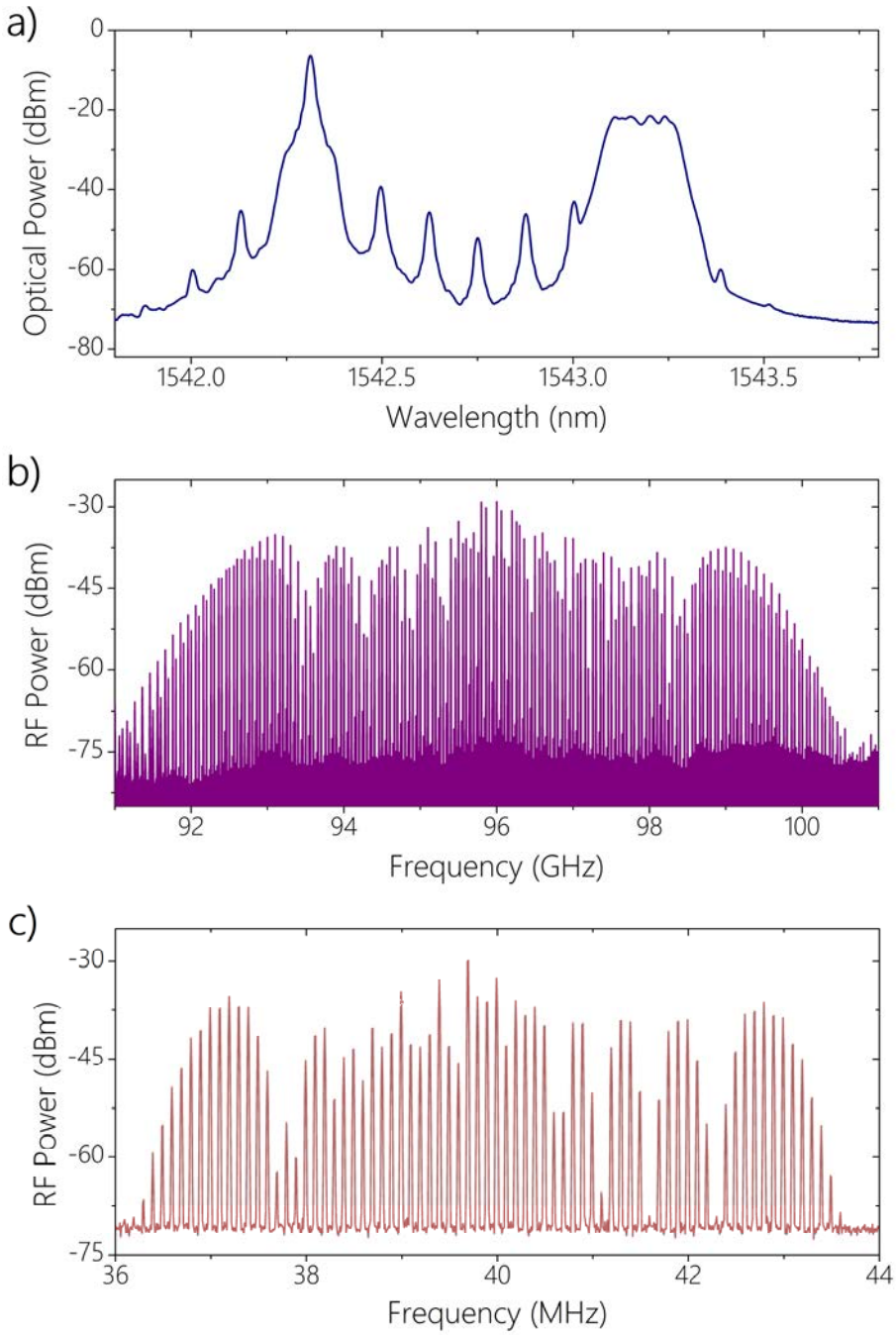


Figure 66. Downconversion process from the optical region down to the THz and RF domains. Here, $f_{THz}$ = 96 GHz, $f_{AOM}$ = 40 MHz, $f_{REP}$ = 100 MHz and $\Delta f_{REP}$ = 100 kHz. The optical dual-comb (a) is generated from one of the *slave* lasers (in this case, the red-shifted one) whose lines are not resolved due to the resolution of the spectrum analyser (0.02 nm). After photomixing, first the THz dual-comb (b) and then the downconverted RF comb (c) are displayed on an electrical spectrum analyser.

In order to access the THz region, the optical amalgam of signals is mixed using a fast photodiode (u2t Photonics, Inc.) with a 3 dB-bandwidth in excess of 110 GHz. With 10 mW of input power regulated by means of a variable optical attenuator, a pair of interleaved OFCs are generated in the THz domain with line spacings of 100 and 100.1 MHz and central frequencies of 96 GHz and 96.04 GHz, respectively. Figure 66 (b) illustrates the pair of interwoven THz combs generated under these conditions. The final downconversion process takes place when the THz combs are overlapped on a Schottky diode (RPG-Radiometer Physics GmbH) with bandwidth between 90 and 180 GHz. The THz signals are transferred from the output of the photodetector using a proper adapter that enables convenient transmission of the waves into the WR-06 waveguide interface of the Schottky diode. After RF amplification, this multiheterodyne downconversion reveals the structure of the final RF comb subject to analysis (see Figure 66 (c)) whose central frequency corresponds to the frequency-shift induced by the AOM (40 MHz) and the line spacing to the mismatch between the repetition frequencies of the combs (100 kHz).

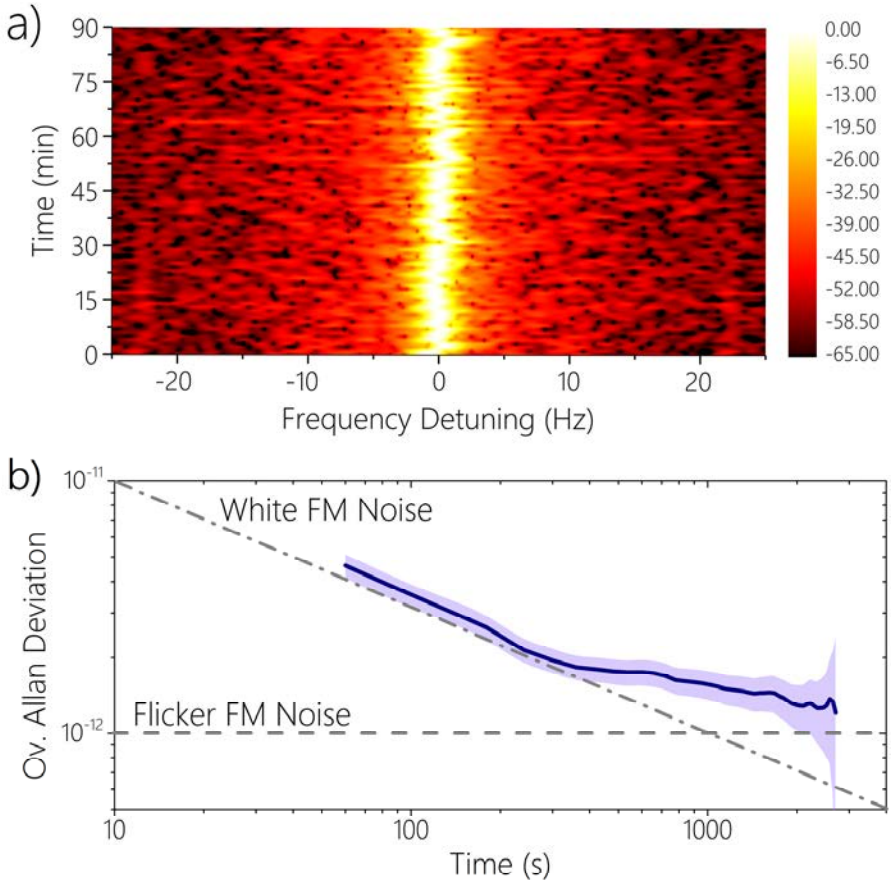


Figure 67. Evaluation of the performance of the EO THz dual-comb. a) Long-term stability analysis of the comb tooth at 95.9 GHz over 90 minutes in steps of 1 minute (the vertical bar on the right side indicates the normalized electrical power in dBm). b) Overlapped Allan deviation (blue trace) of the fractional frequency of the signal at 95.9 GHz and error region (purple trace).

The performance of the system is assessed with the analysis of the linewidth and the long-term stability of one of the lines of the THz dual-comb. When the injection locking mechanism remains stable, $f_{THz}$ is exclusively determined by the frequency separation between the pair of *slave* lasers that filter out the lines of the *master* OFC, which is simply a multiple of the repetition frequency of the latter. In this system, all RF signals driving the EOMs and AOM are locked to the internal reference standard (an oven-controlled crystal oscillator) of a multichannel RF synthesizer (Holzworth Instrumentation, Inc.) with an accuracy of $\sim 10^{-8}$. Under these conditions, the line at 95.9 GHz in Figure 66 (b) is monitored over a period of 90 minutes. The results can be seen in Figure 67 (a), where no drift above ±2.5 Hz is visible. The 3-dB linewidth of the beatnote is below the resolution bandwidth of the spectrum analyser, which is a clear indicator of the high mutual coherence of the system. This behaviour was observed across all the lines of the narrowband THz comb; however, broader linewidths are expected for higher-frequency THz signals and wider bandwidths due to the scaled phase noise of the RF synthesizer. The frequency stability is also studied through the Overlapped Allan Deviation (see Figure 67 (b)), showing a type of noise between white FM and Flicker FM[339].

## 2.3. Experimental Validation

The THz EO dual-comb architecture is validated with the measurement of the transmission spectrum of a microwave filter with cut-off frequency of 97.35 GHz (MI-Wave, Inc.). For that purpose, a THz dual-comb similar to the one shown in Figure 66 (b) but centred at 98 GHz is used to probe the sample in a collinear arrangement. Figure 68 exhibits the part of the experimental setup devoted to the generation and detection of the THz combs (photodetector and Schottky diode) as well as the microwave filter employed as device under test.

In this scenario, the train of interferograms transmitted by the Schottky diode with a refresh rate of $1/\Delta f_{REP}$ = 10 μs is synchronously sampled at 5 GS/s, supplying up to 400 μs of integration time. The Fourier-transformation of this signal unveils the structure of the RF comb, from which the spectral information associated with every frequency marker (in this case, the intensity) is obtained. Then, each RF beatnote is directly assigned to the corresponding absolute frequency of the THz comb. Following this procedure, the recovered transmission profile is depicted in Figure 69 (the signal when no filter is placed in the THz signal path is used as reference for normalization purposes) along with the data provided by the manufacturer. The dots represent the measured response of the filter after

coherently averaging 40 interferograms in 400 μs, showing reasonable agreement with the expected profile. The spectral SNR is again defined as the ratio of the amplitude of every RF beatnote to its standard deviation when no sample is placed. For the aforementioned integration time, the SNR averaged over all the lines of the RF comb is 102. The normalization of this value for a standard integration time of 1 second and the number of spectral lines ($M$ = 75)[112] yields a figure of merit of $SNR \times M$ of $3.83 \times 10^5$.

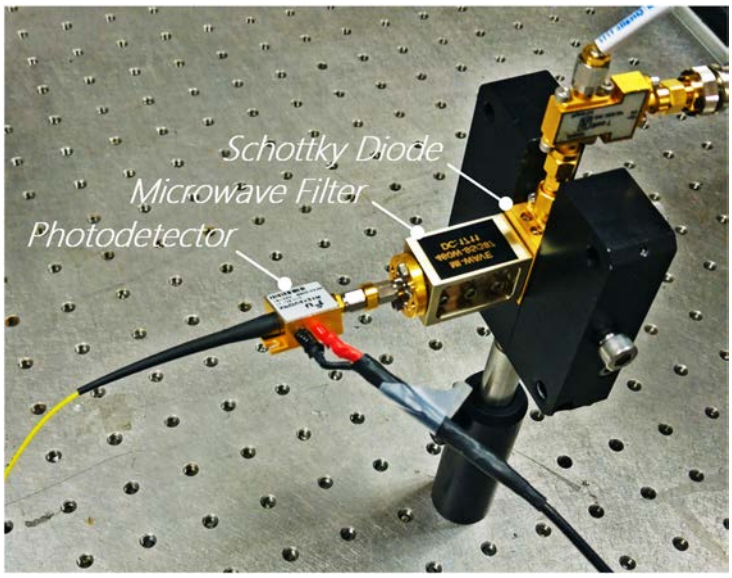


Figure 68. Detail of the experimental setup used for generation and detection of the THz dual-comb including the microwave filter used for validation purposes.

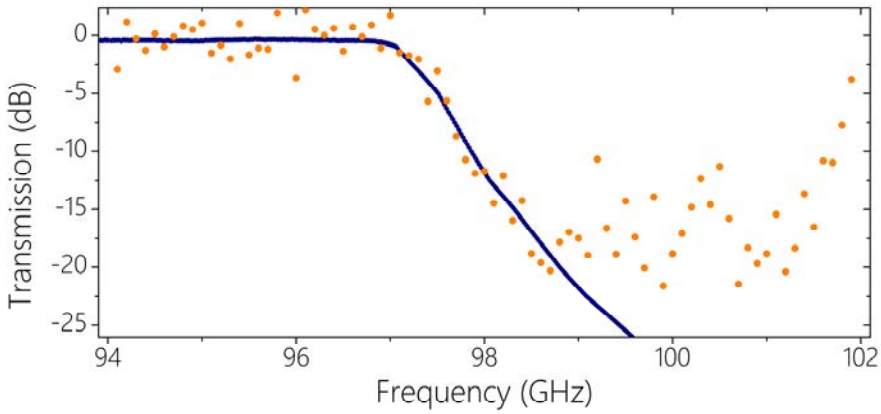


Figure 69. Transmission spectrum (dots) of the microwave filter when sampled with the THz dual-comb for an integration time of 400 μs. The solid blue line indicates the frequency response of the filter specified by the manufacturer. The grey shaded area portrays the range of frequencies where the attenuation of the filter is greater than the amplitude of the RF teeth; hence, their dynamic range is insufficient to resolve the spectral information.

# 3.

# Discussion of the Results

This chapter has presented a new architecture devised to realize absolute dual-comb spectroscopy in the THz range based on photonic synthesis and EO modulation. In a similar fashion to the work introduced in the fourth chapter of this dissertation for the Mid-Infrared region, this approach takes full advantage of well-established techniques and sources to extend the applicability of EO dual-comb architectures beyond the Near-Infrared.

The proposed approach harnesses the use of OIL and coherent multimode sources in the optical domain to synthesize ultra-narrow linewidth THz frequency combs in a photomixer with a level of accuracy only determined by the RF standard employed. The method also features the range of virtues associated with EO dual-comb setups, with absolute control over both central and repetition frequencies of the THz combs (i.e., resolution and measurement speed), as well as very high mutual coherence with the simplicity and robustness typical of commercially available off-the-shelf fibre-coupled components. Unlike other demonstrations, the potential of this approach lies in the fact that all parameters defining the frequencies of each single THz dual-comb mode not only can be arbitrarily chosen but also directly referenced to an RF standard, which leads to superior capabilities in terms of accuracy and stability. This is in clear contrast to the demonstrations of THz dual-comb systems that have been reported so far (those based on MLLs and THz QCLs), which suffer from inherently weak tuning capabilities of the frequency comb parameters. Besides, as these designs rely on the generation of two independent THz combs, elaborate locking schemes or digital post-processing algorithms are commonplace methods to reconstruct the coherence between OFCs and to ensure a high level of accuracy for frequency traceability.

The architecture is successfully validated with the retrieval of the transfer function of a microwave filter in the W-band in a sub-millisecond timescale. With further development, it can be readily scalable up to the THz region if the limitations concerning the achievable bandwidth are addressed. In this sense, there are a number of aspects that need to be borne in mind:

- The bandwidth of the *master* OFC. First and foremost, the span of the optical domain signal used as reference to synthesize THz signals must extend into the THz range. In these systems (i.e., based on EO-OFCs), the most usual methods resort to cascading additional EOMs or nonlinear fibres to widen the span of the *master* OFC, but there are other methods (already reviewed in Section 2.2. of the first chapter of this dissertation) that can also be found in the literature.

- The emission wavelength range of the *master* OFC and the *slave* lasers. In a general sense, the pair of employed *slave* lasers need to be tunable enough so that they can be injected by two teeth of the *master* comb separated by a certain frequency in the THz range.

- The signal quality due to phase noise. The noise of the heterodyne signals between teeth of the *master* OFC that produce the THz radiation is expected to scale due to the multiplicative phase noise of the reference RF generator feeding the EOM that creates the sidebands of the OFC. This way, it is essential to employ a reference synthesizer featuring low noise if one intends to beat distant lines of the *master* OFC to synthesize good-quality signals in the THz region[355]. Of course, the same reasoning can be applied to the THz combs that are used to probe the sample or device under test; however, if they are narrowband, this effect can be overlooked in practical terms.

- The THz generation and detection scheme. This is, undoubtedly, the most stringent requirement imposed by the presented system. The necessity of a pair of square-law detectors with adequate bandwidth in both optical and THz domains places a bottleneck in the generation of THz signals (in this case, the frequency range of the system is limited to approximately 110 GHz). To further extend the capabilities of the system deeper in the THz range, the incorporation of faster square-law detectors (e.g. unitravelling-carrier photodiodes)[356] and Schottky diodes with broader bandwidths, or the use of pair of PCAs in a similar arrangement to that displayed in Figure 29 may provide satisfactory solutions.

Providing that these requisites are adequately satisfied, an upgraded version of the current system that allows for flexible operation in the THz range presents a number of advantages that cater to the needs of several applications. Specifically, terahertz waves are particularly well-suited for gas spectroscopy, offering high discrimination and sensitivity due to the presence of many densely located vibrational and rotational transitions that exhibit narrower linewidths than in other parts of the electromagnetic spectrum. Therefore, a benchtop-sized, easy-to-operate dual-comb spectrometer with high resolution and metrology-grade capabilities represents a step forward for in-field spectroscopy purposes in a spectral region traditionally confined to laboratory environments. One could even envisage the use of such a versatile THz dual-comb source venturing into diverse fields of applications that also take advantage of THz radiation, such as medical diagnosis, pharmaceutical characterization, non-destructive industrial testing or bio-imaging of human tissue, among others[357].

# VI

# General Conclusions and Outlook

# 1.
# General Conclusions

This Ph.D work has presented contributions to dual-comb spectroscopy across the most relevant spectral windows of the electromagnetic spectrum (i.e., Near-Infrared, Mid-Infrared and THz region). Particularly, this thesis work has laid great emphasis on two main factors: first, the use of commercially available devices and well-established techniques in order to alleviate the design complexity of spectroscopic systems with independence of the range of wavelengths; and second, the importance of the external customization of the main parameters that govern the performance of the sources with the ultimate goal of their full adaptability to the application of interest.

The Near-Infrared is, undeniably, the portion of the spectrum where the most mature technology can be conveniently exploited so that new architectures may come to the fore. In this context, this thesis has introduced the first dual-comb spectrometer based on GS and OIL and only relying on three semiconductor lasers. Besides, with a different layout, a novel architecture based again on OIL and, this time, on EO modulation, has proven useful for remote OFC detection by means of a local multiheterodyne arrangement.

These are the very first demonstrations of dual-comb schemes whose synchronization method relies on OIL. The combined use of this method together with a common time base (or a method for clock recovery) which serves as RF reference ensures the mutual coherence of the system. Therefore, it is clear that in those scenarios where the target device under test features a narrow spectral coverage, GS (together with OIL) and EO modulation are suitable techniques that can easily overcome the electronic complexity traditionally linked to the dual-comb detection approach. In addition to this, both methods allow tuning both the OFC central wavelength and its line spacing to match the desired spectral

resolution and optimize the measurement speed. These features have been tested with two different samples in the 1.5 μm region: first, a cell filled with HCN in gas phase in the GS-OIL-based dual-comb scheme, and second, an FBG sensor whose spectral information was encoded into a remote comb in the local multiheterodyne detection system. Both the absorption features of the former and the transmission profile of the latter (with FWHMs in the order of 8 and 25 GHz, respectively) have been successfully recorded using OFCs with different characteristics in a timescale of milliseconds. Figures of merit such as NEAs in the order of $10^{-6}$ (with 1 second of integration time and absorption lengths of a few centimetres) or SNRs of ~$10^{3}$ in 1 second have been achieved with these systems.

The Mid-Infrared is a spectral region of crucial interest for spectroscopy, as the strength of the molecular transitions (in comparison to the weak vibrational overtone transitions in the Near-Infrared) vastly increases the detection sensitivity. However, dual-comb spectroscopy is under development in this spectral window, resulting in an unequalled combination of spectral coverage, resolution, frequency tunability and footprint of the employed setup. The work realized in this Ph.D has focused on the last three ingredients. To that end, a novel scheme based on an EO dual-comb and a DFG module encompassing a single MgO:PPLN crystal and a new method for the generation of coherent multiharmonic signals in DFB QCLs have been proposed.

In relation to the first experiment, the use of DFG as nonlinear mechanism to transfer the structure of Near-Infrared OFCs is still the preferred approach for the spectroscopic assessment of molecules in gas phase in the 3-5 μm range. Furthermore, if the nonlinear media is engineered to be quasi-phase-matchable within the transparency range of the crystal and is also fed by an EO dual-comb, the designed Mid-Infrared dual-comb instrument will feature an excellent level of adaptability to the target gas with potential to cover the whole range if proper input sources are used. This synergy has been exploited to demonstrate the potential of ultra-fast dual-comb absorption spectroscopy of methane in the ν3 band at 3.4 μm with NEAs and SNRs slightly lower but in the same order of magnitude than in Near-Infrared EO dual-combs. This leads to an equivalent LOD in the order of 1 ppm (in 1 metre and 1 second integration time) that would even reach 100 ppb for stronger absorption features.

Deeper in the Mid-Infrared (> 5 μm), QCLs have paralleled the development of dual-comb sources based on nonlinear conversion, filling the long-standing gap of the equivalent Near-Infrared semiconductor laser diode in the Mid-Infrared. With increasing levels of performance, CW room temperature operation and a

compact design, a dual-comb spectrometer based on QCLs is of high interest. However, the main features of QCL-based OFCs are deterministically defined by manufacturing parameters. There is a growing interest in the possibility of externally tuning the comb attributes of QCLs, as some recent examples in the literature reveal. In this sense, this thesis has disclosed a new method that allows for the generation of phase-locked, equally-spaced sidebands with adjustable separation in frequency in a single-mode DFB QCLs. This procedure stems from driving the device above and below threshold with an external RF signal to force it to respond in a nonlinear fashion. Further work in this direction may explore the actual potential of this technique for high-resolution dual-comb spectroscopy, thus leading to a reduction in the line spacing (or analogously, an increase in the resolution) of one or two orders of magnitude in comparison to current QCL-based dual-comb spectrometers.

The distinctive features of THz waves could not be overlooked in this analysis. Hence, this work has also introduced a completely new modality for THz dual-comb spectroscopy that distances itself from the traditional bulky setups based on MLLs or the contemporary but delicate THz QCL-based OFCs. Again, EO modulation and OIL have been cleverly harnessed to implement a scheme that photonically synthesizes THz dual-combs with absolute control over their defining frequencies and unprecedented capabilities in terms of frequency accuracy and stability in this region. With such promising features, a proof-of-principle experiment has demonstrated the potential of the first architecture of this type in the THz domain with the retrieval of the transfer function of a microwave filter in the W-band with an accuracy only determined by an RF standard. The system still preserves a SNR figure of merit in the order of ~$10^3$ in 1 second, as in other EO dual-comb setups revealed along this thesis.

In summary, this Ph.D dissertation has contributed to expand the landscape of possibilities for dual-comb spectroscopy. In such a crowded ecosystem, this author is of the opinion that the best dual-comb source is that one featuring not only enough versatility so that it can meet the requirements of a wide selection of target applications, but also the lowest level of complexity and associated cost. These are, undoubtedly, key elements for dual-comb sources to be eventually used as fully-grown, in-field instruments beyond the boundaries of the research laboratories.

# 2.

# Future Directions

The last section of this Ph.D dissertation will be devoted to highlight some of the lines of future work that may arise from the contributions presented along this document, with particular stress on the current limitations.

The use of EO-OFCs and EO dual-comb schemes is one of the core elements of this thesis work. Clearly, these architectures have undergone tremendous progress and nowadays it is possible to evaluate their proficiency in applications in which the employment of MLLs prevails. Nevertheless, if long-term stability is required or if the main purpose is the deployment of these systems in uncontrolled environments, phase correction algorithms or supplementary mechanisms for frequency stabilization become indispensable. This limitation is inherent to the interferometric setup, which is subject to thermal and acoustic fluctuations that induce a significant amount of phase noise that restricts the coherence and limits the achievable SNR[130]. Coherence-reinforcing methods have already been proposed for EO dual-comb schemes[130,198,209], but the assessment of its operation in industrial environments has not been undertaken to date. The improvement of the performance of these sources for an enhanced usability out of the laboratory will surely stimulate a great deal of interest even for unanticipated applications.

Regarding GS-OIL-based dual-comb spectrometers, the most exciting prospect offered by these setups is the potential for integration. The migration of OFCs to integrated devices is a topic of large interest within the scientific community motivated by the desire to create the most efficient and versatile source in the smallest footprint. Dual-comb spectrometers based on QCLs and microresonators are representative examples of this trend, but their characteristic parameters will always be intrinsically defined by physical properties. In contrast, a GS-OIL-based dual-comb will certainly overcome these limitations enabling an

unlimited control over the main OFC features within the frequency range of operation of the device. There are examples of photonically integrated circuits based on externally injected GS-based OFCs in the literature[62,63] that suggest the possibility of miniaturization of a dual-comb platform based on these techniques in the near future. Indeed, this conception might also be transferred to QCLs based on large-signal modulation to create two coherent multiharmonic signals with easily adjustable line spacing as the basis of a new model of chip-sized dual-comb spectrometer in the Mid-Infrared, providing that a method to reconstruct the mutual coherence between combs is implemented. These designs would expand the range of technologies for dual-comb generation that are compatible with chip-scale integration with the added potential for external customization, an attribute that has not been demonstrated in this type of platform to date.

Mid-Infrared dual-combs based on DFG processes have a long way to go before their realization as fully-fledged spectrometers beyond the demonstration carried out in this Ph.D work. Parameters such as efficiency, phase-matching bandwidth, wavelength coverage or robustness of the design can be accordingly optimized via several mechanisms. Perhaps one of the most straightforward solutions will encompass the adoption of commercially available fibre-coupled waveguide modules with a conversion efficiency up to 1000 times higher than bulk crystals in a robust package that further reduces the footprint of the free-space setup[352]. This approach will also render unnecessary the use of optical amplifiers to compensate the low efficiency of bulk crystals while providing decent levels of optical power for high-sensitive spectroscopy. On the other hand, it would also be attractive to observe the aptitudes of EO dual-combs at longer wavelengths with nonlinear crystals featuring increased transparency. To that end, an OP-GaP crystal used as nonlinear media would be one of the best candidates to perform dual-comb spectroscopy up to 12 μm, as it can be pumped by Near-Infrared sources in the 1-1.5 μm range[353].

In relation to the THz dual-comb architectures based on EO modulation, the main limitation of the current method is the bandwidth of the THz generation and detection system. The most evident approach would involve the utilization of high-end optical photomixers and Schottky diodes with enhanced bandwidth, an upgrade that would certainly expand the spectral coverage of the dual-comb source. If these components were not available, a different solution involving commercial PCAs could be of use in return for a higher level of complexity. This scheme would involve a pair of PCAs in a coherent detection scheme to generate two THz frequency combs in each of them so that the photocurrent resulting from the interference of THz waves in the illuminated receiver reveals the structure of

the downconverted RF comb. Despite the utilization of a free-space arrangement (instead of a waveguide-based platform for transmission) and the need for a stable and marginal mismatch between the central frequencies of the THz combs (in the kHz range due to the bandwidth limitation of the intermediate frequency of the receiver PCA), this approach would readily extend the potential coverage of the system due to the extended bandwidth of these devices (commercial modules provide bandwidths up to 6 THz[358]).

As the dual-comb technology matures, so does the knowledge regarding its possibilities and limitations. In general terms, however, it is unquestionable that this method has propelled numerous advances across a wide range of disciplines with remarkable improvements in resolution, accuracy, measurement speed and sensitivity, all in a single platform. This array of capabilities sets this technique apart, in a similar way to Michelson-based Fourier-transform spectroscopy in the past century. In this sense, the widespread use of commercially available OFCs, the progress of technology in several key areas and the consolidation of a number of improvements that favour extra robustness, versatility and ease of scaling and integration may not only develop the potential of a great number of applications across biological, chemical and physical sciences, but also provide unforeseen results at the borders of the existing fields of research.

# APPENDIX I

## The Electro-Optic Self-Heterodyne Detection Scheme

# Appendix I

# The Electro-Optic Self-Heterodyne Detection Scheme

In Chapter II of this dissertation, within the discussion of the Near-Infrared EO dual-comb architectures, some other unconventional arrangements with different degrees of similarity to traditional setups were also unveiled. One of the them is the so-called self-heterodyne detection scheme, an approach that shares the basic principles of EO dual-comb spectroscopy while featuring an interesting trade-off between measurement speed, number of components involved in the setup and complexity of the electronics for detection. This appendix is devoted to present a full experiment based on this approach and the further validation of the architecture using low-pressure acetylene as gas sample under test.

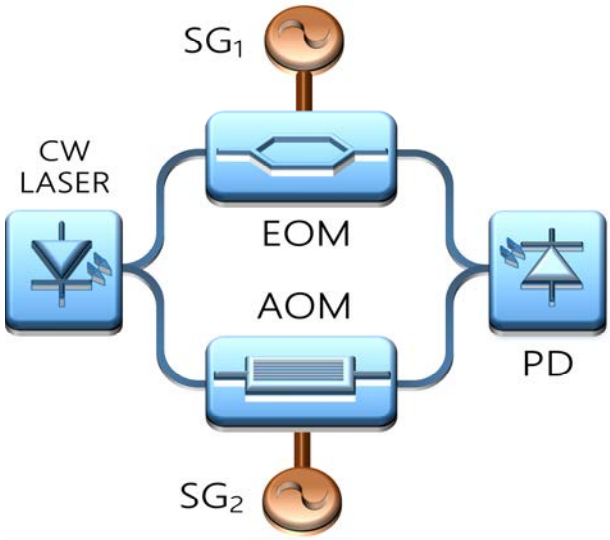


Figure 70. Basic setup for EO self-heterodyne detection. PD: Photodetector; SG: Signal generator.

The basic layout of the EO self-heterodyne detection scheme (see Figure 70) very much resembles that of EO dual-comb interferometers (as the one previously shown in Figure 20). Again, the output light of a CW laser is split into two paths, but this time only one OFC is generated by means of an EOM. The second arm of the interferometer includes an AOM that shifts the central frequency of the CW laser and enables the unambiguous mapping of the downconverted OFC. All the RF generators are referenced to the same time base. Both optical signals are then combined and mixed in a single photodetector, as in classic dual-comb setups. The result is an RF comb which is essentially a replica of the probe OFC folded in the spectrum around the frequency fixed by the AOM.

The effect of removing the second EOM, and therefore, generating only one OFC, is twofold. First, the compression factor of the optical spectrum is now $f_{REP}/2$ instead of $f_{REP}/\Delta f_{REP}$; second, the refresh rate of the interferometric signal is $1/f_{AOM}$ instead of $1/\Delta f_{REP}$. Plainly speaking, this detection system possesses the features of a dual-comb spectrometer in which the separation between the repetition rates of the OFCs is extremely broad. However, in return for the need for faster electronics, this approach possesses compelling aptitudes for ultra-fast spectroscopy. This scenario is particularly attractive in the case of OFCs exhibiting small spans and narrow line spacings, thus relaxing the requirements in terms of RF detection bandwidth while preserving the high-resolution capabilities of the optical source. Clearly, EO-OFCs are perfect candidates for self-heterodyne spectroscopy[103,307–309].

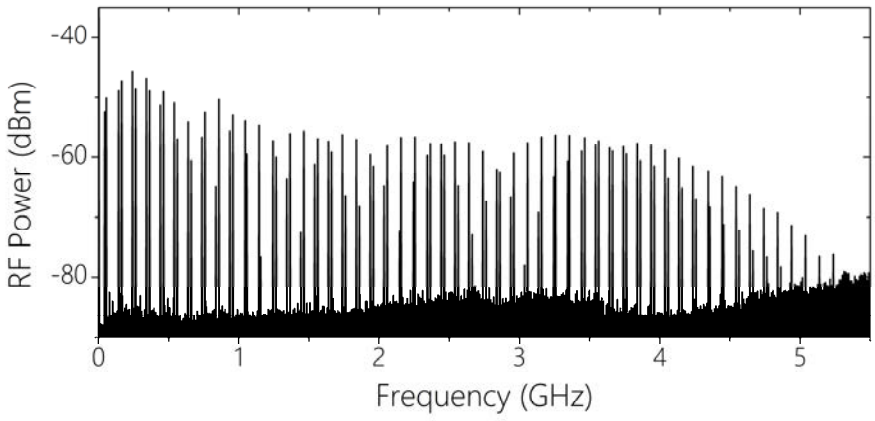


Figure 71. Downconverted RF comb generated after self-heterodyne detection of one single EO-OFC. The beatnotes spread across an RF bandwidth which is roughly half of the span of the OFC.

The potential of the detection technique is evaluated in a fully-fiberized setup encompassing a CW DM laser (Eblana Photonics, Ltd.) emitting up to 5 mW around 1538 nm together with an EO phase modulator (EOSpace, Inc.) and an AOM (Gooch & Housego, Inc.) that are fed by amplified RF signals whose power levels are 30 and 24 dBm, respectively. The frequency-shift induced by the AOM

is 40 MHz, whereas the EOM is driven at a $f_{REP}$ = 100 MHz. The combined optical beams are heterodyned on a fast photodetector (u2t Photonics, Inc.) while the RF signal is simultaneously displayed on an electrical spectrum analyzer and synchronously sampled at 10 GS/s with a fast oscilloscope (Rohde & Schwarz, Inc.), yielding up to 200 μs of integration time. An example of the generated RF comb can be seen in Figure 71, where the downconverted beatnotes at frequencies of $f_{AOM} + kf_{REP}$ and $(f_{REP} - f_{AOM}) + kf_{REP}$ (with $k$ being an integer) are clearly visible. All the beatnotes exhibit 3-dB linewidths below 1 Hz, which is a clear indicator of the mutual coherence of the system.

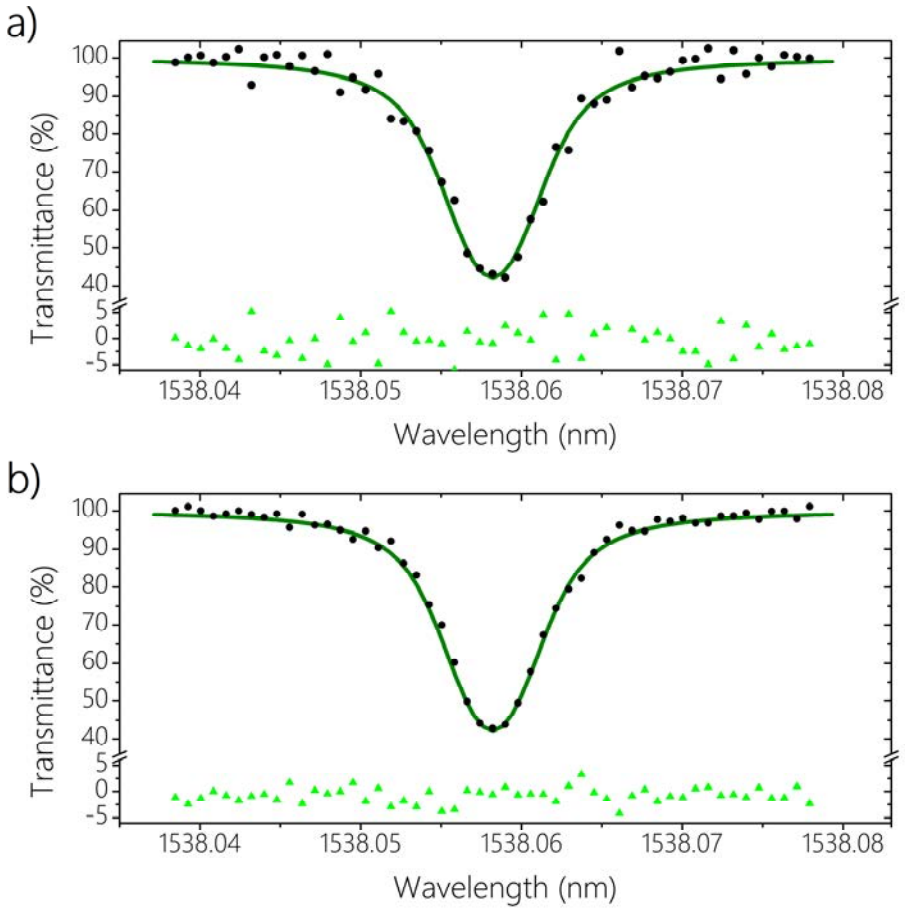


Figure 72. Experimental validation of the EO self-heterodyne detection scheme. Absorption profile of the measured transition of acetylene at 1538.06 nm for an integration time of a) 2 μs and b) 200 μs. The residuals between the experimental data and the HITRAN database line parameters reveal standard deviations of a) 3.03% and b) 1.44%, showing no systematic deviation.

Under these circumstances, the validation of the system is accomplished through the measurement of the ro-vibrational transition of $C_2H_2$ at 1538.06 nm. For that purpose, the emission wavelength of the CW DM laser is roughly adjusted into the vicinity of this absorption feature. A 55 mm length gas cell (placed next to the EOM in the setup shown in Figure 70) filled with this gas at 50 Torr at room

temperature is therefore used as sample under test. At this pressure, the molecular transition exhibits an FWHM of ~0.92 GHz, for which the selected repetition frequency of 100 MHz is well-matched to perform absorption spectroscopy. In conjunction with the gas cell, an optical switch is also harnessed to obtain a reference RF comb instead of employing an additional photodetector for normalization purposes.

The Fourier-transformation of the train of interferograms with a refresh rate of 25 ns ($1/f_{AOM}$) reveals the structure of the RF comb, from which the encoded spectral information of every frequency marker (in this case, amplitude) can be retrieved. The spectral profile of the absorption feature is shown in Figure 72 after calculating the ratio between a reference and an effective measurement of the gas. The dots represent the experimental data for an integration time of 2 μs in Figure 72 (a), while the solid line shows the line parameters retrieved from the HITRAN database[350]. Furthermore, the very high mutual coherence of the scheme is demonstrated by means of the co-adding of spectra over longer averaging times, as shown in Figure 72 (b) for an extended integration time of 200 μs. In both cases, the good agreement between curves is evident. The average spectral SNR of the instrument (i.e., the averaged ratio of the amplitude of every RF beatnote to its standard deviation under zero-gas conditions) is 45 at 2 μs, which leads to a normalized SNR at 1 second integration time of $2.8 \times 10^4$. This figure is slightly higher in comparison to other schemes presented along this thesis, a fact that is mainly attributed to the simplicity of the optical setup and the shorter arms of the interferometer. For this figure of SNR at 1 second, an absorption length of 55 cm and 100 spectral elements, the resultant NEA is $5.7 \times 10^{-7}$ $cm^{-1}Hz^{-1/2}$.

# APPENDIX II

## Additional Effects of Optical Injection Locking on Gain-Switching-based Optical Frequency Combs

# Appendix II

# Additional Effects of Optical Injection Locking on Gain-Switching-based Optical Frequency Combs

The third chapter of this dissertation introduced the OIL technique as an effective method to synchronize two independent oscillators. The underlying principle of this mechanism is rather straightforward: inserting light from an external laser source (*master*) into the cavity of a secondary (*slave*) device under specific conditions of input power. In such a simple way, numerous studies have further revealed a number of collateral benefits that occur in injected devices under stable locking conditions, from broader modulation bandwidths to suppression of relative intensity noise, to mention but a few.

Apart from this range of well-known properties, injection-locked lasers may be subject to other unconventional regimes that may alter the natural performance of these devices. In Chapter III, the effect of the light injected by a *master* CW DM laser into two *slave* GS-based OFCs was evaluated as a function of the position in the spectrum for dual-comb spectroscopy purposes. In this appendix, a different and peculiar response is analysed: the impact of injecting light into the cavity of a laser device under GS but not only in the wavelength region covered by the comb that is generated.

To that end, the *slave* is a DM laser (Eblana Photonics, Ltd.) that is biased at 60 mA and modulated with an amplified RF sinusoidal signal at 28.5 dBm with a frequency of 10 GHz. These driving conditions generate an OFC similar to the one displayed in Figure 36 (which is also shown in Figure 73 (a) for comparison purposes). This *slave* GS-based OFC is then injected by a second DM laser (similar to the *slave*) acting as *master* and emitting an output power of 1 mW. The impact of the injection process on the optical spectrum is illustrated in Figure 73 (b-j).

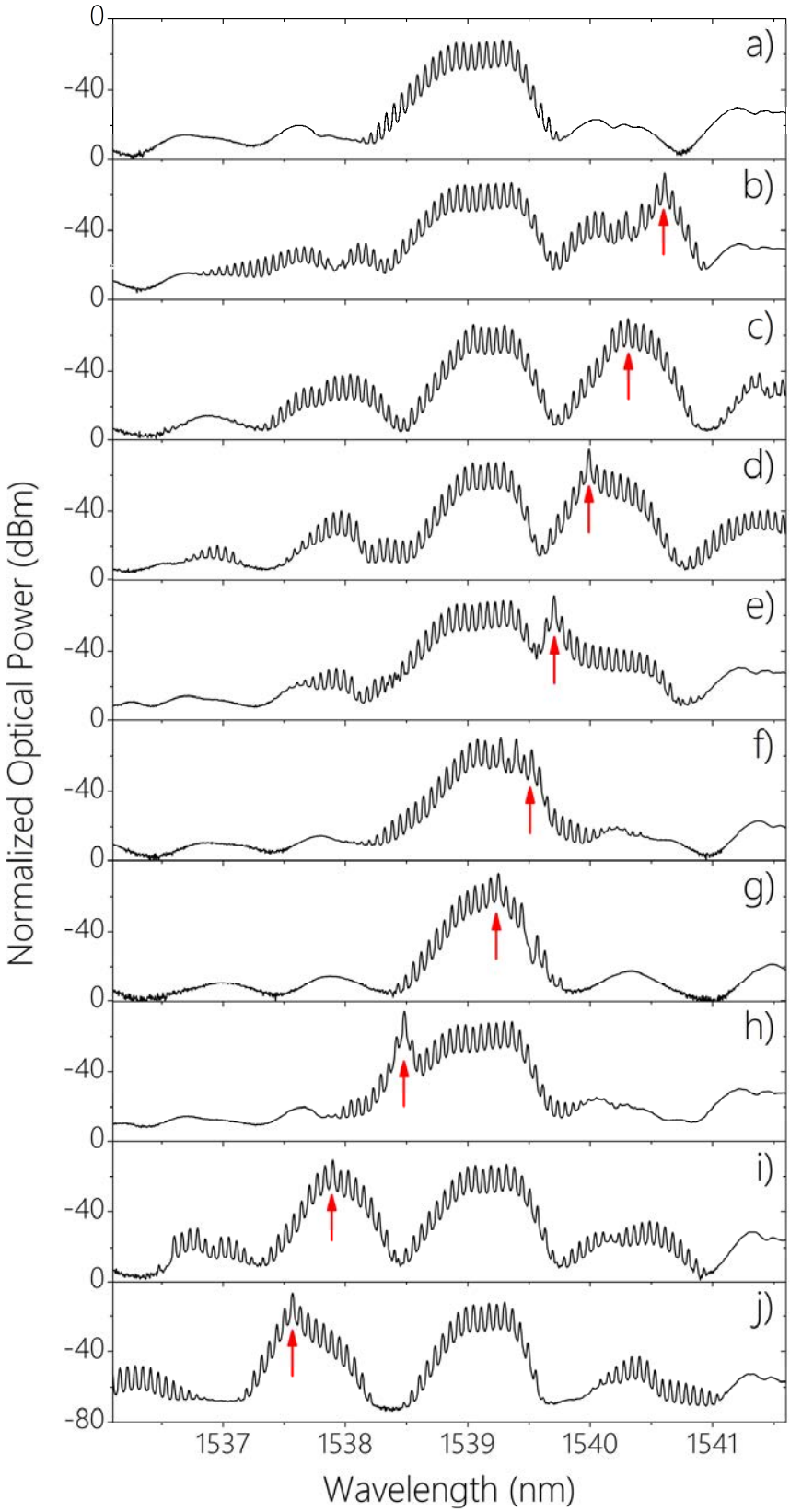


Figure 73. Analysis of the influence of an external laser source injecting a GS-based OFC generated in a DM laser. a) Initial spectrum without injection. b-j) Wavelength sweep of the *master* laser from higher to lower wavelengths across the generated *slave* OFC. The red arrow indicates the emission wavelength of the *master* laser in each case.

From inspection of the results, the distortion of the initial optical spectrum under OIL is evident. Particularly, there are two different effects that can be discerned. First, when the *master* laser injects one line of the *slave* GS-based OFC (see Figure 73 (f-h)), the original structure of the frequency comb becomes significantly altered, with an apparent detrimental effect due to the injected light in terms of flatness and bandwidth. This demonstrates that, although OIL has often been reported in the literature as a complement of GS-based OFCs to improve their performance, the injection conditions play a critical role in the formation of the comb and therefore need to be carefully considered for proper OFC generation.

The second consequence of injecting light into a GS-based OFC is visible when the emission wavelength of the *master* laser does not lie within the span of the generated OFC (see Figure 73 (b-e) and (i-j)). In this case, new combs are formed in some of the adjacent suppressed modes of the DM laser cavity. These OFCs will inherit the same repetition frequency of the original one, but they do not take part in a single comb structure together with the comb generated in the main excited mode of the laser, as the free spectral range of the cavity does not necessarily match the line spacing of the OFCs. Nevertheless, if the modulation frequency was a multiple or sub-multiple of the free-spectral range, a continuum of evenly-spaced lines may be created as a result of merging the ensemble of combs generated in the excited cavity modes. In this sense, this method paves the way for an efficient expansion of the bandwidth of the initial OFC which can be further enhanced through the widespread collection of techniques usually employed to increase the span of these sources.

# SELECTED PUBLICATIONS

**NOTICE**

Most of the publications cited below have been extracted, due to editorial deposit licenses, and deposited independently (see: *tesis_borja_jerez_gonzalez_2019_Anexo*).
Full references have been maintained in this chapter.

# Manuscript [M1]

## Optics Express, 2016

## Citation

**Borja Jerez**, Pedro Martín-Mateos, Estefanía Prior, Cristina de Dios and Pablo Acedo. "Dual optical frequency comb architecture with capabilities from visible to mid-infrared". Optics Express 24 (13), 14986-14994 (2016).

## Publication Details

Optical Society of America (OSA)

Received: April 2016

Published: June 2016

## JCR Impact Factor

3.307 (2016)

# Dual optical frequency comb architecture with capabilities from visible to mid-infrared

**Borja Jerez,* Pedro Martín-Mateos, Estefanía Prior, Cristina de Dios, and Pablo Acedo**

*Departamento de Tecnología Electrónica, Universidad Carlos III de Madrid, C/ Butarque 15, 28911 Leganés, Madrid, Spain*

*bjerez@ing.uc3m.es*

**Abstract:** In this paper, a new approach to dual-comb generation based on well-known optical techniques (Gain-Switching and Optical Injection Locking) is presented. The architecture can be implemented using virtually every kind of continuous-wave semiconductor laser source (DFB, VCSEL, QCL) and without the necessity of electro-optic modulators. This way, a frequency-agile and adaptive dual-comb architecture is provided with potential implementation capabilities from mid-infrared to near ultraviolet. With an RF comb comprising around 70 teeth, the system is validated in the 1.5 μm region measuring the absorption feature of $H^{13}CN$ at 1538.523 nm with a minimum integration time of 10 μs.



**OCIS codes:** (280.4788) Optical sensing and sensors; (140.3520) Lasers, injection-locked; (120.6200) Spectrometers and spectroscopic instrumentation; (300.6310) Spectroscopy, heterodyne.

## References and links

1. T. Udem, R. Holzwarth, and T. W. Hänsch, "Optical frequency metrology," Nature **416**(6877), 233–237 (2002).
2. T. Ideguchi, S. Holzner, B. Bernhardt, G. Guelachvili, N. Picqué, and T. W. Hänsch, "Coherent Raman spectro-imaging with laser frequency combs," Nature **502**(7471), 355–358 (2013).
3. T. Udem, "Spectroscopy: frequency comb benefits," Nat. Photonics **3**(2), 82–84 (2009).
4. S. Schiller, "Spectrometry with frequency combs," Opt. Lett. **27**(9), 766–768 (2002).
5. I. Coddington, W. C. Swann, and N. R. Newbury, "Coherent dual-comb spectroscopy at high signal-to-noise ratio," Phys. Rev. A **82**(4), 043817 (2010).
6. F. Keilmann, C. Gohle, and R. Holzwarth, "Time-domain mid-infrared frequency-comb spectrometer," Opt. Lett. **29**(13), 1542–1544 (2004).
7. I. Coddington, W. C. Swann, and N. R. Newbury, "Coherent multiheterodyne spectroscopy using stabilized optical frequency combs," Phys. Rev. Lett. **100**(1), 013902 (2008).
8. B. Bernhardt, A. Ozawa, P. Jacquet, M. Jacquey, Y. Kobayashi, T. Udem, R. Holzwarth, G. Guelachvili, T. W. Hänsch, and N. Picqué, "Cavity-enhanced dual-comb spectroscopy," Nat. Photonics **4**(1), 55–57 (2010).
9. E. Baumann, F. R. Giorgetta, W. C. Swann, A. M. Zolot, I. Coddington, and N. R. Newbury, "Spectroscopy of the methane ν3 band with an accurate midinfrared coherent dual-comb spectrometer," Phys. Rev. A **84**(6), 062513 (2011).
10. T. Ideguchi, A. Poisson, G. Guelachvili, N. Picqué, and T. W. Hänsch, "Adaptive real-time dual-comb spectroscopy," Nat. Commun. **5**, 3375 (2014).
11. G. Villares, A. Hugi, S. Blaser, and J. Faist, "Dual-comb spectroscopy based on quantum-cascade-laser frequency combs," Nat. Commun. **5**, 5192 (2014).
12. F. R. Giorgetta, G. B. Rieker, E. Baumann, W. C. Swann, L. C. Sinclair, J. Kofler, I. Coddington, and N. R. Newbury, "Broadband phase spectroscopy over turbulent air paths," Phys. Rev. Lett. **115**(10), 103901 (2015).
13. D. A. Long, A. J. Fleisher, K. O. Douglass, S. E. Maxwell, K. Bielska, J. T. Hodges, and D. F. Plusquellic, "Multiheterodyne spectroscopy with optical frequency combs generated from a continuous-wave laser," Opt. Lett. **39**(9), 2688–2690 (2014).
14. P. Martin-Mateos, M. Ruiz-Llata, J. Posada-Roman, and P. Acedo, "Dual-comb architecture for fast spectroscopic measurements and spectral characterization," IEEE Photonics Technol. Lett. **27**(12), 1309–1312 (2015).
15. P. Martín-Mateos, B. Jerez, and P. Acedo, "Dual electro-optic optical frequency combs for multiheterodyne molecular dispersion spectroscopy," Opt. Express **23**(16), 21149–21158 (2015).
16. V. Durán, S. Tainta, and V. Torres-Company, "Ultrafast electrooptic dual-comb interferometry," Opt. Express **23**(23), 30557–30569 (2015).
17. G. Millot, S. Pitois, M. Yan, T. Hovhannisyan, A. Bendahmane, T. W. Hänsch, and N. Picqué, "Frequency-agile dual-comb spectroscopy," Nat. Photonics **10**(1), 27–30 (2015).
18. A. J. Fleisher, D. A. Long, Z. D. Reed, J. T. Hodges, and D. F. Plusquellic, "Coherent cavity-enhanced dual-

#264266 Received 28 Apr 2016; revised 14 Jun 2016; accepted 20 Jun 2016; published 23 Jun 2016

comb spectroscopy," Opt. Express **24**(10), 10424–10434 (2016).
19. S. Papp, K. Beha, P. Del'Haye, D. Cole, A. Coillet, and S. Diddams, "Self-referencing a CW laser with efficient nonlinear optics," in *Nonlinear Optics,* OSA Technical Digest (Online) (Optical Society of America, 2015), paper NTh3A.6.
20. F. C. Cruz, D. L. Maser, T. Johnson, G. Ycas, A. Klose, F. R. Giorgetta, I. Coddington, and S. A. Diddams, "Mid-infrared optical frequency combs based on difference frequency generation for molecular spectroscopy," Opt. Express **23**(20), 26814–26824 (2015).
21. K. F. Lee, N. Granzow, M. A. Schmidt, W. Chang, L. Wang, Q. Coulombier, J. Troles, N. Leindecker, K. L. Vodopyanov, P. G. Schunemann, M. E. Fermann, P. S. J. Russell, and I. Hartl, "Midinfrared frequency combs from coherent supercontinuum in chalcogenide and optical parametric oscillation," Opt. Lett. **39**(7), 2056–2059 (2014).
22. A. Hugi, G. Villares, S. Blaser, H. C. Liu, and J. Faist, "Mid-infrared frequency comb based on a quantum cascade laser," Nature **492**(7428), 229–233 (2012).
23. B. Bernhardt, E. Sorokin, P. Jacquet, R. Thon, T. Becker, I. T. Sorokina, N. Picqué and T. W. Hänsch, "Mid-infrared dual-comb spectroscopy with 2.4 μm Cr2+:ZnSe femtosecond lasers," Appl. Phys. B: Laser and Optics **100**(1), 3-8 (2010).
24. J. Chiles and S. Fathpour, "Mid-infrared integrated waveguide modulators based on silicon-on-lithium-niobate photonics," Optica **1**(5), 350–355 (2014).
25. S. Yamashita and G. J. Cowle, "Single-polarization operation of fiber distributed feedback (DFB) lasers by injection locking," J. Lightwave Technol. **17**(3), 509–513 (1999).
26. S. M. Riecke, H. Wenzel, S. Schwertfeger, K. Lauritsen, K. Paschke, R. Erdmann, and G. Erbert, "Picosecond spectral dynamics of gain-switched DFB lasers," IEEE J. Quantum Electron. **47**(5), 715–722 (2011).
27. R. Zhou, T. N. Huynh, V. Vujicic, P. M. Anandarajah, and L. P. Barry, "Phase noise analysis of injected gain switched comb source for coherent communications," Opt. Express **22**(7), 8120–8125 (2014).
28. P. M. Anandarajah, S. P. Ó. Dúill, R. Zhou, and L. P. Barry, "Enhanced optical comb generation by gain-switching a single-mode semiconductor laser close to its relaxation oscillation frequency," IEEE J. Sel. Top. Quantum Electron. **21**(6), 592 (2015).
29. C. H. Chang, L. Chrostowski, and C. J. Chang-Hasnain, "Injection locking of VCSELs," IEEE J. Sel. Top. Quantum Electron. **9**(5), 1386–1393 (2003).
30. A. R. C. Serrano, C. de Dios Fernandez, E. P. Cano, M. Ortsiefer, P. Meissner, and P. Acedo, "VCSEL-based optical frequency combs: Toward efficient single-device comb generation," IEEE Photonics Technol. Lett. **25**(20), 1981–1984 (2013).
31. E. Prior, C. de Dios, Á. R. Criado, M. Ortsiefer, P. Meissner, and P. Acedo, "Experimental study of VCSEL-based optical frequency comb generators," IEEE Photonics Technol. Lett. **26**(21), 2118–2121 (2014).
32. A. Asahara, S. Chen, T. Ito, M. Yoshita, W. Liu, B. Zhang, T. Suemoto, and H. Akiyama, "Direct generation of 2-ps blue pulses from gain-switched InGaN VCSEL assessed by up-conversion technique," Sci. Rep. **4**, 6401 (2014).
33. R. Zhou, S. Latkowski, J. O'Carroll, R. Phelan, L. P. Barry, and P. Anandarajah, "40 nm wavelength tunable gain-switched optical comb source," Opt. Express **19**(26), B415–B420 (2011).
34. R. Paiella, F. Capasso, C. Gmachl, C. G. Bethea, D. L. Sivco, J. N. Baillargeon, A. L. Hutchinson and A. Y. Cho, "High-speed operation of gain-switched mid-infrared quantum cascade lasers," Appl. Phys. Lett **75**(17), 2536–2538 (1999).
35. R. Paiella, F. Capasso, C. Gmachl, C. G. Bethea, D. L. Sivco, J. N. Baillargeon, A. L. Hutchinson, A. Y. Cho and H. C. Liu, "Generation and detection of high-speed pulses of mid-infrared radiation with intersubband semiconductor lasers and detectors," IEEE Photonics Technol. Lett. **12**(7), 780-782 (2000).
36. H. Simos, A. Bogris, D. Syvridis, and W. Elsäßer, "Intensity noise properties of mid-infrared injection locked quantum cascade lasers: I. Modeling," IEEE J. Quantum Electron. **50**(2), 98–105 (2014).
37. C. Juretzka, H. Simos, A. Bogris, D. Syvridis, W. Elsäßer, and M. Carras, "Intensity noise properties of mid-infrared injection locked quantum cascade Lasers: II. Experiments," IEEE J. Quantum Electron. **51**(1), 2300208 (2015).
38. X. Leijtens, "JePPIX: the platform for Indium Phosphide-based photonics," IET Optoelectron. **5**(5), 202–206 (2011).
39. L. A. Coldren, S. C. Nicholes, L. Johansson, S. Ristic, R. S. Guzzon, E. J. Norberg, and U. Krishnamachari, "High performance InP-based photonic ICs—A tutorial," J. Lightwave Technol. **29**(4), 554–570 (2011).
40. P. P. Vasil'ev, I. H. White, and J. Gowar, "Fast phenomena in semiconductor lasers," Rep. Prog. Phys. **63**(12), 1997–2042 (2000).
41. R. T. Ramos, A. J. Seeds, A. Bordonalli, P. Gallion, and D. Erasme, "Optical injection locking and phase-lock loop combined systems," Opt. Lett. **19**(1), 4–6 (1994).
42. E. K. Lau, L. J. Wong, and M. C. Wu, "Enhanced modulation characteristics of optical injection-locked lasers: A tutorial," IEEE J. Sel. Top. Quantum Electron. **15**(3), 618–633 (2009).
43. S. L. Gilbert, W. C. Swann, and C. Wang, "Hydrogen cyanide $H^{13}C^{14}N$ absorption reference for 1530 nmto 1565 nm wavelength calibration - SRM 2519a," Natl. Inst. Stand. Technol. Spec. Publ. 260–137 (2005).

## 1. Introduction

Although Optical Frequency Combs (OFCs) were first introduced as powerful metrology tools [1], shortly their potential was widely proven in biomedical applications [2] and spectroscopy [3], among others. In relation to the last field, the current trends based on dual-

#264266 Received 28 Apr 2016; revised 14 Jun 2016; accepted 20 Jun 2016; published 23 Jun 2016

comb spectroscopy [4,5] have proven unprecedented frequency resolution, stability and considerable shrinkage in measurement times in comparison to other state-of-the-art spectroscopic techniques, such as Michelson-based Fourier transform spectroscopy. The principle of operation of dual-comb spectroscopy relies on mapping the modes of two OFCs with slightly different repetition frequencies from the optical domain into the radio-frequency (RF) domain, in order to detect and process the information taking full advantage of the broad variety of techniques and methods available in the latter domain. In this context, traditional dual-comb sources have relied on two-laser schemes and mode-locked-based OFCs [6–12]. Nevertheless, the need for synchronization between lasers, restricted repetition frequency, or inherent complexity of these architectures are limitations which usually make these schemes unsuitable to be incorporated in field applications, despite their unassailable capabilities in terms of broadband spectral range and extraordinary precision.

Concurrently, compact OFCs generated by electro-optic modulation of a continuous-wave laser have recently emerged as attractive alternatives when the wide bandwidth of solid-state lasers is not needed [13–18]. Some of the significant features of this approach are the higher power of the spectral components (and, hence, higher signal-to-noise ratio –SNR-), simplicity of use and control (including line spacing), and lower cost, which makes them firm candidates to exploit the full potential of dual-comb spectroscopy in real environments. Modest OFCs developed from standard optical devices can be generated with electro-optic modulators including tens of lines [13–15] or, more recently, even hundreds [18]. Additionally, with further expansion stages or the inclusion of highly nonlinear fibres this number can easily reach not only hundreds but even thousands [16,17,19].

Nevertheless, it is the simplicity of these systems, based on commercial telecommunication components, which conveys an additional hindrance which also needs to be overcome. The employment of these components is a restrictive factor in terms of wavelength range of operation, which is mainly centred around 1.5 μm, being impossible, for instance, to reach wavelengths in the mid-infrared (MIR) region, where the presence of strong vibrational bands in a number of gases is well-known. Although MIR optical frequency combs (OFCs) based on different approaches (Difference Frequency Generation –DFG [20]-, optical parametric oscillators –OPOs [21]-), as well as quantum-cascade laser optical frequency combs (QCL-OFCs [22]) have been satisfactorily demonstrated, the advancement of MIR dual OFCs is still in its early stages [11]. Complex architectures based on mode-locked lasers have already been validated [23], but the lack of consolidated and robust electro-optic modulators in this spectral range (can be found from 400 nm up to 2 μm) [24] confirms that there is still work ahead until dual combs are seamlessly integrated in the MIR, as direct translations of the compact architectures already demonstrated at 1.5 μm are not possible.

In this paper, we introduce a completely new approach to dual-comb sources which intends to overcome the aforementioned drawbacks by combining Gain-Switched Optical Frequency Combs (GS-OFCs) with Optical Injection Locking (OIL). These two techniques have been separately or in conjunction used with different continuous-wave semiconductor laser sources (DFBs [25–28], VCSELs [29–32], Fabry-Pérot laser diodes [33], QCLs [34–37]) in the complete wavelength range from MIR to visible. This way, it is possible to combine them to implement compact, real-time, high-resolution and versatile dual-comb architectures whose capacity can be uninterruptedly exploited not only in NIR but also in adjacent regions of the electromagnetic spectrum.

Moreover, this compact architecture can be integrated using already accessible and validated Photonic Integrated Circuit (PIC) technologies using generic platforms [38,39], thus providing with a potentially low-cost solution to take these systems outside the research laboratories and expand the capabilities of ultra-high resolution dual-comb spectroscopy to other application fields where high-resolution spectral characterization is required, from optical fibre sensors interrogation to biomedical applications.

#264266 Received 28 Apr 2016; revised 14 Jun 2016; accepted 20 Jun 2016; published 23 Jun 2016

## 2. Gain-Switching injection-locked dual-comb architecture

### *2.1. Compact dual-comb architecture description*

The proposed scheme of the dual-comb spectrometer is depicted in Fig. 1. The optical power of a continuous-wave laser diode (from now onward denominated as master) is divided into two optical paths to inject a new pair of laser diodes (slaves). Before splitting the optical power of the master, an isolator is placed to quench unwanted feedback reflections. In order to generate OFCs, both injected slaves are directly modulated through Gain-Switching at slightly different repetition frequencies. These frequencies can be uncomplicatedly tuned by signal generators. Additionally, to cancel mode averaging, one of the OFCs is frequency-shifted with an acousto-optic modulator (AOM) [13]. After polarization matching, both OFCs are combined.

Before being heterodyned on a photodetector, the combined OFCs can either traverse the device under test (DUT) to be characterized or serve as a reference. The resultant periodic interferogram (and the subsequent RF comb after Fourier transformation) is then bandpass-filtered (in order to discard higher order RF combs) to be afterwards digitized by an acquisition system. Finally, a multitone parallel detection scheme with adaptable configuration for ultra-high-speed measurements allows recovering the amplitude and the phase of the spectral components in each RF comb.

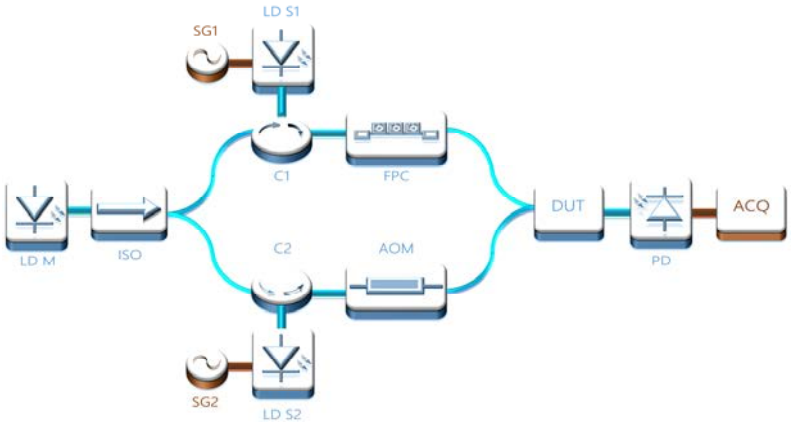


Fig. 1. Experimental setup of the spectrometer. LD M: Laser diode master; ISO: Optical isolator; C1/C2: Circulators; LD S1/2: Laser diode slaves; SG1/2: Signal generators; AOM: Acousto-optic modulator; FPC: Fibre polarization controller; DUT: Device under test; PD: Photodetector; ACQ: Acquisition system.

### *2.2. Gain-Switching*

The principle of operation of Gain-Switching consists of a periodic and sudden switch of the laser gain [40]. In our experiment, this is accomplished by biasing the laser with an electrical current ($I_{bias}$) and applying a large continuous-wave signal that modulates the laser ($I_{RF}$), thus producing a pulsed optical output. This modulation and bias are coupled to the diode laser thanks to a bias-tee element integrated into the laser case. The result in the optical domain is an asymmetric OFC with line spacing equal to the frequency which directly modulates the laser bias current ($f_{REP}$). Since the number of teeth generated depends on the ratios $I_{RF}/I_{bias}$, $I_{bias}/I_{TH}$ (where $I_{TH}$ refers to "threshold current") and $f_{REP}$, a meticulous experimental study of these parameters was carried out for a set of fixed modulation frequencies (up to 12 GHz). Continuous measurements for bias currents ranging from the threshold current up to its maximum (following specifications) were performed for a batch of different modulation powers in order to achieve the best OFCs according to two figures of merit: number of optical

#264266 Received 28 Apr 2016; revised 14 Jun 2016; accepted 20 Jun 2016; published 23 Jun 2016

lines and flatness of the OFC. All lasers were stabilized in current and temperature with standard laser diode controllers.

### *2.3. Optical injection locking*

The process of optical injection relies on the injection of the output optical field of a laser (which is usually denominated as master) into the cavity of a secondary (or slave) laser. Locking takes place when the frequencies (or emission wavelengths) of the master and slave are proximate enough, within the locking range. Therefore, the slave is obliged to perform on the injected wavelength along a certain locking range. In this case, since the optimum bias current of the slave lasers is established in accordance with Gain-Switching operation, a temperature tuning was carried out to adjust their wavelength emission roughly into the vicinity of the molecular transition of interest. With regard to the master, its output power was set about ~10 dB above the output power of the slave lasers (injection ratio) and its wavelength emission was also controlled acting over its temperature. Fibre polarization controllers placed between master and slaves enabled additional control over the injection locking mechanism. An example of the resultant OFC (before combination) is shown in Fig. 2, where the injection of the master laser in one of the teeth of the gain-switched slave lasers is appreciable in the optical spectrum. The proper performance of the injection locking technique is ensured by two facts: first, the ultra-narrow linewidth of the master and slave lasers (Master ≈34 kHz; Slave 1 ≈54 kHz; Slave 2 ≈367 kHz) prevents the interaction between the master and the adjacent slave comb lines; second, the locking range lies below the repetition frequency of the comb for the injection ratio considered in our experiment.

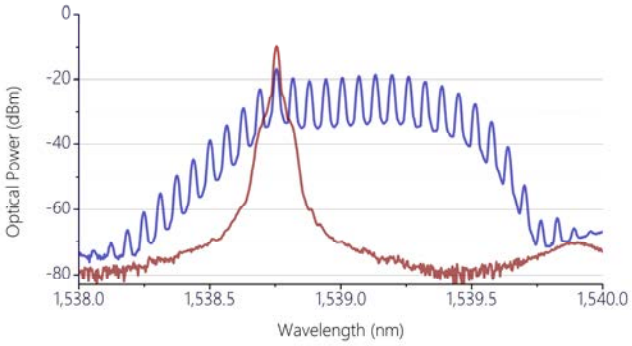


Fig. 2. Example of Gain-Switching and Optical Injection Locking. The red line shows the master laser. After optical injection in the slave laser, a pulsed optical regime is induced on the device using gain switching and, consequently, an OFC is generated (blue line). The injection of the master in one of the teeth of the OFC is discernible. In this example, the wavelength emission is fixed at 1538.75 nm and the repetition frequency of the OFC at 8 GHz. The spectra are measured in an optical spectrum analyser with 20 pm resolution.

### *2.4. Processing techniques: Acquisition of the interferogram*

The processing method is based on the Fourier transformation of the time-domain interferogram (see Fig. 3). A multichannel digital lock-in detection system implemented in Matlab (developed and detailed in a previous work [14]) features flexible configuration in terms of number of channels, integration time and reference frequencies. The RF combs digitized are processed in parallel allowing simultaneous characterization of multiple spectral points. The reference frequency of each channel can be set to coincide with the frequencies of the lines of the RF comb, thus allowing each channel to be analysed concurrently in order to extract the amplitude of each component of the comb. The integration time for each channel is also adaptable, only restricted by its minimum value, which is inversely proportional to the mismatch between repetition rates. Along with an increase in integration time, additional low-

#264266 Received 28 Apr 2016; revised 14 Jun 2016; accepted 20 Jun 2016; published 23 Jun 2016

pass filtering can also be carried out to smooth the final result or to diminish the impact of haphazard environmental effects when the application is not time-critical.

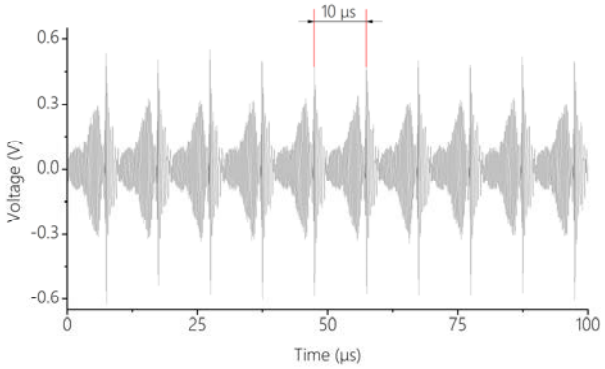


Fig. 3. Time-domain interferogram for a measurement time of 100 µs. The time elapsed between two consecutive pulses (10 µs) corresponds to the reciprocal of the difference between the repetition frequencies (in the example illustrated, 100 kHz)

### *2.5. Additional considerations*

At this point, there are a few noteworthy aspects of the system which must be highlighted. Firstly, since one single laser (master) drives both OFCs, the need for synchronization is dismissed and amplitude and phase fluctuations of the laser are also self-compensated. Additionally, a similar outcome can be gathered from OIL: when phase-locking between both master and slave takes place, the slave is obliged to follow the track of any phase fluctuation which occurs in the master [41]. Further benefits in terms of performance can also be attained when the locking is stable, such as laser spectral narrowing, frequency chirp decrement or noise reduction [42]. Other collateral advantages of the proposed system are the lower influence of Flicker noise as a result of the inclusion of a non-compulsory AOM, which centres the RF comb at its driving frequency, or the improved robustness and versatility for spectral characterization, since the configuration of the dual-comb architecture does not have any effect on the DUT per se. On top of that, and as mentioned before, all these features can be promptly transferred to other spectral regions.

## 3. Experimental validation

The proficiency of the presented architecture is validated with the measurement of the ro-vibrational transition of $H^{13}CN$ at 1538.523 nm [14,17]. For this purpose, the DUT comprises a 55 mm length gas cell filled with $H^{13}CN$ at 100 Torr (HCN-13-H(5.5)-100-FCAPC, Wavelength References Inc.) together with an optical switch (OSW-2X2BA, Fiberstore Inc.) which allows the OFC to bypass the cell and therefore obtain a reference RF comb without the need for a second photodetector, also avoiding imbalances between the signal and reference paths and improving the SNR in 3 dB. For this purpose, the scheme encompasses three Discrete Mode laser diodes (EP 1538-5-DM-H19-FM, Eblana Photonics Ltd.) emitting around 1538.5 nm. The emission wavelength was tuned by means of the temperature and bias current of the laser controller (the tuning range of the lasers is around 4 nm). The optical power of the master was divided into two paths (50/50 optic coupler), which eventually could be regarded as the two arms of an interferometer. Two identical circulators allowed injecting light in both slave lasers, which were then simultaneously modulated through GS at a frequency of 1 GHz and 1.0001 GHz, respectively. One of the OFCs was launched into an acousto-optic modulator (T-M040-0.5C8J-3-F2S, Gooch and Housego PLC) driven at 40 MHz with a RF power around 24 dBm to ensure that each spectral feature in the optical domain is unequivocally mapped into the RF domain. A fibre polarization controller

#264266 Received 28 Apr 2016; revised 14 Jun 2016; accepted 20 Jun 2016; published 23 Jun 2016

(FPC030, Thorlabs Inc.) was introduced in one path to control the polarization state of the optical beams so that both OFCs had parallel linear states of polarization before combining. One InGaAs transimpedance photodetector (PDA10CF, Thorlabs Inc.) was placed to detect the reference and signal combs. The resultant RF combs were bandpass-filtered with standard RF filters (SIF-40+, Mini-Circuits Inc.) and digitized with a 14-bit waveform digitized board (PDA14, Signatec Inc.). The RF signals were synchronously subsampled at 36 MS/s, thus shifting the central frequency of the comb to a normalized frequency of 4 MHz while preserving the line spacing. The generation of all RF signals (slave lasers modulation, AOM modulation and acquisition clock) were carried out by the same phase coherent synthesizer (HS9004A, Holzworth Instrumentation Inc.). No active temperature stabilization or vibration isolation procedures were implemented.

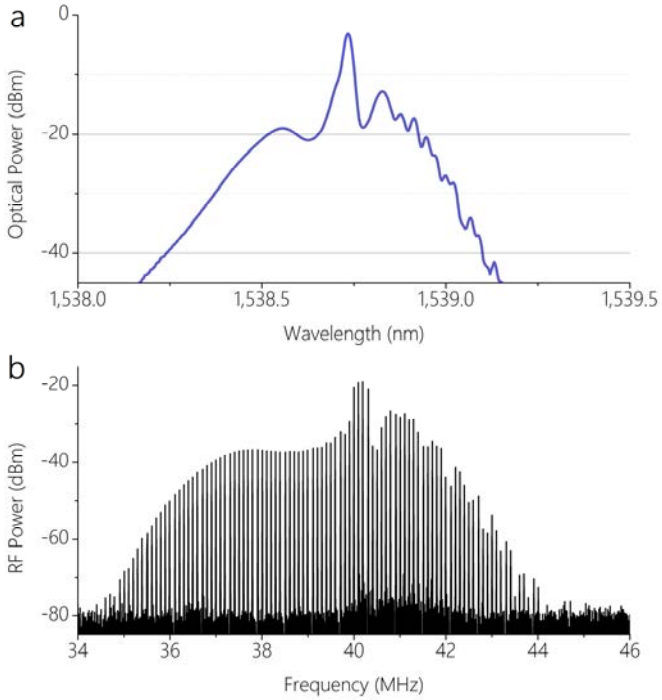


Fig. 4. Gain-switched injection-locked dual combs. a) Optical domain. Around 70 lines are spaced 1 GHz (which corresponds to ~0.55 nm) within a 20-dB span. No expansion stages were included in the setup. b) RF spectra of the comb obtained after Fourier-transforming the signal heterodyned on the photodetector. The central line has the frequency driving the acousto-optic modulator (40 MHz). The rest of modes are located at higher and lower frequencies asymmetrically due to the intrinsic properties of Gain-Switching in the lasers. The separation between lines (i.e., difference between repetition rates) is fixed at 100 kHz.

The combs generated with this approach (optical and RF domain) are illustrated in Fig. 4. With the GS ratios fixed at $I_{RF}/I_{bias} = 1.8$, $I_{bias}/I_{TH} \approx 4$, the repetition frequencies set at 1 GHz and the separation between them at 100 kHz (which leads to a periodicity in the interferograms of 10 μs), the resultant OFC (Fig. 4(a)) contains around 70 lines within a 20-dB span without introducing any sort of expansion stage. This number of lines is two or three times higher than similar schemes with a single expansion stage [13,14]. The comb obtained in the RF domain resulting after downconversion from the optical domain is shown in Fig. 4(b). Additionally, the linewidth of one RF comb line has been evaluated with a spectrum analyzer. As we have observed, the 3-dB linewidth is below the resolution of the device (Resolution Bandwidth = 1 Hz). This is a clear indication of the extremely high coherence between both injection-locked OFCs.

#264266 Received 28 Apr 2016; revised 14 Jun 2016; accepted 20 Jun 2016; published 23 Jun 2016

After processing, the resultant trace representing the ratio between the amplitudes of the measurement and reference combs is shown in Fig. 5 together with Voigt profiles for four different integration times: 10 μs (the minimum value, as the difference between repetition rates is 100 kHz), 50 μs, 100 μs and 500 μs. Additionally, a plot including an average of 20 spectra with an integration time of 20 ms is presented. In this case, the residuals between the experimental spectra and the fitted Voigt profile show a standard deviation of 0.57%. The peak absorption of ~1.07 dB at the central wavelength and linewidth of ~8 GHz denotes excellent agreement with the expected result [43], while the measurement time conforms to the expected ultra-high-speed spectroscopic measurement capabilities of the spectrometer. The noise-equivalent absorption (NEA), defined as $(L_{abs}\ SNR)^{-1}(T/M)^{1/2}$, is $6.87 \times 10^{-6}$ $cm^{-1}$ $Hz^{-1/2}$ at 1 s averaging, where $L_{abs}$ = 5.5 cm, SNR = 100, T = 1 ms and M = 70.

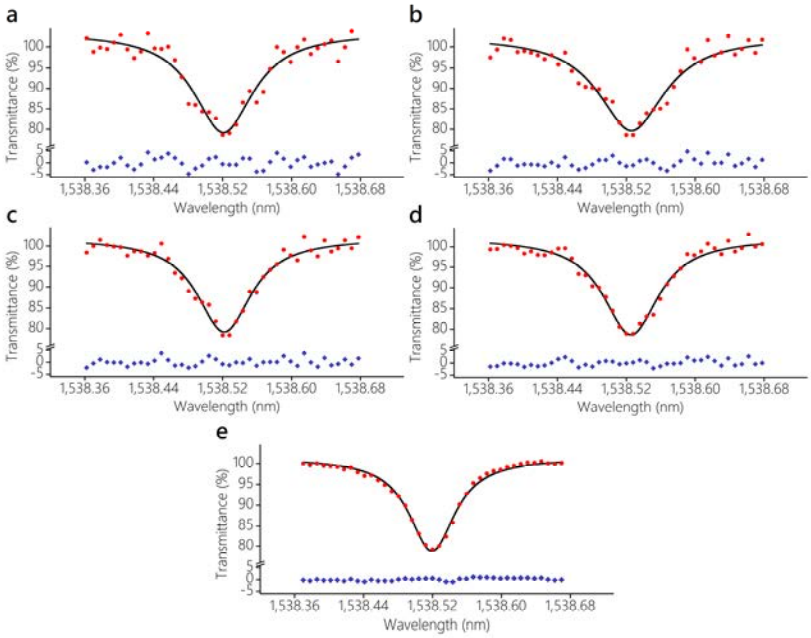


Fig. 5. Experimental validation in the 1.5 μm region. The dots represent the trace of the measured ro-vibrational transition presenting the R(5) line of the 2ν3 band of $H^{13}CN$ for different measurement times together with the residuals: a) 10 μs; b) 50 μs; c) 100 μs; d) 500 μs; e) Average of 20 spectra integrated over 20 ms. The solid line shows the Voigt fitting of the results, leading to standard deviations between the experimental data and the fitted curves of: a) 2.34%; b) 1.89%; c) 1.49%; d) 1.27% and e) 0.57%. A bottom value for the transmittance of 78% (which corresponds to a peak absorption of 1.07 dB) is quantified at the centre of the spectral line, along with a linewidth around 8 GHz. These values agree with the standard values reported in the NIST SRM 2519a.

## 4. Conclusions

We have introduced a compact dual-comb architecture whose performance relies on Gain-Switching, to induce pulsed operation in the lasers and consequently generate OFCs with slightly different frequency spacing without the necessity of electro-optic modulators, and optical injection locking to synchronize them. The presented system maintains the range of advantages of classic electro-optic dual optical frequency comb configurations, such as high resolution, spatial coherence, ultrafast speed of operation and ease control of mode spacing but, at the same time, the GS approach permits the generation of OFCs without resorting to

#264266 Received 28 Apr 2016; revised 14 Jun 2016; accepted 20 Jun 2016; published 23 Jun 2016

wavelength-restrictive optical components. Finally, OIL not only yields coherence between OFCs but also additional benefits in relation to the performance the system.

The GS-OIL dual-comb architecture is firstly validated in the NIR region, but since all the components and techniques have already been demonstrated in the MIR and visible ranges successfully, the deployment to these regions is straightforward. In conclusion, the presented architecture, on one hand, paves the way for compact dual-comb MIR spectroscopy by taking full advantage of a simple scheme and commercially available components, and, on the other hand, provides a compact, integrable (using standard PIC technology) and potentially low-cost solution to, firstly, take these systems outside the research laboratories and, secondly, to expand the capabilities of ultra-high resolution dual-comb spectroscopy to other application fields where high-resolution spectral characterization is required, from optical fibre sensors interrogation to biomedical applications.

**Acknowledgments**

The authors would like to thank the Spanish Ministry of Economy and Competitiveness for supporting the projects under the RTC-2014-2661-7 and TEC-2014-52147-R. The work by Borja Jerez has been performed in the frame of a FPU Program, #FPU014/06338, granted by the Spanish Ministry of Education, Culture and Sports.

#264266 Received 28 Apr 2016; revised 14 Jun 2016; accepted 20 Jun 2016; published 23 Jun 2016

# Manuscript [M2]

## Optics Letters, 2016

## Citation

**Borja Jerez,** Pedro Martín-Mateos, Estefanía Prior, Cristina de Dios and Pablo Acedo. "Gain-Switching injection-locked dual optical frequency combs: characterization and optimization". Optics Letters 41 (18), 4293-4296 (2016).

## Publication Details

Optical Society of America (OSA)

Received: July 2016

Published: September 2016

## JCR Impact Factor

3.416 (2016**)**

# Manuscript [M3]

## Journal of Lightwave Technology, 2017

## Citation

**Borja Jerez**, Frederik Walla, Cristina de Dios, Pedro Martín-Mateos and Pablo Acedo. "Fully frequency-locked multiheterodyne architecture for remote optical frequency comb rapid detection". Journal of Lightwave Technology 35 (19), 4195-4202 (2017).

## Publication Details

Institute of Electrical and Electronics Engineers (IEEE)

Received: February 2017

Published: August 2017

## JCR Impact Factor

3.652 (2017)

# Manuscript [M4]

## ACS Photonics, 2018

## Citation

**Borja Jerez**, Pedro Martín-Mateos, Frederik Walla, Cristina de Dios and Pablo Acedo. "Flexible electro-optic, single-crystal difference frequency generation architecture for ultrafast mid-infrared dual-comb spectroscopy". ACS Photonics 5 (6), 2348-2353 (2018).

## Publication Details

American Chemical Society (ACS)

Received: February 2018

Published: March 2018

## JCR Impact Factor

6.880 (2017)

# Manuscript [M5]

## Optical and Quantum Electronics, 2018

## Citation

**Borja Jerez**, Rolf Szedlak, Pedro Martín-Mateos, Cristina de Dios, Pablo Acedo and Gottfried Strasser. "Large-signal modulation in distributed feedback quantum cascade lasers for coherent multiharmonic signal generation". Optical and Quantum Electronics, 50:351 (2018).

## Publication Details

Springer

Received: May 2018

Published: September 2018

## JCR Impact Factor

1.168 (2017)

# Manuscript [M6]

## Optics Letters, 2019

## Citation

**Borja Jerez,** Frederik Walla, Andrés Betancur, Pedro Martín-Mateos, Cristina de Dios and Pablo Acedo. "Electro-optic THz dual-comb architecture for high-resolution, absolute spectroscopy". Optics Letters 44 (2), 415-418 (2019).

## Publication Details

Optical Society of America (OSA)

Received: November 2018

Published: January 2019

## JCR Impact Factor

3.589 (2017)

# REFERENCES

1. Evenson, K. M., Wells, J. S., Petersen, F. R., Danielson, B. L. & Day, G. W. Accurate frequencies of molecular transitions used in laser stabilization: The 3.39-μm transition in $CH_4$ and the 9.33- and 10.18-μm transitions in $CO_2$. *Appl. Phys. Lett.* **22,** 192–195 (1973).

2. Schnatz, H., Lipphardt, B., Helmcke, J., Riehle, F. & Zinner, G. First phase-coherent frequency-measurement of visible radiation. *Phys. Rev. Lett.* **76,** 18–21 (1996).

3. Udem, T. *et al.* Phase-coherent measurement of the hydrogen 1S-2S frequency with an optical frequency interval divider chain. *IEEE Trans. Instrum. Meas.* **46,** 166–168 (1997).

4. Eckstein, J. N., Ferguson, A. I. & Hänsch, T. W. High-resolution two-photon spectroscopy with picosecond light pulses. *Phys. Rev. Lett.* **40,** 847–850 (1978).

5. Udem, T., Reichert, J., Holzwarth, R. & Hänsch, T. W. Accurate measurement of large optical frequency differences with a mode-locked laser. *Opt. Lett.* **24,** 881–883 (1999).

6. Udem, T., Reichert, J., Holzwarth, R. & Hänsch, T. W. Absolute optical frequency measurement of the cesium $D_1$ line with a mode-locked laser. *Phys. Rev. Lett.* **82,** 3568–3571 (1999).

7. Reichert, J., Holzwarth, R., Udem, T. & Hänsch, T. W. Measuring the frequency of light with mode-locked lasers. *Opt. Commun.* **172,** 59–68 (1999).

8. Diddams, S. A. *et al.* Direct link between microwave and optical frequencies with a 300 THz femtosecond laser comb. *Phys. Rev. Lett.* **84,** 5102–5105 (2000).

9. Jones, D. J. *et al.* Carrier-envelope phase control of femtosecond mode-locked lasers and direct optical frequency synthesis. *Science (80-. ).* **288,** 635–639 (2000).

10. Holzwarth, R. *et al.* Optical frequency synthesizer for precision spectroscopy. *Phys. Rev. Lett.* **85,** 2264–2267 (2000).

11. Hänsch, T. W. Nobel lecture: Passion for precision. *Rev. Mod. Phys.* **78,** 1297–1309 (2006).

12. Hall, J. L. Nobel lecture: Defining and measuring optical frequencies. *Rev. Mod. Phys.* **78,** 1279–1295 (2006).

13. Diddams, S. A. The evolving optical frequency comb. *J. Opt. Soc. Am. B* **27,** B51–B62 (2010).

14. Udem, T., Holzwarth, R. & Hänsch, T. W. Optical frequency metrology. *Nature* **416,** 233–237 (2002).

15. Udem, T. & Riehle, F. Frequency combs applications and optical frequency standards. *Riv. del Nuovo Cim.* **30,** 563–606 (2007).

16. Newbury, N. R. Searching for applications with a fine-tooth comb. *Nat. Photonics* **5,** 186–188 (2011).

17. Diddams, S. A. *et al.* An optical clock based on a single trapped $^{199}Hg^{+}$ ion. *Science (80-. ).* **293,** 825–828 (2001).

18. Del'Haye, P., Arcizet, O., Gorodetsky, M. L., Holzwarth, R. & Kippenberg, T. J. Frequency comb assisted diode laser spectroscopy for measurement of microcavity dispersion. *Nat. Photonics* **3,** 529–533 (2009).

19. Steinmetz, T. *et al.* Laser frequency combs for astronomical observations. *Science (80-. ).* **321,** 1335–1337 (2008).

20. Adler, F., Thorpe, M. J., Cossel, K. C. & Ye, J. Cavity-enhanced direct frequency comb spectroscopy: Technology and applications. *Annu. Rev. Anal. Chem.* **3,** 175–205 (2010).

21. Newbury, N. R., Williams, P. A. & Swann, W. C. Coherent transfer of an optical carrier over 251 km. *Opt. Lett.* **32,** 3056–3058 (2007).

22. Zhang, W. *et al.* Sub-100 attoseconds stability optics-to-microwave synchronization. *Appl. Phys. Lett.* **96,** 211105 (2010).

23. Coddington, I., Swann, W. C., Nenadovic, L. & Newbury, N. R. Rapid and precise absolute distance measurements at long range. *Nat. Photonics* **3,** 351–356 (2009).

24. Cundiff, S. T. & Weiner, A. M. Optical arbitrary waveform generation. *Nat. Photonics* **4,** 760–766 (2010).

25. Delfyett, P. J. *et al.* Optical frequency combs from semiconductor lasers and applications in ultrawideband signal processing and communications. *J. Light. Technol.* **24,** 2701–2719 (2006).

26. Hargrove, L. E., Fork, R. L. & Pollack, M. A. Locking of He-Ne laser modes induced by synchronous intracavity modulation. *Appl. Phys. Lett.* **5,** 4–5 (1964).

27. Vasil'ev, P. P., White, I. H. & Gowar, J. Fast phenomena in semiconductor lasers. *Reports Prog. Phys.* **63,** 1997–2042 (2001).

28. Criado, Á. R. New photonic architectures and devices for generation and detection of sub-THz and THz waves (Ph.D Dissertation). (2013).

29. Matos, L. *et al.* Direct frequency comb generation from an octave-spanning, prismless Ti:sapphire laser. *Opt. Lett.* **29,** 1683–1685 (2004).

30. Bartels, A., Heinecke, D. & Diddams, S. A. Passively mode-locked 10 GHz femtosecond Ti:sapphire laser. *Opt. Lett.* **33,** 1905–1907 (2008).

31. Washburn, B. R. *et al.* Phase-locked, Erbium-fiber-laser-based frequency comb in the near infrared. *Opt. Lett.* **29,** 250–252 (2004).

32. Droste, S., Ycas, G., Washburn, B. R., Coddington, I. & Newbury, N. R. Optical frequency comb generation based on Erbium fiber lasers. *Nanophotonics* **5,** 196–213 (2016).

33. Sinclair, L. C. *et al.* A compact optically coherent fiber frequency comb. *Rev. Sci.*

*Instrum.* **86,** 081301 (2015).

34. Sinclair, L. C. *et al.* Operation of an optically coherent frequency comb outside the metrology lab. *Opt. Express* **22,** 6996–7006 (2014).

35. Lezius, M. *et al.* Space-borne frequency comb metrology. *Optica* **3,** 1381–1387 (2016).

36. Criado, Á. R., de Dios, C., Acedo, P., Carpintero, G. & Yvind, K. Comparison of monolithic optical frequency comb generators based on passively mode-locked lasers for continuous wave mm-wave and sub-THz generation. *J. Light. Technol.* **30,** 3133–3141 (2012).

37. Torres-Company, V. & Weiner, A. M. Optical frequency comb technology for ultra-broadband radio-frequency photonics. *Laser Photonics Rev.* **8,** 368–393 (2014).

38. Träger, F. *Springer handbook of lasers and optics*. *Springer* (2012).

39. Chiles, J. & Fathpour, S. Mid-infrared integrated waveguide modulators based on silicon-on-lithium-niobate photonics. *Optica* **1,** 350–355 (2014).

40. Kobayashi, T., Sueta, T., Cho, Y. & Matsuo, Y. High-repetition-rate optical pulse generator using a Fabry-Perot electro-optic modulator. *Appl. Phys. Lett.* **21,** 341–343 (1972).

41. Zhang, M. *et al.* Broadband electro-optic frequency comb generation in an integrated microring resonator. arXiv ID: 1809.08636 (2018).

42. Wu, R., Torres-Company, V., Leaird, D. E. & Weiner, A. M. Supercontinuum-based 10-GHz flat-topped optical frequency comb generation. *Opt. Express* **21,** 6045–6052 (2013).

43. Shen, P., Gomes, N. J., Davies, P. A., Huggard, P. G. & Ellison, B. N. Analysis and demonstration of a fast tunable fiber-ring-based optical frequency comb generator. *J. Light. Technol.* **25,** 3257–3264 (2007).

44. Yang, T., Dong, J., Liao, S., Huang, D. & Zhang, X. Comparison analysis of optical frequency comb generation with nonlinear effects in highly nonlinear fibers. *Opt. Express* **21,** 8508–8520 (2013).

45. Liu, Y. *et al.* Bandwidth scaling of a phase-modulated continuous-wave comb through four-wave mixing in a silicon nano-waveguide. *Opt. Lett.* **39,** 6478–6481 (2014).

46. Wu, R., Supradeepa, V. R., Long, C. M., Leaird, D. E. & Weiner, A. M. Generation of very flat optical frequency combs from continuous-wave lasers using cascaded intensity and phase modulators driven by tailored radio frequency waveforms. *Opt. Lett.* **35,** 3234–3236 (2010).

47. Yan, X., Zou, X., Pan, W., Yan, L. & Azaña, J. Fully digital programmable optical frequency comb generation and application. *Opt. Lett.* **43,** 283–286 (2018).

48. Yi, X. *et al.* Demonstration of a near-IR line-referenced electro-optical laser frequency comb for precision radial velocity measurements in astronomy. *Nat. Commun.* **7,**

10436 (2016).

49. Beha, K. *et al.* Electronic synthesis of light. *Optica* **4,** 406–411 (2017).

50. Carlson, D. R. *et al.* Ultrafast electro-optic light with subcycle control. *Science (80-. ).* **361,** 1358–1363 (2018).

51. van der Ziel, J. P. & Logan, R. A. Generation of short optical pulses in semiconductor lasers by combined DC and microwave current injection. *IEEE J. Quantum Electron.* **18,** 1340–1350 (1982).

52. Anandarajah, P. M., O'Dúill, S. P., Zhou, R. & Barry, L. P. Enhanced optical comb generation by gain-switching a single-mode semiconductor laser close to its relaxation oscillation frequency. *IEEE J. Sel. Top. Quantum Electron.* **21,** 1801609 (2015).

53. Rosado, A. *et al.* Experimental study of optical frequency comb generation in gain-switched semiconductor lasers. *Opt. Laser Technol.* **108,** 542–550 (2018).

54. de Dios, C. Generación de pulsos cortos mediante diodos láser gain-switching. Estudio de técnicas de compresión experimental basadas en lazos ópticos no ineales NOLM (Ph.D Dissertation). (2010).

55. Ito, T. *et al.* Femtosecond pulse generation beyond photon lifetime limit in gain-switched semiconductor lasers. *Commun. Phys.* **1,** 42 (2018).

56. Zhou, R. *et al.* 40 nm wavelength tunable gain-switched optical comb source. *Opt. Express* **19,** B415–B420 (2011).

57. Anandarajah, P. M. *et al.* Generation of coherent multicarrier signals by gain switching of Discrete Mode lasers. *IEEE Photonics J.* **3,** 112–122 (2011).

58. Anandarajah, P. M. *et al.* Phase shift keyed systems based on a gain switched laser transmitter. *Opt. Express* **17,** 12668–12677 (2009).

59. Criado, Á. R. *et al.* VCSEL-based optical frequency combs: Toward efficient single-device comb generation. *IEEE Photonics Technol. Lett.* **25,** 1981–1984 (2013).

60. Paiella, R. *et al.* High-speed operation of gain-switched mid-infrared quantum cascade lasers. *Appl. Phys. Lett.* **75,** 2536–2538 (1999).

61. Jukam, N. *et al.* Terahertz amplifier based on gain switching in a quantum cascade laser. *Nat. Photonics* **3,** 715–719 (2009).

62. Alexander, J. K. *et al.* Monolithically integrated low linewidth comb source using gain switched slotted Fabry-Pérot lasers. *Opt. Express* **24,** 7960–7965 (2016).

63. Gutierrez Pascual, M. D. *et al.* InP photonic integrated externally injected gain switched optical frequency comb. *Opt. Lett.* **42,** 555–558 (2017).

64. Yang, J., Tang, Y. & Xu, J. Development and applications of gain-switched fiber lasers. *Photonics Res.* **1,** 52–57 (2013).

65. Del'Haye, P. *et al.* Optical frequency comb generation from a monolithic

microresonator. *Nature* **450,** 1214–1217 (2007).

66. Kippenberg, T. J., Holzwarth, R. & Diddams, S. A. Microresonator-based optical frequency combs. *Science (80-. ).* **332,** 555–559 (2011).

67. Del'Haye, P. *et al.* Octave spanning tunable frequency comb from a microresonator. *Phys. Rev. Lett.* **107,** 063901 (2011).

68. Herr, T. *et al.* Temporal solitons in optical microresonators. *Nat. Photonics* **8,** 145–152 (2014).

69. Yi, X., Yang, Q.-F., Yang, K. Y., Suh, M.-G. & Vahala, K. Soliton frequency comb at microwave rates in a high-Q silica microresonator. *Optica* **2,** 1078–1085 (2015).

70. Obrzud, E. *et al.* A microphotonic astrocomb. *Nat. Photonics* **13,** 31–35 (2019).

71. Spencer, D. T. *et al.* An optical-frequency synthesizer using integrated photonics. *Nature* **557,** 81–85 (2018).

72. Stern, B., Ji, X., Okawachi, Y., Gaeta, A. L. & Lipson, M. Battery-operated integrated frequency comb generator. *Nature* **562,** 401–405 (2018).

73. Kippenberg, T. J., Gaeta, A. L., Lipson, M. & Gorodetsky, M. L. Dissipative Kerr solitons in optical microresonators. *Science (80-. ).* **361,** eaan8083 (2018).

74. Li, Y., Jiang, X., Zhao, G. & Yang, L. Whispering gallery mode microresonator for nonlinear optics. arXiv ID: 1809.04878 (2018).

75. Faist, J. *et al.* Quantum cascade laser. *Science (80-. ).* **264,** 553–555 (1994).

76. Bartalini, S., Vitiello, M. S. & de Natale, P. Quantum cascade lasers: A versatile source for precise measurements in the mid/far-infrared range. *Meas. Sci. Technol.* **25,** 012001 (2014).

77. Gkortsas, V.-M. *et al.* Dynamics of actively mode-locked quantum cascade lasers. *Opt. Express* **18,** 13616–13630 (2010).

78. Wang, C. Y. *et al.* Mode-locked pulses from mid-infrared quantum cascade lasers. *Opt. Express* **17,** 12929–12943 (2009).

79. Barbieri, S. *et al.* Coherent sampling of active mode-locked terahertz quantum cascade lasers and frequency synthesis. *Nat. Photonics* **5,** 306–313 (2011).

80. Hugi, A., Villares, G., Blaser, S., Liu, H. C. & Faist, J. Mid-infrared frequency comb based on a quantum cascade laser. *Nature* **492,** 229–233 (2012).

81. Burghoff, D. *et al.* Terahertz laser frequency combs. *Nat. Photonics* **8,** 462–467 (2014).

82. Khurgin, J. B., Dikmelik, Y., Hugi, A. & Faist, J. Coherent frequency combs produced by self frequency modulation in quantum cascade lasers. *Appl. Phys. Lett.* **104,** 081118 (2014).

83. Villares, G. & Faist, J. Quantum cascade laser combs: Effects of modulation and dispersion. *Opt. Express* **23,** 1651–1669 (2015).

84. Villares, G. *et al.* Dispersion engineering of quantum cascade laser frequency combs. *Optica* **3,** 252–258 (2016).

85. Lu, Q., Wu, D., Slivken, S. & Razeghi, M. High efficiency quantum cascade laser frequency comb. *Sci. Rep.* **7,** 43806 (2017).

86. Burghoff, D. *et al.* Evaluating the coherence and time-domain profile of quantum cascade laser frequency combs. *Opt. Express* **23,** 1190–1202 (2015).

87. Cappelli, F., Villares, G., Riedi, S. & Faist, J. Intrinsic linewidth of quantum cascade laser frequency combs. *Optica* **2,** 836–840 (2015).

88. Faist, J. *et al.* Quantum cascade laser frequency combs. *Nanophotonics* **5,** 272–291 (2016).

89. Rösch, M., Scalari, G., Beck, M. & Faist, J. Octave-spanning semiconductor laser. *Nat. Photonics* **9,** 42–47 (2015).

90. Kazakov, D. *et al.* Self-starting harmonic frequency comb generation in a quantum cascade laser. *Nat. Photonics* **11,** 789–792 (2017).

91. Vitiello, M. S., Scalari, G., Williams, B. & de Natale, P. Quantum cascade lasers: 20 years of challenges. *Opt. Express* **23,** 5167–5182 (2015).

92. Dutton, G. IRsweep tackles biologics challenge with spun-out lab method. *Genet. Eng. Biotechnol. News* **38,** 8–9 (2018).

93. Tsang, D. Z., Walpole, J. N., Liau, Z. L., Groves, S. H. & Diadiuk, V. Q-Switching of low-threshold buried-heterostructure diode lasers at 10 GHz. *Appl. Phys. Lett.* **45,** 204–206 (1984).

94. Tammaro, S. *et al.* High density terahertz frequency comb produced by coherent synchrotron radiation. *Nat. Commun.* **6,** 7733 (2015).

95. Abo-Bakr, M. *et al.* Brilliant, coherent far-infrared (THz) synchrotron radiation. *Phys. Rev. Lett.* **90,** 094801 (2003).

96. Barros, J. *et al.* Coherent synchrotron radiation for broadband terahertz spectroscopy. *Rev. Sci. Instrum.* **84,** 033102 (2013).

97. Zaks, B., Liu, R. B. & Sherwin, M. S. Experimental observation of electron-hole recollisions. *Nature* **483,** 580–583 (2012).

98. Banks, H. B., Hofmann, A., Mack, S., Gossard, A. C. & Sherwin, M. S. Antenna-boosted mixing of terahertz and near-infrared radiation. *Appl. Phys. Lett.* **105,** 092102 (2014).

99. Valovcin, D. C. *et al.* Optical frequency combs from high-order sideband generation. *Opt. Express* **26,** 29807–29816 (2018).

100. Dudley, J. M. & Genty, G. Supercontinuum light. *Phys. Today* **66,** 29–34 (2013).

101. Agrawal, G. *Nonlinear fiber optics (5th edition)*. *Academic Press* (2012).

102. Guo, H. *et al.* Mid-infrared frequency comb via coherent dispersive wave generation in silicon nitride nanophotonic waveguides. *Nat. Photonics* **12,** 330–335 (2018).

103. Bourbeau Hébert, N. *et al.* Self-heterodyne interference spectroscopy using a comb generated by pseudo-random modulation. *Opt. Express* **23,** 27806–27818 (2015).

104. Coluccelli, N. *et al.* The optical frequency comb fibre spectrometer. *Nat. Commun.* **7,** 12995 (2016).

105. Gohle, C., Stein, B., Schliesser, A., Udem, T. & Hänsch, T. W. Frequency comb Vernier spectroscopy for broadband, high-resolution, high-sensitivity absorption and dispersion spectra. *Phys. Rev. Lett.* **99,** 263902 (2007).

106. Diddams, S. A., Hollberg, L. & Mbele, V. Molecular fingerprinting with the resolved modes of a femtosecond laser frequency comb. *Nature* **445,** 627–630 (2007).

107. Nugent-Glandorf, L. *et al.* Mid-infrared virtually imaged phased array spectrometer for rapid and broadband trace gas detection. *Opt. Lett.* **37,** 3285–3287 (2012).

108. Griffiths, P. R. & de Haseth, J. A. *Fourier transform infrared spectrometry*. *John Wiley & Sons* (2007).

109. Mandon, J., Guelachvili, G., Picqué, N., Druon, F. & Georges, P. Femtosecond laser Fourier transform absorption spectroscopy. *Opt. Lett.* **32,** 1677–1679 (2007).

110. Mandon, J., Guelachvili, G. & Picqué, N. Fourier transform spectroscopy with a laser frequency comb. *Nat. Photonics* **3,** 99–102 (2009).

111. Hashimoto, K. & Ideguchi, T. Phase-controlled Fourier-transform spectroscopy. *Nat. Commun.* **9,** 4448 (2018).

112. Coddington, I., Newbury, N. & Swann, W. Dual-comb spectroscopy. *Optica* **3,** 414–426 (2016).

113. Schiller, S. Spectrometry with frequency combs. *Opt. Lett.* **27,** 766–768 (2002).

114. Martín-Mateos, P. New spectroscopic techniques and architectures for environmental and biomedical applications (Ph.D Dissertation). (2015).

115. Newbury, N. R., Coddington, I. & Swann, W. Sensitivity of coherent dual-comb spectroscopy. *Opt. Express* **18,** 7929–7945 (2010).

116. Ideguchi, T. Dual-comb spectroscopy. *Opt. Photonic News* **28,** 32–39 (2017).

117. van der Weide, D. & Keilmann, F. Coherent periodically pulsed radiation spectrometer (US Patent 5748309A). (1998).

118. Lee, S.-J., Widiyatmoko, B., Kourogi, M. & Ohtsu, M. Ultrahigh scanning speed optical coherence tomography using optical frequency comb generators. *Jpn. J. Appl. Phys.* **40,** 878–880 (2001).

119. Bernhardt, B. Dual comb spectroscopy (Ph.D Dissertation). (2011).

120. Coddington, I., Swann, W. C. & Newbury, N. R. Coherent multiheterodyne

spectroscopy using stabilized optical frequency combs. *Phys. Rev. Lett.* **100,** 013902 (2008).

121. Coddington, I., Swann, W. C. & Newbury, N. R. Coherent dual-comb spectroscopy at high signal-to-noise ratio. *Phys. Rev. A* **82,** 043817 (2010).

122. Kuse, N., Ozawa, A. & Kobayashi, Y. Comb-resolved dual-comb spectroscopy stabilized by free-running continuous-wave lasers. *Appl. Phys. Express* **5,** 112402 (2012).

123. Cassinerio, M., Gambetta, A., Coluccelli, N., Laporta, P. & Galzerano, G. Absolute dual-comb spectroscopy at 1.55 μm by free-running Er:fiber lasers. *Appl. Phys. Lett.* **104,** 231102 (2014).

124. Truong, G.-W. *et al.* Accurate frequency referencing for fieldable dual-comb spectroscopy. *Opt. Express* **24,** 30495–30504 (2016).

125. Chen, Z., Yan, M., Hänsch, T. W. & Picqué, N. A phase-stable dual-comb interferometer. *Nat. Commun.* **9,** 3035 (2018).

126. Long, D. A. *et al.* Multiheterodyne spectroscopy with optical frequency combs generated from a continuous-wave laser. *Opt. Lett.* **39,** 2688–2690 (2014).

127. Ideguchi, T., Nakamura, T., Kobayashi, Y. & Goda, K. Kerr-lens mode-locked bidirectional dual-comb ring laser for broadband dual-comb spectroscopy. *Optica* **3,** 748–753 (2016).

128. Villares, G. *et al.* On-chip dual-comb based on quantum cascade laser frequency combs. *Appl. Phys. Lett.* **107,** 251104 (2015).

129. Ideguchi, T., Poisson, A., Guelachvili, G., Picqué, N. & Hänsch, T. W. Adaptive real-time dual-comb spectroscopy. *Nat. Commun.* **5,** 3375 (2014).

130. Martín-Mateos, P., Jerez, B., Largo-Izquierdo, P. & Acedo, P. Frequency accurate coherent electro-optic dual-comb spectroscopy in real-time. *Opt. Express* **26,** 9700–9713 (2018).

131. Giaccari, P., Deschênes, J.-D., Saucier, P., Genest, J. & Tremblay, P. Active Fourier-transform spectroscopy combining the direct RF beating of two fiber-based mode-locked lasers with a novel referencing method. *Opt. Express* **16,** 4347–4365 (2008).

132. Deschênes, J.-D., Giaccari, P. & Genest, J. Optical referencing technique with CW lasers as intermediate oscillators for continuous full delay range frequency comb interferometry. *Opt. Express* **18,** 23358–23370 (2010).

133. Roy, J., Deschênes, J.-D., Potvin, S. & Genest, J. Continuous real-time correction and averaging for frequency comb interferometry. *Opt. Express* **20,** 21932–21939 (2012).

134. Burghoff, D., Yang, Y. & Hu, Q. Computational multiheterodyne spectroscopy. *Sci. Adv.* **2,** e1601227 (2016).

135. Sterczewski, L. A., Westberg, J. & Wysocki, G. Computational coherent averaging for free-running dual-comb spectroscopy. arXiv ID: 1805.11146 (2018).

136. Rieker, G. B. *et al.* Frequency-comb-based remote sensing of greenhouse gases over kilometer air paths. *Optica* **1,** 290–298 (2014).

137. Cossel, K. C. *et al.* Open-path dual-comb spectroscopy to an airborne retroreflector. *Optica* **4,** 724–728 (2017).

138. Coburn, S. *et al.* Regional trace gas source attribution using a field-deployed dual frequency comb spectrometer. *Optica* **5,** 320–327 (2018).

139. Schroeder, P. J. *et al.* Dual frequency comb laser absorption spectroscopy in a 16 MW gas turbine exhaust. *Proc. Combust. Inst.* **36,** 4565–4573 (2017).

140. Zhao, X. *et al.* Picometer-resolution dual-comb spectroscopy with a free-running fiber laser. *Opt. Express* **24,** 21833–21845 (2016).

141. Link, S. M. *et al.* Dual-comb modelocked laser. *Opt. Express* **23,** 5521–5531 (2015).

142. Mehravar, S., Norwood, R. A., Peyghambarian, N. & Kieu, K. Real-time dual-comb spectroscopy with a free-running bidirectionally mode-locked fiber laser. *Appl. Phys. Lett.* **108,** 231104 (2016).

143. Liu, Y. *et al.* Unidirectional, dual-comb lasing under multiple pulse formation mechanisms in a passively mode-locked fiber ring laser. *Opt. Express* **24,** 21392–21398 (2016).

144. Bourbeau Hébert, N. *et al.* Self-corrected chip-based dual-comb spectrometer. *Opt. Express* **25,** 8168–8179 (2017).

145. Posada-Roman, J. E., Angelina, H., Jerez, B., Ruiz-Llata, M. & Acedo, P. Laser range finder approach based on a fieldable electro-optic dual optical frequency comb: A proof of concept. *Appl. Opt.* **56,** 6087–6093 (2017).

146. Rösch, M. *et al.* On-chip, self-detected terahertz dual-comb source. *Appl. Phys. Lett.* **108,** 171104 (2016).

147. Dutt, A. *et al.* On-chip dual-comb source for spectroscopy. *Sci. Adv.* **4,** e1701858 (2018).

148. Suh, M.-G. & Vahala, K. J. Soliton microcomb range measurement. *Science (80-. ).* **359,** 884–887 (2018).

149. Coddington, I., Swann, W. C. & Newbury, N. R. Time-domain spectroscopy of molecular free-induction decay in the infrared. *Opt. Lett.* **35,** 1395–1397 (2010).

150. Bernhardt, B. *et al.* Cavity-enhanced dual-comb spectroscopy. *Nat. Photonics* **4,** 55–57 (2009).

151. Hoghooghi, N. *et al.* Broadband coherent cavity-enhanced dual-comb spectroscopy. *Optica* **6,** 28–33 (2019).

152. Zolot, A. M. *et al.* Direct-comb molecular spectroscopy with accurate, resolved comb teeth over 43 THz. *Opt. Lett.* **37,** 638–640 (2012).

153. Okubo, S. *et al.* Ultra-broadband dual-comb spectroscopy across 1.0-1.9 μm. *Appl.*

*Phys. Express* **8,** 082402 (2015).

154. Nürnberg, J. *et al.* An unstabilized femtosecond semiconductor laser for dual-comb spectroscopy of acetylene. *Opt. Express* **27,** 3190–3199 (2019).

155. Akosman, A. E. & Sander, M. Y. Dual comb generation from a mode-locked fiber laser with orthogonally polarized interlaced pulses. *Opt. Express* **25,** 18592–18602 (2017).

156. Zhao, X., Li, T., Liu, Y., Li, Q. & Zheng, Z. Polarization-multiplexed, dual-comb all-fiber mode-locked laser. *Photonics Res.* **6,** 853–857 (2018).

157. Olson, J., Ou, Y.-H., Azarm, A. & Kieu, K. Bi-directional mode-locked Thulium fiber laser as a single-cavity dual-comb Source. *IEEE Photonics Technol. Lett.* **30,** 1772–1775 (2018).

158. Liao, R. *et al.* Dual-comb spectroscopy with a single free-running Thulium-doped fiber laser. *Opt. Express* **26,** 11046–11054 (2018).

159. Draper, A. D. *et al.* Broadband dual frequency comb spectroscopy in a rapid compression machine. arXiv ID: 1901.11059 (2019).

160. Zolot, A. M. *et al.* Broad-band frequency references in the near-infrared: Accurate dual comb spectroscopy of methane and acetylene. *J. Quant. Spectrosc. Radiat. Transf.* **118,** 26–39 (2013).

161. Schroeder, P. J. *et al.* Speed-dependent Voigt lineshape parameter database from dual frequency comb measurements up to 1305 K. Part I: Pure $H_2O$ absorption, 6801–7188 $cm^{-1}$. *J. Quant. Spectrosc. Radiat. Transf.* **210,** 240–250 (2018).

162. Yang, J. *et al.* Speed-dependent Voigt lineshape parameter database from dual frequency comb measurements at temperatures up to 1305 K. Part II: Argon-broadened $H_2O$ absorption, 6801–7188 $cm^{-1}$. *J. Quant. Spectrosc. Radiat. Transf.* **217,** 189–212 (2018).

163. Iwakuni, K. *et al.* Ortho-para-dependent pressure effects observed in the near infrared band of acetylene by dual-comb spectroscopy. *Phys. Rev. Lett.* **117,** 143902 (2016).

164. Shimizu, Y., Okubo, S., Onae, A., Yamada, K. M. T. & Inaba, H. Molecular gas thermometry on acetylene using dual-comb spectroscopy: Analysis of rotational energy distribution. *Appl. Phys. B Lasers Opt.* **124,** 71 (2018).

165. Giorgetta, F. R. *et al.* Broadband phase spectroscopy over turbulent air paths. *Phys. Rev. Lett.* **115,** 103901 (2015).

166. Waxman, E. M. *et al.* Intercomparison of open-path trace gas measurements with two dual-frequency-comb spectrometers. *Atmos. Meas. Tech.* **10,** 3295–3311 (2017).

167. Asahara, A. *et al.* Dual-comb spectroscopy for rapid characterization of complex optical properties of solids. *Opt. Lett.* **41,** 4971–4974 (2016).

168. Kuse, N., Ozawa, A. & Kobayashi, Y. Static FBG strain sensor with high resolution

and large dynamic range by dual-comb spectroscopy. *Opt. Express* **21,** 11141–11149 (2013).

169. Bergevin, J. *et al.* Dual-comb spectroscopy of laser-induced plasmas. *Nat. Commun.* **9,** 1273 (2018).

170. Michaud-Belleau, V. *et al.* Whispering gallery mode sensing with a dual frequency comb probe. *Opt. Express* **20,** 3066–3075 (2012).

171. Cho, B., Yoon, T. H. & Cho, M. Dual-comb spectroscopy of molecular electronic transitions in condensed phases. *Phys. Rev. A* **97,** 033831 (2018).

172. Coddington, I., Swann, W. C. & Newbury, N. R. Coherent linear optical sampling at 15 bits of resolution. *Opt. Lett.* **34,** 2153–2155 (2009).

173. Minamikawa, T. *et al.* Dual-comb spectroscopic ellipsometry. *Nat. Commun.* **8,** 610 (2017).

174. Boudreau, S., Levasseur, S., Perilla, C., Roy, S. & Genest, J. Chemical detection with hyperspectral lidar using dual frequency combs. *Opt. Express* **21,** 7411–7418 (2013).

175. Kray, S., Spöler, F., Först, M. & Kurz, H. Dual femtosecond laser multiheterodyne optical coherence tomography. *Opt. Lett.* **33,** 2092–2094 (2008).

176. Wang, C. *et al.* Line-scan spectrum-encoded imaging by dual-comb interferometry. *Opt. Lett.* **43,** 1606–1609 (2018).

177. Hase, E. *et al.* Scan-less confocal phase imaging based on dual-comb microscopy. *Optica* **5,** 634–643 (2018).

178. Giorgetta, F. R., Coddington, I., Baumann, E., Swann, W. C. & Newbury, N. R. Fast high-resolution spectroscopy of dynamic continuous-wave laser sources. *Nat. Photonics* **4,** 853–857 (2010).

179. Kliebisch, O. *et al.* Unambiguous real-time terahertz frequency metrology using dual 10 GHz femtosecond frequency combs. *Optica* **5,** 1431–1437 (2018).

180. Giorgetta, F. R. *et al.* Optical two-way time and frequency transfer over free space. *Nat. Photonics* **7,** 434–438 (2013).

181. Bourbeau Hébert, N., Boudreau, S., Genest, J. & Deschênes, J.-D. Coherent dual-comb interferometry with quasi-integer-ratio repetition rates. *Opt. Express* **22,** 29152–29160 (2014).

182. Bourbeau Hébert, N., Michaud-Belleau, V., Magnan-Saucier, S., Deschênes, J.-D. & Genest, J. Dual-comb spectroscopy with a phase-modulated probe comb for sub-MHz spectral sampling. *Opt. Lett.* **41,** 2282–2285 (2016).

183. Okubo, S. *et al.* Near-infrared broadband dual-frequency-comb spectroscopy with a resolution beyond the Fourier limit determined by the observation time window. *Opt. Express* **23,** 33184–33193 (2015).

184. Nishiyama, A., Yoshida, S., Hariki, T., Nakajima, Y. & Minoshima, K. Sensitivity

improvement of dual-comb spectroscopy using mode-filtering technique. *Opt. Express* **25,** 31730–31738 (2017).

185. Wu, G., Xiong, S., Ni, K., Zhu, Z. & Zhou, Q. Parameter optimization of a dual-comb ranging system by using a numerical simulation method. *Opt. Express* **23,** 32044–32053 (2015).

186. Smith, B. C., Lomsadze, B. & Cundiff, S. T. Optimum repetition rates for dual-comb spectroscopy. *Opt. Express* **26,** 12049–12056 (2018).

187. Lay, O. P. *et al.* MSTAR: A submicrometer absolute metrology system. *Opt. Lett.* **28,** 890–892 (2003).

188. Yang, R., Pollinger, F., Meiners-Hagen, K., Tan, J. & Bosse, H. Heterodyne multi-wavelength absolute interferometry based on a cavity-enhanced electro-optic frequency comb pair. *Opt. Lett.* **39,** 5834–5837 (2014).

189. Wu, H. *et al.* Long distance measurement up to 1.2 km by electro-optic dual-comb interferometry. *Appl. Phys. Lett.* **111,** 251901 (2017).

190. Zhao, X., Qu, X., Zhang, F., Zhao, Y. & Tang, G. Absolute distance measurement by multi-heterodyne interferometry using an electro-optic triple comb. *Opt. Lett.* **43,** 807–810 (2018).

191. Weimann, C., Lauermann, M., Hoeller, F., Freude, W. & Koos, C. Silicon photonic integrated circuit for fast and precise dual-comb distance metrology. *Opt. Express* **25,** 30091–30104 (2017).

192. Weimann, C. *et al.* Fast high-precision distance metrology using a pair of modulator-generated dual-color frequency combs. *Opt. Express* **26,** 34305–34335 (2018).

193. Ferdous, F., Leaird, D. E., Huang, C.-B. & Weiner, A. M. Dual-comb electric-field cross-correlation technique for optical arbitrary waveform characterization. *Opt. Lett.* **34,** 3875–3877 (2009).

194. Durán, V., Tainta, S. & Torres-Company, V. Ultrafast electrooptic dual-comb interferometry. *Opt. Express* **23,** 30557–30569 (2015).

195. Durán, V., Andrekson, P. A. & Torres-Company, V. Electro-optic dual-comb interferometry over 40 nm bandwidth. *Opt. Lett.* **41,** 4190–4193 (2016).

196. Martín-Mateos, P., Ruiz-Llata, M., Posada-Roman, J. & Acedo, P. Dual-comb architecture for fast spectroscopic measurements and spectral characterization. *IEEE Photonics Technol. Lett.* **27,** 1309–1312 (2015).

197. Martín-Mateos, P., Jerez, B. & Acedo, P. Dual electro-optic optical frequency combs for multiheterodyne molecular dispersion spectroscopy. *Opt. Express* **23,** 21149–21158 (2015).

198. Fleisher, A. J., Long, D. A., Reed, Z. D., Hodges, J. T. & Plusquellic, D. F. Coherent cavity-enhanced dual-comb spectroscopy. *Opt. Express* **24,** 10424–10434 (2016).

199. Fleisher, A. J., Long, D. A. & Hodges, J. T. Quantitative modeling of complex

molecular response in coherent cavity-enhanced dual-comb spectroscopy. *J. Mol. Spectrosc.* **352,** 26–35 (2018).

200. Millot, G. *et al.* Frequency-agile dual-comb spectroscopy. *Nat. Photonics* **10,** 27–30 (2016).

201. Wang, S., Fan, X., Xu, B. & He, Z. Dense electro-optic frequency comb generated by two-stage modulation for dual-comb spectroscopy. *Opt. Lett.* **42,** 3984–3987 (2017).

202. Carlson, D. R., Hickstein, D. D., Diddams, S. A. & Papp, S. B. High-speed ultra-broadband dual-comb spectroscopy using electro-optics. in *The Conference on Lasers and Electro-Optics* paper SW4L.2 (2018).

203. Posada-Roman, J. E., García-Souto, J. A., Poiana, D. A. & Acedo, P. Fast interrogation of fiber bragg gratings with electro-optical dual optical frequency combs. *Sensors* **16,** 1–11 (2016).

204. Bonilla-Manrique, O. E., Martín-Mateos, P., Jerez, B., Ruiz-Llata, M. & Acedo, P. High-resolution optical thickness measurement based on electro-optic dual-optical frequency comb sources. *IEEE J. Sel. Top. Quantum Electron.* **23,** 5300107 (2017).

205. Teleanu, E. L., Durán, V. & Torres-Company, V. Electro-optic dual-comb interferometer for high-speed vibrometry. *Opt. Express* **25,** 16427–16436 (2017).

206. Wang, S., Xu, B., Fan, X. & He, Z. Linear optical sampling technique for simultaneously characterizing WDM signals with a single receiving channel. *Opt. Express* **26,** 2089–2098 (2018).

207. Wang, S., Fan, X., Xu, B. & He, Z. Fast MHz-spectral-resolution dual-comb spectroscopy with electro-optic modulators. *Opt. Lett.* **44,** 65–68 (2019).

208. Kang, J. *et al.* Video-rate centimeter-range optical coherence tomography based on dual optical frequency combs by electro-optic modulators. *Opt. Express* **26,** 24928–24939 (2018).

209. Guay, P., Genest, J. & Fleisher, A. J. Precision spectroscopy of $H^{13}CN$ using a free-running, all-fiber dual electro-optic frequency comb system. *Opt. Lett.* **43,** 1407–1410 (2018).

210. Bourbeau Hébert, N. *et al.* Real-time dynamic atomic spectroscopy using electro-optic frequency combs. *Phys. Rev. Appl.* **6,** 044012 (2016).

211. Durán, V., Schnébelin, C. & de Chatellus, H. G. Coherent multi-heterodyne spectroscopy using acousto-optic frequency combs. *Opt. Express* **26,** 13800–13809 (2018).

212. Carlson, D. R., Hickstein, D. D., Cole, D. C., Diddams, S. A. & Papp, S. B. Dual-comb interferometry via repetition rate switching of a single frequency comb. *Opt. Lett.* **43,** 3614–3617 (2018).

213. Kayes, M. I. & Rochette, M. Fourier transform spectroscopy by repetition rate sweeping of a single electro-optic frequency comb. *Opt. Lett.* **43,** 967–970 (2018).

214. Wang, S. *et al.* Hybrid dual-comb interferometer with easily established mutual coherence and a very high refresh rate. *Opt. Lett.* **43,** 3441–3444 (2018).

215. Suh, M.-G., Yang, Q.-F., Yang, K. Y., Yi, X. & Vahala, K. J. Microresonator soliton dual-comb spectroscopy. *Science (80-. ).* **354,** 600–6003 (2016).

216. Yang, Q.-F., Yi, X., Yang, K. Y. & Vahala, K. Counter-propagating solitons in microresonators. *Nat. Photonics* **11,** 560–564 (2017).

217. Lucas, E. *et al.* Spatial multiplexing of soliton microcombs. *Nat. Photonics* **12,** 699–705 (2018).

218. Pavlov, N. G. *et al.* Soliton dual frequency combs in crystalline microresonators. *Opt. Lett.* **42,** 514–517 (2017).

219. Wang, W. *et al.* Self-locked orthogonal polarized dual comb in a microresonator. *Photonics Res.* **6,** 363–367 (2018).

220. Suzuki, R., Fujii, S., Hori, A. & Tanabe, T. Theoretical study on dual-comb generation and soliton trapping in a single microresonator with orthogonally polarized dual-pumping. *IEEE Photonics J.* **11,** 6100511 (2019).

221. Trocha, P. *et al.* Ultrafast optical ranging using microresonator soliton frequency combs. *Science (80-. ).* **359,** 887–891 (2018).

222. Marin-Palomo, P. *et al.* Microresonator-based solitons for massively parallel coherent optical communications. *Nature* **546,** 274–279 (2017).

223. Bao, C., Suh, M.-G. & Vahala, K. Microresonator soliton dual-comb imaging. arXiv ID: 1809.09766 (2018).

224. Yang, Q.-F. *et al.* Vernier spectrometer using counter-propagating soliton microcombs. arXiv ID: 1811.12925 (2018).

225. Armstrong, J. A., Bloembergen, N., Ducuing, J. & Pershan, P. S. Interactions between light waves in a nonlinear dielectric. *Phys. Rev.* **127,** 1918–1939 (1962).

226. Hum, D. S. & Fejer, M. M. Quasi-phasematching. *Comptes Rendus Phys.* **8,** 180–198 (2007).

227. Maidment, L. *et al.* Long-wave infrared generation from femtosecond and picosecond optical parametric oscillators based on orientation-patterned gallium phosphide. *Appl. Phys. B Lasers Opt.* **124,** 143 (2018).

228. Keilmann, F., Gohle, C. & Holzwarth, R. Time-domain mid-infrared frequency-comb spectrometer. *Opt. Lett.* **29,** 1542–1544 (2004).

229. Schliesser, A., Brehm, M., Keilmann, F. & van der Weide, D. Frequency-comb infrared spectrometer for rapid, remote chemical sensing. *Opt. Express* **13,** 9029–9038 (2005).

230. Brehm, M., Schliesser, A. & Keilmann, F. Spectroscopic near-field microscopy using frequency combs in the mid-infrared. *Opt. Express* **14,** 11222–11233 (2006).

231. Ganz, T., Brehm, M., von Ribbeck, H.-G., van der Weide, D. W. & Keilmann, F. Vector frequency-comb Fourier-transform spectroscopy for characterizing metamaterials. *New J. Phys.* **10,** 123007 (2008).

232. Baumann, E. *et al.* Spectroscopy of the methane ν3 band with an accurate midinfrared coherent dual-comb spectrometer. *Phys. Rev. A* **84,** 062513 (2011).

233. Zhu, F. *et al.* Mid-infrared dual frequency comb spectroscopy based on fiber lasers for the detection of methane in ambient air. *Laser Phys. Lett.* **12,** 095701 (2015).

234. Cruz, F. C. *et al.* Mid-infrared optical frequency combs based on difference frequency generation for molecular spectroscopy. *Opt. Express* **23,** 26814–26824 (2015).

235. Ycas, G. *et al.* High-coherence mid-infrared dual-comb spectroscopy spanning 2.6 to 5.2 μm. *Nat. Photonics* **12,** 202–208 (2018).

236. Ycas, G. *et al.* Mid-infrared dual-comb spectroscopy of volatile organic compounds across long open-air paths. *Optica* **6,** 165–168 (2019).

237. Lind, A. J. *et al.* χ(2) mid-infrared frequency comb generation and stabilization with few-cycle pulses. arXiv ID: 1811.02604 (2018).

238. Yan, M. *et al.* Mid-infrared dual-comb spectroscopy with electro-optic modulators. *Light Sci. Appl.* **6,** e17076 (2017).

239. Herman, D. I. *et al.* Real-time liquid-phase organic reaction monitoring with mid-infrared attenuated total reflectance dual frequency comb spectroscopy. *J. Mol. Spectrosc.* **356,** 39–45 (2019).

240. Nader, N. *et al.* Versatile silicon-waveguide supercontinuum for coherent mid-infrared spectroscopy. *APL Photonics* **3,** 036102 (2018).

241. Baumann, E. *et al.* Dual-comb spectroscopy with tailored spectral broadening in Si3N4 nanophotonics. arXiv ID: 1811.05906 (2018).

242. Timmers, H. *et al.* Molecular fingerprinting with bright, broadband infrared frequency combs. *Optica* **5,** 727–732 (2018).

243. Kowligy, A. *et al.* Infrared electric-field sampled frequency comb spectroscopy. arXiv ID: 1808.10275 (2018).

244. Zhang, Z. *et al.* Asynchronous midinfrared ultrafast optical parametric oscillator for dual-comb spectroscopy. *Opt. Lett.* **37,** 187–189 (2012).

245. Zhang, Z., Fang, X., Gardiner, T. & Reid, D. T. High-power asynchronous midinfrared optical parametric oscillator frequency combs. *Opt. Lett.* **38,** 2077–2079 (2013).

246. Zhang, Z., Gardiner, T. & Reid, D. T. Mid-infrared dual-comb spectroscopy with an optical parametric oscillator. *Opt. Lett.* **38,** 3148–3150 (2013).

247. Jin, Y., Cristescu, S. M., Harren, F. J. M. & Mandon, J. Two-crystal mid-infrared optical parametric oscillator for absorption and dispersion dual-comb spectroscopy.

*Opt. Lett.* **39,** 3270–3273 (2014).

248. Jin, Y., Cristescu, S. M., Harren, F. J. M. & Mandon, J. Femtosecond optical parametric oscillators toward real-time dual-comb spectroscopy. *Appl. Phys. B Lasers Opt.* **119,** 65–74 (2015).

249. Khodabakhsh, A., Mandon, J., Pan, Q., Abbas, M. A. & Harren, F. J. M. Mid-infrared dual-comb spectroscopy in an electrical discharge. in *Light, Energy and the Environment* paper FM2B.5 (2018).

250. Kara, O., Zhang, Z., Gardiner, T. & Reid, D. T. Dual-comb mid-infrared spectroscopy with free-running oscillators and absolute optical calibration from a radio-frequency reference. *Opt. Express* **25,** 16072–16082 (2017).

251. Kara, O., Maidment, L., Gardiner, T., Schunemann, P. G. & Reid, D. T. Dual-comb spectroscopy in the spectral fingerprint region using OPGaP optical parametric oscillators. *Opt. Express* **25,** 32713–32721 (2017).

252. Muraviev, A. V., Smolski, V. O., Loparo, Z. E. & Vodopyanov, K. L. Massively parallel sensing of trace molecules and their isotopologues with broadband subharmonic mid-infrared frequency combs. *Nat. Photonics* **12,** 209–214 (2018).

253. Tomberg, T., Muraviev, A., Ru, Q. & Vodopyanov, K. L. Background-free broadband absorption spectroscopy based on interferometric suppression with a sign-inverted waveform. *Optica* **6,** 147–151 (2019).

254. Parriaux, A., Hammani, K. & Millot, G. Two-micron all-fibered dual-comb spectrometer based on electro-optic modulators and wavelength conversion. *Commun. Phys.* **1,** 17 (2018).

255. Villares, G., Hugi, A., Blaser, S. & Faist, J. Dual-comb spectroscopy based on quantum-cascade-laser frequency combs. *Nat. Commun.* **5,** 5192 (2014).

256. Wang, Y., Soskind, M. G., Wang, W. & Wysocki, G. High-resolution multi-heterodyne spectroscopy based on Fabry-Perot quantum cascade lasers. *Appl. Phys. Lett.* **104,** 031114 (2014).

257. Hangauer, A., Westberg, J., Zhang, E. & Wysocki, G. Wavelength modulated multiheterodyne spectroscopy using Fabry-Pérot quantum cascade lasers. *Opt. Express* **24,** 25298–25307 (2016).

258. Sterczewski, L. A., Westberg, J. & Wysocki, G. Molecular dispersion spectroscopy based on Fabry-Perot quantum cascade lasers. *Opt. Lett.* **42,** 243–246 (2017).

259. Westberg, J., Sterczewski, L. A. & Wysocki, G. Mid-infrared multiheterodyne spectroscopy with phase-locked quantum cascade lasers. *Appl. Phys. Lett.* **110,** 141108 (2017).

260. Jouy, P. *et al.* Dual comb operation of $\lambda$~8.2 μm quantum cascade laser frequency comb with 1 W optical power. *Appl. Phys. Lett.* **111,** 141102 (2017).

261. Lu, Q. Y., Manna, S., Wu, D. H., Slivken, S. & Razeghi, M. Shortwave quantum

cascade laser frequency comb for multi-heterodyne spectroscopy. *Appl. Phys. Lett.* **112,** 141104 (2018).

262. Westberg, J. *et al.* Dual-comb spectroscopy using plasmon-enhanced-waveguide dispersion-compensated quantum cascade lasers. *Opt. Lett.* **43,** 4522–4525 (2018).

263. Hillbrand, J., Andrews, A. M., Detz, H., Strasser, G. & Schwarz, B. Coherent injection locking of quantum cascade laser frequency combs. *Nat. Photonics* **13,** 101–104 (2019).

264. Klocke, J. L. *et al.* Single-shot sub-microsecond mid-infrared spectroscopy on protein reactions with quantum cascade laser frequency combs. *Anal. Chem.* **90,** 10494–10500 (2018).

265. Bagheri, M. *et al.* Passively mode-locked interband cascade optical frequency combs. *Sci. Rep.* **8,** 3322 (2018).

266. Sterczewski, L. A. *et al.* Multiheterodyne spectroscopy using interband cascade lasers. *Opt. Eng.* **57,** 011014 (2018).

267. Mirov, S. B. *et al.* Progress in mid-IR lasers based on Cr and Fe-doped II-VI chalcogenides. *IEEE J. Sel. Top. Quantum Electron.* **21,** 1601719 (2015).

268. Bernhardt, B. *et al.* Mid-infrared dual-comb spectroscopy with 2.4 μm $Cr^{2+}$:ZnSe femtosecond lasers. *Appl. Phys. B Lasers Opt.* **100,** 3–8 (2010).

269. Duval, S. *et al.* Femtosecond fiber lasers reach the mid-infrared. *Optica* **2,** 623–626 (2015).

270. Yu, M. *et al.* Silicon-chip-based mid-infrared dual-comb spectroscopy. *Nat. Commun.* **9,** 1869 (2018).

271. Tonouchi, M. Cutting-edge terahertz technology. *Nat. Photonics* **1,** 97–105 (2007).

272. Janke, C., Först, M., Nagel, M., Kurz, H. & Bartels, A. Asynchronous optical sampling for high-speed characterization of integrated resonant terahertz sensors. *Opt. Lett.* **30,** 1405–1407 (2005).

273. Yasui, T., Saneyoshi, E. & Araki, T. Asynchronous optical sampling terahertz time-domain spectroscopy for ultrahigh spectral resolution and rapid data acquisition. *Appl. Phys. Lett.* **87,** 061101 (2005).

274. Yasui, T., Kabetani, Y., Saneyoshi, E., Yokoyama, S. & Araki, T. Terahertz frequency comb by multifrequency-heterodyning photoconductive detection for high-accuracy, high-resolution terahertz spectroscopy. *Appl. Phys. Lett.* **88,** 241104 (2006).

275. Elzinga, P. A. *et al.* Pump/probe method for fast analysis of visible spectral signatures utilizing asynchronous optical sampling. *Appl. Opt.* **26,** 4303–4309 (1987).

276. Bartels, A. *et al.* High-resolution THz spectrometer with kHz scan rates. *Opt. Express* **14,** 430–437 (2006).

277. Bartels, A. *et al.* Ultrafast time-domain spectroscopy based on high-speed asynchronous optical sampling. *Rev. Sci. Instrum.* **78,** 035107 (2007).

278. Gebs, R., Klatt, G., Janke, C., Dekorsy, T. & Bartels, A. High-speed asynchronous optical sampling with sub-50fs time resolution. *Opt. Express* **18,** 5974–5983 (2010).

279. Klatt, G., Gebs, R., Janke, C., Dekorsy, T. & Bartels, A. Rapid-scanning terahertz precision spectrometer with more than 6 THz spectral coverage. *Opt. Express* **17,** 22847–22854 (2009).

280. Finneran, I. A. *et al.* Decade-spanning high-precision terahertz frequency comb. *Phys. Rev. Lett.* **114,** 163902 (2015).

281. Kliebisch, O., Heinecke, D. C. & Dekorsy, T. Ultrafast time-domain spectroscopy system using 10 GHz asynchronous optical sampling with 100 kHz scan rate. *Opt. Express* **24,** 29930–29940 (2016).

282. von Ribbeck, H.-G. *et al.* Spectroscopic THz near-field microscope. *Opt. Express* **16,** 3430–3438 (2008).

283. Klatt, G., Nagel, M., Dekorsy, T. & Bartels, A. Rapid and precise read-out of terahertz sensor by high-speed asynchronous optical sampling. *Electron. Lett.* **45,** 310–311 (2009).

284. Yokoyama, S., Yokoyama, T., Hagihara, Y., Araki, T. & Yasui, T. A distance meter using a terahertz intermode beat in an optical frequency comb. *Opt. Express* **17,** 17324–17337 (2009).

285. Yasui, T., Kabetani, Y., Ohgi, Y., Yokoyama, S. & Araki, T. Absolute distance measurement of optically rough objects using asynchronous-optical-sampling terahertz impulse ranging. *Appl. Opt.* **49,** 5262–5270 (2010).

286. Klatt, G. *et al.* High-resolution terahertz spectrometer. *IEEE J. Sel. Top. Quantum Electron.* **17,** 159–168 (2011).

287. Good, J. T. *et al.* A decade-spanning high-resolution asynchronous optical sampling terahertz time-domain and frequency comb spectrometer. *Rev. Sci. Instrum.* **86,** 103107 (2015).

288. Gebs, R. *et al.* Time-domain terahertz spectroscopy based on asynchronous optical sampling with femtosecond semiconductor disk laser. *Electron. Lett.* **46,** 75–77 (2010).

289. Yasui, T. *et al.* Fiber-based, hybrid terahertz spectrometer using dual fiber combs. *Opt. Lett.* **35,** 1689–1691 (2010).

290. Yasui, T. *et al.* Enhancement of spectral resolution and accuracy in asynchronous-optical-sampling terahertz time-domain spectroscopy for low-pressure gas-phase analysis. *Opt. Express* **20,** 15071–15078 (2012).

291. Hsieh, Y.-D. *et al.* Terahertz comb spectroscopy traceable to microwave frequency standard. *IEEE Trans. Terahertz Sci. Technol.* **3,** 322–330 (2013).

292. Hsieh, Y.-D. *et al.* Dynamic terahertz spectroscopy of gas molecules mixed with unwanted aerosol under atmospheric pressure using fibre-based asynchronous-optical-sampling terahertz time-domain spectroscopy. *Sci. Rep.* **6,** 28114 (2016).

293. Yasui, T. *et al.* Real-time absolute frequency measurement of continuous-wave terahertz radiation based on dual terahertz combs of photocarriers with different frequency spacings. *Opt. Express* **23,** 11367–11377 (2015).

294. Hsieh, Y.-D. *et al.* Spectrally interleaved, comb-mode-resolved spectroscopy using swept dual terahertz combs. *Sci. Rep.* **4,** 3816 (2014).

295. Yasui, T. *et al.* Super-resolution discrete Fourier transform spectroscopy beyond time-window size limitation using precisely periodic pulsed radiation. *Optica* **2,** 460–467 (2015).

296. Vieira, F. S., Cruz, F. C., Plusquellic, D. F. & Diddams, S. A. Tunable resolution terahertz dual frequency comb spectrometer. *Opt. Express* **24,** 30100–30107 (2016).

297. Yasui, T. *et al.* Adaptive sampling dual terahertz comb spectroscopy using dual free-running femtosecond lasers. *Sci. Rep.* **5,** 10786 (2015).

298. Hu, G. *et al.* Measurement of absolute frequency of continuous-wave terahertz radiation in real time using a free-running, dual-wavelength mode-locked, erbium-doped fibre laser. *Sci. Rep.* **7,** 42082 (2017).

299. Hu, G. *et al.* Dual terahertz comb spectroscopy with a single free-running fibre laser. *Sci. Rep.* **8,** 11155 (2018).

300. Baker, R. D., Yardimci, N. T., Ou, Y.-H., Kieu, K. & Jarrahi, M. Self-triggered asynchronous optical sampling terahertz spectroscopy using a bidirectional mode-locked fiber laser. *Sci. Rep.* **8,** 14802 (2018).

301. Rösch, M. *et al.* Heterogeneous terahertz quantum cascade lasers exceeding 1.9 THz spectral bandwidth and featuring dual comb operation. *Nanophotonics* **7,** 237–242 (2018).

302. Yang, Y. *et al.* Terahertz multiheterodyne spectroscopy using laser frequency combs. *Optica* **3,** 499–503 (2016).

303. Westberg, J. *et al.* Terahertz dual-comb spectroscopy using quantum cascade laser frequency combs. in *The Conference on Lasers and Electro-Optics* paper STu4D.2 (2018).

304. Sterczewski, L. A. *et al.* Terahertz hyperspectral imaging with dual chip-scale combs. arXiv ID: 1812.03505 (2018).

305. Ideguchi, T., Poisson, A., Guelachvili, G., Hänsch, T. W. & Picqué, N. Adaptive dual-comb spectroscopy in the green region. *Opt. Lett.* **37,** 4847–4849 (2012).

306. Potvin, S. & Genest, J. Dual-comb spectroscopy using frequency-doubled combs around 775 nm. *Opt. Express* **21,** 30707–30715 (2013).

307. Long, D. A., Fleisher, A. J., Plusquellic, D. F. & Hodges, J. T. Multiplexed sub-Doppler spectroscopy with an optical frequency comb. *Phys. Rev. A* **94,** 061801 (2016).

308. Long, D. A., Fleisher, A. J., Plusquellic, D. F. & Hodges, J. T. Electromagnetically induced transparency in vacuum and buffer gas potassium cells probed via electro-

optic frequency combs. *Opt. Lett.* **42,** 4430–4433 (2017).

309. Long, D. A., Fleisher, A. J. & Hodges, J. T. Direct frequency comb saturation spectroscopy with an ultradense tooth spacing of 100 Hz. arXiv ID: 1812.09342 (2018).

310. Carlson, D. R., Wu, T.-H. & Jones, R. J. Dual-comb intracavity high harmonic generation for precision spectroscopy in the XUV. in *The Conference on Lasers and Electro-Optics* paper ED_2_2 (2015).

311. Glenn, R. & Mukamel, S. Nonlinear transmission spectroscopy with dual frequency combs. *Phys. Rev. A* **90,** 023804 (2014).

312. Bennett, K., Rouxel, J. R. & Mukamel, S. Linear and nonlinear frequency- and time-domain spectroscopy with multiple frequency combs. *J. Chem. Phys.* **147,** 094304 (2017).

313. Jeon, J., Kim, J. W., Yoon, T. H. & Cho, M. Dual frequency comb photon echo spectroscopy. *J. Opt. Soc. Am. B* **32,** 223–234 (2019).

314. Ideguchi, T., Bernhardt, B., Guelachvili, G., Hänsch, T. W. & Picqué, N. Raman-induced Kerr-effect dual-comb spectroscopy. *Opt. Lett.* **37,** 4498–4500 (2012).

315. Ideguchi, T. *et al.* Coherent Raman spectro-imaging with laser frequency combs. *Nature* **502,** 355–358 (2013).

316. Mohler, K. J. *et al.* Dual-comb coherent Raman spectroscopy with lasers of 1-GHz pulse repetition frequency. *Opt. Lett.* **42,** 318–321 (2017).

317. Ideguchi, T. *et al.* Microfluidic single-particle chemical analyzer with dual-comb coherent Raman spectroscopy. *Opt. Lett.* **43,** 4057–4060 (2018).

318. Chen, K. *et al.* Spectral focusing dual-comb coherent anti-Stokes Raman spectroscopic imaging. *Opt. Lett.* **42,** 3634–3637 (2017).

319. Coluccelli, N. *et al.* Fiber-format dual-comb coherent Raman spectrometer. *Opt. Lett.* **42,** 4683–4686 (2017).

320. Carlson, D. R., Hickstein, D. D., Diddams, S. A. & Papp, S. B. An ultrafast electro-optic dual comb for linear and nonlinear spectroscopy. in *Light, Energy and the Environment* paper FT4B.2 (2018).

321. Hipke, A., Meek, S. A., Ideguchi, T., Hänsch, T. W. & Picqué, N. Broadband Doppler-limited two-photon and stepwise excitation spectroscopy with laser frequency combs. *Phys. Rev. A* **90,** 011805 (2014).

322. Meek, S. A., Hipke, A., Guelachvili, G., Hänsch, T. W. & Picqué, N. Doppler-free Fourier transform spectroscopy. *Opt. Lett.* **43,** 162–165 (2018).

323. Nishiwaya, A., Nakajima, Y., Nakagawa, K. & Minoshima, K. Precise and highly-sensitive Doppler-free two-photon absorption dual-comb spectroscopy using pulse shaping and coherent averaging for fluorescence signal detection. *Opt. Express* **26,** 8957–8967 (2018).

324. Asahara, A. & Minoshima, K. Development of ultrafast time-resolved dual-comb spectroscopy. *APL Photonics* **2,** 041301 (2017).

325. Kim, J. W., Cho, B., Yoon, T. H. & Cho, M. Dual-frequency comb transient absorption: Broad dynamic range measurement of femtosecond to nanosecond relaxation processes. *J. Phys. Chem. Lett.* **9,** 1866–1871 (2018).

326. Kim, J. W., Yoon, T. H. & Cho, M. Interferometric measurement of transient absorption and refraction spectra with dual frequency comb. *J. Phys. Chem. B* **122,** 9775–9785 (2018).

327. Lomsadze, B. & Cundiff, S. T. Frequency comb-based four-wave-mixing spectroscopy. *Opt. Lett.* **42,** 2346–2349 (2017).

328. Lomsadze, B. & Cundiff, S. T. Frequency combs enable rapid and high-resolution multidimensional coherent spectroscopy. *Science (80-. ).* **357,** 1389–1391 (2017).

329. Lomsadze, B. & Cundiff, S. T. Multi-heterodyne two dimensional coherent spectroscopy using frequency combs. *Sci. Rep.* **7,** 14018 (2017).

330. Lomsadze, B., Smith, B. C. & Cundiff, S. T. Tri-comb spectroscopy. *Nat. Photonics* **12,** 676–680 (2018).

331. Stover, H. L. & Steier, W. H. Locking of laser oscillators by light injection. *Appl. Phys. Lett.* **8,** 91–93 (1966).

332. Kobayashi, S. & Kimura, T. Injection locking characteristics of an AlGaAs semiconductor laser. *IEEE J. Quantum Electron.* **16,** 915–917 (1980).

333. Lau, E. K., Wong, L. J. & Wu, M. C. Enhanced modulation characteristics of optical injection-locked lasers: A tutorial. *IEEE J. Sel. Top. Quantum Electron.* **15,** 618–633 (2009).

334. Wieczorek, S., Krauskopf, B., Simpson, T. B. & Lenstra, D. The dynamical complexity of optically injected semiconductor lasers. *Phys. Rep.* **416,** 1–128 (2005).

335. Herbert, C. *et al.* Discrete mode lasers for communication applications. *IET Optoelectron.* **3,** 1–17 (2009).

336. O'Dúill, S. P., Zhou, R., Anandarajah, P. M. & Barry, L. P. Analytical approach to assess the impact of pulse-to-pulse phase coherence of optical frequency combs. *IEEE J. Quantum Electron.* **51,** 1200208 (2015).

337. Gilbert, S. L., Swann, W. C. & Wang, C. M. *Hydrogen cyanide $H^{13}C^{14}N$ absorption reference for 1530 nm to 1565 nm wavelength calibration - SRM 2519a. National Institute of Standards and Technology. Special Publication 260-137* (2005).

338. Hodgkinson, J. & Tatam, R. P. Optical gas sensing: A review. *Meas. Sci. Technol.* **24,** 012004 (2013).

339. Riley, W. J. *Handbook of frequency stability analysis. NIST Special Publication 1065* (2008).

340. Browning, C. *et al.* Gain-switched optical frequency combs for future mobile radio-over-fiber millimeter-wave systems. *J. Light. Technol.* **36,** 4602–4610 (2018).

341. Fan, L. *et al.* Tunable ultra-broadband microwave frequency combs generation based on a current modulated semiconductor laser under optical injection. *IEEE Access* **5,** 17764–17771 (2017).

342. Chandran, S., Mahon, S., Ruth, A. A., Braddell, J. & Gutierrez, M. D. Cavity-enhanced absorption detection of $H_2S$ in the near-infrared using a gain-switched frequency comb laser. *Appl. Phys. B Lasers Opt.* **124,** 63 (2018).

343. Bordonalli, A. C., Fice, M. J. & Seeds, A. J. Optical injection locking to optical frequency combs for superchannel coherent detection. *Opt. Express* **23,** 1547–1557 (2015).

344. Wu, D. S., Slavik, R., Marra, G. & Richardson, D. J. Direct selection and amplification of individual narrowly spaced optical comb modes via injection locking: Design and characterization. *J. Light. Technol.* **31,** 2287–2295 (2013).

345. Richter, D., Fried, A. & Weibring, P. Difference frequency generation laser based spectrometers. *Laser Photonics Rev.* **3,** 343–354 (2009).

346. Zondy, J. J. The effects of focusing in type-I and type-II difference-frequency generations. *Opt. Commun.* **149,** 181–206 (1998).

347. Chu, T.-B. & Broyer, M. Intracavity cw difference frequency generation by mixing three photons and using Gaussian laser beams. *J. Phys.* **46,** 523–533 (1985).

348. Richter, D. & Weibring, P. Ultra-high precision mid-IR spectrometer I: Design and analysis of an optical fiber pumped difference-frequency generation source. *Appl. Phys. B Lasers Opt.* **82,** 479–486 (2006).

349. Martín-Mateos, P., Porro, A. & Acedo, P. Fully adaptable electro-optic dual-comb generation. *IEEE Photonics Technol. Lett.* **30,** 161–164 (2018).

350. Rothman, L. S. *et al.* The HITRAN2012 molecular spectroscopic database. *J. Quant. Spectrosc. Radiat. Transf.* **130,** 4–50 (2013).

351. Liu, Z. *et al.* Room-temperature continuous-wave quantum cascade lasers grown by MOCVD without lateral regrowth. *IEEE Photonics Technol. Lett.* **18,** 1347–1349 (2006).

352. Richter, D. *et al.* High-power, tunable difference frequency generation source for absorption spectroscopy based on a ridge waveguide periodically poled lithium niobate crystal. *Opt. Express* **15,** 564–571 (2007).

353. Schunemann, P. G., Zawilski, K. T., Pomeranz, L. A., Creeden, D. J. & Budni, P. A. Advances in nonlinear optical crystals for mid-infrared coherent sources. *J. Opt. Soc. Am. B* **33,** D36–D42 (2016).

354. Hinkov, B., Hugi, A., Beck, M. & Faist, J. Rf-modulation of mid-infrared distributed feedback quantum cascade lasers. *Opt. Express* **24,** 3294–3312 (2016).

355. Fortier, T. M. *et al.* Generation of ultrastable microwaves via optical frequency

division. *Nat. Photonics* **5,** 425–429 (2011).

356. Ishibashi, T., Muramoto, Y., Yoshimatsu, T. & Ito, H. Unitraveling-carrier photodiodes for terahertz applications. *IEEE J. Sel. Top. Quantum Electron.* **20,** 3804210 (2014).

357. Dhillon, S. S. *et al.* The 2017 terahertz science and technology roadmap. *J. Phys. D. Appl. Phys.* **50,** 043001 (2017).

358. TOPTICA Photonics. *http://www.toptica.com/products/terahertz-systems.* Last Accessed 02/2019.

# ABOUT THE AUTHOR

Borja Jerez González was born in Madrid in 1991. He received the B.Sc. degree in Industrial Electronics and Automation Engineering, and the M.Sc. degree in Industrial Engineering from the Universidad Carlos III Madrid, Spain, both with honours, in 2013 and 2015, respectively.

Since 2013, he has been working in the Electronics Technology Department at the same university. His research interests include the analysis and design of optical frequency combs and dual-comb architectures for their use in a range of applications such as the detection of volatile organic compounds or the measurement of fibre sensors.

In 2015, he was granted a scholarship for the realization of the doctoral thesis by the Spanish Ministry of Education, Culture and Sports. During the Ph.D he worked in the implementation of versatile, target-specific dual-comb systems in various regions of the electromagnetic spectrum (Near-Infrared, Mid-Infrared and the THz range) and the further demonstration of their feasibility using a number of laser devices, advanced optical techniques and samples under test.

In his free time, he enjoys travelling, spending time with friends and of course, having a good meal. He is also deeply interested in sport, fitness and healthy lifestyle.

Borja is also a fervent supporter of the greatest football team in history: Real Madrid.